UNIVERSITY OF BELGRADE
FACULTY OF PHYSICS

Aleksandar V. Matković

INVESTIGATING THE OPTICAL PROPERTIES OF GRAPHENE WITH SPECTROSCOPIC ELLIPSOMETRY

dissertation

Belgrade, 2015

UNIVERZITET U BEOGRADU
FIZIČKI FAKULTET

Aleksandar V. Matković

ISPITIVANjE OPTIČKIH OSOBINA GRAFENA POMOĆU SPEKTROSKOPSKE ELIPSOMETRIJE

doktorska disertacija

Beograd, 2015

Mentor:

dr Radoš Gajić,
naučni savetnik,
Institut za fiziku, Univerzitet u Beogradu

Članovi komisije:

dr Ivanka Milošević,
redovni profesor
Fizički fakultet, Univerzitet u Beogradu

dr Ivan Belča,
vanredni profesor
Fizički fakultet, Univerzitet u Beogradu

dr Zoran Radović,
redovni profesor u penziji
Fizički fakultet, Univerzitet u Beogradu

Datum odbrane:

Acknowledgements

First, I would like to thank my mentor Prof. dr. Radoš Gajić. I have been able to experience diverse aspects of research throughout my PhD studies with his guidance. I have had freedom to work on my own ideas and projects, which helped me a lot to become an independent researcher. More than that, what I have learned from him is his great passion for both science and creative thinking. I am thankful to graduate under his guidance.

I am grateful to my colleagues dr. Borislav Vasić, dr. Goran Isić and dr. Marko Spasenović, who have helped me many times during my studies through fruitful discussions, comments, advices, and ideas.

I would like to thank my colleagues and fellow PhD students Angela Beltaos, Marijana Milićević and Uroš Ralević with whom I have started experimental work on graphene exfoliation, device fabrication, infrared spectroscopy and spectroscopic ellipsometry.

Also, I would like to thank all the colleagues from Center of Solid State Physics and New Materials, and its Graphene Laboratory for their help and for creating a friendly work environment. Specially I would like to express my gratitude to the head of the center of Solid State Physics and New Materials Professor Zoran Popović.

Furthermore, I am grateful to Professor Nebojša Romčević for his support in writing a project proposal and for all the help in managing the industry project "Graphene based functional inks and printing of Radio-frequency identification tags".

I would like to thank Professor Milivoj R. Belić from Texas A&M University at Qatar, for helpful discussions, comments and suggestions, and for his support during preparation of the thesis.

I would like to acknowledge financial support by the Serbian Ministry of Science through Projects OI 171005, III 45018, by the EU FP7 project NIM_NIL (gr. a. No 228637 NIM_NIL: www.nimnil.org), and by Qatar National Research Foundation through Project NPRP 7-665-1-125.

I am grateful to the spin-off company of the Institute of Physics, Senzor Infiz d.o.o. for giving me the access and training for their photolithography equipment. Also I would like to thank the Centre of Microelectronic Technologies and Single Crystals,

a Division of the Institute of Chemistry, Technology and Metallurgy, University of Belgrade, in particular to dr Milče Smiljanić and Žarko Lazić for their help regrading graphene device fabrication, and to the head of the centre Professor Dana Vasiljević-Radović for enabling the collaboration.

I would like to thank company Accurion GmbH, in particular to Arash Mirhamed for the imaging ellipsometry measurements, to dr. Peter Thiesen for helpful discussions, comments and suggestions, and to Stephan Ferneding the CEO of Accurion.

I would like to thank Manisha Chhikara and to her supervisor Prof. dr. Gvido Bratina, from University of Nova Gorica, Slovenia. A fruitful collaboration between our research groups have resulted with several joint publications, and was essential for my dissertation. In particular I am thankful to Miss Chhikara, for preparation of numerous samples of CVD graphene that I have used in my research, as well as for helpful discussions, comments and suggestions.

I am grateful to my family for their support and understanding.

Last but not least, I would like to thank a very special person, Dragana. Thank you for your love, unconditional support, for believing in me, and for sticking with me through my entire studies. Without your support I would never decide to pursuit a scientific career.

Podaci o doktorskoj disertaciji

Naslov doktorske disertacije

ISPITIVANjE OPTIČKIH OSOBINA GRAFENA
POMOĆU SPEKTROSKOPSKE ELIPSOMETRIJE

Rezime

Disertacija se bavi problemom merenja optičkih osobina grafena u vidljivom i ultraljubičastom delu spektra. Takodje, u disertaciji demonstrirano je kako se promene optičkih osobina mogu povezati sa praćenjem procesa sinteze, transfera, kao i interakcije grafena sa supstratom. Osim značaja za fundamentalno razumevanje optičkih osobina grafena, prikazani rezultati mogu se iskoristiti za implementaciju elipsometrije kao tehnike za kontrolu kvaliteta u novim tehnologijama zasnovanim na grafenu. Sa daljim razvojem ovih tehnologija, neophodno je imati adekvantne merne tehnike koje nisu osetljive samo na prisustvo mono-atomskog sloja, već su u stanju da pouzdano detektuju fine promene u osobinama ovih ultra tankih filmova. Zbog svojih brojnih prednosti, elipsometrija je zasigurno jedna od tehnika koja će biti korišćena za kontrolu kvaliteta, kao i procesa sinteze u budućim tehnologijama za masovnu proizvodnju grafena.

U disertaciji optičke osobine grafena su merene pomoću tehnika nulirajuće i spektroskopske elipsometrije. Ispitivani su uzorci monoatomskih slojeva grafena, sintetisanih pomoću mikromehaničke eksfolijacije i depozicije iz gasne faze. Takodje, istaknut je značaj korišćenja korelacionih merenja za formiranje optičkih modela i interpretaciju elipsometarskih merenja grafena.

Optičke konstante grafena su dobijene pomoću matematičke inverzije, a zatim parametrizovane pomoću modela dielektrične funkcije grafena. Predloženi model kompleksnog indeksa prelamanja grafena je zasnovan na Fano rezonantnom profilu. Ovaj model ima samo četiri parametra čije se vrednosti mogu jednostavno povezati sa osobinama eksitona u M-tački, koji izaziva crveni pomeraj apsorpcionog maksimuma u ultraljubičastom delu spektra. Različiti parametri modela dielektrične funkcije su prezentovani u disertaciji. Ovi parametri opisuju različite optičke osobine grafena koje su rezultat interakcije izmedju grafena i njegove okoline, eksternih

elektroda ili ostataka transfer rezista.

Takodje, disertacija ispituje nekoliko dodatnih problema vezanih za pouzdanost elipsometarskih merenja i interpretaciju podataka, u slučaju kada se mere atomski tanki filmovi, kao što je grafen. Diskutuje se pravilan izbor supstrata, uglova incidencije, korelacionih merenja i funkcija minimizacije. Opisane procedure bi trebalo koristiti kao uputstvo za elipsometarska merenja i interpretaciju podataka atomski tankih filmova kao što su MoS_2, WS_2, WSe_2 i mnogih drugih 2D materijala.

Ključne reči
grafen, optičke osobine grafena, spektroskopska elipsometrija

Naučna oblast - Fizika

Uža naučna oblast - Fizika kondenzovane materije i statistička fizika

UDK broj - 538.9 (043.3)

Information about the thesis

Title of the thesis

INVESTIGATING THE OPTICAL PROPERTIES OF GRAPHENE WITH SPECTROSCOPIC ELLIPSOMETRY

Abstract

The dissertation addresses the problem of retrieving the optical properties of graphene in the visible and UV ranges using ellipsometry. Additionally, it is demonstrated how changes in these properties could be related to various fabrication aspects including the transfer process and the interaction of graphene with various substrates. Besides their importance in advancing the fundamental understanding of optical properties of graphene, these results could be used for implementation of ellipsometry as a quality control in graphene-based technologies. As these technologies expand, it will be increasingly important to have tools which are able not only to detect the presence of a graphene layer but also to give information of subtle changes in the properties of these ultra thin films. Ellipsometry, due to its numerous advantages, is most definitely one of the techniques that will be employed as a quality control tool in the future mass production of graphene.

In the dissertation optical properties of graphene were studied using spectroscopic ellipsometry and null spectroscopic imaging ellipsometry techniques. The studied samples were atomically thin layers of graphene synthesized by micromechanical exfoliation and chemical vapor deposition. These samples were supported by various substrates, such as silicon wafers with thin SiO_2 films, transparent (sapphire) and metallic (gold) substrates. An importance of using corroborated measurements for building up an appropriate optical models has been shown as well.

Optical parameters of graphene have been retrieved using a point-by-point inversion process, and afterwards parameterized by a dielectric function model. A proposed parametrization function of graphene's complex refractive index is based on a Fano resonant profile. This model has only four fitting parameters, and their values can be easily related to the properties of the M-point exciton that causes the red shift of the prominent absorption peak in the UV. Various set of model param-

eters have been given. These describe the different optical properties of graphene which are a result of an interaction between graphene layer and its surroundings, as external electrodes or transfer residue.

In addition, the dissertation addresses several issues regarding ellipsometric measurements and data interpretation, when measuring atomically thin samples, as graphene. This includes a proper choice of a substrate, incident angles, corroborated measurements and minimization functions. The same process should be followed as a good practice guide for the interpretation of ellipsometric measurements of other atomically thin layers, as MoS_2, WS_2, WSe_2 and many more emerging 2D materials.

Keywords
graphene, optical properties of graphene, spectroscopic ellipsometry

Scientific field - Physics

Subfield - Condensed Matter Physics and Statistical Physics

UDK number - 538.9 (043.3)

Contents

Acknowledgements iv

Podaci o doktorskoj disertaciji vi

Information about the thesis viii

Table of contents x

1. INTRODUCTION 1

1.1. Graphene's structure and electronic properties 3
1.1.1. Crystal structure 3
1.1.2. Dispersion relation 5
1.1.3. Joint Density Of States function (JDOS) 13
1.1.4. Van Hove singularities in two dimensions 17
1.1.5. Electric field effect in graphene 20
1.2. Optical properties of graphene 24
1.2.1. Direct interband transitions 25
1.2.2. Electron-hole interaction, excitons 29
1.2.3. Previous studies in optical properties of graphene 31
1.2.4. Exciton-shifted van Hove peak in absorption 36
1.3. Technological motivation and statement of the thesis 40
1.3.1. Potential application in electronics and flexible electronics . . 41
1.3.2. Potential application in photonics 43
1.3.3. Composites, inks and coatings based on graphene 47
1.3.4. Energy applications 49
1.3.5. Statement of the thesis 51

2. FABRICATION AND CHARACTERIZATION METHODS 54
2.1. Graphene fabrication methods 54
2.1.1. Overview of various fabrication techniques 55
2.1.2. Micromechanical exfoliation 59
2.1.3. Chemical vapor deposition (CVD) 61
2.1.4. Graphene transfer techniques 62
2.1.5. UV photolithography and device fabrication 65
2.2. Graphene characterization 70
2.2.1. Optical microscopy 70
2.2.2. Raman spectroscopy 74
2.2.3. Scanning probe microscopy 78
2.2.4. Fourier transform infrared spectroscopy 84
2.2.5. Measurements of direct current electrical characteristics 88

3. KEY EXPERIMENTAL METHOD: SPECTROSCOPIC ELLIPSOMETRY 94
3.1. Working principle 94
3.1.1. Optical elements 96
3.1.2. Jones calculus 100
3.1.3. Representation of optical elements and measurements by Jones matrices 103
3.1.4. Spectroscopic null imaging ellipsometry 107
3.1.5. Rotating polarizer spectroscopic ellipsometry 111
3.2. Data analysis and Fresnel equations 115
3.3. Correlation measurements 121
3.4. Retrieval of optical properties from ellipsometric data 125
3.4.1. Modeling of optical properties 125
3.4.2. Point-by-point inversion and minimization functions suitable for 2D materials 128
3.4.3. Using substrate interference to enhance sensitivity of SE measurements 136

4. SPECTROSCOPIC ELLIPSOMETRY OF GRAPHENE 142
4.1. Obtaining complex refractive index of graphene using SNIE 143
4.1.1. SNIE measurements of exfoliated graphene 144

4.1.2. SNIE data interpretation and Fano resonant profile modeling of graphene's complex refractive index 147
4.2. SNIE mapping of graphene layer and water layer trapped underneath graphene 150
4.3. Influence of transfer residue on optical properties of CVD graphene . 153
4.3.1. CVD graphene on sapphire: Sample preparation and characterization 153
4.3.2. SE measurements of CVD graphene on sapphire 156
4.3.3. Optical properties of CVD graphene on sapphire: Influence of transfer residue 158
4.4. Influence of gold substrate on optical properties of graphene 162
4.4.1. CVD graphene on gold: Sample preparation and characterization 163
4.4.2. Measurements of direct current electrical characteristics 166
4.4.3. SE measurements of CVD graphene on gold substrate 167
4.4.4. Optical properties of CVD graphene on gold 171
4.4.5. KPFM analysis of graphene/gold interface 173

5. CONCLUSION 176

Bibliography 178

APPENDICES 201

A. Derivations 202

A.1. Tight binding 202
A.2. The Dirac equation 205
A.3. Saddle points in 2D: M point logarithmic van Hove singularity 206
A.4. Fermi golden rule derivation of the interband optical conductivity of graphene in the linear dispersion relation approximation 209

B. Recipes 214

B.1. Substrate preparation 214
B.2. Micromechanical exfoliation 217
B.3. Wet transfer 219
B.4. UV photolithography 221

C. MATLAB codes **226**
C.1. JDOS calculation 226
C.2. Optical models based on Fresnel equations 228
C.3. Point-by-point inversion 230
C.4. Fano model for graphene 232
C.5. Checking for Kramers-Kronig consistency 234

CV and list of publications **236**

1. INTRODUCTION

Graphene, a novel nanomaterial, was first isolated in 2004 by K. S. Novoselov and coworkers [1]. Essentially, graphene is a single atomic layer of graphite, where the carbon atoms are arranged into a hexagonal, honeycomb-like, structure. In a sense graphene is the first truly two-dimensional material, with its thickness reaching a theoretical limit of only one atomic layer. Its discovery has opened a whole new field of research, that considers not only graphene but many other crystal structures that can be obtained as single layers, these are referred to as Van der Waals' materials; in other words materials that have their unit cells connected in at least one direction by van der Waals' forces [2, 3, 4].

Graphene's very simple crystal structure gives rise to many unique properties and phenomena that have drawn a large amount of interest both from the fundamental side, and from the application driven side of the research community and hi-tech industry. As an example, from the year 2000 up to the year 2015 there were over 60000 publications with "graphene" as research topic (according to ISI Web Of Science). The industry follows the scientific contributions as can be seen by the number of published patents, which is greater than 14000 for the same time period, with significant contributions starting from the year 2009. Interestingly, the number-one patent holder regarding graphene is Samsung inc. with over 700 published patents in total [5].

These statistics clearly show a great amount of interest that graphene has received over the last decade. This attention was received for a reason. There are many different properties of graphene in which all the other materials known to

man fail to even compare, and for this reason graphene has earned a nickname "magic material". It has unparalleled electrical properties, as carrier mobility over two orders of magnitude greater than bulk silicon, and a micrometer-scale ballistic transport at room temperatures [6]. It is capable to sustain extremely high densities of electric current (six orders of magnitude greater than copper) [7] and yet it can conduct electricity in the limit of no electrons. The unexampled thermal conductivity of graphene is several times greater than of the any other known material [8]. Graphene also has unique mechanical properties. As it will be shown later on, these properties come from the three $sp2$ hybridized orbitals that lie in plane and form the hexagonal mesh of graphene. Young's modulus of graphene is about five times greater than of the bulk steel [9], while at the same time graphene can be folded by 180° over only 0.2 nm length, without breaking its crystal structure. The crystal lattice of graphene (and graphite) is so densely packed that it is impermeable to any gases, even H_2 [10]. Also, graphene has an extremely high quantum efficiency for light-matter interactions, is strongly optically nonlinear and contains plasmons with peculiar properties [11, 12, 13, 14]. All of these epoch-making properties were experimentally confirmed. However, in most cases this holds only for the very best graphene available, that is usually supported by an adequate substrate as hexagonal boron-nitride. Still and all, as the research field of graphene grows, and as mass-production techniques get ever better, many new potential applications are starting to arise.

The introduction chapter will discuss on graphene's structure and electronic properties (Sec. 1.1) where the tight binding approximation will be employed to obtain the dispersion relation and joint density of states function of graphene. These will be related to the optical properties of graphene in Sec. 1.2 where an interband absorption coefficient will be estimated in the framework of an electromagnetic perturbation theory. Furthermore, within Sec. 1.2 current state of research regarding optical properties of graphene is presented, with a focus on the interband absorption in the visible and ultraviolet ranges. The third section (Sec. 1.3) of the introduction, will discuss some of the potential applications of graphene, with a focus on obstacles that need to be overcome if graphene is to be the next disruptive technology. The final subsection (Sec. 1.3.5) of the introduction is the statement of the thesis in relation to the potential applications of graphene and ellipsometry as a contact-less tool for graphene characterization.

1.1. Graphene's structure and electronic properties

This section gives a short overview of some of the basic approaches in solid-state physics [15], applied to the case of graphene. The goal of this section is to show how graphene's simple crystal structure stands behind its unexampled properties, from the linear dispersion relation and Dirac like fermions, to the critical points in the joint density of states function, and how these govern most of the physically observable properties of graphene. These are all important for better understanding of graphene's optical properties, that will be the focus of the second section (Sec. 1.2).

First (Sec. 1.1.1), crystal structure of graphene is discussed, and the first Brillouin zone, high symmetry points and high symmetry directions in $\vec{k}$ space are shown. Later (Sec. 1.1.2), analytical form of dispersion relation of graphene is obtained using the nearest neighbor tight binding approximation. Valleys in the dispersion relation that are close to the Fermi level are discussed in more detail, and the relation with the Dirac equation is shown. As the main focus of the dissertation are optical properties of graphene, dispersion relation is used to obtain the joint density of states function (JDOS) within Sec. 1.1.3. Consequences of the JDOS function are seen in the optical properties of graphene, especially in the part of the spectra where these are governed by the interband transitions (from the near-infrared to ultraviolet). Furthermore, critical points in JDOS function stand behind various "features" in the optical properties of the solids. Critical point in JDOS function of graphene that is of the particular interest in this dissertation is examined in Sec. 1.1.4. Here a logarithmic or $M1$ van Hove singularity in graphene's JDOS is observed, at the energy that corresponds to the interband transitions near the saddle point in graphene's dispersion relation (M-point). Finally, in this section a short overview of the electric field effect in graphene is presented (Sec. 1.1.5).

1.1.1. Crystal structure

Graphene, as an isolated layer of graphite has a very simple hexagonal crystal structure. Unit cell of graphene contains two carbon atoms that are related to each other by a mirror plane. This plane lies perpendicular to the graphene plane and in the

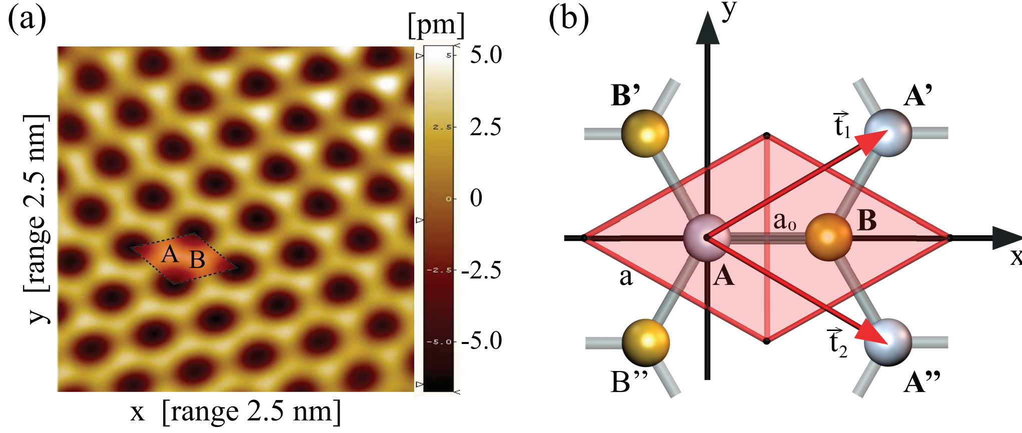

Figure 1.1.: (a) A height image of a highly oriented pyrolytic graphite (HOPG) surface, obtained by an atomic force microscope [16]. Here single carbon atoms are resolved. The unit cell is marked by dot-dashed lines, and its area is red-shaded. (b) shematic representation of a unit cell of graphene marked by the red-shaded area. A and B denote atomic sites, a_0 is the distance between two carbon atoms; a is the length of a unit cell's side; $\vec{t_1}$ and $\vec{t_2}$ are primitive translations.

direction that connects two centers of the neighboring hexagons. These two atomic sites within a unit cell are most commonly refereed as A and B sites, and a hexagonal crystal structure could be imagined as two interweaved trigonal structures that contain only A and only B atoms.

Figure 1.1(a) shows an atomic force microscope (AFM) image of a highly oriented pyrolytic graphite (HOPG) surface (curtesy of [16]). The image was obtained in the contact mode, in high vacuum environment and at room temperature. Here, a hexagonal structure of graphene (graphite layer) can be seen, also a unit cell is marked by dot-dashed lines and its area is red-shaded. Schematic representation of a unit cell with neighboring carbon atoms is shown in Fig.1.1(b). Here the center of the coordinate system is placed at the A site. Two primitive translation vectors $\vec{t_1}$ and $\vec{t_2}$ are shown. Any point outside of the unit cell that can be connected by any possible combination of these vectors to a point within the unit cell, has to be identical with the point in the unit cell that it connects to. The distance between two neighboring carbon atoms is $a_0 = 1.42\mathring{A}$. Length of a primitive translation vectors is $|\vec{t}| = a = \sqrt{3}a_0$. The exact point of each atomic site shown in Fig.1.1(b) is needed for the tight binding calculation (Sec. 1.1.2) and is given in appendix A.1.

Fourier transformation of a hexagonal crystal lattice, results again with a hexagonal structure. Figure 1.2 shows graphene's crystal structure in $\vec{k}$ space. High symmetry points Γ, M, K and K' are also marked. Of particular importance for the physics of graphene are the two points K and K'. These are often called "Dirac points" for reasons that will become clear later (see Sec. 1.1.2 and App. A.2). Vectors $\vec{b}_1$ and $\vec{b}_2$ are primitive translations in $\vec{k}$ space. Interestingly, no combination of these vectors can connect K and K' points, and in order to do this one vector must be subjected to the reflection operation. This gives rise to K valley degeneracy and chirality in graphene, which is also discussed further within the text. In Fig.1.2 light-blue shaded areas represent various possibilities for the choice of the first Brillouin zone (BZ). The irreducible part of the Brillouin zone (IBZ) is shown as red shaded triangle connecting Γ, M and K points. The IBZ area is contained twelve times in the entire Brillouin zone. In order to obtain density of states, as well as joint density of states functions it is necessary to integrate over the entire BZ. The smallest possible area for integration is the IBZ, and the obtained density of states function when integrating over this area needs only to be multiplied by a factor of twelve. Numerical code for summation over the IBZ is shown in appendix C.1.

Figure 1.2(a) shows the most common choice of the BZ. Here only one third of the each K valley is contained within the BZ. This could lead to a false conclusion that there are six K valleys within the BZ. However if chosen differently, as in Fig. 1.2(b), then the number of K valleys within the BZ becomes more apparent. Also, for the sake of integration, a simple square choice is shown in Fig. 1.2(c), with height of $2\pi/a$ and length $2\pi/\sqrt{3}a$. This area contains one half of the BZ. Integration over the BZ will be discussed within Sec. 1.1.3 where graphene's joint density of states function is obtained.

1.1.2. Dispersion relation

In this sub-section, graphene's dispersion relation is calculated, and its properties discussed. The derivation presented here follows guidelines from [15, 17, 18, 19, 20, 21].

Band structure of graphene, as a single layer of graphite, was first calculated by P.

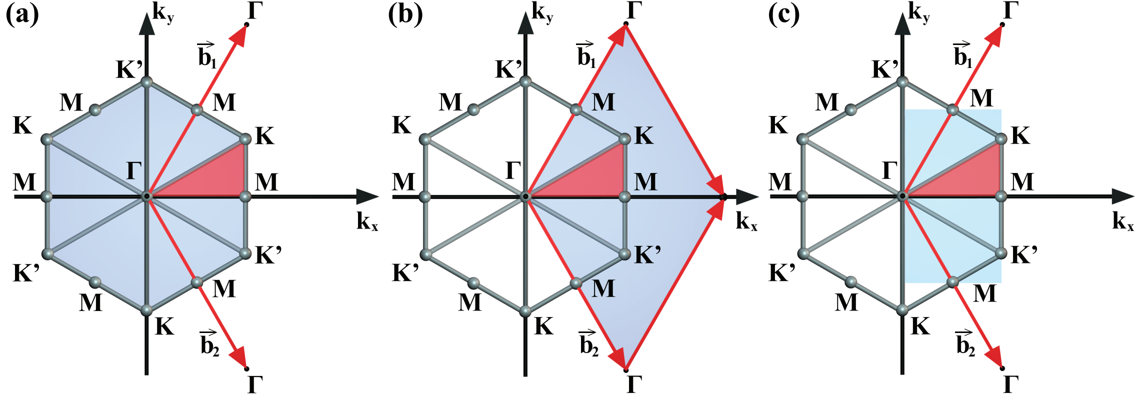

Figure 1.2.: Schematic representation of a crystal lattice of graphene in $\vec{k}$ space, light-blue shaded areas represent various choices for the BZ, while the red-shaded triangular area represents the IBZ. (a) most common choice of BZ, here only one third of each K valley is within the BZ. (b) an alternative choice of BZ where two entire K valleys lie within it. (c) Square half of the BZ with height of $2\pi/a$ and length $2\pi/\sqrt{3}a$, this area is quite simple for integration. $\vec{b}_1$ and $\vec{b}_2$ represent primitive translations in $\vec{k}$ space.

R. Wallace [20] using tight binding method. Starting point is Schrödinger equation $E\Psi = H_{op}\Psi$. Wave function Ψ can be written as a set of basis (known) functions:

$$\Psi = \sum_m \Psi_m u_m(\vec{r}). \tag{1.1}$$

In a tight binding approximation basis functions u_m are atomic wave functions around each carbon atom. Coefficients Ψ_m come from solving the matrix equation:

$$E\Psi_n = \sum_m H_{mn}\Psi_m. \tag{1.2}$$

Indices m and n "run" over all the basis functions in a unit cell. Considering only the upper shell of carbon, $2s^2p^2$ levels give four basis functions for each carbon atom in the unit cell. This would give $H_{nm} = H_{4N\times 4N}$, where N denotes a number of carbon atoms in the unit cell. In general, that would result with eight basis functions:

$$E\left\{\Psi\right\}_n = \sum_m \left[H\right]_{mn}\left\{\Psi\right\}_m, \tag{1.3}$$

where $\{\Psi\}_n$ and $\{\Psi\}_m$ would be 8×1 matrices, and $[H]_{mn}$ would be 8×8 matrix. However, the set of basis functions could be further reduced. Carbon atoms in

graphite are $sp2$ hybridized, giving three σ bonds that lie in a carbon plane and one un-hybridized π_z bond per each carbon atom. σ bonds lie away from the chemical potential and are in general responsible for binding energies and mechanical properties of graphite and graphene, giving a total of six out of eight basis functions that could be neglected. The remaining two π_z orbitals are near the chemical potential and in the approximation of a perfectly flat graphene only these should be considered when electronic and optical properties of graphene are discussed. Regarding a perfectly flat graphene, this condition although valid, can be neglected in most cases that do not involve bending of a graphene plane over several percent on a scale of a single unit cell. Considering only π_z orbitals, results with only two basis function. This significantly simplifies Eq. 1.3, where $\{\Psi\}_n$ and $\{\Psi\}_m$ are now 2×1 matrices, and $[H]_{mn}$ is a 2×2 matrix.

Furthermore, Eq. 1.3 needs to be valid for a periodic structure, meaning that solutions could be written as:

$$\{\Psi\}_m = \{\phi\}\, exp(i\vec{k}\vec{r}_m). \tag{1.4}$$

Returning Eq. 1.4 to Eq. 1.3 results with:

$$E\{\phi\} = \Big[\sum_m [H]_{mn} exp(i\vec{k}(\vec{r}_m - \vec{r}_n))\Big]\{\phi\}, \tag{1.5}$$

where for every given $\vec{k}$ the result of a summation will be a 2×2 matrix. Lets denote this matrix as $[h(\vec{k})]_n$ where:

$$\Big[\sum_m [H]_{mn} exp(i\vec{k}(\vec{r}_m - \vec{r}_n))\Big] = \Big[h(\vec{k})\Big]_n. \tag{1.6}$$

Considering only nearest neighbor hopping and the fact that there are two atoms per unit cell, results with two possible types of contribution to $[h(\vec{k})]_n$, on-site and hopping to the nearest neighbor. This gives total of four components of the hamiltonian, i.e. four elements of the 2×2 matrix.

On-site components H_{AA} and H_{BB} are simply evaluated as:

$$H_{AA}(\vec{k}) = \int \phi_A^*(\vec{r} - \vec{r}_A)\hat{H}\phi_A(\vec{r} - \vec{r}_A)\,\mathrm{d}r = \epsilon_A, \tag{1.7}$$

$$H_{BB}(\vec{k}) = \int \phi_B^*(\vec{r} - \vec{r}_B)\hat{H}\phi_B(\vec{r} - \vec{r}_B)\,\mathrm{d}r = \epsilon_B. \tag{1.8}$$

Here ϵ_A and ϵ_B represent on-site energies. On the other hand, hopping components of hamiltonian are:

$$H_{AB}(\vec{k}) = \int \phi_A^*(\vec{r}-\vec{r}_A)\hat{H}\phi_B(\vec{r}-\vec{r}_B)\,\mathrm{d}r = t_{AB}\cdot exp(i\vec{k}(\vec{r}_A-\vec{r}_B)), \tag{1.9}$$

$$H_{BA}(\vec{k}) = \int \phi_B^*(\vec{r}-\vec{r}_B)\hat{H}\phi_A(\vec{r}-\vec{r}_A)\,\mathrm{d}r = t_{BA}\cdot exp(i\vec{k}(\vec{r}_B-\vec{r}_A)). \tag{1.10}$$

Hopping contributions $H_{AB}(\vec{k})$ and $H_{BA}(\vec{k})$ are solved by summation over the nearest neighbors, which in the case of a B site would be three A site atoms (detailed derivations are given in appendix A.1). Carrying out the nearest neighbor summation, gives:

$$H_{AB}(\vec{k}) = t_{AB}\cdot exp(\frac{ik_xa}{\sqrt{3}})\Big[1+\exp\big(-i\frac{\sqrt{3}}{2}k_xa\big)\cdot\cos\big(\frac{k_ya}{2}\big)\Big], \tag{1.11}$$

$$H_{BA}(\vec{k}) = t_{BA}\cdot exp(-\frac{ik_xa}{\sqrt{3}})\Big[1+\exp\big(i\frac{\sqrt{3}}{2}k_xa\big)\cdot\cos\big(\frac{k_ya}{2}\big)\Big]. \tag{1.12}$$

Returning back to hamiltonian $[h(\vec{k})]_n$ and substituting obtained solutions for all its components, results in:

$$h(\vec{k}) = \begin{pmatrix} H_{AA} & H_{AB} \\ H_{BA} & H_{BB} \end{pmatrix}, \tag{1.13}$$

$$h(\vec{k}) = \begin{pmatrix} \epsilon_A & t_{AB}e^{\left(i\frac{k_xa}{\sqrt{3}}\right)}\left(1+2e^{\left(-\frac{i\sqrt{3}}{2}k_xa\right)}\cos\frac{k_ya}{2}\right) \\ t_{BA}e^{\left(-i\frac{k_xa}{\sqrt{3}}\right)}\left(1+2e^{\left(+\frac{i\sqrt{3}}{2}k_xa\right)}\cos\frac{k_ya}{2}\right) & \epsilon_B \end{pmatrix}. \tag{1.14}$$

It is worth mentioning that at this point A and B sites do not need to contain the same atoms. As an example, this derivation could be easily modified to obtain a band structure of hexagonal boron-nitride (hBN), only by considering that $\epsilon_A \neq \epsilon_B$ and that $t_{AB} \neq t_{BA}^*$ which is the case thus far. However, in the case of graphite and graphene two identical carbon atoms are occupying both A and B sites and following holds:

$$t_{BA} = t_{AB}^* = t, \tag{1.15}$$

$$\epsilon_A = \epsilon_B = 0. \tag{1.16}$$

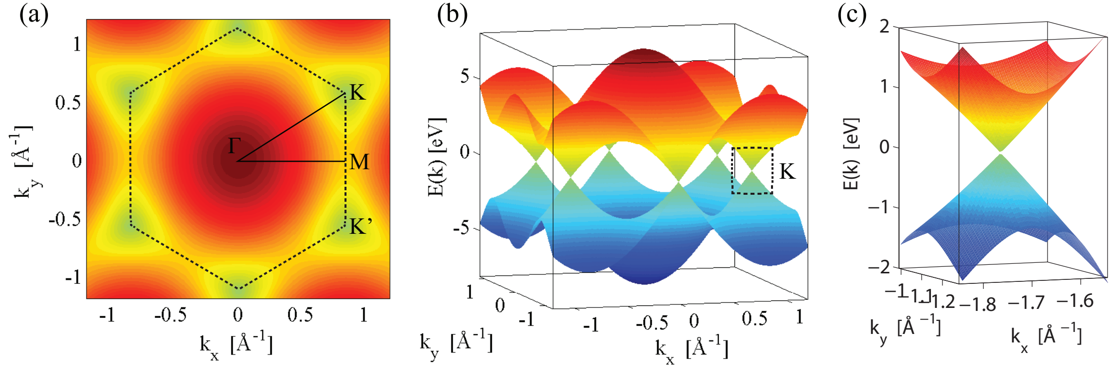

Figure 1.3.: Dispersion relation of graphene (Eq. 1.20, plotted in MATLAB) obtained using nearest neighbor tight binding approximation. Here blue surfaces represent valence band, while red surfaces represent conduction band components of the dispersion relation. (a) top-down view with high symmetry points and directions marked. (b) 3D view of the dispersion relation. (c) zoomed-in region, marked with a dashed square in (b), also known as the "Dirac cone", showing a linear dispersion relation.

If on-site energies are considered as non-zero, the resulting dispersion relation would only be shifted by a constant value. By replacing Eq.-s 1.15 and 1.16 into Eq. 1.14 gives:

$$h(\vec{k}) = \begin{pmatrix} 0 & t^* e^{\left(i\frac{k_x a}{\sqrt{3}}\right)} \left(1 + 2e^{\left(-\frac{i\sqrt{3}}{2}k_x a\right)} \cos\frac{k_y a}{2}\right) \\ t e^{\left(-i\frac{k_x a}{\sqrt{3}}\right)} \left(1 + 2e^{\left(+\frac{i\sqrt{3}}{2}k_x a\right)} \cos\frac{k_y a}{2}\right) & 0 \end{pmatrix}, \tag{1.17}$$

$$h(\vec{k}) = \begin{pmatrix} 0 & h_0^* \\ h_0 & 0 \end{pmatrix}. \tag{1.18}$$

Here h_0 is given by:

$$h_0 = t \cdot exp(-\frac{ik_x a}{\sqrt{3}})\left[1 + \exp{(i\frac{\sqrt{3}}{2}k_x a)} \cdot \cos{(\frac{k_y a}{2})}\right] \tag{1.19}$$

The eigenvalues then are (detailed derivation is presented in appendix A.1):

$$E(k) = \pm t\sqrt{1 + 4\cos\frac{k_y a}{2}^2 + 2\cos\frac{k_y a}{2} \cdot \cos\frac{\sqrt{3}k_x a}{2}}. \tag{1.20}$$

Figure 1.3 shows the dispersion relation (Eq. 1.20). For values of $\vec{k}$ where $E(\vec{k}) \to 0$ states are near the Fermi level, in undoped graphene. These states are responsible

for electron transport in graphene. As shown if Fig. 1.3 (a), on the first look there are six valleys that satisfy this condition. However, if the first Brillouin zone is defined as shown by the dashed line in Fig. 1.3 (a), then only one third of each valley is within the first Brillouin zone, giving total of two valleys near Fermi level. The exact points of minima are high symmetry points K and K'. These points are not equivalent, they are chiral, i.e. connected by a reflection operation. This mirror plane lies perpendicular to graphene's plane, in a Γ-M direction. Interestingly, as shown in Fig. 1.3 (b), and zoomed-in (c), valence and conduction bands "touch" at K and K' points. This means that graphene is a semi-metal, or a semiconductor with a zero band-gap. One even more unique property of graphene becomes apparent from its dispersion relation; near these K and K' points, dispersion relation is linear. As an example, this very unique property would result with a zero effective mass of electrons in graphene.

It is a common practice for semiconductors [22, 23] to approximate the dispersion relation in the vicinity of the points closest to the Fermi level. Unlike graphene's dispersion relation that can be written in a very compact analytical form (Eq. 1.20), dispersion relations of semiconductors are usually very complicated. To simplify band structures around those minimal values a Taylor series expansion is most commonly used [22, 23]. When the same treatment is applied to graphene, so caled "Dirac cones" and linear dispersion relation are obtained.

Starting from the matrix equation (Eq. 1.5) and using Eq. 1.18, gives:

$$E\{\phi\} = \begin{bmatrix} 0 & h_0^* \\ h_0 & 0 \end{bmatrix} \{\phi\} \Rightarrow E = \pm|h_0|\,. \tag{1.21}$$

Here h_0 is given as (Eq. 1.19). Now by finding a first derivate of h_0 in the vicinity of K and K' and with the respect of k_x and k_y independently, we can obtain Taylor expansion coefficients. Starting with the vicinity of K point, gives:

$$\left.\frac{\partial h_0}{\partial k_x}\right|_K = -\frac{i\sqrt{3}at}{2}\, 2e^{i\sqrt{3}k_x a/2} \cos\left(\frac{k_y a}{2}\right)\Bigg|_K = \frac{i\sqrt{3}at}{2}\,, \tag{1.22}$$

$$\left.\frac{\partial h_0}{\partial k_y}\right|_K = -\frac{2at}{2}\, e^{i\sqrt{3}k_x a/2} \sin\left(\frac{k_y a}{2}\right)\Bigg|_K = \frac{\sqrt{3}at}{2}\,. \tag{1.23}$$

The same procedure is repeated in the vicinity of K' point, giving:

$$\left.\frac{\partial h_0}{\partial k_x}\right|_{K'} = \left.\frac{\partial h_0}{\partial k_x}\right|_K = \frac{i\sqrt{3}at}{2}\,, \tag{1.24}$$

$$\left.\frac{\partial h_0}{\partial k_y}\right|_{K'} = -\left.\frac{\partial h_0}{\partial k_y}\right|_{K} = -\frac{\sqrt{3}at}{2}\,. \tag{1.25}$$

Note that results for K' simply follow from the chiral relation with K (mirror plane in k_x direction). This gives Taylor series expansion of h_0 near K and K' as:

$$h_0\Big|_K \approx \frac{i\sqrt{3}at}{2}k_x + \frac{\sqrt{3}at}{2}k_y = \frac{\sqrt{3}at}{2}(ik_x + k_y)\,, \tag{1.26}$$

$$h_0\Big|_{K'} \approx \frac{i\sqrt{3}at}{2}k_x - \frac{\sqrt{3}at}{2}k_y = \frac{\sqrt{3}at}{2}(ik_x - k_y)\,. \tag{1.27}$$

Now the resulting Schrödinger equation expanded around k valleys can be written as:

$$E\{\phi\} = \begin{bmatrix} 0 & \frac{\sqrt{3}at}{2}(-ik_x + k_y) \\ \frac{\sqrt{3}at}{2}(ik_x + k_y) & 0 \end{bmatrix} \{\phi\}\,. \tag{1.28}$$

From here to find the dispersion relation requires solving a two component differential equation. The derivation for the solution of this differential equation has the same mathematical form as the Dirac equation [24]. The detailed derivation is given in appendix A.2. For this reason K valleys are often called "Dirac cones". Since electrons that occupy states in these "Dirac cones" are responsible for electron transport in graphene, they are called "Dirac fermions". In the linear regime energy-momentum Hamiltonian has a form:

$$H_{lin} = v_F\vec{\sigma}\vec{p}, \tag{1.29}$$

where $\vec{\sigma}$ denotes Pauli spin matrices and v_F is a Fermi velocity of carriers in graphene. The detailed derivation of Eq. 1.29 is given in appendix A.2.

Eigenvalues of Eq. 1.29 give linear dispersion relation in the vicinity of K points:

$$E_{\pm}(k) = \pm\hbar v_F k\,. \tag{1.30}$$

The sign $\pm$ in Eg. 1.30 corresponds to the electron and hole parts of the dispersion relation, and $k = |\vec{k}|$. Here, more suitable coordinate system is a cylindrical one, centered at K point; more details on coordinate transformation are given in the next subsection. Fermi velocity simply follows from Eq. 1.28, considering $p \Rightarrow i\hbar\nabla$, as:

$$v_F = \frac{\sqrt{3}at}{2\hbar} \approx 0.833 \cdot 10^6 m/s\,. \tag{1.31}$$

here, $t = 2.575\,eV$ is taken from [25]. As can be seen, velocity of electrons in graphene is about three orders of magnitude smaller than the speed of light in

vacuum. It means that carriers in graphene do not travel at relativistic speeds, by are described by the Dirac equation.

The fact that electron transport in graphene is described by the massless Dirac equation, makes it possible to use graphene as an effective medium (vacuum) where relativistic quantum tunneling described by the Klein paradox [26] and other relevant quantum electrodynamics (QED) phenomena can be tested experimentally [27]. In contrast to electrons and holes in condensed-matter physics, which are normally described by separate Schr$\ddot{o}$dinger equations, electrons and holes in graphene are interconnected exhibiting properties analogous to the charge-conjugation symmetry in QED. The two-component wavefunction that describes graphene is very similar to the spinor wavefunctions in QED, but the 'spin' index for graphene indicates sublattices rather than the real spin of electron and is usually referred to as pseudospin σ.

In high-energy physics, one defines the helicity of a particle as the projection of its spin onto the direction of propagation, as: $\eta = \vec{q}\,\vec{\sigma}/|q|$ [28]. It is a Hermitian and unitary operator. Here, $\vec{\sigma}$ represents the true physical spin of the particle. In the absence of a mass term, the helicity operator commutes with the Dirac Hamiltonian, and the helicity is a good quantum number. Then, one may identify helicity and chirality.

For the case of graphene, the same definition for helicity holds, but the Pauli matrices define now the sublattice pseudospin instead of the true spin. As a consequence, chirality is a preserved quantum number in elastic scattering processes induced by impurity potentials that vary smoothly on the lattice scale. In this case, inter-valley scattering is suppressed, and the chirality thus conserved. This effect gives rise to the absence of backscattering in graphene [29] and is at the origin of Klein tunneling [28].

Regarding the Klein paradox, graphene has been suggested as a platform to experimentally observe this effect by M. I. Katsnelson and coworkers [27]. They have showed that massless Dirac fermions in graphene allow a close realization of Klein's gedanken experiment, whereas massive chiral fermions in bilayer graphene offer an interesting complementary system that elucidates the basic physics involved. In bilayer graphene quasiparticles are also chiral and described by spinor wavefunctions, but have a parabolic dispersion. First experimental observations of Klein tunneling have been demonstrated in top-gated graphene devices. R. J. Young and coworkers [30] have shown ballistic tunneling (with $T \approx 1$) through a potential barrier gen-

erated in graphene by a Pd top-gate electrode with only 20 nm length. As a gate dielectric ∼10 nm of hydrogen silsesquioxane and ∼20 nm of HfO_2 have been used. Klein tunneling through longer barriers (60-1700 nm) have been demonstrated by N. Stander and coworkers [31], also using a top-gated configuration. There, a mixture of diffusive and ballistic transport regimes occur, depending on the length of the channel.

1.1.3. Joint Density Of States function (JDOS)

This sub-section considers derivation of the joint density of states function, and its guided by [15, 22, 23, 32, 33]. The main goal of chapter 1 is to relate optical properties of graphene to its dispersion relation, and to provide some guidelines on what to expect when optical properties of graphene are retrieved by spectroscopic ellipsometry. The spectral ranges of interest are the visible and ultraviolet (UV). As it will be discussed in greater detail further in the text, the main contribution to optical properties in this range comes from the interband transitions. However, the detailed calculation for the contribution of the interband transitions to the dielectric function $\epsilon(\omega)$ of graphene is quite difficult. For this reason an approximate solution is considered, and the interband absorption of graphene is estimated within the perturbation theory. This will consider the Fermi golden rule, which gives the probability per unit time $W_{\vec{k}}$ that a photon of energy $\hbar\omega$ makes a transition at a given $\vec{k}$ point in Brillouin zone; which can be written as:

$$W_{\vec{k}} \cong \frac{2\pi}{\hbar} |\langle v|H'|c\rangle|^2 \delta\Big[E_c(\vec{k}) - E_v(\vec{k}) - \hbar\omega\Big]. \tag{1.32}$$

Here, H' represents the matrix element for the electro-magnetic perturbation, and is given by:

$$H' = -\frac{e\vec{A}\vec{p}}{mc}. \tag{1.33}$$

Fermi golden rule exploits the fact that the wave vector for the light is small compared to the Brillouin zone dimension. Let us estimate this. Considering the visible and UV ranges, the wave vector for the light is in the order of $10^4 cm^{-1}$ while Brillouin zone dimensions are in the order of $10^8 cm^{-1}$, giving a four orders of magnitude difference. In Eq. 1.32 δ stands for a delta function and represents

energy conservation at $\vec{k}$, which as discussed is well justified. Furthermore, in Eq. 1.32 c and v stand for conduction and valence band states, respectively.

By integrating Eq. 1.32 over $\vec{k}$ in the entire Brillouin zone, the following relation is obtained:

$$W_{\vec{k}} \cong \frac{2\pi}{\hbar} \int\limits_{BZ} |\langle v|H'|c\rangle|^2 \frac{2}{4\pi^2}\, \delta\Big[E_c(\vec{k}) - E_v(\vec{k}) - \hbar\omega\Big]\, \mathrm{d}^2k. \tag{1.34}$$

Here $\frac{2}{4\pi^2}$ comes from the integration in two dimensions. Let us assume that $|\langle v|H'|c\rangle|^2$ is independent of $\vec{k}$, or at least that its change with changing $\vec{k}$ could be neglected in comparison with a delta function. This significantly simplifies the integral over $\vec{k}$, giving:

$$W_{\vec{k}} \cong \frac{2\pi}{\hbar} |\langle v|H'|c\rangle|^2 \frac{2}{4\pi^2} \int\limits_{BZ} \delta\Big[E_c(\vec{k}) - E_v(\vec{k}) - \hbar\omega\Big]\, \mathrm{d}^2k. \tag{1.35}$$

The integral in Eq. 1.35 represents the number of states per unit volume per unit energy range which occur with an energy difference between c and v bands equal to the photon energy. This is the definition of the joint density of states (JDOS) function, and its written as:

$$\rho_{cv}(\hbar\omega) = \frac{2}{4\pi^2} \int\limits_{BZ} \delta\Big[E_c(\vec{k}) - E_v(\vec{k}) - \hbar\omega\Big]\, \mathrm{d}^2k. \tag{1.36}$$

It would be very convenient to convert the integral over $\vec{k}$ space into the integral over energy. This could be simply carried out by introduction of as constant energy line (surface in 3D case) S in $\vec{k}$ space such that the constant energy difference is exactly the photon energy: $E_c - E_v = \hbar\omega$. Then $S\mathrm{d}S$ would be a constant energy surface in $\vec{k}$ space. Here $\mathrm{d}^2k = \mathrm{d}S\mathrm{d}k_n$, and k_n is an element of a wave vector normal to S. Now, simply by using a definition of a gradient of $E(\vec{k})$ as:

$$|\nabla_k E(\vec{k})|\mathrm{d}k_n = \mathrm{d}E, \tag{1.37}$$

and considering the energy difference between c an v bands:

$$|\nabla_k (E_c - E_v)|\mathrm{d}k_n = \mathrm{d}(E_c - E_v), \tag{1.38}$$

results with the relation between the integration over $\vec{k}$ and integration over energy:

$$\mathrm{d}^2k = \mathrm{d}k_n\mathrm{d}S = \mathrm{d}S\, \frac{\mathrm{d}(E_c - E_v)}{|\nabla_k (E_c - E_v)|}. \tag{1.39}$$

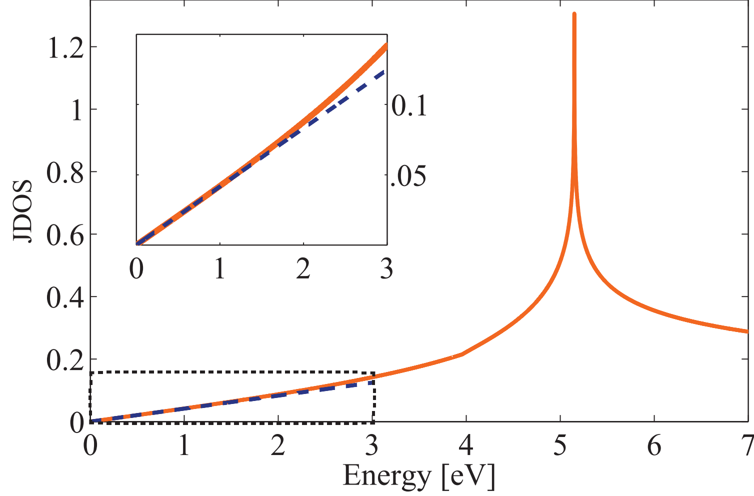

Figure 1.4.: Graphene's joint density of states function, numerically calculated from the dispersion relation (solid line) and a linear approximation (dashed line). Inset shows enlarged part of JDOS in the energy range where deviation from the linear approximation does not exceed 10%. Following values of parameters were used: $t = 2.575\,eV$ and $a = 0.2459\,nm$

By returning Eq. 1.39 into Eq. 1.36 gives:

$$\rho_{cv}(\hbar\omega) = \frac{2}{4\pi^2} \int\int \frac{\mathrm{d}S\,\mathrm{d}(E_c - E_v)\,\delta(E_c - E_v - \hbar\omega)}{|\nabla_k(E_c - E_v)|}. \tag{1.40}$$

By carrying out the integral over $\mathrm{d}(E_c - E_v)$, gives:

$$\rho_{cv}(\hbar\omega) = \frac{2}{4\pi^2} \int \frac{\mathrm{d}S}{|\nabla_k(E_c - E_v)|} \Bigg|_{E_c - E_v = \hbar\omega}. \tag{1.41}$$

Until this point derivation of JDOS was quite general, restricting only to a two-dimensional case. Now let us introduce the dispersion relation of graphene (Eq. 1.20), obtained within a tight binding approximation. Quite simply, the difference between the energy of the conduction and valence bands at a given $\vec{k}$ is described as:

$$E_c - E_v = 2|E(\vec{k})|\,. \tag{1.42}$$

Returning into Eq. 1.41 results with the joint density of states function for graphene:

$$\rho_{cv}(\hbar\omega) = \frac{2}{4\pi^2} \int \frac{\mathrm{d}S}{|\nabla_k(2|E(\vec{k})|)|} \Bigg|_{2|E(\vec{k})| = \hbar\omega}. \tag{1.43}$$

Eq. 1.43 could be analytically solved when only the nearest neighbor hopping is considered. It's solution is very similar to the solution of graphene's and graphite's

density of states functions [20, 34]. The solution contains a complete elliptic integral of the first kind. However, there is a much faster way to numerically calculate both density of states and joint density of states. Numerical code used for solving the integral in Eq. 1.43 is given in appendix C.1 and its based on a simple histogram of the dispersion relation. The results of numerical solution of Eq. 1.43 are shown in Fig. 1.4, with parameters $t = 2.575\, eV$, $a = 0.2459\, nm$ and k point sampling of only $10^{-4}\, cm^{-1}$ (for more computational details see appendix C.1). Used hopping energy is taken from [25] where it has been obtained from ab-initio calculations without consideration of electron-hole interactions.

Let us first focus on the low energy part of JDOS. Equation 1.30 represents the linear approximation of graphene's dispersion relation. Before returning it to Eq. 1.43, let us change the coordinate system from Cartesian to cylindrical, since in the linear approximation the dispersion relation is represented by Dirac cones, this gives:

$$|E(\rho, \varphi)| = v_F \hbar \rho\,. \tag{1.44}$$

A standard cylindrical coordinate system transformations were used: $k_x = \rho \cos(\varphi)$, $k_y = \rho \sin(\varphi)$, and $\rho = \sqrt{k_x^2 + k_y^2}$. Now let us calculate $\nabla 2|E|$ using the linear dispersion relation (Eq. 1.44) in a cylindrical system:

$$\nabla_{\rho,\varphi}(2|E|) = 2\frac{\partial}{\partial \rho} v_F \hbar \rho + \frac{2}{\rho}\frac{\partial}{\partial \varphi} v_F \hbar \rho = 2 v_F \hbar\,. \tag{1.45}$$

Now returning to Eq. 1.43 gives:

$$\rho_{cv}(\hbar\omega) = \frac{2}{4\pi^2} \int \frac{\mathrm{d}S}{|\nabla_{\rho\varphi}(2|E|)|}\Bigg|_{2|E(\rho,\varphi)|=\hbar\omega}, \tag{1.46}$$

$$\rho_{cv}(\hbar\omega) = \frac{1}{4\pi^2 v_F \hbar} \int \mathrm{d}S = \frac{1}{4\pi^2 v_F \hbar} \cdot A_c \cdot 2\pi \cdot \rho. \tag{1.47}$$

Here, A_c stands for the unit cell area and is given as $A_c = 3\sqrt{3}a^2/2$. By returning Eq.-s 1.31 and 1.44, into Eq. 1.47, gives:

$$\rho_{cv}(\hbar\omega) = \frac{A_c}{4\pi v_F^2 \hbar^2}\hbar\omega = \frac{\sqrt{3}}{2\pi t^2}\hbar\omega\,. \tag{1.48}$$

In the vicinity of K points (Dirac cones) joint density of states function is expected to be a linear function of energy. Inset of Fig. 1.4 shows linear JDOS compared to JDOS calculated numerically, as previously described. Deviation from the linear JDOS approximation greater than 10% occurs for the energies that are greater than 3 eV. This indicates that linear approximations of the dispersion relation and the

joint density of states function of graphene are valid even for incident photon energies in the visible spectral range. Let us now focus on the part of the spectra where the linear approximation is not valid ($\hbar\omega > 3eV$, i.e. in the UV range).

In Fig. 1.4 there is a distinct maximum at energy that equals $2t$. This would be a point of interest in the joint density of states function. At this point (when $\hbar\omega = 2t$) denominator in Eq. 1.43 vanishes. These points in energy are called joint critical points, or van Hove singularities [22, 23]. Around these critical points, the photon energy is effective in inducing electronic transitions over a relatively large region of the Brillouin zone, compared to transitions away from these critical points. In general, critical points occur at high symmetry points in Brillouin zone. These points give rise to "features" observed in the optical properties. Positions of these features are related to photon energies that are required for an interband transition of an electron in the vicinity of a high symmetry point in Brillouin zone.

As will be discussed in detail later on, the "feature" seen in Fig. 1.4 at $\hbar\omega = 2t$ is a logarithmic or $M1$ van Hove singularity that corresponds to interband transitions in the vicinity of M point in the Brillouin zone of graphene.

1.1.4. Van Hove singularities in two dimensions

As it was previously discussed (Sec. 1.1.3), for the case when a denominator in Eq. 1.43 vanishes, JDOS function has a critical point, or a van Hove singularity. Critical points are classified into categories based on weather the band separation increases or decreases as we move away from the critical point [22, 23]. This information is obtained by expanding the energy difference function $E_c(\vec{k}) - E_v(\vec{k})$ (i.e. a joint dispersion relation) into a Taylor series around the critical point ($\vec{k_0}$), as:

$$E_c(\vec{k}) - E_v(\vec{k}) \approx E_g(\vec{k_0}) + a_1(k_1 - k_{01})^2 + a_2(k_2 - k_{02})^2 + a_3(k_3 - k_{03})^2 + ... \quad (1.49)$$

Here $E_g(\vec{k_0})$ represents the energy gap at the critical point and number of components (1,2,3...) represents the number of dimensions of $E_g(\vec{k})$, i.e. x, y, z directions. Here, parabolic approximation is assumed, and Taylor expansion coefficients are calculated as a partial second order derivative of the energy difference at the critical

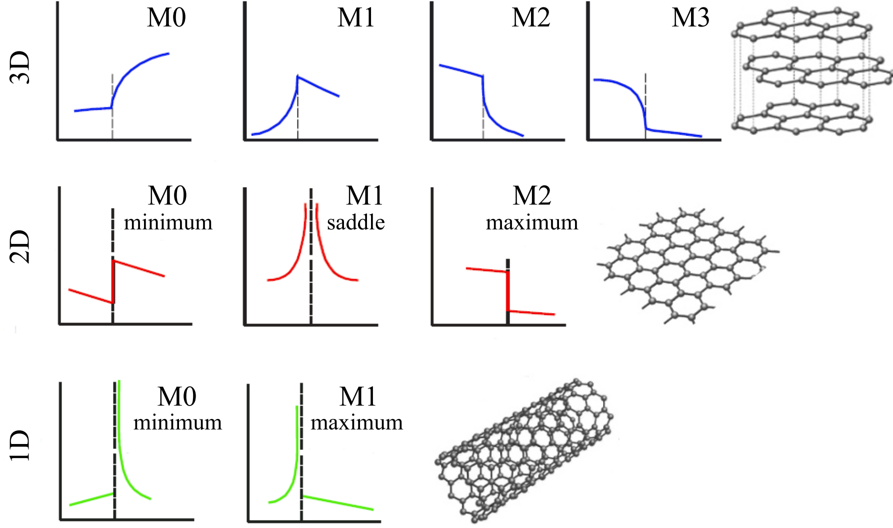

Figure 1.5.: Schematic representation of the classification of critical points in 3D (top), 2D (middle) and 1D (bottom) [23]. In all sub-figures x-axis represents photon energy $\hbar\omega$, while y-axis represents JDOS for a quadric dispersion relation. Vertical lines represent critical points.

point ($\vec{k}_0$):

$$2a_i = \frac{\partial^2}{\partial k_i^2}\left[E_c(\vec{k}) - E_v(\vec{k})\right]. \tag{1.50}$$

The classification of the critical points is made according to how many of these Taylor expansion coefficients are negative. In a case of a 3D system there are four different types of critical points, in a 2D system there are three, and in a 1D system only two. Figure 1.5 shows typical profile of JDOS for all the possible types of critical points. These typical profiles of JDOS are obtained for a parabolic approximation in the vicinity of the critical points. Furthermore, Figure 1.5 shows schematically (right side) carbon based materials in 3D, 2D and 1D. As an example, optical spectra of carbon nanotubes are enhanced by the fact that for all possible critical points JDOS tends to infinity. This makes possible the detection of resonant Raman, and infra-red spectra from a single carbon nanotube [35, 36, 37].

A common examples of a critical point in 3D, are related to interband transitions with minimal photon energies that can overcome the band-gap of a semiconductor. These points are usually $M0$ critical points, meaning that all three a_i coefficients are positive. There are two possibilities that do satisfy this condition, minimum in both bands and a minimum in one and maximum in the other band. These two cases

would correspond to direct and indirect band-gap semiconductors, respectively.

Let us now examine the case of interest here, the critical point in JDOS of graphene at photon energy $\hbar\omega = 2t$. Considering $t = 2.575\,eV$ [25], this critical point is expected to be deep in the UV region. As can be seen from the dispersion relation of graphene (Eq. 1.20 and Fig. 1.3) this critical point corresponds to the interband transitions of an electron at the M high symmetry point in the Brillouin zone.

By expanding the $E_c(\vec{k}) - E_v(\vec{k})$ function of graphene around M point, gives:

$$E_c(\vec{k}) - E_v(\vec{k}) = 2|E(\vec{k})| = 2|E(\vec{k}_M)| + \sum_{i=x,y} a_i (k_i - k_{Mi})^2 \,. \tag{1.51}$$

Here, the band gap at M point simply gives $2|E(\vec{k}_M)| = 2t$, while the Taylor expansion coefficients could be obtained as:

$$2a_i = 2t\,\frac{\partial^2}{\partial k_i^2}\left[\sqrt{1 + 4\cos\frac{k_y a}{2}^2 + 2\cos\frac{k_y a}{2}\cdot\cos\frac{\sqrt{3}k_x a}{2}}\,\right]. \tag{1.52}$$

Carrying out the partial second order derivative (details in App. A.3) gives:

$$a_1 = \frac{\partial^2}{\partial k_x^2}\left[2|E(\vec{k})|\right] = \frac{2t}{\sqrt{3}} > 0\,, \tag{1.53}$$

$$a_2 = \frac{\partial^2}{\partial k_y^2}\left[2|E(\vec{k})|\right] = -\frac{10t}{\sqrt{3}} < 0\,. \tag{1.54}$$

Now, by returning Eq.-s 1.53 and 1.54 into 1.51, gives the Taylor series expansion of the graphene's joint dispersion relation in the vicinity of the M point:

$$E_c(\vec{k}) - E_v(\vec{k}) \approx 2t + \frac{2t}{\sqrt{3}}(k_x - \frac{2\pi}{\sqrt{3}a})^2 - \frac{10t}{\sqrt{3}}(k_y)^2\,. \tag{1.55}$$

The result of the calculation of Taylor expansion coefficients gives us $a_1 > 0$ and $a_2 < 0$, meaning that the M point singularity is so called $M1$ type, or a 2D saddle point singularity, or logarithmic singularity. Interestingly this indicates that for the M point interband transition energies, JDOS function has a logarithmic discontinuity, theoretically giving an infinite number of states that could contribute to the interband absorption of a photon with an energy that corresponds to the interband transition at M point, i.e. $\hbar\omega = 2t$. It is worth mentioning that M point interband transition do occur away from the linear part of the dispersion relation of graphene ($\hbar\omega > 3\,eV$), meaning that parabolic band approximation employed here is valid.

As it will be discussed in the next section of the introduction, logarithmic van Hove singularity is expected to result with a theoretical 100% light absorbtion at

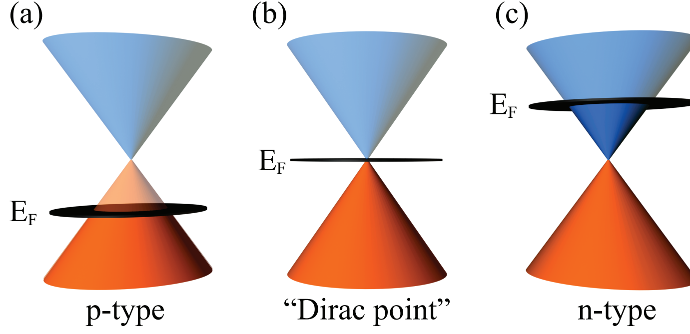

Figure 1.6.: Schematic representation of the shift of the Fermi level E_F with respect to the charge neutrality point (CNP) or "Dirac point". (a) $E_F < CNP$ gives holes as majority carriers (p-type). (b) $E_F = CNP$ equal contribution of both electrons and holes. (c) $E_F > CNP$ gives electrons as majority carriers (n-type).

$\hbar\omega = 2t$ even for a single-layer graphene. When various sources of broadening are introduced, theoretical 100% absorption is reduced to a more realistic value (10-20%), still giving a prominent absorption peak in the UV range.

1.1.5. Electric field effect in graphene

Before focusing on optical properties, this sub-section will discuss on one of the most important effects in graphene, the electric field effect. Here, only a short overview of the subject is presented. More details on device fabrication and electrical characteristics measurements are given in Sec. 2.1.5 and 2.2.5, and appendix B.4.

By "the electric field effect" it is referred to a possibility to control electrical properties of a material (as resistivity) by an externally applied electric field. This concept has been employed in field effect transistors, and a most common example would be a metal-oxide field effect transistor (MOSFET). However a question stands, is it possible to make an all metallic transistor? For this, a channel would have to be made out of metal, similarly as electrodes and external leads are made. The benefits of such approach would be much lower residual resistivity of the channel, higher current densities, and consequently higher operating frequencies. However, free carriers in metal would screen the external electric field, and would significantly

reduce the electric field effect. As an example, let us consider a MOSFET channel made out of very thin gold film. Some thinnest possible continuous gold film that could be made are still several nanometers thick (usually ~7 nm). If we were to apply an external electric field of the order that is near the breakdown field of SiO_2 (~1 V per nm), resulting channel resistivity modulation would be only about 1% of the total channel resistivity, rendering the device useless.

The obvious choice would be to fabricate thinner metal films, however quality and continuity of these films is the major issue when reducing their thickness below several nanometers. An ideal case would be to have an atomically thin single crystal material. Until discovery of graphene[1] this was considered as impossible, and alternative candidates such as carbon nanotubes were used in various proof-of-concept devices [38, 39, 40, 41, 42].

The main advantage of graphene is the fact that a single atomic layer has a well defined crystal lattice, stable at ambient conditions and room temperature. Furthermore, graphene is semi-metal, meaning that near the Fermi level there are very few electronic states that can contribute to the current flow, as well as to the screening of the external electric field. As a result the field modulation of ~10× are commonly reported in graphene at room temperatures. Compared to metallic channels where the same modulation is ~0.01× . Graphene gives three orders of magnitude better electric field modulation of the channel resistivity than if the channel was made out of the thinnest possible metallic film.

This field modulation could be imagined in a manner where Fermi level is shifted by the applied field with the respect to the Dirac point. Dependent on the direction of the shift, more electron or hole states will be available near the Fermi level and as a result electrons or holes will become majority carriers in graphene. This is schematically represented in Fig. 1.6. This effect is referred to as "electric field doping". Commonly, when graphene's resistivity is measured, Dirac point is referred to as charge neutrality point (CNP), since at this point both electron and hole contribution to the current flow through graphene channel is equivalent. As it was previously stated, electrons that do contribute to the current flow lie in states near the Fermi level. Even for very high applied external fields (e.g. through electrolytic gating [43]) linear approximation of the dispersion relation is valid.

One of the most simple approaches to measure electrical properties of graphene is so call two-point-probe setup (2pp). Here direct current (DC) total device resistivity can be measured as a function of an applied back-gate voltage. For this

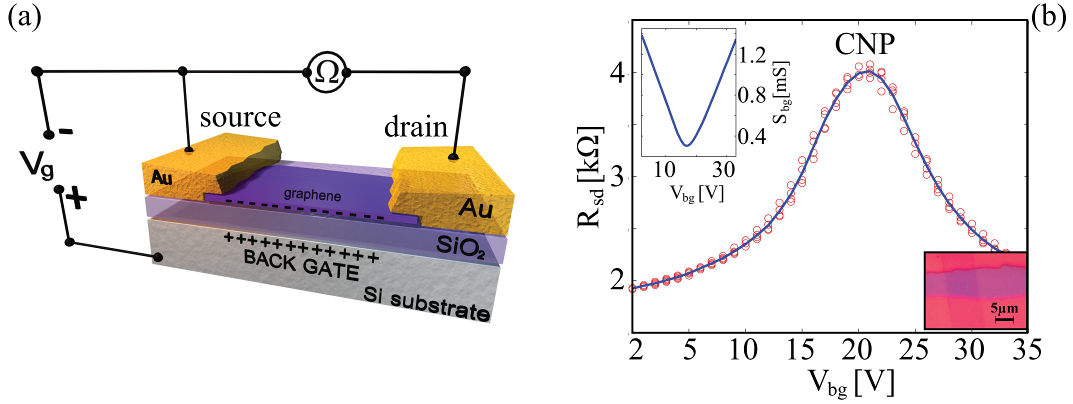

Figure 1.7.: (a) schematic representation of the two-point-probe (2pp) measurement setup. (b) source-drain resistivity R_{sd} as a function of a back-gate voltage V_{bg}. Top-left inset of (b) shows conductivity of graphene channel with deduced contact resistivity, while bottom-right inset of (b) shows a microscope image of the device with gold electrodes on the top and bottom.

purpose graphene is commonly supported by a substrate that serves at the same time as a back-gate electrode, as doped silicon wafer with a thin insulating layer of silicon-dioxide (SiO_2/Si). Graphene, as a channel material, is deposited over the oxide surface and two electrical contacts are fabricated. These contacts are usually defined by a lithography process (for more details see Sec. 2.1.5 and App. B.4). Now by applying a constant (DC) electric field between one of the contacts and a silicon substrate, Fermi level in graphene can be modulated. In order to retrieve the information on the Fermi level shift, an additional contact is required, or a significantly more elaborate setup to determine the position of the Fermi level in graphene [44, 45]. Simply by measuring the change in resistivity between two contacts on graphene, the position of the Fermi level relative to the CNP can be obtained, as well as carrier mobility, type and the amount of unintentional doping. Figure 1.7(a) shows schematic representation of the 2pp experimental setup, while Fig. 1.7(b) shows a typical total source-drain resistivity as a function of the applied back-gate voltage. Maximum in $R_{sd}(V_{bg})$ curve indicates position of the CNP. If the V_{bg} polarity is set as shown in 1.7(a), then the left side from the CNP peak has holes as the majority carriers, while the right side has electrons. Slope of the curve can be related to carrier mobility. As can be seen in Fig. 1.7(b) the entire curve is shifted upwards for a constant value, this value represents resistivity of the external

contacts.

More details on how to interpret DC measurements of graphene's electrical properties, as well as how to modify graphene through the applied voltage are shown later in the text. For now, let us focus back on the optical properties of graphene and see how does logarithmic M-point van Hove singularity in the JDOS of graphene affect interband absorption and the complex dielectric function of graphene both in the visible and in UV ranges.

1.2. Optical properties of graphene

This section focuses on optical properties of graphene. Spectral ranges of interest are the visible and UV. In these ranges spectroscopic ellipsometry measurements are carried out (see chapter 4: SPECTROSCOPIC ELLIPSOMETRY OF GRAPHENE). In these spectral ranges interband transitions have a major influence on the optical response of graphene.

First subsection (Sec. 1.2.1) discusses interband transitions in general and presents a derivation for an interband absorption coefficient in the framework of an electromagnetic perturbation theory. Later on this method is applied for the case of graphene. Especially, the influences that a linear dispersion relation approximation and M-point van Hove singularity in JDOS have on the optical properties of graphene are discussed. Afterwards, in Sec. 1.2.2 the influence of electron-hole interaction on the optical properties is briefly considered in general, with the focus on hyperbolic excitons.

Next, an overview of the literature regarding optical properties of graphene is presented in subsections 1.2.3 and 1.2.4. The former focuses on the linear dispersion relation regime (the infrared and visible ranges), and a possibility to modify optical properties of graphene by electrostatic gating (Pauli blocking). Afterwards, a short overview of the literature focusing on the ellipsometric measurements of graphene's optical properties, and sample thickness are presented.

The final subsection 1.2.4 gives an overview of the reported data regarding the optical properties of graphene in the UV range. Here a prominent absorption peak arises from the critical point in JDOS. Furthermore, a signature of many-body interactions in graphene that is visible through its optical properties is discussed here, an exciton-shifted van Hove peak in absorption. Finally, a possibility to modify this prominent absorption peak through electrostatic gating, ambient or substrate interaction is discussed. The mechanism controlled here is the relative strength between electron-electron and electron-hole interactions that as a consequence have significant changes of the peak's position, width, intensity and asymmetry.

1.2.1. Direct interband transitions

This subsection presents a short overview of the interband transitions in general [22, 23, 46, 47], afterwards focusing on the case of graphene. Here, the results for graphene's joint density of states function (obtained in Sec. 1.1.3) are employed. The exact calculations of graphene's optical properties [25] go beyond the scope of this dissertation. Thus the goal of this sub-section is only to estimate the optical properties of graphene in the visible and ultraviolet ranges and to relate them to the dispersion relation and JDOS. This is carried out by calculating the interband absorption of graphene in perturbation theory. Also, here Pauli blocking is neglected by assuming that the Fermi level is exactly at the Dirac point. Pauli blocking is discussed later on (Sec. 1.2.3). Furthermore, it is worth mentioning that this subsection and several other use both centimeter-gram-second (CGS) and meter-kilogram-second (MKS) systems of units to better suite a particular case, and whenever need the differences were accounted for.

One of the most important technique for characterization of solids are optical absorption measurements. This is one of the simplest experimental setups in the solid state spectroscopy, yet it can give a clear insight into various processes occurring in a solid at the atomic level. Let us focus on the interband transitions and their affect on the absorption of light. Here one of the most important observable values is the absorption coefficient $\alpha_{abs}(\hbar\omega)$. It is defined as the number of transitions at a given photon energy ($\hbar\omega$) per unit volume, per unit time, per incident electromagnetic flux.

The incident electromagnetic flux can be calculated using Poynting vector, as:

$$\vec{S} = \frac{c}{8\pi} Re\left\{\vec{E}^{*} \times \vec{H}\right\} . \tag{1.56}$$

Here c stands for the speed of light in vacuum. The electromagnetic field variables $\vec{E}$ and $\vec{H}$ could be related to the vector potential $\vec{A}$, as:

$$\vec{E} = \frac{1}{c}\frac{\partial}{\partial t}\vec{A} = \frac{i\omega}{c}\vec{A}, \tag{1.57}$$

$$\mu\vec{H} = \vec{B} = \vec{\nabla} \times \vec{A}. \tag{1.58}$$

Here a non-magnetic material is assumed ($\mu = 1$), and by taking the the curl of $\vec{A}$ while considering the vector potential as $\vec{A} = A_0 exp(i\vec{K}\vec{r} - i\omega t)$, where $\vec{K}$ is the propagation constant for the light, gives $\vec{H} = i\vec{K} \times \vec{A}$. Now, by returning the

electromagnetic field variables, expressed through the vector potential into eq. 1.56 gives:

$$\vec{S} = \frac{c}{8\pi} Re \left\{ -\frac{i\omega}{c} \vec{A}^* \times (i\vec{K} \times \vec{A}) \right\} , \tag{1.59}$$

$$\vec{S} = \frac{\omega}{8\pi} Re \left\{ (\vec{A}^* \cdot \vec{A})\vec{K} - (\vec{A}^* \cdot \vec{K})\vec{A} \right\} . \tag{1.60}$$

Considering the case of a transverse plane wave ($\vec{A}^* \cdot \vec{K} = 0$), eq. 1.60 becomes:

$$\vec{S} = \frac{\omega}{8\pi} \frac{n\omega}{c} |A|^2 \hat{K} . \tag{1.61}$$

Here n stands for the real part of the refractive index, while $\hat{K}$ is the unit vector along the propagation direction. The other part required for the absorption coefficient is the transition probability per unit time, per unit volume. This can be calculated using Fermi golden rule:

$$W = \frac{2\pi}{\hbar} |H'_{vc}|^2 \rho_{cv}(\hbar\omega) . \tag{1.62}$$

Here, $\rho_{cv}(\hbar\omega)$ is joint density of states function, obtained in Sec. 1.1.3. Furthermore, at finite temperatures, Fermi distribution should be considered in a sense that at a given photon energy $\hbar\omega$ there has to be an electron in the valence band, and there has to be an unoccupied state in the conduction band for the interband transition to occur. This can be written as:

$$f(E_v)[1 - f(E_c)] - f(E_c)[1 - f(E_v)] = f(E_v) - f(E_c) = 1 - 0 = 1 . \tag{1.63}$$

Here, f stands for the Fermi-Dirac distribution, and in the case of optical properties of graphene in the visible and UV, it is safe to assume that all the states in the valence band will be filled, while all the states in the conduction band will be empty, and the temperature dependence can be neglected at room temperatures.

The matrix element $|H'_{vc}|^2$ in Eq. 1.62 can be written in terms of the electromagnetic interaction hamiltonian:

$$H'_{vc} = \langle v|H'_{em}|c\rangle = -\frac{e}{mc} \langle v|\vec{A}(\vec{r}, t) \cdot \vec{p}|c\rangle . \tag{1.64}$$

The wave vector of the light $\vec{K}$ is small relative to the Brillouin zone dimensions, as a result the spatial dependence of the vector potential can be ignored. Considering this and taking the square of the absolute value of Eq. 1.64 results with:

$$|H'_{vc}|^2 = \left(\frac{e}{mc}\right)^2 |A|^2 |\langle v|p|c\rangle|^2 . \tag{1.65}$$

Here $\langle v|p|c\rangle$ couples states with the same electron wave vector in the valence and conduction bands. Let us assume that $|\langle v|p|c\rangle|^2$ is slowly varying with $\vec{k}$ in comparison to the joint density of states function $\rho_{cv}(\hbar\omega)$, then $|\langle v|p|c\rangle|^2$ could be considered as independent of $\vec{k}$, similarly as in Sec. 1.1.3.

Now lets return to the absorption coefficient $\alpha_{abs}(\hbar\omega)$ considering Eq.-s 1.61, 1.63 and 1.65 :

$$\alpha_{abs}(\hbar\omega) = \frac{\hbar\omega\left(\frac{e}{mc}\right)^2|A|^2|\langle v|p|c\rangle|^2\rho_{cv}(\hbar\omega)(f(E_v)-f(E_c))}{\frac{\omega}{8\pi}\frac{n\omega}{c}|A|^2}\,, \tag{1.66}$$

$$\alpha_{abs}(\hbar\omega) = \frac{16\pi^2e^2\hbar}{m^2cn}|\langle v|p|c\rangle|^2\frac{\rho_{cv}(\hbar\omega)}{\hbar\omega}\,. \tag{1.67}$$

If n could be considered as a constant, which will be shown later on that is a good assumption in a certain spectral range (NIR and parts of the visible), then the absorption coefficient would be the function of joint density of states per incident photon energy:

$$\alpha_{abs}(\hbar\omega) \propto \frac{\rho_{cv}(\hbar\omega)}{\hbar\omega}\,. \tag{1.68}$$

It is convenient to relate the optical absorption coefficient to the imaginary part of the dielectric function, or to calculate the absorption using Beer-Lambert law. The former could be easily expressed as:

$$\epsilon_2(\hbar\omega) = \frac{nc\hbar}{\hbar\omega}\alpha_{abs}(\hbar\omega)\,, \tag{1.69}$$

$$\epsilon_2(\hbar\omega) = \left(\frac{4\pi e\hbar}{m}\langle v|p|c\rangle\right)^2\frac{\rho_{cv}(\hbar\omega)}{(\hbar\omega)^2}\,. \tag{1.70}$$

If $\langle v|p|c\rangle$ is considered as constant, the imaginary part of the dielectric function depends on the joint density of states function per square of the incident photon energy:

$$\epsilon_2(\hbar\omega) \propto \frac{\rho_{cv}(\hbar\omega)}{(\hbar\omega)^2}\,. \tag{1.71}$$

In order to calculate how much light would a graphene layer with thickness d absorb, lets assume that there is a parallel beam of light with intensity I_0 propagating perpendicular to the plane of graphene (shown in inset of Fig. 1.8). Graphene layer has the absorption coefficient α_{abs}. The intensity of the beam transmitted through graphene (I) is given by Beer-Lamberts law, as:

$$I = I_0e^{-\alpha_{abs}d} = T\cdot I_0\,. \tag{1.72}$$

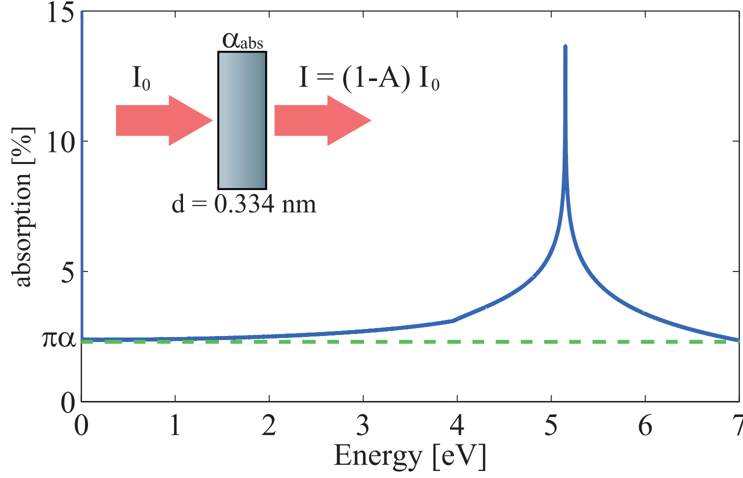

Figure 1.8.: Absorption of a free standing single-layer graphene sheet calculated from the joint density of states function (shown in Fig. 1.4). Scaling parameter was estimated in the low energy limit, and was found to be: $C = 1.6725\, eV^2/nm$. Thickness of graphene used to calculate the absorption was fixed to the inter-layer spacing of graphite ($d = 0.334\, nm$). Only interband transitions have been accounted for.

Here T stands for the transmittance. If reflection is neglected, absorbance is then obtained as:

$$I_0 = AI_0 + TI_0\,, \tag{1.73}$$

$$A = 1 - e^{-\alpha_{abs} d}\,. \tag{1.74}$$

Let us now focus on the case of graphene. As was shown in Eq. 1.68, absorption coefficient is a function of JDOS per incident photon energy. Assuming that the real part of the refractive index n and $\langle v|p|c\rangle$ are constant, absorption coefficient could be written as:

$$\alpha_{abs}(\hbar\omega) = C \cdot \frac{\rho_{cv}(\hbar\omega)}{\hbar\omega}\,. \tag{1.75}$$

Here C is the scaling parameter. It is obvious that if JDOS is linear with $\hbar\omega$ then absorption coefficient has to be constant. In the part of the spectra where linear dispersion relation of graphene holds, optical conductivity of graphene is equal to the universal optical conductivity: $\sigma_0 = e^2/4\hbar$. This translates to absorption by a single layer graphene of $\pi\alpha$, where α stands for the fine structure constant $\alpha \approx 1/137$. Now scaling parameter can be easily evaluated using Beer-Lamberts law, relation for linear JDOS (Eq. 1.48) and taking thickness of graphene to be $d = 0.334\, nm$ (inter-

layer separation in graphite), resulting with $C = 1.6725\,eV^2/nm$. The detailed derivation of graphene's optical conductivity is given in appendix A.4, in the region where a linear dispersion approximation holds.

Now, let us use numerically calculated JDOS, and return it to Eq. 1.75. The results are shown in Fig. 1.8. Since scaling parameter is obtained in the low energy limit, absorption there is set to $\pi\alpha$. As expected, a prominent peak in absorption appears in the UV part of the spectra (exactly at $2t$). This peak corresponds to the logarithmic van Hove singularity in JDOS function of graphene. The prominent peak is positioned at the energy that corresponds to the interband transitions in the vicinity of the M point (saddle point) in Brillouin zone.

This dissertation considers optical properties of graphene in the visible and ultraviolet ranges (~1-5.5 eV). As it was shown in this and previous section, starting only from the crystal structure and only one parameter t (the nearest neighbor hopping energy), considering a tight binding approximation and considering only interband absorption calculated within the perturbation theory, two main features arise. First, at lower energies, in the near-infrared (NIR) and most of the visible ($\hbar\omega < 3\,eV$) range, absorption coefficient can be considered as constant. This was shown to be a consequence of the linear approximation of the dispersion relation. Further discussion and experiments confirming this are presented in the following subsection (Sec. 1.2.3). The other feature of interest in the optical properties of graphene lies in the UV range. As described, it is manifested as a pronounced absorption peak which is related to M-point Van Hove singularity in JDOS. Experiments confirming this, and also showing excitonic shift related to this absorption peak are shown and discussed in Sec. 1.2.4.

1.2.2. Electron-hole interaction, excitons

A neutral Coulomb correlated electron-hole pair can form when a photon is absorbed by a non-metal, or by a material with low carrier concentration at the Fermi level. An incident photon excites an electron from an occupied state in a valence band, into an empty one in a conduction band. This process leaves behind a positively charged hole, or a missing electron in the density of the ground state from which the electron was removed. The negatively charged electron is then attracted by the

hole by Coulomb force. Furthermore, this attraction is weakened by the screening reaction of the electronic system to the excited electron-hole pair. This gives rise to a new neutral excitation in the electronic system, a new quasiparticle, an exciton [48].

An electron-hole pair subjected to Coulomb interaction leads either to bound states or scattering states. In the case of the bound states, the total energy of the electron-hole pair is smaller than the sum of the eigenenergies of the individual particles. This commonly leads to a formation of discreet states below the band gap. On the other hand, the scattering states are commonly characteristic for the electron-hole pairs that are excited above the band gap. In this case excitons are much harder to detect in the optical spectra, and these scattered excitonic states usually contribute to an increase of the absorbtion, with the respect to the independent-particle picture. Commonly the excited electron-hole pair is called "exciton" only when it is excited in a bound state.

It has been well documented that excitons give rise to prominent features in optical spectra of semiconductors and insulators near the energy of a band gap [48, 49]. These are the lowest energy, or M0 critical point excitons. They are characteristic since the bound excitonic states are formed within the band gap, meaning that they do not overlap with the band states. There are two extreme models used to describe the electron-hole interaction in this case.

The Wannier-Mott model assumes that the electron-hole interaction is weak (in the order of ten millielectron volts). The effective-mass model is employed and the hydrogen atom like Hamiltonian results. The radii of the exciton "orbits" in this case are at least several interatomic spacings or larger. This is usually the case for small band-gap semiconductors with small effective mass and high dielectric constants.

The other extreme model is the Frenkel exciton. In this case the electron and hole are localized on one site or a small number of sites. It basically represents an excited atom or ion in the crystal. Much smaller exciton radii than in the case of Wannier-Mott excitons gives much larger exciton binding energies. There are also charge transfer excitons, that are characteristic for M0 transitions. These are characteristic for ionic crystals and molecular crystals (e.g. pentacene). Although there is an underlaying mechanism for the charge transfer separation, these are usually interpreted as Frenkel excitons.

More important for the thesis are electron-hole interactions that do occur away from the M0 threshold. The electron-hole interaction is present for electron-hole

pairs produced by exciting any electron to any excited state, not just at M0. At an M1 critical point any discrete bound electron-hole pair will be degenerate with other excited states into which it may decay. Such excited state is called a hyperbolic exciton. These states are observable in optical spectra if the decay times are not too great.

In the case of a hyperbolic exciton, the excitonic states are not independent of the band states. As a result, the absorption spectra are not simply the sum of the two individual spectra, as it would commonly be the case for M0 excitons. The final excited state of the system is a superposition of both the discrete and continuum excited states. When this superposition is used to evaluate the electric-dipole matrix element, interference effect occur upon squaring, and the strength of the coupling of two types of excitations has a strong effect on the appearance of the resultant absorption spectra [49]. These are seen as shifts of the absorption peak, broadening, and an appearance of a dip on either high- or low-energy side of the peak. Such effect was first described by U. Fano [50], and the resulting line shapes are called Fano lines, or Fano resonant profiles. For this reason, hyperbolic excitons give rise to Fano line shapes in the absorption spectra, away from the band gap.

Interestingly, M1 exciton formed in graphene is most likely the best and most prominent example of a hyperbolic exciton. This is the case mainly due to the confinement in two dimensions, which both increases exciton binding energy and reduces screening by the electronic system. Experimental observations of a hyperbolic exciton in graphene will be discussed in greater detail further in the text (Sec. 1.2.4).

1.2.3. Previous studies in optical properties of graphene

This sub-section is focused on previous studies of graphene's optical properties, and will present a current state of research in this field. Later, the following subsection (Sec. 1.2.4) will focus on the current state of research regarding optical properties of graphene in the UV, and the exciton-shifted van Hove peak in absorption.

Graphene strongly interacts with light making optical spectroscopy a powerful tool for probing the unusual physics of graphene [51]. This strong light-matter interaction allowed for the initial discovery of graphene [1], since one single atomic

layer can absorb as much as ~2.3 % [52, 53, 54, 55, 56, 57, 58, 59, 60]. This allowed for graphene to be "found" or more precisely visualized by an ordinary optical microscope. Here a Fabry-Perot interference, commonly introduced by an underlaying thin SiO_2 layer is used to enhance the visibility of graphene [61, 62, 63, 64]. One of the contribution of this dissertation is the application of Fabry-Perot interferences to enhance the sensitivity of ellipsometric measurements, and increase the reliability of the obtained optical properties of graphene (will be discussed later on, in chapters 3 and 4).

Light absorption in graphene could be separated into two major components: intraband and interband [44, 47, 53, 65, 66]. The relative importance of each component depends largely on the spectral range of interest. In the far-infrared region, the optical response of graphene is dominated by the free-carrier, or the intraband response [47, 53, 67]. In this region optical response is well described by the Drude model. The interband contribution is here neglected. There are two justifications for this. First, intraband contribution is much larger than the interband contribution in this range. Second, in the realistic case of graphene some minimal amount of doping is inevitable, this will result with Pauli blocking and will prohibit interband transitions.

For the incident photons with energies above ~100 meV (mid-IR) the intraband contribution can be neglected [47] and the optical response is dominated by the interband component. Interband contribution to the absorption function was discussed in the previous section. As describe there the interband response is frequency independent in the mid- and near-IR as well as a large part of the visible (up to about 3 eV). Optical conductivity can be calculated from the dispersion relation obtained within the tight-binding approximation [47, 52, 53, 54, 55, 59, 68]. In the linear dispersion regime (Eq. 1.30) absorption coefficient, and consequently optical conductivity is determined solely by fundamental constants $\sigma(\omega) = \pi e^2/2h$. As it was shown, this corresponds to an absorbance of $A(\omega) = \pi\alpha \approx 2.3\%$. This was experimentally confirmed by reflection measurements in the near- and mid-IR by K. F. Mak and co-workers [58], and transition measurements through suspended single- and bi-layer graphene in the visible, by R. R. Nair and co-workers [60].

The independence of the interband optical absorption on both frequency and material properties (as encoded in the Fermi velocity v_F) is the consequence of the linear approximation. The absorption coefficient of graphene obtained within perturbation theory, and with linear approximation, gives perfect cancelation of

both $\hbar\omega$ and v_F, thus resulting with a constant value that is neither frequency nor material property dependent. As it can be shown a square of the transition matrix element is proportional to v_F^2, since $\vec{k}$ (or $\hbar\omega$) dependence has been neglected. Joint density of states, as it was shown in Eq. 1.48, is proportional to $\hbar\omega/v_F^2$. Finally, the product of these two need to be divided by the incident photon energy of $\hbar\omega$ (Eq. 1.66), thus giving the perfect cancelation of both $\hbar\omega$ and v_F. In a sense this comes from the 2D analysis of graphene, since Hamiltonian describing linear bands (Eq. 1.30) has no intrinsic energy scale with which to compare the incident photon energy, thus being both frequency and material property independent. This is just an approximation, and is not a realistic case. However, as it is show by [58], this is a very good approximation. K. F. Mak and coworkers [58] have shown that absorption of a single layer graphene in the spectral range from 0.5-1.2 eV is equal to $\pi\alpha$ $\pm 10\%$. Furthermore, number of different graphene samples, with different unintentional doping (as seen by position of $2E_F$ and as a consequence of Pauli blocking), still had the same absorption in that spectral range. This in a sense confirms independence of the material properties. In a more realistic case second nearest neighbor hopping, ω dependence of the matrix element, triangular warping [17, 35, 37], or even many-body interactions at low photon energies [69], all need to be included in the absorption calculation. These would result with a correction to the optical conductivity of graphene obtained within linear approximation of the dispersion relation.

The linear model, although very good in a certain range (0.5-3 eV), fails both at lower and at higher energies. The former is a consequence of Pauli blocking, while the later is the consequence of the van Hove singularity (see Sec. 1.2.4). Let us now focus on the lower limit of the linear model for absorption. As it was stated, in Sec. 1.2.1 Pauli blocking is neglected, and linear model is used also at zero energy. This approximation is valid if considered that Fermi level lies exactly at the Dirac point. However, this is not a realistic case, and as was discussed in Sec. 1.1.5, some unintentional doping is inevitable. As a consequence, Fermi level will not lie exactly at the Dirac point. Let us assume that the sample is slightly n-doped, i.e. that the Fermi level lies above the Dirac point. This means that interband transitions with photon energies lower than $2E_F$ (where E_F is the Fermi energy relative to the Dirac point), will be forbidden, since there will be no unoccupied states in the conduction band. This is schematically represented in Fig. 1.9(a). Similarly in a case of p-doping, for photon energies lower than $2E_F$ there will no electrons in the

valence band (schematically represented in Fig. 1.9(b)). This effect is referred to as Pauli blocking of the interband transitions. Linear dispersion approximation is still valid here, so only by slightly changing the absorption (or optical conductivity) function we can account for the Pauli blocking still within the linear regime. This can be simply carried out as in [47, 59, 70]:

$$\sigma(\hbar\omega) = \frac{\pi e^2}{4h}\Big[\tanh\big(\frac{\hbar\omega + 2E_F}{4k_BT}\big) + \tanh\big(\frac{\hbar\omega - 2E_F}{4k_BT}\big)\Big]\,. \tag{1.76}$$

Here k_BT accounts for the thermal broadening, where k_B is Boltzmann constant. For $T \rightarrow 0K$ the expression within the brackets becomes Heaviside (step) function $h(\hbar\omega - 2E_F)$. If local impurities are taken int account, further broadening is introduced.

Furthermore, if the Fermi level in graphene is shifted by the electrostatic gating (as shown in Sec. 1.1.5), it is possible to manipulate optical properties of graphene as well. This was first demonstrated by Z. Q. Li and coworkers [44], through reflectance measurements in the mid-IR range. Here graphene was connected to a circuit with several Ohmic contacts, and the position of the Fermi level was controlled by a DC back-gate voltage. Figure 1.9(c) shows the real part of optical conductivity reported in [44], for various back gate voltages (relative to CNP) from 10 V to 70 V. This demonstrates the control of Pauli blocking of interband transition in graphene by electrostatic gating. However, electrostatic gating is limited by the breakdown of the oxide layer. Some highest possible carrier concentrations achievable through electrostatic gating are $\sim 5 \times 10^{12}\, cm^{-1}$. Considering $n = E_F^2/\pi\hbar^2 v_F^2$ gives the corresponding shift of the Fermi level of 200-250 meV. This means that optical properties of graphene can be manipulated by electrostatic gating in the mid-infrared region [44]. However to introduce even higher carrier concentrations and to shift $2E_F$ further to the near-IR and visible, an electrolyte gating is used [43, 45, 71, 72]. This concept utilizes so called proton gels, similarly as in Li-ion batteries. Through electrolyte gating it is possible to induce carrier concentration as high as $10^{14}\, cm^{-1}$, which corresponds to the shift of the Fermi level even over 1 eV. This way it is possible to put the edge of the Pauli blocking all the way into the visible range (∼2 eV or 620 nm) [43].

Next subsection (1.2.4) will discuss on the upper limit of the linear model and on the exciton-shifted van Hove peak in absorption. But prior to that, let us focus on various techniques that have been employed to analyze optical properties of graphene thus far, with focus on ellipsometry. As already stated, various reflection [43, 44,

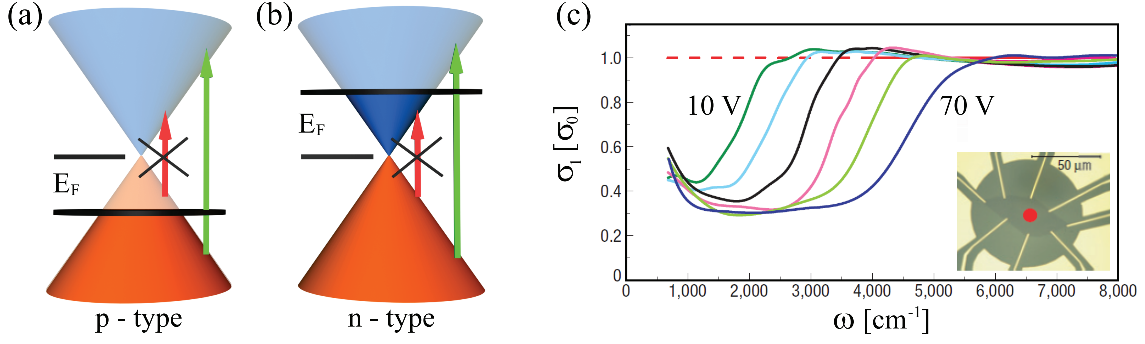

Figure 1.9.: (a) and (b) schematic representation for Pauli blocking of the interband transitions in graphene for p-type and n-type doping, respectively. (c) real part of graphene's optical conductivity (reprinted from [44]), for various voltages (10-70 V) applied in a back-gate configuration. Inset of (c) shows a microscope image of the device.

58, 65] and transmission [60, 73] measurements of graphene have been carried out. However reflection and transmission measurements can obtain only the absorption coefficient, or the imaginary part of the dielectric function.

Spectrophotometry has been employed by A. Gray and co-workers [62] to obtain complex refractive index of exfoliated graphene. Furthermore, Ref. [62] investigates influence of an interference that occurs within SiO_2 layer, and how this interference can be used to enhance measurement sensitivity. First results on ellipsometry measurements of graphene's complex refractive index were reported in 2010. Spectroscopic ellipsometry (SE) was employed by V. G. Kravets and co-workers [74] and J. W. Weber and co-workers [75]. Both results were reported for exfoliated single-layer graphene in the visible and UV ranges. Complex refractive index of exfoliated single-layer graphene obtained using spectroscopic null imaging ellipsometry (SNIE) was first reported by U. Wurstbauer and co-workers [76]. Ellipsometric mapping and layer counting by SNIE, ellipsometric contrast as well as Brewster angle microscopy were demonstrated by O. Albrektsen and co-workers [77]. Several other results regarding ellipsometry measurements of exfoliated graphene were reported [78, 79, 80, 81, 82, 83]. Contribution of this dissertation to ellipsometry of exfoliated graphene is described in Sec. 1.3.3 and chapter 4, as well as within [82, 83].

Ellipsometry has already set its place firmly within semiconductor industry, as a in-line and post-fabrication control tool. Similarly in the growing industry of graphene, as various fabrication methods are being developed, ellipsometry is em-

ployed along with them. As it will be discussed in detail later on, chemical vapor deposition (CVD) arises as one of the dominant methods for mass-production of graphene. First results on ellipsometry of CVD graphene transferred on a dielectric substrate were reported by F. J. Nelson and co-workers [84, 85]. Ellipsometry can be very useful as a contact-less in-line growth control tool, as demonstrated by M. Losurdo and co-workers [86, 87, 88]. The other possibility is to use ellipsometry as a post-fabrication control tool. Here ellipsometry can be used to characterize the interaction between graphene and a copper substrate on which it was grown [89, 90], or to characterize remaining transfer residue [91], or a quality of metallic contacts when graphene is transferred over a pre-fabricated structures [92]. Chang and co-workers [66] have employed ellipsometry to investigate how chemical doping with nitric acid modifies the complex optical conductivity. Contribution of this dissertation to employing ellipsometry as a tool for post-fabrication control of CVD graphene is described in Sec. 1.3.3 and chapter 4, as well as within [91, 92].

Besides chemical vapor deposition there are other graphene synthesis methods where ellipsometry has also been successfully employed. Ellipsometry was used to characterize optical properties and number of layers for graphene grown on SiC [93, 94, 95, 96, 97], and graphene obtained by reduction from graphene oxide [98, 99]. Recently (in the year 2014) several studies have used ellipsometry to characterize optical properties of other materials that could be obtained as single atomic layers. These materials are often referred as Van der Waals (VdW) materials. Complex dielectric functions of single-layer MoS_2 and WSe_2 were reported by [100, 101, 102, 103].

1.2.4. Exciton-shifted van Hove peak in absorption

This subsection focuses on the optical properties of graphene in the UV part of the spectra, and gives an overview on the current state of research in this area. As it was discussed in Sec.-s 1.2.1 and 1.2.3, in the UV range only interband contribution is considered. And as it was demonstrated (Sec. 1.1.3) linear approximation of the dispersion relation is not valid for incident photon energies above 3 eV. Here optical properties are governed by the transitions that occur in the vicinity of M point in Brillouin zone (a saddle point in dispersion relation). For energies that

correspond to interband transitions at the M point, joint density of states function has a logarithmic van Hove singularity. Observable consequence is a prominent absorption maximum in the UV part of the spectra.

Since graphene is a semi-metal, with low intrinsic carrier concentration, one might intuitively expect that many-body effects would be weak in graphene. This expectation holds for most of the infrared and visible range, and an independent particle picture (as introduced by interband absorption calculated within perturbation theory) gives very good agreement with the experimental results. However, screening of Coulomb interaction in graphene is also significantly reduced, since carriers are confined in a 2D plane and density of states is vanishing at the Dirac point. Several theoretical studies have predicted the influence of many-body effects on the optical properties of graphene. A deviation from the universal optical absorbance ($\pi\alpha$) through a reduction in absorption at low photon energies is expected, as reported by E. G. Mishchenko [69]. Furthermore, the appearance of Fermi edge singularities and their consequence on the optical properties of graphene were reported by [104, 105]. Experimental confirmation of these many-body effects in graphene would require very precise measurements at well defined carrier densities and low temperatures, and has not been reported thus fahr.

One clear and robust signature of many-body interactions in the optical spectra has already been identified experimentally [43, 65, 74, 73, 82, 89, 91, 106]. This is the exciton-shifted van Hove peak in absorption at the M point. Let us first consider the independent particle picture, introduced by interband absorption calculated within perturbation theory. As it was considered in Sec. 1.2.1 the resonance feature in the UV arises from interband transitions near the saddle point (M point) in Brillouin zone. In this approximation absorption should be determined essentially by the JDOS function (as in Fig. 1.8). Near the critical point, absorption should be proportional to $\propto -log|1 - \frac{\hbar\omega}{\hbar\omega_0}|$, meaning that the peak should be positioned at $\hbar\omega_0 = 2t$ and it should be symmetric near the singularity. The sheet conductivity predicted within the framework of GW ab-initio calculations, reported by L. Yang and co-workers [25], shows a symmetric absorption peak at about 5.2 eV. These calculations do not include electron-hole interaction.

However experimental measurements of reflectance [65], transmittance [73] and ellipsometry [74], all show that the resonant peak is red-shifted by as much as 600 meV from the expected position, and that it is asymmetrical. The observed discrepancies can be explained by taking into account excitonic corrections to the

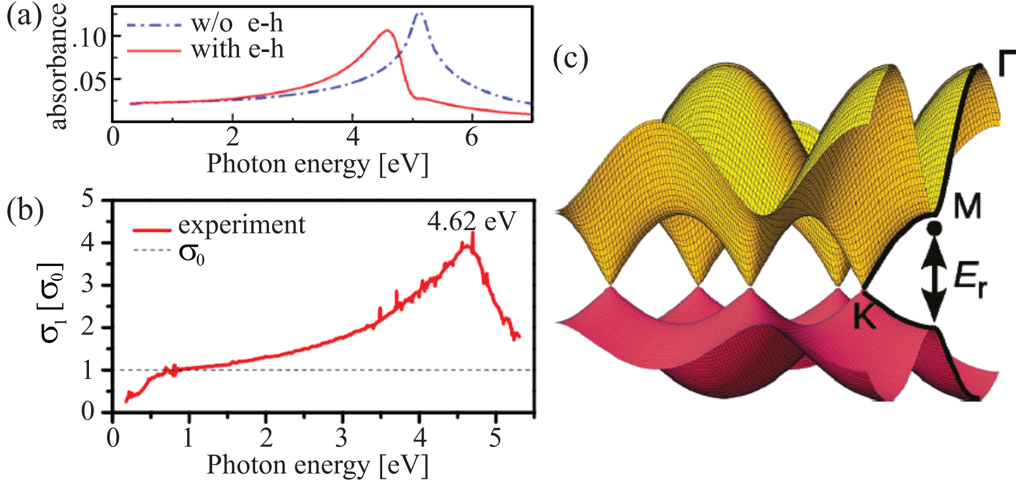

Figure 1.10.: (a) Absorbance of single-layer graphene obtained by ab-initio calculations with (solid line) and without (dashed line) electron-hole interaction (reprinted from Ref. [25]). (b) Measured optical conductivity of a single-layer graphene (reprinted from Ref. [65]). (c) Schematic representation of a dispersion relation of graphene (high symmetry points are marked), and band-to-band transitions in the vicinity of a saddle-point (M point). E_r denotes a resonant energy of the prominent absorption peak, while solid dot represents excitonic state that lies below the valence band (reprinted from Ref. [73]).

optical response of graphene near the saddle-point singularity. This can be modeled by an exciton resonance at an energy below the saddle point singularity that couples strongly with the existing continuum of electronic states in the conduction band. Phenomenological description of this exciton-shifted absorption peak can be written within a Fano model [23, 46, 50, 107]. For the case of graphene, Fano resonant model was first introduces to calculate real part of the optical conductivity and to model the absorption of a single layer graphene by D.-H. Chae and co-workers [73] and K. F. Mak and co-workers [65]. First reports of a Fano resonant profile used for modeling a complex refractive index of graphene were reported by [82, 83], and are a part of this dissertation (see chapter 4). The strong excitonic effect observed in the optical response of graphene reflect the reduced dielectric screening in a 2D system and the vanishing density of states function at the Dirac point.

As it is possible to "tune-in" interband absorption of graphene in the infrared region through Pauli blocking mechanism, would it be also possible to tune the

exciton-shifted peak in absorption by changing the Fermi level in graphene? Although a mechanism here would be much more complicated than in the case of Pauli blocking, a result would be tunable optical properties of graphene in the visible and UV ranges, and would have many different potential applications in opto-electronics [108].

Several studies [43, 66, 89, 90, 92, 109] have shown that by changing the doping level in graphene, a balance between the electron-electron (e-e) interaction and the electron-hole (e-h) interaction can be modified, which causes the change of the absorption peak's shape and position. In the case of graphene doped by an electric field (through electrochemical gating), as theoretically predicted by L. Yang [109], a further red shift and broadening of the prominent absorption peak has been observed by K. F. Mak and co-workers [43], indicating a suppression of e-e interaction. The other way to introduce doping of graphene is through the interaction with its surroundings. Y.-C. Chang and co-workers [66] have investigated how chemical doping with nitric acid modifies the complex optical conductivity, and found a negligible shift of the prominent peak. Optical properties of graphene grown on a copper substrate have been investigated by P. K. Gogoi and co-workers [89], and by M. Losurdo and co-workers [90]. In that case, the interaction with the substrate mainly suppresses e-h interaction, and the absorption peak was found to be blue shifted and symmetrical, similar to the expectations of the independent particle model [25], where the electron-hole interaction has not been accounted for. A part of this dissertation (see section 4 and Ref. [92]) investigates how does an interaction with a gold substrate affect the exciton-shifted peak in absorption.

1.3. Technological motivation and statement of the thesis

Since the initial discovery [1] research field of graphene was rapidly expanding in the last decade. One of the reasons for this expansion is the fact that graphene samples are relatively easy to make in a laboratory and do not require expensive fabrication equipment. However this was only enough to create an initial "boom" of graphene, what actually stands behind its rapid expansion is a tremendous amount of possible application for graphene. There are many different properties of graphene in which all the other materials known to man fail to even compare, for this reason graphene has earned a nickname "magic material". However, many of those properties, although true, are not possible to exploit in real-life applications. The goal of this section is to give an overview of realistic applications for graphene. For most of the mentioned applications below, a date will be given when it's commercialization is expected. These estimates are based on the development schedules of industry leaders an are taken from [110, 111] and [5].

Graphene uniquely combines many different properties that make it very attractive for numerous applications. In terms of its properties, graphene has a potential to replace other materials in existing applications, and to revolutionize many aspects of our everyday lives. Whether graphene will reach its full potential remains to be seen, however one thing is certain, graphene is the first two-dimensional atomic crystal available to us.

Graphene has a room temperature electron mobility of $2.5 \times 10^5\, cm^2/Vs$ and has a micrometer-scale ballistic transport at room temperatures [6]. Furthermore it exhibits an ambipolar effect, thus having both electron and hole mobilities the same. As a contrast electron mobility in silicon is $1500\, cm^2/Vs$ and hole mobility is $450\, cm^2/Vs$. Graphene has an ability to sustain extremely high densities of electric current (six orders of magnitude greater than copper) [7]. Regarding mechanical properties, Young's modulus of graphene is $\sim 1\, TPa$ and intrinsic strength of $\sim 130\, GPa$ [9]. Compared to other materials, Young's modulus of steel is $\sim 0.2\, TPa$, and only two materials stronger than graphene are diamond and "carbyne" (an imagined 1D chain of carbon atoms). Thermal conductivity of graphene is $3000\, W/mK$ [8], closest known bulk materials would be silver and copper with thermal conductivity of $\sim 400\, W/mK$. Interestingly, crystal lattice of graphene (and graphite) is

so densely packed that it is impermeable to any gases, even H_2 [10]. Furthermore, graphene can be relatively easily chemically functionalized. This allows for various modifications of "fine tuning" of its properties [112, 113, 114], and for novel sensor applications [115].

However, most of these characteristics have been achieved only for the highest-quality samples (exfoliated samples) [1], and deposited on special substrates like single crystal hexagonal boron nitride [6, 116]. Graphene will be of even greater interest for industrial applications when the quality of the mass-produced graphene reaches these outstanding performances achieved by the highest quality samples.

This section is split into five subsections. First four subsections present different fields for graphene application, namely: electronics, photonics, composites and energy related applications. Each of these subsections presents a short overview of the currently available proof-of-concept devices, as well as advantages and drawbacks for implementation of graphene in these fields. The final subsection is the statement of the thesis in relation to the potential applications of graphene and ellipsometry as a contact-less tool for graphene characterization.

1.3.1. Potential application in electronics and flexible electronics

Graphene based integrated electronics is one of the main driving ideas for the development of graphene field. There, graphene would serve as a channel, utilizing its confinement of electrons in a two-dimensional electron gas, its high mobility, ballistic transport and electric field effect. In a case of analogue electronics, proof of concept devices already exist [117], and commercially available high frequency amplifiers based on graphene are expected by the year 2025 [5, 110, 111]. On the other hand, logic or digital transistors, and the entire idea of post-thin-film transistors might never be realized based on graphene. Here one of graphene's very interesting property stands in a way. Graphene is a semi-metal, meaning that with no band gap there is no way to obtain a logical zero (no current going through the device). However, other two-dimensional materials like MoS_2, or chemically modified graphene might be used in next generation logic transistors. Estimates are that this technology will not be implemented prior to 2030 [5, 110, 111]. These applications require high quality graphene samples, and current state of the growth technology (see section 2.1) limits the commercialization of graphene in electronics.

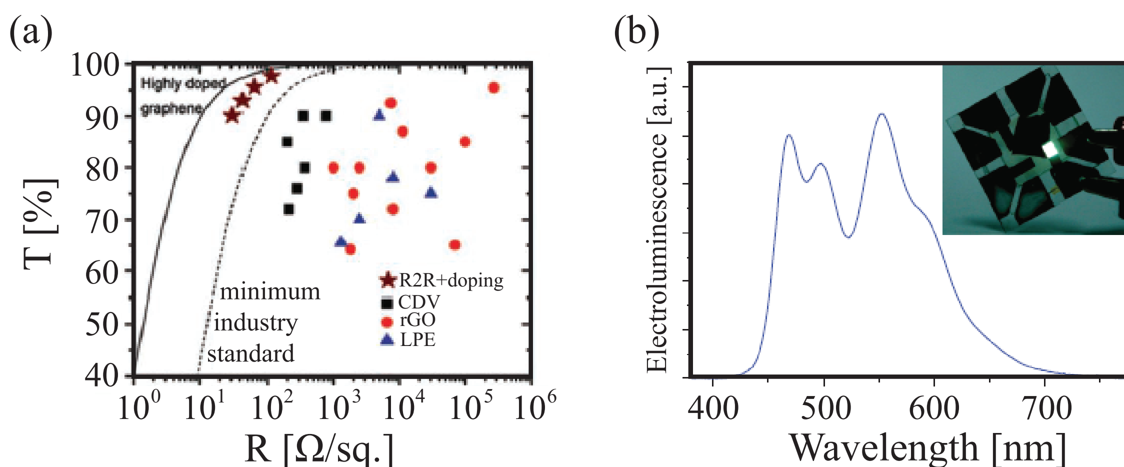

Figure 1.11.: (a) Sheet resistance versus transmission of various graphene films (reprinted from [118, 119]). The dashed line represents a minimum industry standard for ITO replacement, while solid line represents highly doped exfoliated graphene. Transmission is controlled mainly by the number of graphene layers. R2R stands for Roll-to-roll CVD process; rGO stands for reduced Graphene Oxide; LPE stands for Liquid Phase Exfoliation. (b) Electroluminescence spectra of a flexible OLED with graphene electrodes (reprinted from [120]). Inset of (b) shows a functioning device.

There are other aspects of electronics, especially flexible electronics, where graphene is most likely to find its place in the near future. These do not require highest quality samples, and could be produced by a standard chemical vapor deposition technique. In applications such as touch screens, smart windows, flexible e-paper, flexible organic light emitting diodes (OLEDs) and similar, graphene based products are expected to appear on the market by the year 2020.

Graphene applied in flexible electronics will most likely serve as a transparent electrode for either flexible touch screens, or flexible OLEDs. There are two most important properties that graphene must have here. First its transparency must be high, and second its sheet resistance must be low. Currently on the market this job is done by Indium Thin Oxide (ITO) with 80% transparency and sheet festivity of $\sim 30\,\Omega/\square$. Comparison of sheet resistance versus transmittance show in Fig. 1.11(a), for various types of grpahene. There are other important factors, as fabrication price, contact resistance, layer roughness and ease of patterning. Currenty graphene is better in all of these than ITO, but when exfoliated graphene is considered.

However, CVD graphene still is not fahr from reaching the industry threshold. Its low production cost, compatible patterning and negligible roughness brings it closer to replacing ITO. Also graphene has superior flexibility, mechanical and chemical stability [121]. For flexible OLEDs grpahene needs to have bending radius of 5 to 10 mm, which is easily achievable. Its work function needs to be between 4.7 eV and 4.9 eV, which can be tuned by chemical doping. However, sheet resistance is not good enough to replace ITO, and it has to be strictly $< 30\,\Omega/\Box$. One way to increase sheet resistivity is to use chemically doped graphene, as with HNO_3 [122]. However, this is a tradeoff between carrier mobility and sheet resistivity. A proof of concept flexible OLED device was demonstrated by T.-H. Han and co-workers [120], where sheet resistivity issue was overcome by transferring several (usually four) CVD grown graphene layers on top of each other. Still, final drawback for the flexible OLED applications is contact resistance between graphene and external metallic leads. Flexible OLEDs based on graphene are expected by the end of 2016.

Somewhat less rigorous applications in flexible electronics are touch screens. Here transparency of over 90% and sheet resistivity of $50 - 300\,\Omega/\Box$ is required to meet the industry threshold. Furthermore, for low transparency touch screens (those that are not designed to be placed over a display), or smart windows, or even solar cells industry standards are even lower, and graphene made by liquid phase exfoliation is applicable. These ”low quality” products that utilize graphene's transparency, flexibility and electrical conductivity are expected to be commercially available by the year 2020 [5, 110, 111, 118].

1.3.2. Potential application in photonics

As it was discussed in Sec. 1.2, graphene's unique optical properties are opening many potential applications in photonics [5, 108, 110, 111]. Major advantage concerns an independent absorption in a wide wavelength range, and the possibility of changing optical properties by electrostatic gating (through Pauli blocking). In addition, the large carrier mobility gives potentially extremely fast response that graphene opto-electronic devices could achieve. Rapid expansion of optical communications, and a constant demand of ever faster networks, will soon be needing a next generation of network components. This subsection will discuss potential

applications of graphene in active components as photodetectors and optical modulators.

Research results regarding graphene-based photodetectors started appearing in 2009, both as conceptual and proof-of-concept devices, and are now one of the most actively studied type of graphene-based devices [108, 110]. Main advantage of graphene photodetectors is constant response in a wide spectral range, from infrared to ultraviolet. In addition, high carrier mobility of graphene enables very fast extraction of photo-generated carriers, giving high operating bandwidth of these devices. Theoretical bandwidth limit is as much as 1.5 THz [123], and is limited by the saturation carrier velocity [124]. In practice, proof of concept devices have been realized that can operate at 640 GHz [123]. However, stable devices are still limited to ∼10 GHz bandwidth. Such a device is presented in Fig. 1.12(a-c), and its working principle will be discussed later on. As a comparison, the most high-speed optical networks use germanium based photodetectors. Current bandwidth limitation of Ge-based photodetectors is ∼80 GHz [125]. Photodetectors with higher bandwidth can be realized based on III-V semiconductors (as InGaAs), and their current bandwidth limitation is at ∼150 GHz [126]. However, these are significantly more expensive compared to both Ge- and graphene-based devices.

Due to the lack of a bandgap, graphene-based photodetectors must have a different carrier extraction model than the one used in a semiconductor-based photodetectors. One way to extract carriers from graphene would be to apply a large bias across the detection area, thus forcing a photocurrent to follow the drift of the electric field. However this is not a good approach, besides having to provide a constant power to the device it would have a large dark current. One way to reduce, or even completely eliminate the bias voltage requirements is to use a local potential variation near the graphene/metal interface to extract photo-generated carriers [129, 123, 127]. Schematic representation and a scanning electron microscopy image of such device are shown in Fig. 1.12(a) and (b), respectively. Here doping of graphene by a metallic contact is used to create a voltage drop across the detection area. For this reason two different metals, in this case palladium and titanium are required to introduce p- and n-type doping, respectively. Figure 1.12(c) shows relative response versus light intensity modulation frequency. For this particular device geometry, bandwidth of 16 GHz was archived. Inset of Fig. 1.12(c) shows an eye diagram at 10 GHz, confirming stable operation of the device at near-infrared frequencies (used in optical communications) and at room temperature. Slight modifications of the

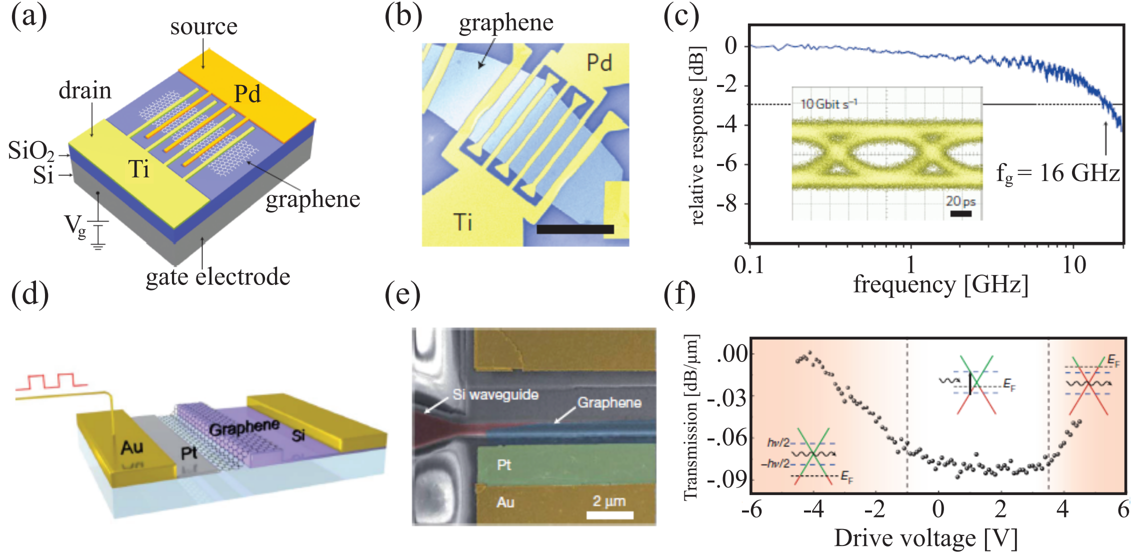

Figure 1.12.: (a), (b) and (c) schematic representation, scanning electron microscopy image and relative response versus light intensity modulation frequency (respectively) of a graphene photodetector that utilizes local potential variation for photo-generated carrier extraction (reprinted from [127]). Inset of (c) eye diagram of the device at operating frequency of 10 GHz. (d), (e) and (f) schematic representation, scanning electron microscopy image and a static electro-optic response at the different drive voltages (respectively) of a graphene-based broadband optical modulator (reprinted from [128]). The device uses Pauli blocking princple to modulate optical absorption of graphene in the infrared range, as schematically represented in inset of (f).

geometry can give bandwidth of ∼40 GHz [127].

One more drawback for graphene-based photodetectors is a relatively small light absorption (2.3 %) [60]. To address this issue plasmonic nanostructures have been introduced at the graphene surface in order to create an enhancement of the local electric field and thus increase absolute absorption of the device [130]. The other approach is to integrate graphene into a silicon waveguide in order to increase light-graphene interaction length [131]. However, these approaches to increase total light absorption of the device almost in all cases limit the frequency range where they are applicable, and thus affect the frequency independent absorption function of graphene. Since current limit of Ge based photodetectors is ∼80 GHz, and considering current trends of the expansion of optical networks, low-cost photodetectors

with a bandwidth over 100 GHz will be needed by the year 2020. For graphene to be competitive against InGaAs and other III-V semiconductor-based photodetectors, samples with carrier mobility over 20000 cm^2/Vs need to be mass produced at low-cost.

Beside photodetectors, optical modulators are also very promising type of opto-electronic devices for graphene implementation. Optical modulators are active building blocks for optical networks, that are used to encode transmission data by light modulation. Commonly various types of Si-based integrated devices are used [132]. There are several light modulating principles, as interference (e.g. Mach-Zender interferometer) [133], ring resonators [134], electro-absorption modulators [135], and others. These devices usually have narrow operating spectral range and low switching times. The later is due to a large resistance in the p-n junction through the Si core region. As a result, bandwidth limitations of these devices are usually at ∼50 GHz.

By employing a field effect in graphene, combined with its low and constant absorption in a wide spectral range, and its ultrafast response (due to high carrier mobility), proof-of-concept devices have achieved switching at 1 GHz in the near-infrared range [128]. Here a silicon waveguide is covered with a single layer CVD grown graphene. By electric field modulation Fermi level in graphene is shifted. This causes a change in absorption due to Pauli blocking (as discussed in 1.2.3). Since graphene covers a relatively long section of the waveguide (several micrometers), multiple refections occur, and when $2E_F$ is above (or below) the light frequency no absorption occurs. On the other hand, with $E_F \approx 0\,eV$, each reflection of the light that propagates within a waveguide causes loss, and after a sufficient length the light is modulated according to the applied gate voltage. Figure 1.12(d-f) respectively show schematic representation, scanning electron microscopy image and a static electro-optic response at the different drive voltages for such optical modulator (reprinted from [128]). With further device optimization, and higher quality graphene (higher carrier mobility) simulations suggest possible bandwidths of ∼500 GHz [131].

Limitations for graphene-based optical modulators are similar as for graphene-based photodetectors. Here low-cost large-area (over 1 mm^2) of high quality graphene is required, in some cases even supported by single crystal substrates as hBN, in order to achieve high enough mobilities that will allow switching faster than 80 GHz.

1.3.3. Composites, inks and coatings based on graphene

Most of the potential applications of graphene are actually not hi-tech ones [5, 111] and do not exploit properties as high carrier mobility, ambipolarity, universal optical conductivity or electric field doping. These applications consider an integration of graphene into products such as composites, inks, paints and various types of coatings. These applications mostly use mechanical, thermal or electrical properties of graphene. In most cases there is no need for large or high quality samples, usually only large volumes and low-cost are required. Chemical synthesis of graphene (see Sec. 2.1.1) either through reduction from graphene oxide (rGO) or through liquid phase exfoliation (LPE) is commonly employed.

Products of chemical synthesis of graphene are usually liquids containing suspended graphene-based particles, i.e. various paints and inks. These could be integrated into a large variety of products such as printed electronics [136], anti-static layers, electromagnetic interference shielding, self-regulating heaters, thermal conducting layers, gas and corrosion barriers, conductive textile, and many more. Currently on the market there are metallic based paints, as sliver or copper, or pains containing nanoparticles, that are used for screen-printing of conductive and thermal layers, but their high price limits their use, and whenever possible laminated foils are used. The other major competitor for graphene-based paints is so called "carbon black". This is a material produced by the incomplete combustion of heavy petroleum products. It has a paracrystalline form, meaning that there is a local lattice (in the order of several hundred unit cells) but there is no larger crystalline structure. In a sense chemically synthesized graphene is similar to carbon black, only with several orders of magnitude greater domains, or as usually referred in this case, flakes.

Another interesting application for liquid processed graphene is ink-jet printing. This would allow for relatively high resolution ($\sim$10 μm) printing of various conductive structures [137], making it possible to simply print linear electronics circuits on a piece of paper. If besides graphene other Van der Waals materials would be used in a printing process, it would allow for printing of non-linear components as well, such as diodes, light emitting diodes, and transistors. The printing process is not limited to paper, and as it was demonstrated by F. Torrisi and co-workers

[136] structures could be printed on glass, or Si wafers. These devices are inferior to Si-based electronics, but in some special cases they have their advantages. As an example, screen printing of radio frequency identifiers (RFIDs), using graphene-based paints, has been patented by Vorbeck corp. [138], and is currently comparable to laminated RFIDs considering performance, but still at a higher price.

Regarding composite structures with high breaking strength and light weight, current quality of mass-produced graphene will hardly win over carbon fibers. However, graphene can be used with carbon fibers and similar composite materials to either improve existing properties or to introduce new ones (as electrical or thermal conductivity) [30]. This approach was used, and patented by Head inc. [139]. There, a small amount (5-10 %) of chemically synthesized graphene was added into the resin that is used for binding of carbon fiber layers. This simple modification resulted with ∼20 % increase in breaking strength. This was used in a first commercial product that utilizes graphene, a tennis racket. These products appeared on the market in the beginning of 2014.

Most of the major companies in carbon business have already established programs for development of a low-cost graphene and its implementation into coatings, inks, paints and composites. Although, Head inc. is the first to come up with a commercial product, many others are expected to follow up in the next several years [5, 110, 111].

Using currently available LPE or rGO graphene is limited to the flake size of about 1 μm, with reasonable low fabrication cost. A real breakthrough in the fields of inks and composites will occur when these synthesis processes are improved and capable of producing flakes with lateral dimension grater than 10 μm. As an example, this increase in flake size would allow for multiple overlapping of one flake between several fibers in a carbon fiber composites, resulting with a ten times increase in breaking strength of the composite material (without any increase in mass) [30]. This breakthrough will bring many new composite materials with several times greater Young's modulus, thermal and electrical conductivity, than currently available ones.

1.3.4. Energy applications

Carbon-based materials have already been used in various energy applications, and it would be surprising if graphene had no part in this field. This subsection will discuss two major energy related applications for graphene, solar cells and energy storage in either lithium-ion or supercapacitor based batteries. There are many other potential energy related applications for graphene, as in fuel cells [140] where graphene serves as a supporting material for platinum catalysts, or in H_2 storage where potential use of graphene, graphene oxide and titanium-graphene oxide composites has been considered [141]. However, these wont be discussed in more details here.

One of the most interesting potential application of graphene is in the next generation of solar cells. There are two ways that graphene can be implemented into photovoltaic solar cells. First, graphene could be used as the active material. This is very similar application as in photodetectors (see Sec. 1.3.2). The main advantage here is a large spectral range where light absorption is possible [60, 65], however the main drawback is that the light absorption is rather small (2,3 % per layer). One straightforward solution would be to increase the number of layers, however after some 4-5 layers of graphene it becomes much harder to extract photo-generated carriers without an applied bias. The other approach that could be utilized is to stack multiple devices similar to the one shown in Fig. 1.12(a), only separated by a thin dielectric layer. Although this could result with very high light-to-current conversion ratio, these devices would be extremely expensive to fabricate, not only from the side of graphene fabrication and transfer technology, but also because rare metals have to be used as electrodes. The other way to increase light absorption in graphene would be through various plasmonic structures [130], but these would both limit the spectral range and significantly increase fabrication costs. For these reasons, graphene as an active material in solar cells most likely will not be used in the near future.

The other potential application for graphene in solar cells is as a transparent and/or distributed electrode in quantum dot or dye-sensitized solar cells [142]. Interestingly, graphene can be used both as electron [142] and hole [143] conducting electrode, since doping of graphene can be used to change majority carriers (see Sec. 1.1.5). Furthermore, ambipolarity gives the same (or at least very similar) carrier mobility of both electrons and holes. Proof-of-concept devices already exist [142]. Low cost fabrication methods [144] as LPE or rGO are suitable for these electrodes.

Regarding the distributed electrode in dye-sensitized solar cells, graphene could replace commonly used Pt (not a transparent electrode), due to its high conductivity, high specific surface area and good electro catalytic activity. Furthermore by doping (as with HNO_3 [122]) conductivity can be increased and electrode work-function can be fine tuned. All these properties are very important for photovoltaic solar cells. Flexible solar cells with graphene electrodes are expected to appear by the year 2025 [5, 110, 111, 118].

Very promising field of application for graphene is energy storage, more precisely as an electrode in lithium-ion batteries and supercapacitors. Li-ion batteries were introduced in the mid seventies [145], and have suffered from poor electrical conductivity of cathodes. A decade latter T. Nakajima and co-workers from Asahi Kasei corp. have introduced and patented [146] integration of carbon based materials into cathodes for Li-ion batteries. Due to Li-intercalation of carbon, increased conductivity and significantly increased electrode surface area, this relatively simple improvement have increased power density of Li-ion batteries by at least one order of magnitude. Currently amorphus carbon, graphite powders and carbon black are used in all Li-ion battery anodes. This had a tremendous impact on our everyday life, since these improved Li-ion batteries could store enough power and still be light weight enough to support widespread of mobile electronic devices, as laptops, mobile phones and many others.

Graphene is a logical next step for Li-ion batteries, since it is basically much higher quality type of carbon-based material to be integrated as an advanced conductive filler into cathodes. Furthermore, graphene opens possible new electrode structures as encapsulated nanoparticles and sandwich-type nanocomposites [147, 148]. Integration of these structures into Li-ion battery anodes could significantly increase their power density. This could result with a next big leap in the energy storage technology.

There is yet another, even more promising potential application for graphene in energy store. Graphene has proven as a good choice for electrodes in supercapacitors [149, 150]. These are an alternative versions of batteries, where electrical energy is stored electrostatically, rather than chemically. The energy is stored within an electrochemical double-layer capacitor [151], similarly as the electrolytic gating is introduced with ion-gels [43, 45, 71, 72] (see Sec. 1.2.3). The efficiency of these devices is determined by the surface area of the electrode and the charge separation at the electrode-electrolyte interface.

The advantages of using graphene as electrodes for supercapacitors, comes from its high electrical conductivity, controllable pore or defect structures (with rGO, chemical or plasma treatments), its resistance to oxidative processes, its stability at high temperatures and good heat conductivity. The first prototype of graphene-based supercapacitor was realized by M. D. Stoller and co-workers [149]. The first microscopic supercapacitor based on rGO was realized by M. F. El-Kady and R. B.Kaner [150]. They have demonstrated flexible and planar micro-supercapacitors that could be integrated on the chip. These devices show some of the highest power densities ever reported.

Major issues for integration of graphene into supercapacitors besides fabrication cost, are large irreversible capacitance, heating and relatively low life-time of these devices. Other carbon-based materials are also used for supercapacitor electrodes, as arrays of carbon nanotubes [151]. However low cost graphene [144] as rGO and LPE gives better price-to-value ratio than carbon nanotubes. Performance of these devices could be improved using higher quality graphene, or by having a better control over a number and type of defects, or using self-assembly nanostructures (as graphene flowers [152]) to maximize surface area or to use electrolytes better suited for these novel electrodes.

1.3.5. Statement of the thesis

As it was shown in previous sections of this chapter, there are many potential application for graphene. Most of these applications require some very special and strict sets of properties that graphene must have if it is to be implemented into these technologies. As an example, for OLED transparent electrodes (Sec. 1.3.1) graphene must have sheet resistance of less than $30\,\Omega/\square$ with transparency over 80%. In the same time its surface roughness must be low, its work function needs to be between 4.7 eV and 4.9 eV, and it must make low resistivity Ohmic contacts with external leads [110, 120]. It is clear that this and many other applications will require very good control over graphene properties, and this needs to be achieved in a mass-production of the material.

To have a good control over graphene's properties, one must first understand the mechanism behind them, and needs to have a reliable set of tools to measure them.

Furthermore, these tools need to be easily implemented in a mass-production process, as an assembly line or a growth chamber. One of the already proven techniques both in fundamental research and in various industrial applications is ellipsometry [153, 154, 155]. It is an optical technique used mainly for investigating the dielectric properties and thicknesses of thin films in many different fields, such as solid state physics, bio-physics, thin film technology and microelectronics, for both fundamental research and industrial applications. In the industry it can be used both as in-line and post-fabrication control tool. It takes the advantages of being very fast, non-destructive and contactless. Furthermore, ellipsometry measures complex dielectric constant and relies on measuring angles and frequencies rather than light intensity, thus having no requirements for a reference spectra. By using light interference it can be sensitive to the film thickness in the order of a fraction of an angstrom (i.e. it can unambiguously detect an incomplete mono-atomic layer).

As graphene technology develops, it is necessary to have adequate tools that are not only sensitive to the presence of a mono-layer graphene itself, but that can detect subtitle changes in the properties of this ultra thin film. Ellipsometry is proved to be one of the most useful techniques that will be employed as a quality control tool in the future mass production of graphene.

This dissertation and the publications directly related to it [82, 83, 91, 92, 156] address the issue of optical properties of graphene in the visible and UV ranges, and how changes in these properties could be related to various issues in fabrication, transfer and interaction with a substrate. These could be implemented as a quality control in various graphene fabrication processes. In the dissertation and in the related publications, optical properties of graphene are obtained using spectroscopic ellipsometry and null spectroscopic imaging ellipsometry techniques. The chosen spectral range is the most common probing range in an in-line environment. The data interpretation process is optimized for the case of an atomically thin layer on various substrates (thin SiO_2 films, transparent and metallic substrates), and an importance of using corroborated measurements for building up an appropriate optical models is shown. A model for graphene's complex refractive index is proposed. This model is based on a Fano resonant profile. Values of the model parameters can be easily related to the properties of the M-point exciton that causes the red shift of the logarithmic van Hove singularity of the absorption function in UV (see Sec. 1.2.4). The model for graphene's complex refractive index reported in [82, 83] was adopted by a manufacturer of spectroscopic imaging ellipsometers, Accurion GmbH

and is currently being distributed within the software of a Nanofilm_ep4 ellipsometers. Numerical codes used within the model are given in Appendix C4, and are explained in Chapter 4. Ellipsometric mapping was also employed to resolve spatial distribution of a water layer trapped between graphene and a substrate [83].

Furthermore, specific potential applications for using ellipsometry as a quality control tool in graphene technology are addressed within the dissertation. Namely, the influence of the transfer residue on the optical properties in the case when graphene is transferred over a transparent substrate is addressed [91]. This is very interesting both from the measurement, and from the transfer technology points of view. Measurements of mono-atomic layers, and thin (few nanometers) transparent residue layers on transparent substrates are rather difficult, since almost negligible phase shift occurs due to the lack of multiple reflections. From the side of the graphene transfer technology, this is the case of an interest for transparent conductive electrodes. As an example in the case of the flexible OLEDs [120], graphene needs to be transferred several times on a transparent substrate. For this technology it is necessary to have a reliable tool that can quickly check if no transfer residue is remaining after each graphene layer has been transferred. This is quite difficult since even few nanometers of the transparent residue layer (placed on a transparent substrate) can affect the electrical contacts between two graphene sheets and significantly increase sheet resistance. As it is shown within the dissertation (see Chapter 4 and Ref. [91]), ellipsometry can give fast and contactless way to probe this issue.

The influence of the metallic substrate interaction on the optical properties of graphene is also discussed within the dissertation and within Ref. [92]. This is interesting both from the fundamental aspect, and for the potential application of ellipsometry as a quality control tool in graphene technology. Through the change in the optical properties of graphene it is possible to examine many body interaction between the excitonic state and the states near the Fermi level, which is shifted by the interaction with the underlaying metallic substrate. It was found that in this case an electron-hole interaction of the M-point exciton is suppressed by several hundred meV-s. On the other hand charge transfer between graphene and the underlaying gold substrate was found to be about 50 meV [92]. From the quality control point of view, this is important since it demonstrates how a contactless technique can be used to confirm the contact quality between graphene and an external metallic electrode.

2. FABRICATION AND CHARACTERIZATION METHODS

2.1. Graphene fabrication methods

The market for graphene applications is driven by the development of the production processes. As it has been demonstrated [5, 110], graphene can be synthesized at cost-effective scale both by bottom-up (atom-by-atom growth) or top-down (exfoliation from bulk) approaches. This section will present various fabrication processes (Sec. 2.1.1), focusing on the two that have been used in the publications related to the dissertation: micromechanical exfoliation (Sec. 2.1.2 and App. B2) and chemical vapor deposition (CVD) (Sec. 2.1.3).

Fabrication is not the only process required for various applications of graphene, there are many other steps, some of which are similar to the processes standardized within the silicon based industry, while some are novel and maybe even more critical than the growth process itself. This section will focus on two processes that are most commonly used in graphene device fabrication. First, CVD graphene grown on a metal foil or thin metal films requires a transfer step usually to a dielectric substrate. This transfer process can significantly reduce the quality of the as-grown graphene if not done properly. Various transfer approaches are discussed within Sec. 2.1.4, with focus on those used within the publications related to the dissertation (see also App. B3). The second process that will be discussed is fabrication of metallic contacts on graphene, again with a focus on the specific case used within the dissertation; UV photolithography (Sec. 2.1.5 and App. B4).

2.1.1. Overview of various fabrication techniques

As it was mentioned in the previous chapter, graphene was first synthesized by a micromechanical fabrication technique [1]. Although this techniques gives the best sample quality thus fahr, it is very difficult to scale up the production of graphene via this route. Samples made by micromechanical exfoliation are mostly used in fundamental research or for proof-of-concept devices. Several years after the initial discovery, significant part of the research in the field was devoted to solving a problem of mass synthesis of graphene, and hundreds of mass production approaches were proposed. Interestingly many different approaches gave significantly different material properties. These differences usually come from variations in grain or crystallite size and the way they overlap or interconnect to form large continuous films. Number of layers and control over the number of layers also varies for different production approaches. The final product is called "graphene" although it might not preserve most of the properties that pristine graphene has. Some fabrication methods can parry exfoliated graphene (as CVD), while others preserve only few properties that are of an interest for specific applications (as rGO and LPE). From the variety of the proposed routes for mass production of graphene only several were widely accepted. These are shown in Fig. 2.1, where sample quality as a function of a mass-production cost is presented. Micromechanical exfoliation and chemical vapor deposition techniques will be explained in more detail later in the text (Sec. 2.1.2, 2.1.3 and App. B2). Let us now focus on several other synthesis approaches, and review their advantages and drawbacks.

One of the commonly used synthesis routs of graphene is growth from silicon-carbide (SiC). Single crystal SiC has crystal planes that end either with carbon or silicon atoms, and are referred to as a carbon- or silicon-sides (faces). Graphitic layers can be obtained on the surface of SiC by sublimation of silicon atoms [157]. Growth of graphene and multi-layer graphene has been demonstrated on both Si-side [117] and C-side [158, 159] of a SiC wafer. 6H-SiC (0001) surface is the most commonly used C-side, and it was the one on which the first turbostratic growth of few-layer graphene (about three-layers) has been demonstrated [158]. However, this approach initially suffered from very small (less than one hundred nanometers) and randomly oriented crystalline domains, and very low control over the number of

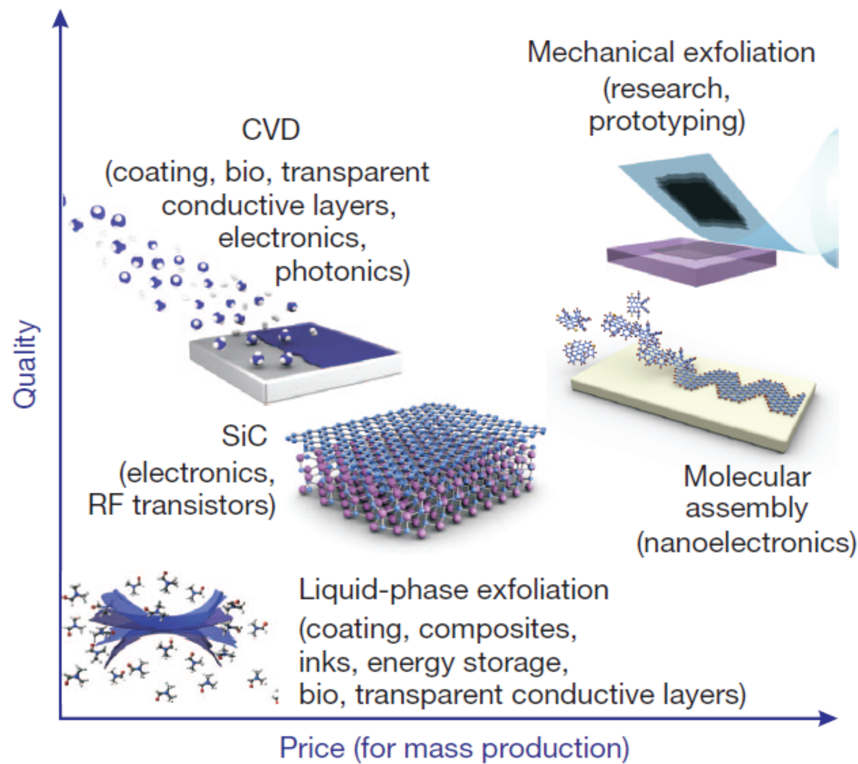

Figure 2.1.: Several most commonly used fabrication methods of graphene (Reprinted from [110]). Methods position in the chart illustrates the sample quality versus mass-production costs; potential applications are also noted for each method.

layers. Still these films were only one nanometer thin in average, and have preserved many properties of pristine graphene. By optimization of the growth conditions and surface preparation, controllable growth of predominantly bi-layer graphene was demonstrated on a C-face of a SiC by T. Ohta and coworkers [160]. However crystalline size remained an issue. There is a possible trade-off between number of layers and crystalline size. Namely, if graphene is grown on a Si-face, much larger crystalline domains can be obtained, reaching a fraction of a millimeter [117]. This is more than enough surface area for most integrated electronics. However number of layers is much harder to control in this case and predominantly multi-layer graphene is obtained.

There are two major drawbacks for SiC synthesis route. First is high cost of SiC wafers, and the fact that these are very difficult to fabricate with a diameter that would be suitable for integration with Si-based electronics (30 inches). Second, Si

sublimation requires high temperatures, usually over 1000°C, and high vacuum environment. These temperatures are not compatible with Si-based technology and graphene synthesized in this manner would have to be transferred onto a desired substrate. All these significantly increase the fabrication cost. Growth of graphene on SiC was demonstrated at atmospheric pressure (in argon atmosphere) [161], interestingly giving larger crystalline domains. Furthermore, terraces on the C-face of a SiC wafer are inevitable. These terraces cause growth of additional layers in their vicinity, thus significantly contributing to carrier scattering. A major breakthrough in SiC based growth of graphene will occur when a successful growth from SiC thin films (less than 20 nm) is achieved either on Si or SiO_2/Si wafers. Until then SiC based graphene will remain limited to very specific applications [5, 110], as in high-frequency analogue electronics [117].

Several low-quality and low-cost fabrication methods as liquid phase exfoliation (LPE) and reduction from graphene oxide (rGO) take a significant share in the field of graphene synthesis [144]. Liquid phase exfoliation of graphite [162, 163] and other Van der Waals' materials [164] is based on exposing the material (usually a powder consisting of small crystal grains) to the solvent with surface tension chosen to match the energy of Van der Waals' forces holding layers together. As a result flakes in these solvents tend to "split" or exfoliate, thus increasing total surface area of the material by several orders of magnitude, without any change in the total mass. For exfoliation of graphene a non-aqueous, high boiling point solvents as N-methyl-2-pyrrolidone (NMP) is used [163]. The process can be significantly speeded up by sonication, shearing and filtration. Resulting suspensions could be consisted of almost exclusively single-, bi- and tri-layer graphene.

There are many different methods to deposit graphene from the suspension within the solvent, as simple drop-cast, screen printing [165], ink-jet printing [136], or Langmuir-Blodgett based self assembly [166]. Advantages of LPE based graphene are low-cost of mass-production [144], non-chemically modified starting material (graphite powder) and ease of functionalization and intercalation (simply by addition into the suspension). However there are several drawbacks that limit wider application of these materials. Crystalline (or flake) lateral size is relatively small, usually less than one micrometer in diameter for flakes that have less than five-layers. This results with large film resistivity, mainly due to high resistivity of the overlapping points between individual flakes. Furthermore, solvents as NMP remain trapped in the structure during the deposition, even further increasing both sheet

resistivity and surface roughness. A breakthrough in this synthesis technique is expected with optimization to increase lateral flake size to over 10 μm, in addition with further development of functionalization, and in finding a suitable way to chemically bond and interconnect flakes creating a continuous films [5].

Process of graphene synthesis by reduction from graphene oxide (GO) is very similar to the LPE process [164, 167, 168]. The major difference between these two processes is the fact that prior to sonication graphite is oxidized. This increase interlayer separation, and makes exfoliation much more efficient (even in water). The resulting suspension consists of almost only single-layer flakes of GO. However an additional step is required to reduce graphene oxide into graphene. This step can be preformed either in solution, or after the film deposition. GO can be reduced either by annealing, or exposure to UV light or through chemical reduction. However, the remaining material is never fully reduced, and has a significant amount of defects. For this reason it is called reduced graphene oxide (rGO) and not graphene.

Besides here mentioned, there are other very interesting fabrication methods, as bottom-up molecular assembly of graphene nano-ribbons [169]. Using this method it is possible to fabricate nano-ribbons with well defined edges and geometries, and even to make much more elaborate interconnections as "T" and "Y" joints. However, bottom-up molecular assembly is limited to metallic substrates and fabrication cost are currently too high for applications in electronics. There are also ways to grow graphene on dielectric substrates, as demonstrated by molecular beam epitaxy [170]. However, quality of these films is still not comparable with CVD graphene transferred onto a dielectric substrate, and fabrication costs are several times greater. One more interesting fabrication approach is laser ablation of graphite [171]. However this fabrication process produces structures similar to spray-coating of chemically exfoliated graphene (LPE or rGO), but at much higher cost.

The following subsections will focus on two most commonly used techniques for graphene fabrication: micromechanical exfoliation (Sec. 2.1.2) and CVD growth (Sec. 2.1.3). These two methods were also used within the publications that are related to the dissertation [82, 83, 91, 92].

2.1.2. Micromechanical exfoliation

Micromechanical exfoliation technique is based on a well known method in mineralogy called cleavage. It exploits the tendency of crystalline materials to split along definite crystallographic structural planes [172]. These planes of relative weakness are a result of the regular locations of atoms and ions in the crystal. It is not required that material has Van der Waals' forces in the direction perpendicular to the cleavage plane, since cleavage techniques include exfoliation (pealing), cutting and controlled breaking (as with Si wafers). Based on the direction (i.e. parallel to a crystallographic plane) in which cleavage occurs it can be split into basal, cubic, octahedral, dodecahedral, rhombohedral and prismatic. It is also possible to cut crystals along more elaborate planes, this can be used to create well defined terraces on the atomic level. However, this is not usually referred to as cleavage.

Basal cleavage, or cleavage parallel to the crystallographic {001} plane is the most common one. All of the two-dimensional Van der Waals' materials have their unit cells connected by Van der Waals' forces in a direction perpendicular to the basal {001} plane. In material science, basal cleavage is used to obtain near perfectly flat surfaces of highly oriented pyrolytic graphite (HOPG), or mica group materials and others. In the scanning tunneling and the scanning electron microscopy, and in the atomic force microscopy these materials have been used as substrates, since after cleavage they gave almost perfectly flat surfaces ranging from tens to thousands of micrometers. These surfaces are excellent for imaging nanostructures that are deposited on them, as nano-powders, self-assembly nanostructures, quantum dots, or whenever a substrate imperfections would affect measurements of nanoscopic structures.

As said, the result of cleavage is near perfect surface of the material along well defined crystallographic plane, and it does not matter how many layers of the material are remaining below the exposed surface. Micromechanical exfoliation is based on cleavage but has one additional requirement, there should be no material left under the surface produced by cleavage, i.e. cleavage should give only one atomic layer of the material. Although it might sound impossible, micromechanical exfoliation is actually favorable process, and if done properly it should produce surfaces of only one atomic layer with relatively high yield. Micromechanical exfoliation exploits weak Van der Waals' forces existing in crystal graphite. In all the cases exfoliated graphene needs to be supported (or at least partly supported) by a substrate. If

the substrate is properly chosen and prepared, flake of a crystal graphite with a cleaved surface will "hold" to the surface of the substrate also by Van der Waals' forces. The trick in micromechanical exfoliation lies in the fact that Van der Waals' forces between the cleaved surface of graphite (i.e. the surface layer) and the substrate are stronger than the forces between each graphene layer in graphite. So if we would have a flat substrate surface with a graphite flake firmly attached to it by Van der Waals' forces, an additional cleavage of that surface would remove all the graphite but that last layer which remains on the substrate. As a result a single layer graphene is obtained. Detailed exfoliation and substrate preparation procedures are given in appendices B1 and B2. Micromechanical exfoliation can be used to prepare mono-atomic layers of not only graphite by of many other Van der Waals' materials as MoS_2, WS_2, WSe_2 [3, 4].

Properties of the exfoliated graphene are unparalleled. The exfoliation process is conceived in a way that the resulting graphene layer is not exposed to anything but other graphite layers, substrate and the ambient. Exfoliated samples are always single crystals, usually with well defined crystal edges. Number of layers is always constant. Any number of layers could be produced by this method, although thinner structures (less than ten layers) are more favorable. Since starting material (crystal graphite) has very low amount of defects, obtained graphene samples have lowest amount of defects in their crystal structure compared to any other synthesis methods. Most of the unexampled properties of graphene (see Sec. 1.3) have been demonstrated on the exfoliated samples.

However there are many drawbacks of this method. The biggest one is that it would be almost impossible and certainly never cost-effective to scale up the production of exfoliated graphene to an industrial level. For this reason exfoliated graphene is used in fundamental research, proof-of-concept (or prototype) devices, and could be extended to very small series of highly sophisticated devices. There are also technical issues as, no direct control over the number of layers, flakes size, shape and position on the substrate. All these technical issues can be overcome by statistics, i.e. making large number of samples and using those that were best suited for the planned experiment. Depending on the requirements, the yield is usually one-tenth or even one-hundredth of the prepared samples.

2.1.3. Chemical vapor deposition (CVD)

Chemical vapor deposition (CVD) has been used for thin layer deposition in semiconductor industry for decades [173]. The process always consist of a precursor material that is introduced in a growth (deposition) chamber as a vapor. Precursor deposits on a substrate, where a chemical reaction occurs, either within the precursor, or precursor and carrier gas, or precursor and a substrate. As a result the desired material is deposited on a substrate. There are many different types of CVD processes as thermal, plasma enhanced, cold wall, hot wall, reactive CVD and others. Also many different precursors can be used. Precursors can either be solid, liquid or gas. However, the precursor is always introduced into a growth chamber as a vapor [174]. Solid precursors are either vaporized, or dissolved using a proper solvent, and then vaporized and introduced to the growth chamber. The transport of a precursor is usually aided by a carrier gas (or gas mixtures). The process and precursor type is usually dictated by the desired material quality, thickness, structure and cost.

Graphene can be grown by CVD on various metallic surfaces using many different processes and precursors, even growth with chocolate as a precursor has been demonstrated [175]. However, predominant method is thermal low pressure CVD (LP CVD) with hydrocarbon gasses as precursors and various metals as substrates.

Initially graphite layers were grown on nickel by exposure of heated (900°C) Ni surface to methane by A. E. Karu and M. Beer [176]. These thin graphite layers were used as a sample support for electron microscopy. The first results of growing graphene by a CVD process were carried out by LP CVD on single crystal iridium [177]. Since Ir is expensive, the process was translated to other metallic substrates, ideally metallic foils and thin films that are compatible with the existing silicon industry. Graphene growth on nickel [178] and cobalt [179, 180] results with multilayer structures. The reason is high solubility of carbon in these metals [178, 179, 181, 182, 183]. A simple approach to reduce the number of layers would be to use metal that has very low solubility of carbon. As it turns out the metal of choice is copper. The first results of a single-layer CVD graphene greater than several square centimeters, were reported by X. Li and coworkers [184] There, a polycrystalline Cu foils were used as a substrate. Interestingly, due to a low solubility of carbon in copper, the CVD process is self-limiting, resulting with over 95 % coverage of the single-layer graphene. Remaining less than 5 % consists of bi- and tri-layer graphene [184, 185]. The fact that graphene grown on copper is self-limiting to a single atomic

layer is a great advantage for copper as a material of choice for CVD growth. LP CVD growth of graphene on copper was scaled up to the industrial level by S. Bae and coworkers [121], resulting with thirty inch diameter continuous films.

The process of LP CVD growth of graphene on copper goes as followed: Carbon atoms are introduced to a growth chamber as hydrocarbons. As they come to the contact with a Cu substrate that is held at over 1000°C hydrocarbons decompose and graphene starts to nucleate on the surface of Cu. Nucleation grains are single crystal, but as each grain grows they start to collide and to form grain boundaries. These boundaries are considered as defects, since they do not have the regular hexagonal crystal structure. Resulting film is continuous and can be considered as polycrystalline graphene. Besides grain boundaries, CVD grown graphene films also have wrinkles, these are the consequence of the step-edges (grain boundaries) in copper substrate, as well as the difference between the thermal expansion coefficients of copper and graphene [186]. These wrinkles do not have to follow grain boundaries of graphene. All of these are a problem for using CVD graphene in electronics, since properties of a device would depend on the number of grain boundaries and wrinkles that happen to be in the channel.

There are ways to optimize growth of graphene on copper, by better preparation of the copper surface, single crystal domains over 4.5 mm^2 were demonstrated [187]. Furthermore, controlling copper surface oxidation can result with even a centimeter scale single crystal domains [188].

For some applications it would be desirable to grow only bi-layer or only tri-layer graphene. An interesting way to achieve this was introduced by mixing copper and nickel in a certain percent, thus making the growth process self limiting to very specific number of graphene layers [189].

2.1.4. Graphene transfer techniques

Graphene grown by CVD is always supported by a metallic substrate, either as a foil, thin film or single crystal. To exploit most of graphene's properties it is necessary to have graphene supported an insulating substrate. For this reason graphene transferring process has been developed. Besides freeing CVD grown graphene from

its metallic substrate, this technique is also applied for detaching graphene grown on a SiC, and for transfer of exfoliated flakes, of both graphene and other 2D materials, and even for creating Van der Waals' heterointerfaces. The later refers to a transfer of one VdW material over the other and so on, creating a stack or a "sandwich" of 2D crystals [190, 191].

The transfer process, in its simplest form, goes as followed: First a sacrificial layer is deposited over graphene, this layer supports graphene during the transfer procedure. Then graphene is detached for its original substrate, and transferred onto a desired substrate. After placement the supporting (sacrificial) layer is removed, leaving graphene on the desired substrate. Although the process is essentially very simple, graphene is still a single atomic layer, and this process can introduce large amount of unintentional doping, cracks, wrinkles and defects, all of which can render transferred graphene layer useless. There are many steps that can be done to minimize damaging graphene during this process. Based on the way that graphene is detached from its original substrate, transfer process can be classified as "wet" of "dry". In a case of a wet transfer both faces of graphene come to a contact with a liquid at some point during the transfer process, while with the dry transfer liquid comes in contact only with one side, thus leaving the other side uncontaminated. Dry transfer is most commonly used for exfoliated samples of various VdW materials [191]. For this purpose samples are exfoliated on a specially prepared substrates, usually on a poly(dimethysiloxane) (PDMS) film supported by a silicon wafer. After exfoliation graphene/PDMS stack is detached from the silicon, turned "up side down" and placed on the targeted substrate. Finally PDMS is removed, exposing what is then a top surface to the solvent liquid. However this method is not possible for CVD grown graphene. In the case when a supporting substrate is not easily removed in a solvent, a wet transfer procedure is used, and it will be the focus of the remaining text in this subsection.

Graphene wet transfer technique was adopted from the carbon nanotubes, where as a supporting layer either PDMS [192] or poly(methyl methacrylate) (PMMA) [193] were used. The first demonstration of a wet transfer of exfoliated graphene was reported by A. Reina and coworkers [194]. There a graphene flakes exfoliated on a SiO_2/Si substrates were supported by a PMMA layer, and SiO_2 layer was etched using hydrofluoric acid. After placement of a graphene/PMMA stack on a targeted substrate, supporting PMMA layer was rinsed away with acetone. Transfer of CVD graphene from Ni or Cu foils and thin films is carried out in a similar manner as

for exfoliated graphene, with a difference that etching of a metal layer is done with aqueous solution of $FeCl_3$ or HCl [178, 195]. As a supporting layer PMMA is most commonly used. A simpler way to support graphene would be to use thermal release tapes [121]. These tapes are designed in a manner that after heating up to a certain temperature (usually above 90°C) the glue film degrades and the material held by the tape is released. Big advantages of using these tapes as a support for graphene transfer are low-cost, simplification of the fabrication steps and most importantly these are compatible for integration in a roll-to-roll mass-production [121]. However, the major disadvantage is the fact that after the material is released, a lot of tape residue remains on the top surface. This residue prohibits fabrication of external contacts, and limits the use of this technique to the case when the top side of the graphene film is not used after the transfer process.

A transfer process used within the dissertation is adopted from [195, 196, 197], and details are presented in App. B3. In order to minimize the introduction of cracks and folds during rinsing of the sacrificial PMMA layer, it is important to allow the stacked structure to relax on the targeted substrate. This is carried out by heating the targeted substrate with grphene/PMMA stack on top of it, and by drop-casting additional PMMA to dissolve the existing film and allow for graphene to relax and follow morphology of the targeted substrate [195]. This way number of cracks in graphene film is significantly reduced, and folds created by thermal mismatch of graphene and copper, as well as folds originating from copper terraces. The average distance between two folded structures is increased from about 2 μm to over 10 μm.

After the graphene layer is firmly attached to the desired substrate, PMMA layer needs to be rinsed. This is done most commonly in acetone and deionized water. However, a thin layer of undissolved PMMA always remains on the surface of the sample. This layer can be between one and ten nanometers thick, and tends to form even larger structures near any folds or defects in graphene film [196]. Most common way of cleaning graphene from the transfer residue is thermal annealing at temperatures ranging from 250°C to 500°C, in formic gas mixture (H_2:Ar). However, this process can introduce a large amount of cracks as well as structural defects [198]. The other, very promising approach is to let the remaining PMMA residue dissolve in an acetic acid for an extended period of time. As it was demonstrated by M. Her and coworkers [197], this method can produce very clean graphene surfaces with very low amounts of cracks, folds and transfer residue. There are many other methods

to aid graphene transfer, and to minimize the waste of metallic foils, as H_2 bubble assisted etching of the metallic foil [199, 200] and using plastic frames to support graphene/PMMA structure and avoid deposition of thick PMMA layer [200].

2.1.5. UV photolithography and device fabrication

As it was discussed in Sec. 1.1.5, by having an electrical contact on graphene, and a parallel electrode separated by an insulating layer, as in a case of a simple parallel plate capacitor, one can change the position of the Fermi level in graphene with the respect to the Dirac point. As a parallel plate electrode, simplest would be to use the silicon substrate (usually highly doped), this is referred to as a "back-gate" electrode. By applying a voltage between graphene and a back-gate, carrier concentration and a type of the majority carriers in graphene can be changed from its equilibrium value. The energy used to do this is supplied by the voltage generator, and as soon as the generator is switched off the amount of carriers in graphene will return to the value dictated by the unintentional doping (i.e. substrate and ambient interaction).

To be able to exploit an electric field effect in graphene, only one electrical (metallic) contact is required. In some cases (large LPE, rGO or CVD films) it is as simple as attaching (bonding/soldering) a wire to the graphene electrode, however if the sample is only few micrometers large, or the separation between two electrodes needs to be small (from few nanometers to few micrometers) the process of making an electrical contact to graphene sheet becomes much more elaborate. To be able to track the change of the Fermi level position in graphene, the easiest would be to have at least two electrical contacts, and to monitor the change of the resistivity (as shown in Fig. 1.7). This subsection will present various methods of making microscopic electrical contacts to graphene sheet, and will focus in greater detail on the fabrication methods used within the dissertation: positive mask UV photolithography and shadow mask deposition of gold electrodes. The technical details regarding the fabrication steps are given in App. B4.

Lithography processes were developed as an essential toolbox for miniaturization of integrated electronics. Various lithography processes that can fabricate structures on a nanometer scale are the core of a modern microelectronics and present some

of the finest and most advanced fabrication processes achieved by the mankind. Current state-of-the-art processes can mass-produce electrodes that are less than 20 nm apart from each other. Most of the lithography processes are developed for the silicon-based industry, and luckily graphene is compatible with many of these techniques. Various lithography processes can be used in graphene-based devices to fabricate top-gate, side-gate or buried-gate electrodes, or to pattern graphene to form various geometries as Hall-bars, or to encapsulate graphene in various dielectric films (as Al_2O_3, or HfO_2). The focus here will be on the simplest of all processes, defining a set of microscopic metallic contacts.

There are two different approaches to fabricate metallic contacts: one is to evaporate metal through a predefined pattern (shadow mask or "lift-off"), the other is to cover the entire surface of the sample by a metallic layer, and then to selectively etch the metallic film to create a desired pattern. The later has many advantages, regarding resolution, metallic film adhesion, and metallic film thickness limitations. This process is commonly employed to make contacts with Si-integrated elements (as MOSFET-s). However, etching of metallic films is not possible for the case of graphene-integrated devices. This is simply because etchants used to selectively remove gold films will also remove graphene layer. For this reason, shadow-mask and lift-off techniques are predominantly used for graphene-based microscopic device fabrication, and the focus of this subsection will be on various processes included into these two techniques.

Simpler of the two would be a shadow-mask technique. There, a metallic mask is places over the sample surface and using micrometer screws or piezo-manipulators the mask is positioned as desired over the sample. The mask is usually made out of steel or nickel foils with less than 100 micrometers thickness (these foils are very rigid) and have openings with the desired contact geometry. These openings are usually defined by laser ablation and are limited to about 10 micrometers in resolution. Afterwards, a metallic film is deposited over the mask/sample stack. Metallic film deposition is usually done by either physical vapor deposition (PVD) or sputtering. In this case PVD would be the deposition method of choice, since the material is deposited with a top-down direction, while in the case of sputtering metallic film can cover side walls as well (For more details regarding PVD process, see App. B4). After the deposition, shadow-mask is simply removed leaving the desired structure on the surface of the sample. The main advantage is that no photoresist was used, meaning that no chemicals have come in the contact with

the sample. Also, adhesion of the metallic film on the surface is not an issue since it is not exposed to any stress, unlike in the case of a lift-off. This is important since no adhesion metallic layers need to be deposited prior to the main metallic film. These adhesion layers (usually Ti, Pd or Pt) can create strong Schottky barriers between metallic film and graphene channel. The main drawback of this technique is low spatial resolution, and poorly defined contact edges (usually several micrometer gradients). This technique is limited to about 50 micrometers resolution. Resolution depends mainly on the complexity of the device geometry, and in some very special cases shadow mask technique can make structures with spatial resolution of less than one micrometer.

In most cases fabrication of metallic contacts on graphene uses a lithography based process with a photoresist patterning, metallic film deposition and finally lift-off (or stripping). Based on the manner that a photoresist is patterned, this can be split into electron-beam lithography (EBL), direct laser writing (DLW) and UV photolithography. Each has its own advantages and disadvantages. DLW is best suited for fast device prototyping, however its resolution is limited to about 1 μm. EBL has a superior resolution, capable of producing patterns with about 10 nm line width. However, EBL is most complicated technique, and has issues with aligning the patterned structure with a randomly oriented graphene samples. UV photolithography is fastest of the three, however sample geometries are limited to those predefined on the mask, and its resolution is comparable with DLW technique.

Regardless of the photoresist patterning process all the other processes are the same. These are schematically presented in Fig. 2.2. The process goes as as followed: First a photoresist is spin-coated over the entire substrate (Fig. 2.2(b)). The photoresist is made out of long polymer chains, chosen in such a way that after exposure to UV light or electron beam irradiation these chains are broken and the polymer can be selectively monomerized. This process of selective monomerization is shown in Fig. 2.2(c), for the case of UV photolithography. There, a lithography mask is placed over the photoresist and the entire structure is exposed to a parallel beam of UV light. Light passes only through the well defined pattern in the mask (made by another EBL or DLW process), thus selectively exposing the resist. Afterwards exposed parts of the resist are washed away, this is possible since monomerized parts dissolve about hundred times faster than the parts where long polymer chains have not been broken. This step is called development, and as a result gives a patterned photoresist layer (Fig. 2.2(d)). Next, a metallic film (usually gold) is deposited over

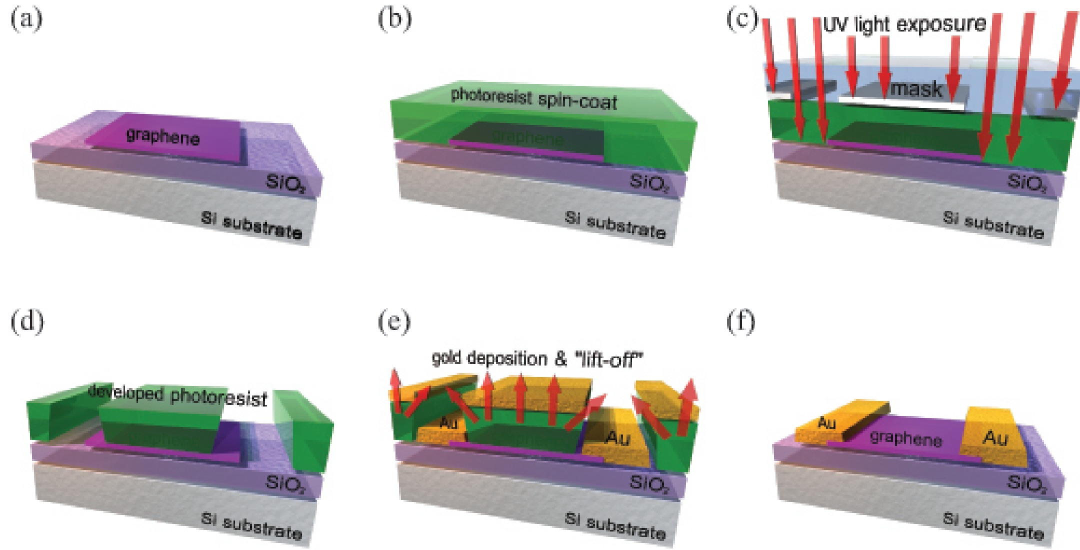

Figure 2.2.: (a) to (f) schematic representation of the positive mask UV photolithography process for deposition of microscopic gold electrodes over graphene.

the entire structure. Next, the most crucial step, called lift-off, removes unwanted resist layers along with the metallic film deposited over them. This is possible since the photoresists made for lift-off expand in certain chemicals (usually acetone). By doing this the remaining resist pushes away metallic film that is deposited over it (Fig. 2.2(e)), and only the desired metallic structure that holds to the sample surface remains (Fig. 2.2(f)). There are many parameters of the process, as contact geometries, photoresist thickness, exposure and development time, metallic film thickness, use of adhesion layers, and many other. All of these need to be fine tuned to obtain desired structures on the sample surface. The details regarding a specific set of parameter for UV photolithography used within the dissertation is given in App. B4.

The main advantage of this procedure is high spatial resolution of the metallic contacts. In case of UV photolithography and DLW, two metallic pads on graphene sample can be separated by about one micrometer of the device channel. EBL can create much shorter channels, reaching almost 10 nm of channel length. However, the major drawback is the fact that graphene surface is exposed to photoresist and solvents used for the lift-off. All of these tend to contaminate graphene devices and affect their properties. Processes to remove the photoresist residue are very similar

to those used for the removal of transfer residue (see. Sec. 2.1.4).

Once the contacts are fabricated, they can be used to electrically probe graphene and to obtain information on many of its properties. This will be the topic of the next section.

2.2. Graphene characterization

As it was shown in the previous section, there are many ways to fabricate graphene and graphene-based materials. Different synthesis techniques will give materials with different properties, so it is important to have a "tool-box" that can reliably characterize various types of graphene.

This section will focus on some of the most common methods used for graphene characterization, as optical microscopy, Raman and infrared spectroscopies, scanning probe microscopy, and measurements of direct current electrical characteristics of graphene. All of these methods are not only used to locate the samples and determine their properties, but are also used to corroborate ellipsometric measurement by defining values for parameters within optical models, which is a topic of the next chapter.

2.2.1. Optical microscopy

In almost all cases graphene samples are not spatially uniform over the entire substrate. This is quite obvious in the case of exfoliated graphene where micrometer sized flakes are randomly positioned on the centimeter sized substrate (for more details see Sec. 2.1.2 and App. B2). Also, transferred CVD graphene or deposited LPE graphene films might not be uniform, having multi-layer regions, overlapped regions, or regions with large amounts of residue. For all these reasons simple optical microscopy is a very powerful tool to quickly select regions of interest on the substrate, even by naked eye. Besides locating the samples, or regions of interest, optical microscopy can be used to quickly estimate number of layers, and to calculate surface area of the sample. This subsection will focus on exfoliated graphene on a SiO_2/Si substrates. However, the discussion is quite general and can be applied to graphene synthesized by other routes, or to other Van der Waals' materials, if their complex refractive indices are taken into account.

Graphene was first visualized by an optical microscope on a SiO_2/Si substrate with about 300 nm thick oxide layer [1]. Since graphene absorbs about 2.3 % of the incident light, it should be visible on any bulk substrate, but as a dim shadow.

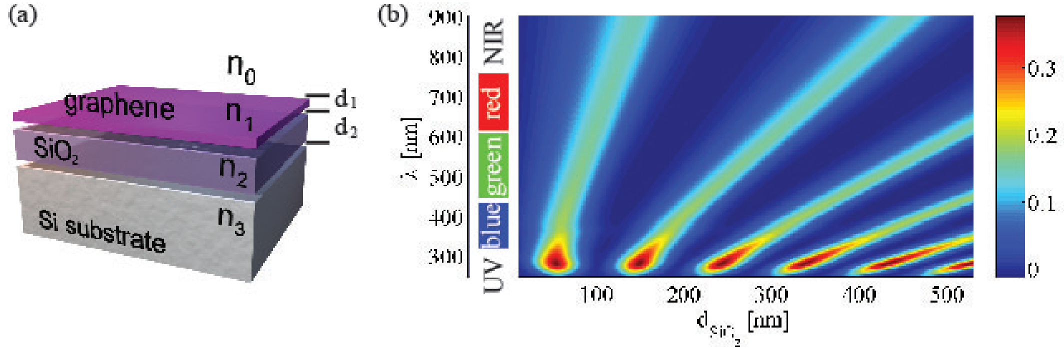

Figure 2.3.: (a) Schematic representation of the optical model used to calculate contrast between graphene and its substrate. (b) Contrast map $C(d_2, \lambda)$ as a function of SiO_2 thickness d_2 and incident light wavelength λ. Numerical aperture has not been accounted for. The contrast map has been obtained by plotting Eq. 2.7 in MATLAB, as a function of both thickness of the SiO_2 layer and incident light wavelength.

Taking into account any existing structure on the surface of the substrate and minor imperfections of the optical microscope, it becomes almost impossible to spot graphene on bulk materials. There is a reason why graphene is easy to find of a 300 nm SiO_2/Si, and it is the interference of the visible light within the SiO_2 layer. If the thickness of the oxide layer is increased by only 5 % (315 nm), the contrast is significantly reduced [61, 201]. Also, optical contrast viewed by a naked eye or color cameras is a very subjective quantity, and various groups have reported the different contrast of graphene viewed by an optical microscope [201].

It is relatively simple task to optimize contrast of graphene on a SiO_2/Si substrates, and it was first reported by P. Blake and coworkers [61]. This can be done within a simple model using only Fresnel equations [153]. These are based on a set of Maxwell equations for electromagnetic field, written on a boundary conditions between two materials. In the case of graphene over SiO_2/Si we have a four phase system with three boundary conditions, as shown in Fig. 2.3(a). Considering normal incidence of light, reflected light intensity can be easily obtained as:

$$I = \Bigg| \left(r_1 e^{i\left(\phi_1+\phi_2\right)} + r_2 e^{-i\left(\phi_1-\phi_2\right)} + r_3 e^{-i\left(\phi_1+\phi_2\right)} + \right.$$
$$\left. + r_1 r_2 r_3 e^{i\left(\phi_1-\phi_2\right)} \right) \times \left(e^{i\left(\phi_1+\phi_2\right)} + r_1 r_2 e^{-i\left(\phi_1-\phi_2\right)} + \right.$$

$$+r_1 r_3 e^{-i\left(\phi_1+\phi_2\right)} + r_2 r_3 e^{i\left(\phi_1-\phi_2\right)}\Big)^{-1}\Big|^2 . \qquad (2.1)$$

Here, r_1, r_2, r_3, ϕ_1 and ϕ_2 stand for:

$$r_1 = \frac{n_0(\lambda) - n_1(\lambda)}{n_0(\lambda) + n_1(\lambda)} , \qquad (2.2)$$

$$r_2 = \frac{n_1(\lambda) - n_2(\lambda)}{n_1(\lambda) + n_2(\lambda)} , \qquad (2.3)$$

$$r_3 = \frac{n_2(\lambda) - n_3(\lambda)}{n_2(\lambda) + n_3(\lambda)} , \qquad (2.4)$$

$$\phi_1 = \frac{2\pi n_1(\lambda) d_1}{\lambda} , \qquad (2.5)$$

$$\phi_2 = \frac{2\pi n_2(\lambda) d_2}{\lambda} . \qquad (2.6)$$

n_0 to n_3 stand for complex refractive indices written as $Re\{\mathrm{n}\}$-$iIm\{\mathrm{n}\}$, and denote air, graphene, SiO_2 and Si, respectively. Complex refractive index of graphene was obtained using a Fano resonant model, with parameters taken from [83]. Thickness of graphene was kept fixed at $d_1 = 0.335\,nm$, which is equal to the extension of the π orbitals out of the graphene plane [202]. In order to optimize the contrast equation 2.1 can be considered as a function of both wavelength of the incident light λ and thickness of the SiO_2 layer d_2, i.e. $I = I(d_2, \lambda)$. Contrast can be evaluated as the difference of the reflected light intensity from the substrate covered with graphene and the bare substrate. This can be written as:

$$C(d_2, \lambda) = \frac{I(n_1 = n_0) - I(n_1)}{I(n_1 = n_0)} . \qquad (2.7)$$

Now, by varying d_2 and λ a contrast map can be obtained, as shown in Fig. 2.3(b). As it can be seen, maximal contrast appears in the UV region, near the exciton-shifted van Hove peak in absorption (see Sec. 1.2.4). For UV light it is possible to have contrast over 30 %, if the substrate has about 65 nm thick SiO_2 layer. However, if we consider looking for graphene by the naked eye, we need to account for the fact that our eyes are most sensitive to the shades of green (between 500 nm and 600 nm). The SiO_2 thicknesses of choice would than be about 90 nm and about 290 nm, with ± 10 nm of tolerance. The expected contrast would then be about 10 % when white light is used. Fifgure 2.4 shows the difference between graphene and a SiO_2/Si substrate for two different SiO_2 thicknesses of 85 nm (Fig. 2.4(b)) and 295 nm (Fig. 2.4(c)).

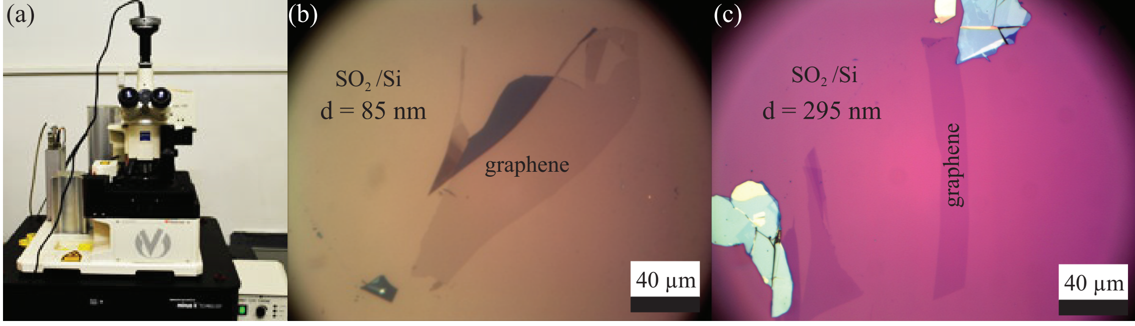

Figure 2.4.: (a) Zeiss reflection microscope, used for sample detection. (b) and (c) single-layer graphene samples on a SiO_2/Si substrate with SiO_2 thicknesses of 85 nm and 295 nm, respectively. Different color of the substrate comes from the different SiO_2 thickness, i.e. the different condition for the destructive interference of light due to the change in the optical path within SiO_2.

There is yet another way to even further increase the contrast. The microscope setup does not have to be top-down, but light source and focusing optics can be tilted from the axis that is perpendicular to the sample plane by an arbitrary angle θ. This setup is called Brewster angle microscopy (BEM), since the best contrast can be obtained when the microscope tilting angle is set to be near the Brewster angle of the sample. In that case, either for the sample or for the bare substrate the condition for the destructive interference of the *s*-component of the electromagnetic field (component perpendicular to the plane of incidence) can be satisfied, while for the other it is not. This could give 100% contrast if monochromatic polarized light is used. In Sec. 4.1.1 Fig. 4.1(a) and (b) shows a comparison between convectional reflection microscope images and BEM images of the same samples. BEM images were taken with monochromatic polarized light $\lambda = 430\,nm$ with a full width at half maximum of 10 nm. Incident angle was $\theta = 60°$ for both samples, which is near the Brewster angle of both structures. Even with these parameters that are not optimized for the maximum contrast, the difference in contrast between top-down microscopy and BEM is quite obvious.

The light interference within SiO_2 layer used for achieving better contrast and easier detection of graphene has been also used to increase sensitivity of ellipsometric measurements. This is discussed within Sec. 3.4.3 and within references [83, 92].

2.2.2. Raman spectroscopy

Raman spectroscopy is used to observe vibrational, rotational, and other low-frequency modes of a material. It is based on inelastic scattering of monochromatic light, usually from a laser in the visible range. The laser light interacts with molecular vibrations, phonons or other excitations in the system, resulting in the energy of the reflected (or transmitted) photons being shifted up or down. The shift gives information about the energy of the vibrational modes in the system [46].

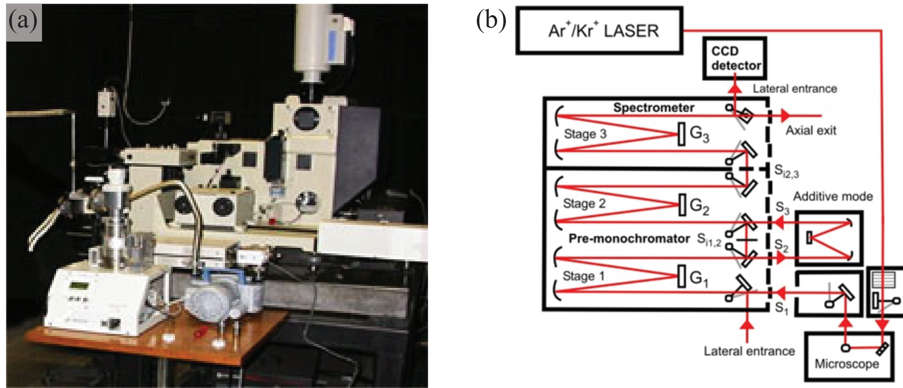

Figure 2.5.: (a) Jobin Yvon T64000 Raman spectrometer used for measurements of graphene's Raman spectra. (b) Schematic representation of optical path and elements of JY T64000 monochro-mator capale of working in a triple additive or subtractive mode.

Raman spectroscopy has proven as a very useful toll for characterization of graphene [203, 204]. This subsection will focus on some of the most prominent features of graphene's Raman spectra, and will discuss the information about sample quality, number of layers and doping that can be obtained from the Raman spectra. Within the thesis several raman spectroscopy systems have been employed for measuring graphene's Raman spectra, all of the measurements were carried out at room temperature and under ambient conditions. Figure 2.5(a) shows a Jobin Yvon T64000 Raman spectrometer, which was most commonly used for sample characterization, while a schematic representation of the optical elements and path is shown in Fig. 2.5(b).

Let us focus on phonon dispersion of graphene. Since unit cell of graphene contains two carbon atoms, there are six phonon dispersion bands [15], three acoustic branches (A) and three optical phonon branches (O). Two branches (one acoustical and one optical) have atomic vibrations perpendicular to the graphene plane. These

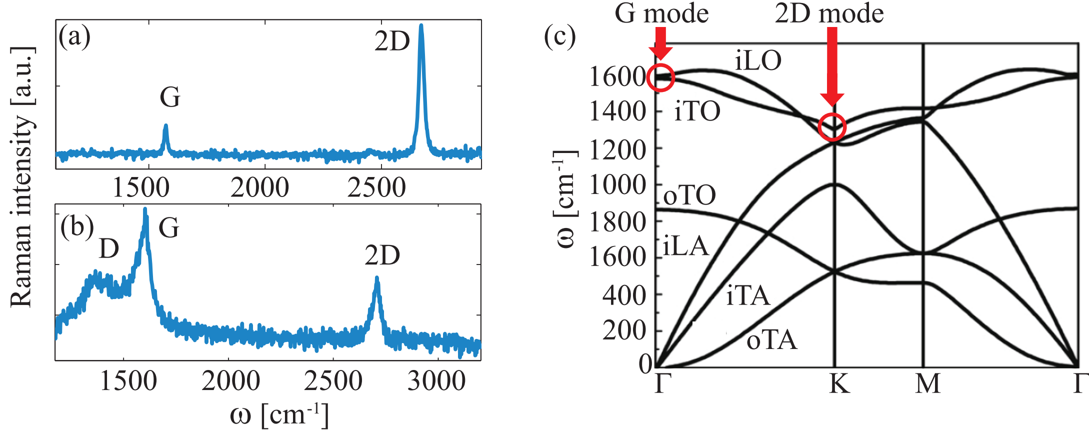

Figure 2.6.: (a) Raman spectra of a single-layer exfoliated graphene. (b) Raman spectra of a single-layer CVD graphene with significant amount of defects. (c) Phonon dispersion of graphene (reprinted from [205].)

are referred to as out-of-plane modes (o). The remaining four branches are in-plane modes (i). These in-plane vibrations can be either longitudinal (L) or transversal (T), with the respect to the A-B carbon-carbon direction. Following this classification, the phonon dispersion branches of graphene can be denoted as: iLO, iTO, oTO, iLA, iTA and oTA. Phonon dispersion is shown in Fig. 2.6(c). At Γ point iLO and iTO are degenerate. They belong to the E_{2g} representation and therefore are Raman active modes [203]. This is the only first-order Raman active mode in graphene. It is denoted as G mode and its frequency is usually at $\sim$ 1580 cm^{-1} (when measured with a 514 nm green laser). This mode is present in graphene, multi-layer graphene, various types of graphite, carbon nanotubes, and in many other materials that have $sp2$ hybridized carbon-carbon bonds.

Besides G mode, there are two more most prominent modes in Raman spectra of graphene. A double-resonant mode, usually denoted as $2D$ or G' is present at a frequency of $\sim$ 2700 cm^{-1} (with a 514 nm laser). This mode originates from a second order process involving two iTO phonons near K point. This mode is called $2D$ since it has approximately double the frequency of a defect-induced mode D. However $2D$ mode is not related to any defects in the structure and is even more prominent in highest quality (defect free) samples. The other prominent second-order process involves one iTO phonon and one defect. It is referred to as disorder-induced or

D-band and its frequency is usually at $\sim 1350\,cm^{-1}$ (with a 514 nm laser). Presence of a D band suggest imperfections in the crystal structure or crystal edges, and is commonly found in polycrystalline (CVD) samples. Figure 2.6(a) and (b) shows Raman spectra of single-layer exfoliated and CVD grown graphene, respectively. As discussed in the previous section, exfoliated graphene is defect free and has only G and $2D$ modes. On the other hand, CVD graphene (Fig. 2.6(b)) has crystal boundaries with irregular crystal structure, as well as microscopic cracks, folds and transfer residue. All these cause a prominent D-mode.

None of the previously mentioned characterization techniques can unambiguously confirm number of layers in a graphene sample. In most cases this is easily done by examining the Raman spectra of the sample. For this, a profile of the second-order $2D$ mode is used. In a case of a single-layer graphene $2D$ mode can be well fitted with a single Lorentzian line. However, having two or more layers will give different and more complicated $2D$ peak profiles. Figure 2.7(a) shows $2D$ mode for a single- to five-layer graphene (bottom-up) and $2D$ mode of HOPG (N-layer graphene). This method is very reliable for counting number of layers, up to five or six layers of graphene. For more layers it becomes much harder to distinguish fine structural difference of the mode profile, compared with a bulk graphite [203, 206].

Furthermore, Raman spectroscopy can be used to determine type and amount of the unintentional doping and strain induced within the sample. Uniaxial strain is the easiest to detect in Raman spectra, since it breaks the symmetry of graphene's crystal structure, lifting the degeneracy of iTO and iLO in the Brillouin zone center (Γ point) and causing G mode to split [207]. In order to distinguish splitting of G mode from the mode broadening it is required to apply uniaxial strain on the order of 0.5 %. However, uniaxial strain is not commonly present within the samples, especially not at such a high intensity. More common is bi-axial strain, introduced by the mismatch of the thermal expansion coefficients of graphene and supporting sample, or introduced during micromechanical exfoliation, or during transfer process. Unfortunately, bi-axial strain is much harder to distinguish from doping of graphene, only by examining Raman spectra of the sample.

If strain can be neglected, it is relatively straight forward to determine type and amount of the carrier concentration in graphene by examining positions, widths (full width at half maximum; FWHM) and relative intensities of G and $2D$ modes. These were first reported by measuring Raman spectra of exfoliated [45] and CVD [208] graphene, while a carrier concentration in graphene was controlled by electrolyte

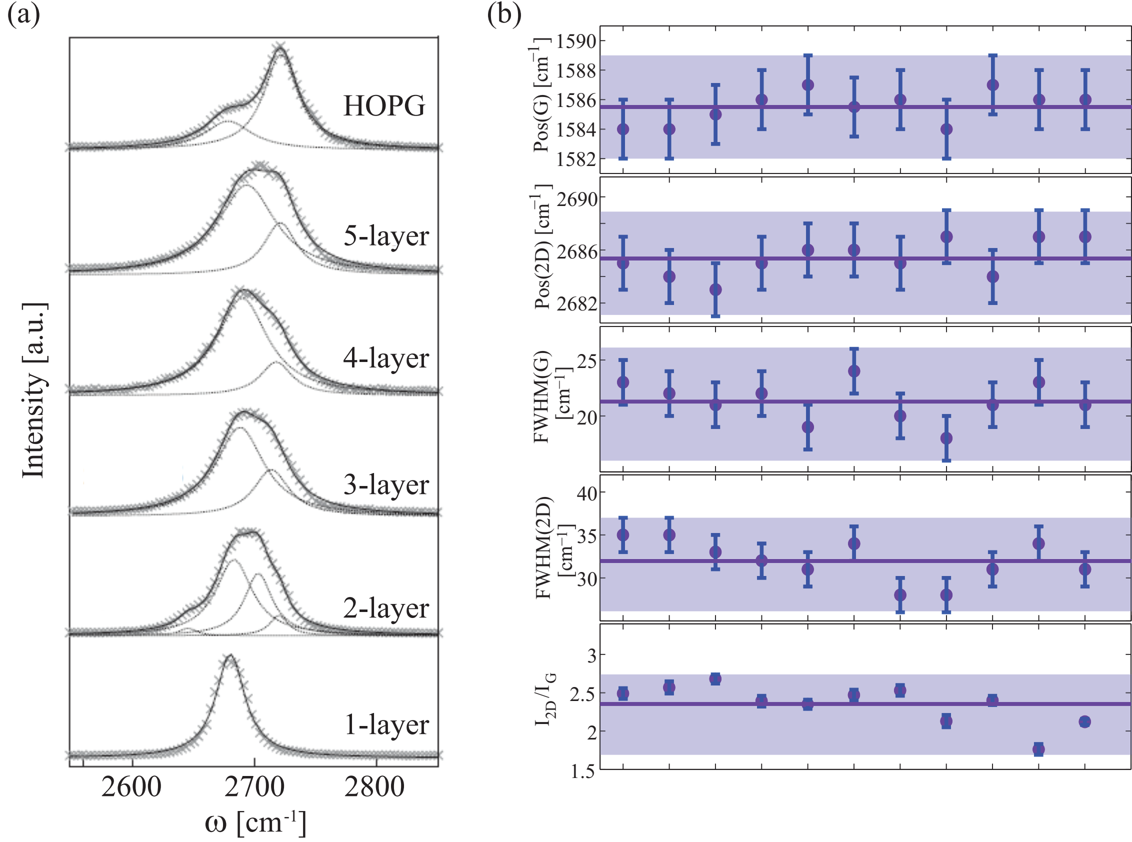

Figure 2.7.: (a) Raman spectra of a double-resonance ($2D$) mode, for various layer numbers of exfoliated graphene (reprinted from [206]). HOPG denotes highly oriented pyrolytic graphite, i.e. N-layers of graphene. (b) Spatial variations of G and $2D$ modes width (full width at half maximum - FWHM), position and relative intensities. Measurements were taken on a single-layer CVD graphene transferred onto a SiO_2/Si substrate.

gating. Figure 2.7(b) shows fitting results for ten measurements with the different position (several micrometers apart) of the laser spot on the same single-layer CVD graphene sample transferred onto a SiO_2/Si substrate. G and $2D$ modes of the measured spectra were fitted with single Lorentzian lines. Both the peak positions, widths and the relative intensities indicate a weak p-doping of graphene [45, 208], which is most likely caused by the transfer process [45, 208]. Considering averaged data (solid lines in Fig. 2.7(b)) gives hole concentration of about $6(\pm 2) \times 10^{12}\, cm^{-2}$, corresponding to the Fermi level (E_F) shift of about $-0.2(\pm 0.05)\, eV$, from the Dirac point. Large uncertainty comes from the local variations of the mode's positions, widths and intensities, marked as shaded area in Fig. 2.7(b). These point-to-

point variations were attributed to spatially non-uniform adhesion, resulting in non-uniform doping by the substrate and non-uniform strain [209, 210, 211]. For this reason, using Raman spectroscopy alone to determine low amounts of doping in the sample is not very reliable. However, error introduced by the spatial non-uniformity remains the same regardless of the doping level within the sample, and higher levels of doping can be much more reliably detected by Raman spectroscopy [45, 208].

2.2.3. Scanning probe microscopy

Scanning probe microscopy (SPM) is a group of measuring techniques, that are generally used for imaging surfaces with an atomic spatial resolution. There are many different SPM techniques, but some common constitutes to all are a scanning probe and a feedback loop for controlling the probes height. Different techniques use different types of probes and feedback mechanisms, ranging from simple very sharp tips of a tungsten wire, that can be used for scanning tunneling microscopy (STM), or probes that use optical leaver in a feedback loop as in atomic force microscopy (AFM) as shown in Fig. 2.8(a), or more elaborate probes as scanning single electron transistor (SSET) [212], or scanning gate microscopy (SGM) [213]. One of the simplest measurements that can be carried out using most SPM techniques is measuring sample topography. Height sensitivity and lateral resolution can vary from several micrometers to below one nanometer, but commonly SPM systems have at lest one order of magnitude better height sensitivity than the lateral resolution. Some of more advanced techniques can measure (and map) surface potential, local density of states, Young's modulus and many other material (surface) properties. This subsection will focus on two SPM techniques, applied on the case of graphene: tapping mode atomic force microscopy (TAFM) and Kelvin probe force microscopy (KPFM).

Many different AFM and STM techniques have proven as very useful for investigation of various graphene's properties [214]. First ever image of a single-layer graphene was made by an AFM [1]. Also, Young's modulus of graphene was measured by an AFM technique [9]. Local density of states was measured by scanning tunneling spectroscopy (STS) as well as Landau level splitting in high magnetic fields

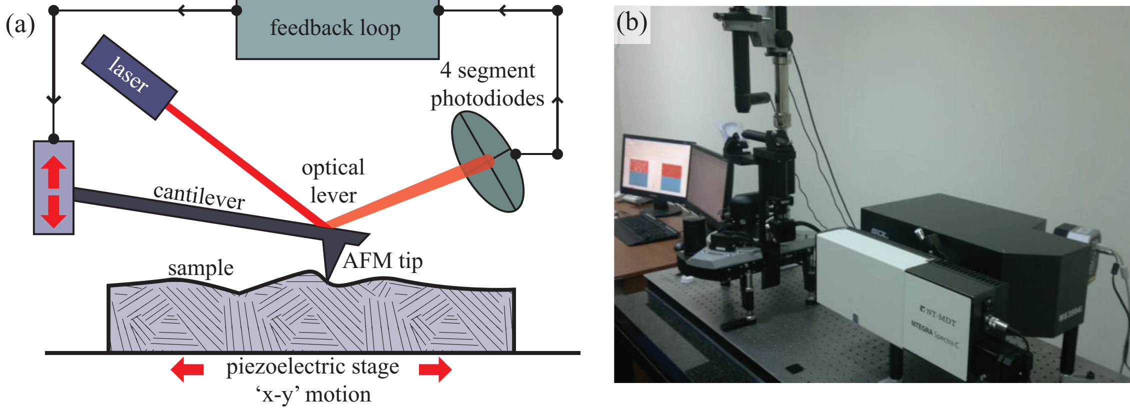

Figure 2.8.: (a) Schematic representation of an AFM measurements setup. (b) NTEGRA spectra, coupled SPM and confocal Raman system that was used in the dissertation.

[215, 216]. Electron-hole puddles, that form in pristine graphene as a consequence of localized charged impurities in the substrate have been first visualized by SSET [217], and STS mapping [218]. These electron-hole puddles are the strongest contributors to graphene's resistivity in the charge neutrality point. Besides investigation of graphene's properties, SPM techniques can be used for nano-scale lithography of graphene, either by molecular manipulation [219], local anodic oxidation [220] or dynamic plowing lithography [221]. In the dissertation tapping mode AFM was used mainly to corroborate ellipsometric measurements (see Sec. 3.3). For this TAFM was employed for measurements of sample height, surface roughness and detection of any nanoscopic dirt particles, or chemical or polymer residue on the surface. Figure 2.8(b) shows NTEGRA Spectra SPM system coupled with a confocal Raman spectrocope. This system has been employed in the dissertation.

TAFM is commonly used in ambient measurements, to avoid formation of a liquid meniscus layer (most commonly from water vapor). This layer keeps the tip sticking to the surface, and greatly reduces both height sensitivity and lateral resolution, since the effective area of interaction between the tip and the sample surface is significantly increased by this liquid meniscus layer. Also, TAFM significantly reduces any damage to the sample caused by the tip, compared with a contact AFM technique.

In tapping mode, the cantilever is driven to oscillate up and down at near its resonance frequency by a small piezoelectric element mounted in the AFM tip holder. However, the amplitude of this oscillation is typically 100 to 200 nm. The interaction

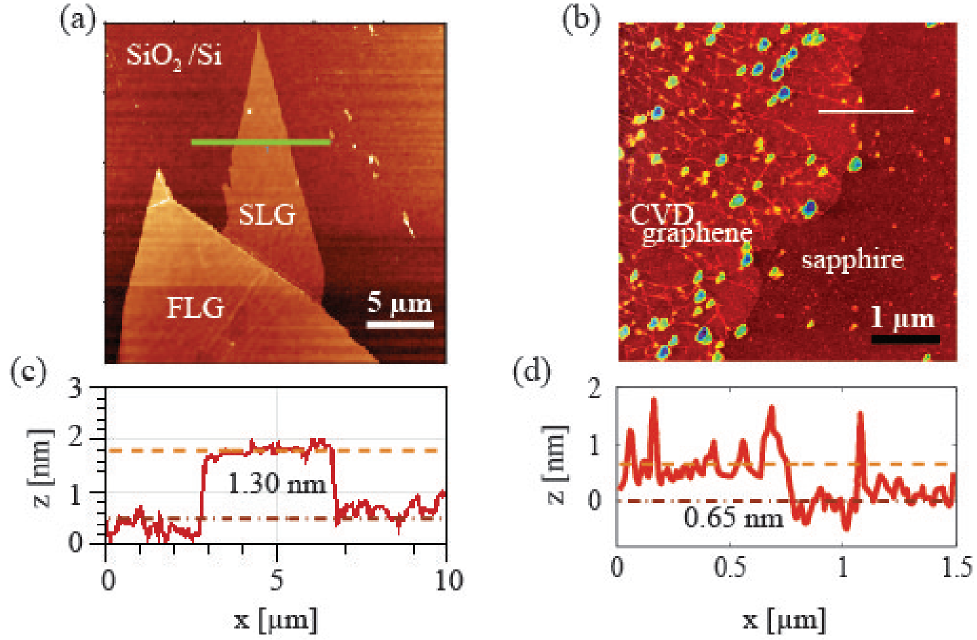

Figure 2.9.: (a) [222] and (b) TAFM topography images of an exfoliated single-layer graphene flake and transferred single-layer CVD graphene, respectively. (c) and (d) height profiles of denoted lines in (a) and (b) showing single-layer graphene/dilectric substrate step edge.

of forces acting on the cantilever when the tip comes close to the surface, as Van der Waals' forces, or electrostatic forces and others, cause the amplitude of this oscillation to decrease as the tip gets closer to the sample. First a certain amplitude that is smaller than the free space oscillations of the tip is set, and the height between the tip and the sample is reduced until this set value of oscillation amplitude is reached. During the scanning, if the sample surface changes, the amplitude of the tip oscillations will change as well. Then, the height between the sample and tip is changed to restore this set value. At each point during the scan, this height change is recorded, and as a result it gives a topography image of the scanned sample area. TAFM topography images of exfoliated and CVD graphene are shown in Fig. 2.9(a) and (b) with the corresponding sample/substrate step edges shown in Fig.2.9(c) and (d).

Interestingly, in Fig. 2.9 both samples are single-layer graphene (confirmed by Raman spectroscopy), yet TAFM has detected values of 1.3 nm and 0.65 nm, non matching the expected 0.334 nm thickness. There are several issues that need to be taken into consideration when interpreting AFM data. First, the sample usually

have some trapped liquid layers underneath [74, 82, 92], most commonly a water and air mixture. These can vary, depending on the fabrication method. In the case shown in Fig. 2.9(a), exfoliated graphene has not been thermally annealed, thus a larger water layer underneath is expected. On the other hand, in 2.9(b), CVD graphene has been thermally annealed to remove most of the transfer residue, this has resulted also with a partial removal of a water inter-layer. There is also another issue that needs to be taken into consideration. Images obtained by AFM are also dependent on the material properties of the tip and the sample, and various thicknesses of graphene have been reported in the literature [1, 64, 223, 224, 225, 226]. As an example: K. S. Novoselov and coworkers [1] have reported single-layer exfoliated graphene thickness of 1 nm to 1.6 nm, measured by TAFM. A. Gupta and coworkers [224] have reported 0.7 nm as an average height of a single-layer exfoliated graphene, also measured by TAFM. P. Nemes-Incze and coworkers [223] have analyzed how various approach parameters of TAFM can affect the height measurements of single- and multi-layer graphene on a dielectric substrates, and have found that an error as high as 1 nm can arise while measuring multi-layer graphene height by TAFM. The measurement error arises from the change in an interaction force between the tip and the sample as the type of material changes (graphene/dielectric), while a change in height also occurs. This is confirmed by the fact that steps between different number of layers on the same exfoliated graphene sample commonly have 0.335 nm step height. For all these reasons, TAFM is not reliable enough to determine a number of layers of a graphene sample.

TAFM height profiles are not the only relevant information for correlation with ellipsometry. By analysis of the topography maps it is possible to obtain surface roughness of the sample, or to visualize dirt of transfer residue that is too small to be spotted by optical microscopy. As an example, in Fig. 2.9(a) and (b), graphene samples have significantly different structure. In Fig. 2.9(a) exfoliated graphene is atomically smooth with only few localized dirt particles, while a transferred CVD graphene (Fig. 2.9(b)) has transfer residue island few tens of nanometers in size, in addition to wrinkles (for more details on CVD graphene see Sec. 2.1.3). These residue islands are to small to see by an optical microscope. Also, there would be only few of them present within a focused laser spot used for Raman measurement, meaning that their contribution to D-band or presence of the vibrational modes of the polymer that constitutes these islands might be too small to detect. All of these information are required to better interpret ellipsometry measurements, and for this

reason TAFM is very useful tool in correlation with ellipsometry.

The final part of this subsection addresses Kelvin probe force microscopy (KPFM). This particular SPM technique that has been used in the experimental part of the dissertation (Sec. 4.4) to probe graphene/gold interface. KPFM is also known as surface potential microscopy. It is an atomic force microscopy (AFM) based technique that can map the work function of the surface at a microscopic level. It was pioneered by M. Nonnenmacher and coworkers [227]. The work function of a surface represents the minimum thermodynamic work (i.e. energy) required to extract an electron form the surface of the material into a vacuum state just above the materials surface. The final electron position is far from the surface on the atomic scale, but still too close to the solid to be influenced by ambient electric fields in the vacuum. The work function is not a characteristic of a bulk material, but rather a property of the surface of the material and depends on the crystallographic orientation, roughness, imperfection, impurities and contaminations of the surface. The work function relates to many surface phenomena, including catalytic activity, reconstruction of surfaces, doping and band-bending of semiconductors, charge trapping in dielectrics and corrosion. The map of the work function produced by KPFM gives information about the composition and electronic state of the local structures on the surface of a solid.

KPFM measurements presented in the dissertation (and in Ref. [92]) were done using the two-pass technique [228]. In the first pass, a topographic line was measured in the tapping mode. In the second pass, the tip was lifted by 30 nm and moved across the surface following the topographic profile, obtained from the first scan. During the second pass, a combination of an AC and DC voltage was applied between the tip and the grounded silicon substrate. The frequency of the AC voltage was matched to the resonant frequency of the cantilever. The DC component was then adjusted to cancel an electrostatic force between the tip and the sample, resulting with a zero amplitude of the cantilever oscillations (near its resonant frequency). This procedure was repeated for every point of a selected area of the sample. Resulting KPFM maps show the applied DC component, *i.e.* the contact potential difference (CPD) between the sample and the AFM tip. An example of a KPFM map is shown in Fig. 2.10(a). The map shows a two-point probe device made by transferring CVD graphene over pre-fabricated gold electrodes on a SiO_2/Si substrate. The device is similar to the one shown in Fig. 2.13.

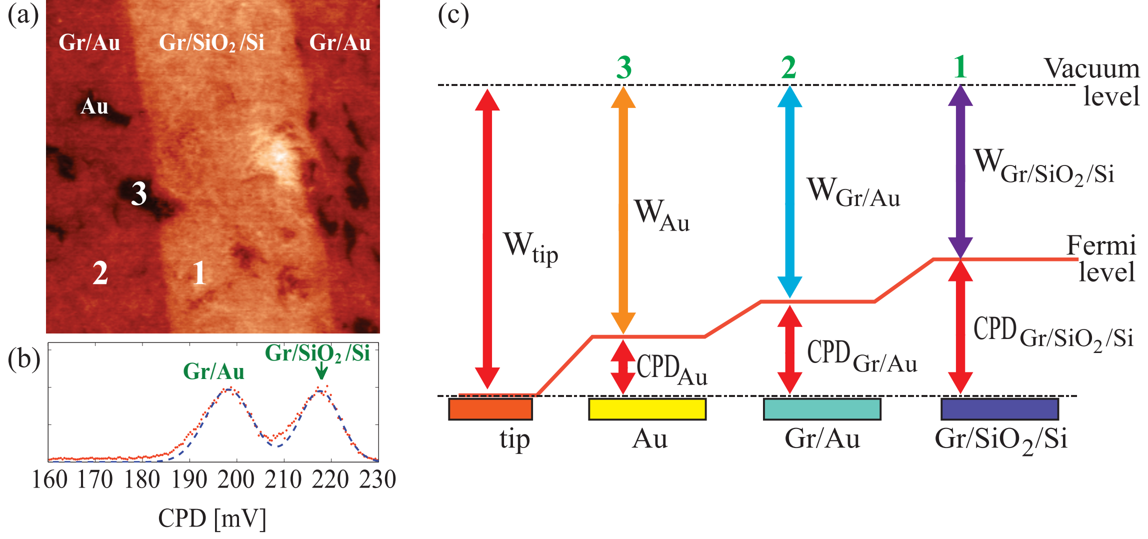

Figure 2.10.: (a) KPFM map of a CVD graphene covering two gold electrodes and forming a channel between them. Scanned area is 50×50 μm^2. 1, 2 and 3 denote areas of graphene over SiO_2 (channel), graphene over electrodes, and bare electrodes, respectively. (b) corresponding histogram of (a), two dominant peaks are fitted with single Gaussian lines. (c) schematic representation of the relation between measured CPD and work function of each surface. W denotes work function.

In order to analyze KPFM maps, CPD histograms are used (Fig. 2.10(b)). Each peak in a CPD histogram corresponds to a different surface on a KPFM map. Relative shifts of the peaks represent the difference between work functions of the two surfaces. The relation between a work function (W) of a given surface and measured CPD is shown in Fig. 2.10(c). If a work function of a tip (W_{tip}) used in the measurements is known, then it is possible to obtain work functions of the measured surfaces. However, if W_{tip} is not known, then only a relative difference between work functions of two surfaces can be measured. Here described procedure for KPFM measurements and data interpretation is used in chapter 4 (and Ref. [92]) to investigate interaction between graphene and a underlaying gold substrate.

2.2.4. Fourier transform infrared spectroscopy

Infrared spectroscopy is an optical spectroscopy that deals with the infrared region of the electromagnetic spectrum [46]. It covers a range of techniques, mostly based on absorption spectroscopy. As with all spectroscopic techniques, it can be used to identify and study various vibrational modes of solid, liquid, or gaseous samples. A basic IR spectrum is essentially a graph of infrared light absorbance (or transmittance) on the vertical axis vs. frequency or wavelength on the horizontal axis. Typical units of frequency used in IR spectra are reciprocal centimeters (or wave numbers), with the units cm^{-1}. A common laboratory instrument, that was also used in the dissertation is a Fourier transform infrared (FTIR) spectrometer.

An FTIR spectrometer simultaneously collects high spectral resolution data over a wide spectral range. This confers a significant advantage over a dispersive spectrometer which measures intensity over a narrow range of wavelengths at a time. The term Fourier transform infrared spectroscopy originates from the fact that a Fourier transform (a mathematical process) is required to convert the raw data into the actual spectrum.

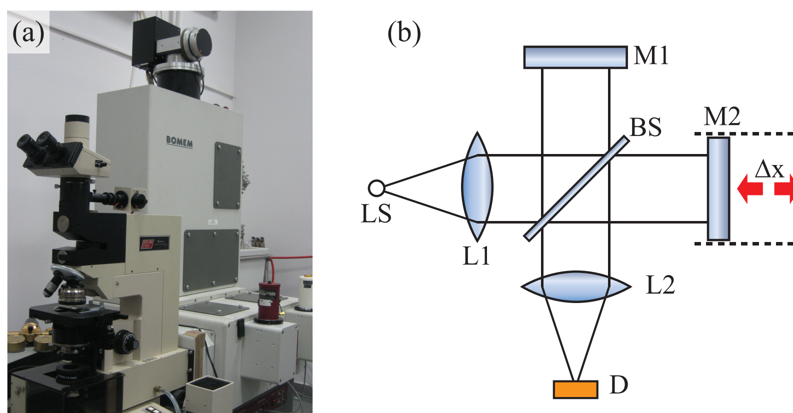

Figure 2.11.: (a) FTIR spectroscope Bomem DA8 equipped with an IR microscope. (b) scheme of the Michelson interferometer.

A FTIR spectroscope equipped with an IR microscope that has been used to obtain the data presented in this subsection is shown in Fig. 2.11(a). FTIR spectroscopy is based on the Michelson interferometer shown in Fig. 2.11(b). The source covers a large spectral range and is located at the focal point of lens $L1$, giving a parallel coherent incident beam. This beam is separated into two parts by the beam splitter (BS). The reflected part is focused onto the detector D after reflection

from the stationary mirror M1 and after a second split by the beam splitter. The transmitted part of the light is also focused onto the detector after it was reflected from the mirror M2 and split again by the beam splitter. The mirror M2 is mobile and can glide a distance Δx. In this way interference fringes develop at the detector. Their intensity $I(x)$ depends on the position x of the mirror M2, or more precisely by the difference in the optical path between the two beams. $I(x)$ is called an interferogram function. A Fourier transform of the interferogram gives the measured intensity spectrum.

Let us assume that an electric field vector of the incident beam can be written as:

$$E_I(x,t) = E_0 \cos\left(kx - \omega t\right), \tag{2.8}$$

then an electric field at the detector (see Fig. 2.11(b)) is:

$$E_D(x,t) = \frac{1}{2}\left(E_0 \cos\left(k_0 x - \omega_0 t\right) + E_0 \cos\left(k_0(x + 2\Delta x) - \omega_0 t\right)\right). \tag{2.9}$$

Here $2\Delta x$ is the path difference between the two beams. For $x = 0$ both mirrors are at the same distance from the beam splitter. By choosing $x = 0$ and substituting $2\Delta x = 2x$ and $k_0 = 2\pi\nu_0$, light intensity at the detector is:

$$I(x) = c_0\epsilon_0 \left\langle E^2 \right\rangle = \frac{c_0\epsilon_0 E_0^2}{4}(1 + \cos\left(4\pi\nu_0 x\right)). \tag{2.10}$$

Rewriting this equation by using a spectral intensity $I(\nu) = c_0\epsilon_0 E_0^2 \delta(\nu - \nu_0)/2$ gives:

$$I(x) = \frac{1}{2}\int_0^\infty I(\nu)(1 + \cos\left(4\pi\nu x\right))\, d\nu\,. \tag{2.11}$$

The interferogram $I(x)$ holds the whole information about the spectrum $I(\nu)$. If rewritten as:

$$I'(x) = I(x) - \frac{1}{2}\int_0^\infty I(\nu) d\nu = \frac{1}{2}\int_0^\infty I(\nu)\cos\left(4\pi\nu x\right) d\nu\,. \tag{2.12}$$

then $I'(x)$ is the Fourier transform of $I(\nu)$ performed with a cosine function.

Let us now focus on FTIR spectroscopy of graphene. As it was discussed in the first chapter, in the infrared range there are both intraband and interband contributions to optical properties of graphene. Intraband component is expected to be dominant in the fahr infrared region (10-250 cm^{-1}), while Pauli blocking of the

interband component is expected to be in the mid infrared range (2501000 cm^{-1}) [184]. Here measurements were carried out in the near infrared region (1000-12500 cm^{-1}), where optical conductivity of graphene is expected to be constant and equal to the universal optical conductivity ($\sigma_0 = e^2/4\hbar$), as it was shown in Sec. 1.2.1 and App. A.4. Analysis of infrared spectra of graphene in the near infrared range can be of particular importance for counting the number of graphene layers in the sample. In this part of the spectra graphene layers weakly interact with each other and optical conductivity (or absorption) is linearly proportional to the number of layers. This is a big advantage over Raman spectroscopy, or over SPM, since neither one of these techniques is very reliable for measuring the exact number of layers for samples with more five or six layers of graphene.

Infrared spectroscopy of graphene has been carried out on exfoliated samples of single- and few-layer graphene. The samples were supported by a SiO_2/Si substrate with about 300 nm thick oxide layer. The chosen SiO_2 thickness gives higher sensitivity of the measurements between 5000 cm^{-1} and 7000 cm^{-1}. An increased sensitivity is based on the multiple reflections within the SiO_2 layer, similarly as an increased contrast of graphene on a substrate is achieved in the visible range (see Sec. 2.2.1). Measurements were carried out in reflection mode, in argon environment and at room temperature. Incident beam was focused on the sample by an infrared microscope with 15× magnification lens. Spot size was controlled with an aperture, resulting with a spot diameter of 70 μm. This was confirmed by a knife edge measurements of the spot size.

Since infrared spectroscopy measurements require a reference sample, each time after the sample was measured, a spectra of a nearby SiO_2/Si substrate was measured as a reference. A relative reflectance was expressed as: $(R_{sample} - R_{substrate})/R_{substrate}$. Relative reflectance spectra of a single-layer sample is shown in Fig. 2.12(a), and for two-, five- and eight-layer samples in Fig. 2.12(c). As it can be seen, due to the choice of the substrate thickness highest relative difference (or contrast) is in the middle of the measured range where the light intensity is strongest. In order to interpret measured spectra optical models based on Fresnel equations have been used, similarly as in Sec. 2.2.1. A normal incidence is considered. Optical properties of the substrate and layer thickness of a SiO_2 are considered as known. Graphene is introduced as a surface charge on an interface between SiO_2 and ambient air (or argon gas). In this case light absorption occurring within graphene is defined by a real part of its optical conductivity.Optical conductivity of graphene in the near

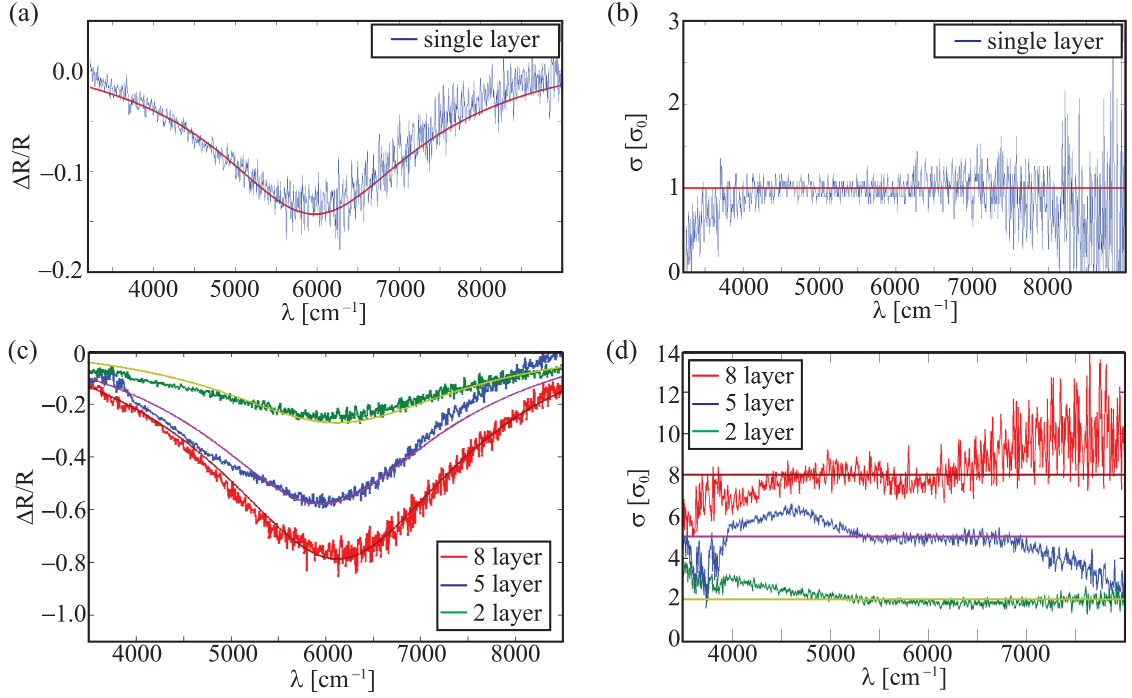

Figure 2.12.: (a) measured and fitted $\Delta R/R = (R_{sample} - R_{substrate})/R_{substrate}$ spectra for single-layer graphene sample. (b) optical conductivity of single-layer graphene calculated from (a). (c) measured and fitted spectra of two-, five- and eight-layer graphene samples, and (d) their corresponding optical conductivities.

infrared range has been discussed in Sec.-s 1.2.1, 1.2.3 and a detailed derivation has been given in App. A.4. Simulated $\Delta R/R = (R_{sample} - R_{substrate})/R_{substrate}$ spectra are shown as smooth lines in Fig. 2.12(a) and (c). The measured data has been used in the optical model to retrieve optical conductivity of graphene by mathematical inversion. This process is also referred to as a point-by-point inversion and ti is discussed in the next chapter, since it is also used to retrieve optical properties of graphene from spectroscopic ellipsometry measurements.

Obtained optical conductivity of single-layer graphene is shown in Fig. 2.12(b), presented in the units of universal optical conductivity $\sigma_0 = e^2/4\hbar$. As it can be seen, in the high sensitivity range, obtained optical conductivity is linear and equal $\sigma_0 \pm 10\%$. This demonstrate that optical properties of graphene in this range are not governed neither by the material properties nor by the energy of the incident photons, but rather by universal constants, and interestingly these constants can be measured at room temperature, with a fairly simple setup. The same data

interpretation process has been used to interpret measured spectra of few layer graphene samples. As expected in this range interaction between layers is weak and optical conductivity scales as $N \cdot \sigma_0$ where N represents the number of graphene layers.

2.2.5. Measurements of direct current electrical characteristics

As it has been discussed in Sec. 1.1.5 and 2.1.5, by having an electrical contact on graphene and an additional parallel electrode it is possible to change carrier concentration and probe electrical properties of graphene. This subsection will focus on measurements of direct current electrical characteristics of graphene with two metallic contacts and a silicon substrate as a back gate electrode. This contact geometry is referred to as two-point-probe (2pp) and is very similar to a MOSFET transistor. This subsection will show that type and amount of unintentional doping, carrier mobility and presence of Schottky barriers can be seen from these electrical measurements.

High crystal quality of graphene has as a consequence an excellent electrical properties. These are usually expressed through carrier mobility μ. Room temperature values as high as 250 000 cm^2/Vs have been reported for "ripple-free" graphene [6], i.e. graphene sandwiched between two sheets of hBN. However, values of μ for exfoliated graphene on a SiO_2/Si substrates were found to vary between 2 000 cm^2/Vs and 20 000 cm^2/Vs, at room temperatures [229]. Imperfections as microscopic ripples and charged impurities can introduce scattering and reduce carrier mobility. Both of these can be significantly minimized if graphene is fabricated in very clean environment and if it is placed over atomically flat substrates as mica or hBN [6]. Interestingly it has been shown that adsorbed molecules and ions on the surface of graphene do not change carrier mobility, but only change the amount of doping [115]. This would leave only scattering caused by ripples as a dominant factor in the carrier mobility reduction. However, there is one intrinsic source of scattering, phonons. These can not be eliminated at room temperature, and will set a fundamental limit for carrier mobility, and consequently a fundamental limit for graphene-based device performance at room temperatures. This limit of μ has

been estimated at about 400 000 cm^2/Vs, with electron mean free path of several micrometers, all at room temperature [229]. Reported experimental values for exfoliated graphene on a hBN substrate (250 000 cm^2/Vs) are not fahr from this limit [6]. Phonon scattering has been found to have very small contribution to carrier mobility [229], since mobility away from the charge neutrality point has been found as temperature independent both for graphene and bi-layer graphene [229]. Only when Fermi level is in the vicinity of the Dirac point, there is a significant temperature dependence of the channel resistivity [229].

By measuring the resistivity of graphene channel between two metallic contacts as a function of a gate voltage (applied between one of the contacts and a back-gate electrode) $R_{ds}(V_{bg})$ type of the majority carriers can be determined, the amount of unintentional doping and ripples of graphene sheet can be estimated. The measurement setup and typical results for the total devise resistance $R_{ds}(V_{bg})$ are shown in Fig.-s 1.7 and 2.13. When total device resistance is measured, it includes a series of resistors, consisted of graphene channel, thin metallic electrodes defined by the lithography process, larger macroscopic electrodes used to bond to the microscopic pads and finally all the external wires. All of these are not dependent on the applied back-gate voltage, except for the resistance of the channel, meaning that total resistance can be split into two components: $R_{ds}(V_{bg}) = R_g(V_{bg}) + R_S$. Here, $R_g(V_{bg})$ denotes resistance of the channel and R_S denotes all the other constant contributions. Resistivity ρ can be simply obtained by taking the channel geometry into account, i.e. multiplied by width W over length L of the channel. Part of the channel that lies underneath gold electrodes is not taken into account, since it is considered that it can not contribute to the part that exhibits electric field effect, but rather is added to the constant part R_S. This constant part of the resistance is usually obtained either by fitting [229, 230], or by using so called "dummy" devices [42]. Fitting is carried out considering that due to linear dispersion relation, conductivity of graphene should be linear away from the neutrality point, or resistivity should be a function of $\propto 1/V_{bg}$. Measured conductivity of the entire device will always be "sub-linear" and when a constant resistance (or resistivity) is deduced it should result with a linear dependence. This can be written as $S_g(V_{bg}) = 1/(R_g(V_{bg}) - R_S)$ and R_S is found by the condition that S_g is linear away from the neutrality point. The other way to estimate the contact resistance is to fabricate "dummy" devices. These have all the same contact geometries made by the same processes, but instead of a graphene channel a thin highly conductive film is used. This film can either

be fabricated during metallic film deposition, or in the case of exfoliated graphene, thicker samples (over 20 layers) are usually used. These devices do not show any field effect when a back gate voltage is applied, and their total resistivity closely matches R_S. Both methods should result with the same value for contact resistance, and commonly an average between these two is used [42]. However, having conductivity does not mean having carrier mobility as well, to have the exact value of carrier mobility, besides conductivity it is required to know the exact value of Fermi velocity. In the case of exfoliated graphene it is safe to assume $v_F = \frac{\sqrt{3}at}{2\hbar} \approx 10^6 m/s$ (Eq. 1.31). However, in the case of CVD graphene, electron transport is affected by the grain boundaries and wrinkles, and this method is unreliable for estimating carrier mobility.

Maximum in the $R_{ds}(V_{bg})$ curve (Fig. 2.13(c)) corresponds to the charge neutrality point (CNP). At this point both electrons and holes are equally favorable as majority carriers within the channel. This is in a sense as close as a given experimental setup can approach in positioning Fermi level at the Dirac point. The value of the applied back-gate voltage will indicate the type and the amount of unintentional doping. If the voltage generator is connected as shown in Fig. 2.13(a), then positive values of CNP will indicate intrinsic hole or p-doping of graphene. The value of the applied back-gate voltage can be easily related to the amount of carriers that were added to graphene sheet in order to reach CNP. This is done by considering a parallel plate capacitor made by graphene as one electrode and a silicon substrate as the other. Capacitance per unit area is given by: $C = \epsilon_0 \epsilon_r / d$, where ϵ_r, d are determined by the type and the thickness of the dielectric material, usually SiO_2. Surface charge density is given by: $\rho_S = C \cdot V_{bg}$. Finally, the electron density in graphene can be written as: $n = \rho_S / e$, or: $n = (\epsilon_0 \epsilon_r V_{bg})/(de)$. Here, e stands for the electron charge. Electron density can be easily related to the position of the Fermi level in graphene as: $n = E_F^2 / \pi \hbar^2 v_F^2$. However this depends on the Fermi velocity as well.

The other direct current measurement setup that can be made with the same contact geometry is shown in Fig. 2.13(b). In this case back-gate electrode is connected to the mass of the entire circuit. However, this is not necessary and the same measurement setup can be made with varying back-gate voltage. This setup measures current through the channel I_{ds} as a function of a voltage applied over the channel V_{ds}. With these measurements it is possible to probe the quality of metallic contacts with graphene channel. If these contacts have a constant resistivity regardless of the current density through them or a voltage drop applied across them,

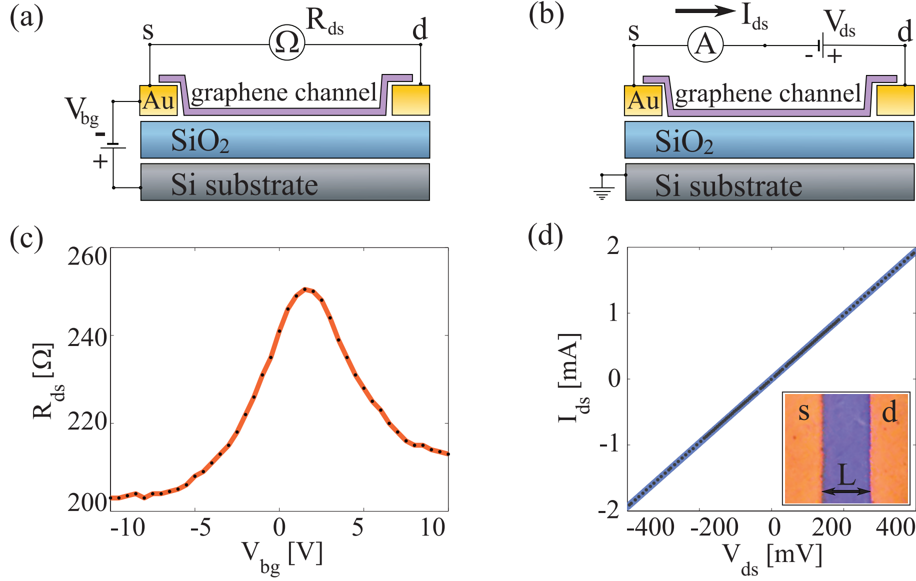

Figure 2.13.: 2pp device made by transferring CVD graphene over prefabricated gold electrodes. (a) shows a schematic representation of the setup used for (c) DC measurements of the total source-drain resistivity (R_{ds}) as a function of back gate voltage (V_{bg}). CNP was found to be at 2 ($\pm$0.5) V, indicating weak *p*-doping. (b) shows a schematic representation of the setup used for (d) DC measurements of the source-drain current (I_{ds}) as a function of an applied voltage between source and drain electrodes (V_{ds}), where a linear dependence confirms that the contacts are Ohmic. Inset of (d) shows a microscope image of the graphene channel (middle) and gold source and drain electrodes (left and right sides), here L indicates channel length (17 μm).

they are referred as Ohmic contacts. Then $I_{ds}(V_{ds})$ should be linear, as shown in Fig. 2.13(d). There are two reasons for deviation from the linear curve. One quite obvious would be device breakdown caused by high current density. This would determine operational limit.

The other reason for deviation from the linear curve would be formation of Schottky barriers on the contact between graphene channel and metallic electrodes. This would be determined by the type of the metal that contacts graphene [231]. Whenever a contact between two materials with different charge concentration is formed a charge redistribution occurs at the interface. This is driven by the difference in the charge density, and carriers from the material with the higher charge density

will go to the material with the lower charge density. Obviously, this process can not continue indefinitely, as carriers travel through the interface an electrostatic potential barrier forms at the interface. These two processes balance each other, and form an interface dipole [23]. This dipole acts as a diode, or a *p*-*n* junction. Larger the initial difference in the carrier concentration will create bigger potential drop at the dipole layer. From the electrical circuit point of view this is seen as a diode with higher threshold voltage. These diodes are referred to as Schottky diodes, and are a common problem of making an electrical contact with a semiconductor. In the case of graphene it is obviously inevitable to crate Schottky barriers since most metals have larger carrier concentration than graphene. There are several studies that show how this graphene/metal interface behaves, as first principles [231], electrical transport [232], scanning tunneling spectroscopy [233], angle-resolved photoemission spectroscopy [234], Raman spectroscopy [235], KPFM and ellipsometry [92] studies of various graphene/metal interfaces.

In a case of a two-point probe, each contact will form a Schottky diode. These two diodes will be of opposite polarity (i.e. turned "back-to-back"). Such a device is called barrier induced transfer time (BARITT) diode. This type of behavior is easy to see from the $I_{ds}(V_{ds})$, since diodes causes strong deviation from the linear curve, one at the positive side, and the other at the negative side of V_{ds}. A clear example is given in Ref. [38] for a 2pp device with a single single-walled semiconducting carbon nanotube as a channel.

If the device shows a linear $I_{ds}(V_{ds})$, applying the back-gate voltage will only change the angle of the line, as channel resistivity changes. However, if the Schottky barriers are formed, application of a back-gate voltage will affect the dipole layer. It was demonstrated by Y.-J. Yu and coworkers [228], that by applying a back-gate voltage it is possible to tune in the work function of graphene, and consequently increase or reduce the effect of Schottky barriers.

One of the best match metals for contacting graphene is gold [231]. As it can be seen from Fig. 2.13(d), grphene/gold interface forms Ohmic contacts. Strongest dipoles were found between graphene and palladium, and graphene and titanium [129, 123, 127], forming opposite polarities of Schottky diodes. As discussed within Sec. 1.3.2, this has been employed to fabricate graphene based photodetectors with a "built-in" voltage drop.

There is one more thing to consider whenever electrical measurements of graphene are carried out. Since graphene is only one atomic layer thin, its interactions with

the environment can strongly affect its electrical properties. This has been exploited to make gas detectors with graphene that are capable of detecting single molecule adsorption and desorption events [115]. However, for electrical characterization of graphene this is an unwanted effect. If direct current measurements are carried out in ambient air, any applied voltage is compensated by the water vapor that is attracted to the graphene sheet by the electric field. Adsorption and desorption of water molecules is very slow process and strong hysteresis appears when $R_{ds}(V_{bg})$ is measured in succession.

There are several ways to avoid these effects. One would be to encapsulate graphene with a dielectric layer. The simplest would be to spin-coat a layer of PMMA over the device, or more elaborate to cover the device with a thin layer of Al_2O_3 or HfO_2. Another approach would be to deposit graphene on a hydrophobic surface, as self-assembled layer of hexamethyldisilazane (HMDS). This was demonstrated by M. Lafkioti and coworkers [236], where a significant suppression of the hysteretic behavior under ambient conditions was reported. Another approach would be to carry out measurements in an inert atmosphere. as argon gas. Figure 1.7(b) show DC measurements in Ar gas flow. Prior to measurements, sample was kept in Ar gas environment for over 24 hours, to eliminate most of the surface contaminants. Measurements presented in Fig.2.13(c) and (d) were carried out in low vacuum (8×10^{-3} mbar), in order to avoid dipolar adsorbates from the ambient environment [236, 237]. Prior to measurements, sample was left to de-gas and stabilize in vacuum for over 24 hours. Once the samples are stabilized, and ambient conditions are constant, hysteretic behavior is negligible in both $R_{ds}(V_{bg})$ and $I_{ds}(V_{ds})$ measurements. As an example results shown in Fig.2.13(c) and (d) were repeated several times during 72 hours, and shifts of no more than $\pm0.5\,V$ of the charge neutrality point were detected. Position of the CNP is the most sensitive value to any changes due to adsorption of the polar ambient molecules.

3. KEY EXPERIMENTAL METHOD: SPECTROSCOPIC ELLIPSOMETRY

3.1. Working principle

In ellipsometry, p- and s-polarized light waves are irradiated onto a sample at an angle θ, which is usually chosen to be near the Brewster angle of the sample. After the light interaction with the sample the state of polarization is changed. Ellipsometry detects this change, either by analyzing the reflected or in the transmitted component of the light. Incident, transmitted and reflected beams all lie in the same plane, which is referred to as the plane of incidence. Naturally, surface of the sample is perpendicular to the plane of incidence. p-polarized waves are those with their electric field vector oscillating parallel to the plane of incidence. s-polarized waves have their electric field vector oscillating perpendicular to the plane of incidence, and parallel to the sample surface (when considering perfectly flat samples).

The polarization of light can be represented by superimposing two waves with their electric field vectors oscillating parallel and perpendicular to the plane of incidence, i.e. p- and s-waves (see Sec. 3.1.2). The relative change in the state of polarization can be described by two values. In ellipsometry, almost exclusively values of ψ and Δ are used to represent this change. They stand for the amplitude ratio and phase difference between p- and s-polarizations, respectively. (ψ, Δ) are commonly related to the ratio between complex amplitude reflection (or transmission) coefficients for the electric field vector parallel ($r_p = E_{rp}/E_{ip}$) and perpendicular ($r_s = E_{rs}/E_{is}$) to the plain of incidence, and as a result of ellipsometric measurements a complex value ρ is obtained:

$$\rho = \frac{r_p}{r_s} = tan(\psi)\, exp(i\Delta)\,. \tag{3.1}$$

By knowing the change in the state of the polarization (ρ) that was introduced by the sample, it is possible to reconstruct structure and optical properties of the sample which could cause this change. Data analysis is the topic of the next section (Sec. 3.2).

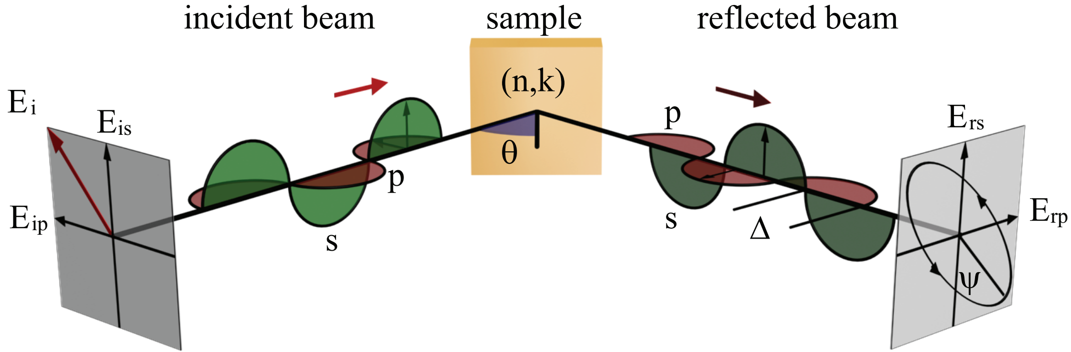

Figure 3.1.: Measurement principle of ellipsometry.

Let us now focus on the simplest case in order to demonstrate the working principle of ellipsometry. Figure 3.1 shows a +45° linear polarized (see Sec. 3.1.2) parallel beam that irradiates a perfectly flat sample under an angle θ. This specific polarization is chosen since it has the same light intensity of both p- and s-waves, and both waves are in phase (linear polarization). Expressed in the values of (ψ, Δ), a +45° linear polarization has $\psi = 45°$ (or $tan(\psi) = 1$) and $\Delta = 0°$.

After interaction with the sample, state of the polarization will be changed. Let us focus on the reflected component. In general, this change in the polarization will result with an elliptical polarization. Here both an amplitude ψ and phase Δ between p- and s-waves have changed from the initial state $(\psi, \Delta) = (45°, 0°)$. Although, in Fig. 3.1, ψ is marked in a fourth quadrant, the same value should be obtained from each quadrant, since ψ is defined from the absolute value of the amplitude ratio $(0° \leq \psi \leq 90°)$. This can be employed to minimize any nonlinearities existing in the measurement setup, and is usually referred to as four zone averaging (see Sec.-s 3.1.4 and 3.1.5). On the other hand, the phase difference can range between −180°

and +180°, and for some special values will give linear or circular reflected polarized light. As an example this is employed in null ellipsometry (Sec. 3.1.4).

There are several advantages of ellipsometry, but the most important one is that ellipsometry is an absolute measurement technique, i.e. it does not require a reference measurement since the measured values do not depend directly on the light intensity. Furthermore, commonly measured values are angles or frequencies, which can be obtained with great precision. As a result, ellipsometry is one of the most precise techniques for measuring the change in the state of polarization of the light. Regarding applications of ellipsometry, as it was mentioned earlier, ellipsometry is a contactless and very fast technique, which is very important for implementation of ellipsometry as an in-line or post-fabrication control tool.

The major drawback of ellipsometry is that rarely the change in the state of polarization is a value of interest, but rather some properties of the sample, as dielectric function, thickness or interface roughness. To obtain these a data interpretation procedure needs to be carried out. This procedure can increase uncertainty of the obtained data.

3.1.1. Optical elements

This subsection will focus on some of the most common elements used in ellipsometric setups, showing their working principles, advantages and disadvantages. As it was stated, ellipsometry measures a relative change in the state of polarization after light interaction with the sample. For this it is required to know the polarization of the incident and reflected (or transmitted) beams. Both can be achieved using polarizers.

A polarizer is an optical element that transmits only one polarization of light which lies in parallel to the optical axis of the polarizer. It is used to extract linearly polarized light from unpolarized light, prior to sample irradiation. After light is reflected from the sample another polarizer is placed before the light detector, and it is used to detect the state of polarization from the intensity of the transmitted light. In this case it is referred to as an analyzer. Polarizer and analyzer are the same type of elements, only they are named differently due to the difference in their

roles.

Polarizers are commonly made out of calcite crystal ($CaCO_3$). Calcite has the electron concentration distributed inhomogeneously toward different direction in the crystal. The refractive index of calcite varies accordingly. This is referred to as optical anisotropy, and materials that have their properties significantly different along one direction are referred to as uniaxial materials. In uniaxial materials, propagating electric field exhibits two different refractive indices. These are referred to as an ordinary (n_o) and extraordinary (n_e) refractive indices. In the case of calcite, n_o is greater than n_e, and the axis that lies in the direction of n_o is referred to as slow axis, while an axis that lies in the direction of n_e is called fast or optical axis of the crystal. Usually, polarizers are designed to transmit only light that is polarized parallel to the optical axis. There are other uniaxial materials that have ordinary refractive index greater than the extraordinary. This is the case of quartz, and fast (optical) axis is then related to the direction of n_o. An optical anisotropy that results from a refractive index difference is referred to as birefringence.

At normal incidence uniaxial materials can only introduce a phase shift between ordinary and extraordinary rays. So a question remains: how to build a polarizer out of an uniaxial crystal? At oblique incidence ordinary and extraordinary rays propagate at different transmission angles. This principle is used in the most of the polarizers that are based on uniaxial materials, and a most common example is a Glan-Taylor prism.

A schematic representation of a Glan-Taylor prism is shown in Fig. 3.2. The working principle is based on a total reflection at the critical angle: $sin(\theta_c) = 1/n$. In uniaxial materials θ_c varies depending on the direction of electric field due to anisotropy of the refractive index. By the proper choice of θ_c it is possible to remove ordinary ray (in the case of calcite) using total reflection. This condition can be written as: $1/n_o < sin(\theta_c) < 1/n_e$. Larger the difference between n_o and n_e will give larger region of θ_c that satisfies this condition. In the case of calcite, critical angle has to be in the range of: $37.1° < \theta_c < 42.3°$. One more important property of a polarizer is the spectral region where it is applicable. If the polarizer is made out of calcite it can work from the UV to the mid-infrared region ($\lambda = 0.21 - 5\mu m$).

In Fig. 3.2 there are two identical prisms separated by a thin interspace filled with air. The reason for using the second prism is to ensure parallel exiting beam, which significantly simplifies the integration of a Glan-Taylor prism in an optical setup. The spacing between prisms is air, but two prisms can be glued together. This is the

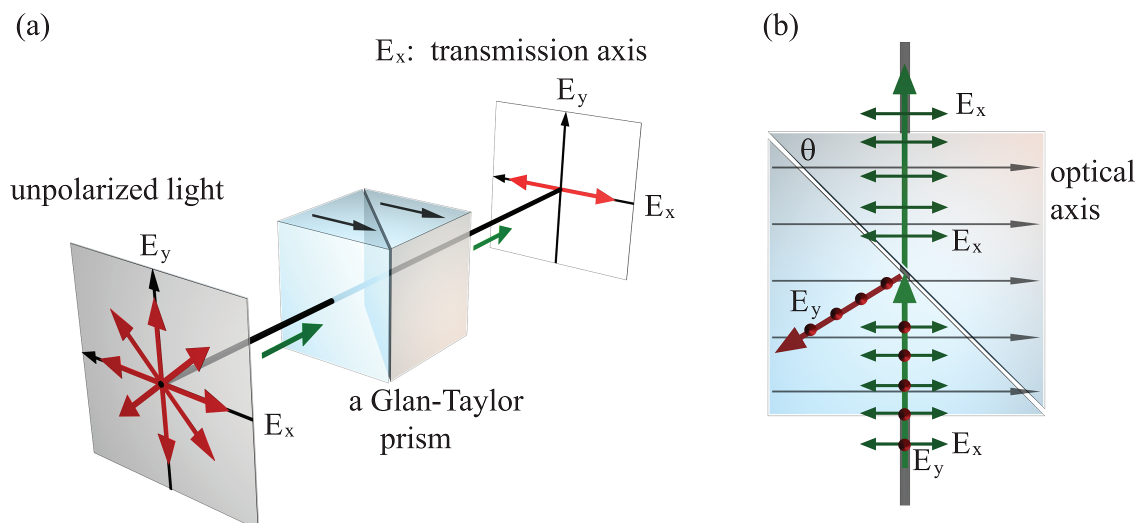

Figure 3.2.: (a) Schematic representation of a GlanTaylor prism used as a polarizer (analyzer) and (b) top-down view of its structure.

case of a Glan-Thompson prism. Although this simplifies the fabrication process, the glue changes (reduces) the range for the critical angle, and more importantly reduces the spectral range, since most glue materials absorbs light in the UV.

Also, in a Glan-Taylor prism (Fig. 3.2) optical axis has the same orientation in both prisms. This does not have to be a case. Similar construction that has optical axis of the second prism rotated by 90° is called a Rochon prism. In a Rochon prism, both prisms touch each other leaving no space in between, and no glue material. It works similarly as a Glan-Taylor prism, however in a Rochon prism both ordinary and extraordinary rays are transmitted with one being parallel to the incident beam, while the other is transmitted under an angle. There are two main advantages of a Rochon prism over a Glan-Taylor prism, first since there is no spacing between two prisms, a parallel transmitted ray is not shifted at all. This is very important since most ellipsometers use rotating polarizers and analyzers. Another advantage of a Rochon prism is that due to its construction the difference between n_o and n_e does not have to be as big as in a Glan-Taylor prism and other materials as quartz or more commonly MgF_2 can be used. A Rochon prism made out of MgF_2 can be used for ellipsometry measurements deep into the UV region (even up to $\sim$10 eV, or $\sim$0.12 μm). The major drawback of a Rochon prism, compared to a Glan-Taylor prism is relatively low efficiency in separating ordinary and extraordinary rays. However it is still good enough for these polarizers to be widely used in ellipsometry.

Regardless how a polarizer (analyzer) is made, most important property is how good are ordinary and extraordinary rays separated. This is expressed through a parameter called extinction ratio. In the case when an extraordinary ray is the transmitted one, the extinction ratio is then given as: $k = |E_e|^2/|E_o|^2 = I_e/I_o$, and in the case of a Glan-Taylor prism made out of calcite the extinction factor can be as high as $k \sim 10^5$.

Another commonly used element in ellipsometric setups is a compensator or a retarder. It is usually placed between polarizer and analyzer, and is used to convert linear polarization to circular and vice versa.

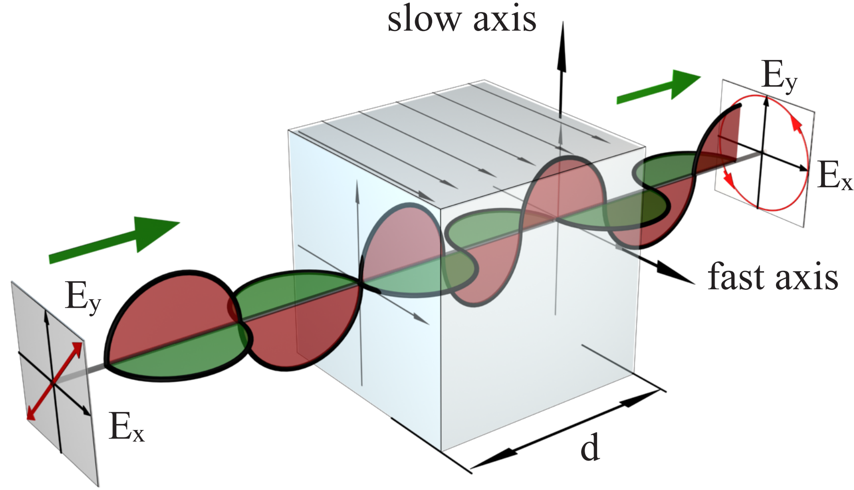

Figure 3.3.: Change in the state of polarization by a compensator (retarder), shown for a case when a 45° linear polarization is turned into ccw circular polarization, for this a specific thickness (d) is required.

Compensators also use optical anisotropy and are made out of one single birefringent crystal. Figure 3.3 shows a working principle of a compensator. At normal incidence, compensator generates a phase difference between ordinary and extraordinary rays. This phase difference is given as:

$$\delta = \frac{2\pi}{\lambda}|n_e - n_o|d\,, \tag{3.2}$$

where d is the thickness of the compensator. The main downside is that a phase difference δ depends on the wavelength λ directly and not only through refractive indices of the material. Compensators with $\delta = \pi/2$ are referred to as quarter-wave plates, since their phase difference corresponds to a wavelength of $\lambda/4$. Introducing a

phase difference between ordinary and extraordinary rays can create various circular and elliptic polarizations out of a linearly polarized light. Figure 3.3 shows a compensator that changes a +45° linear polarized parallel beam into a counterclockwise (ccw) circular polarized beam.

If the element is fixed, obviously control over a phase shift is not possible. In that case the element is referred to as a retarder. As an example a retarder can be pre-designed to act as a quarter-wave plate, for a specific wavelength of the incident light. But if we would like to have a quarter-wave plate for incident light in a desired spectral range, an element obviously has to be tunable. If the element has an external control of a phase shift it is referred to as a compensator. A simplest way to control a phase shift would be to rotate a retarder in a x-y plane. These elements are referred to as rotating compensators, and are commonly used in ellipsometric setups.

Compensators use uniaxial materials. However, calcite is not used for compensators since $|n_e - n_o|$ is quite large. This would require very thin compensators, and their d would become comparable with the wavelength λ, resulting with Fabry-Perot interferences within a compensator. Instead of calcite, MgF_2 is widely used, with an additional advantage of being transparent deep into the UV region.

3.1.2. Jones calculus

Jones calculus considers a set of matrix equations that is used to represent polarized light and optical elements that can change the state of light polarization. Polarized light is represented by a two component vector, referred to as Jones vector and linear optical elements are presented by 2×2 Jones matrices. These matrices are very useful to describe changes in the state of polarization of the light as it passes through many optical elements in a measurement setup. It gives a basis for understanding a particular ellipsometric setup. Jones calculus applies only to fully polarized light. If light is randomly polarized, partially polarized or incoherent, Muller calculus is used. Jones calculus is presented in this subsection, while the rest of this section uses Jones calculus to describe optical elements and ellipsometric setups used in the experimental section of the dissertation. Although, a more accurate description of

the ellipsometric setup can be written using Muller matrices, in the dissertation only Jones matrices are used, since they are sufficient to describe basic working principles of ellipsometric setups.

The polarization of light can be represented by superimposing two waves that oscillate parallel to two perpendicular planes (x-y). Jones vector uses this, and represents light as a two component column vector:

$$\vec{E}(\vec{z},t) = \begin{bmatrix} E_{x0}\, exp(\, i(\omega t - Kz + \delta_x)\,) \\ E_{y0}\, exp(\, i(\omega t - Kz + \delta_y)\,) \end{bmatrix} = exp(\, i(\omega t - Kz)\,) \begin{bmatrix} E_{x0}\, exp(\, i\delta_x\,) \\ E_{y0}\, exp(\, i\delta_y\,) \end{bmatrix} . \tag{3.3}$$

The first component represents an electric field oscillations parallel to x plane, while the second component represents an electric field oscillations perpendicular to x and parallel to y plane. E_{x0} and E_{x0} stand for the electric field amplitudes of x and y components, respectively. ω stands for the light wavelength, and K stands for the light wave vector. δ_x and δ_y present a phase difference of each component. The term $exp(\, i(\omega t - Kz)\,)$ can be omitted, since ellipsometric measurements consider only a relative changes in the light intensity. By doing so Eq. 3.3 gives a commonly used expression for Jones vector:

$$\vec{E}(\vec{z},t) = \begin{bmatrix} E_{x0}\, exp(\, i\delta_x\,) \\ E_{y0}\, exp(\, i\delta_y\,) \end{bmatrix} = \begin{bmatrix} E_x \\ E_y \end{bmatrix} . \tag{3.4}$$

Here x and y components of the electric field are given as:

$$E_x = E_{x0}\, exp(\, i\delta_x\,) = |E_x|\, exp(\, i\delta_x\,)\,, \tag{3.5}$$

$$E_y = E_{y0}\, exp(\, i\delta_y\,) = |E_y|\, exp(\, i\delta_y\,)\,. \tag{3.6}$$

It is usually more convenient to consider a phase difference, rather than each component phase separately. In that case, x and y components of the electric field vector can be written as:

$$E_x = E_{x0}\, exp(\, i(\delta_x - \delta_y)\,) = |E_x|\, exp(\, i(\delta_x - \delta_y)\,)\,, \tag{3.7}$$

$$E_y = E_{y0} = |E_y|\,. \tag{3.8}$$

It is worth mentioning that this phase difference $(\delta_x - \delta_y)$ is actually the phase difference Δ that is commonly presented as a measured value in ellipsometry (see Sec. 3.1).

The light intensity can be easily calculated from the Jones vector, as:

$$I = I_x + I_y = E_{x0}^2 + E_{y0}^2 = |E_x|^2 + |E_y|^2 = E_x E_x^* + E_y E_y^* \,. \tag{3.9}$$

Using normalized light intensity $I = 1$, various states of polarization can be written within Jones calculus as:

- a linear polarization in x direction ($\delta_x = \delta_y = 0$): $E_{lin,x} = \begin{bmatrix} 1 \\ 0 \end{bmatrix}$.
- a linear polarization in y direction ($\delta_x = \delta_y = 0$): $E_{lin,y} = \begin{bmatrix} 0 \\ 1 \end{bmatrix}$.
- a $+45°$ linear polarization ($\delta_x = \delta_y = 0$): $E_{+45°} = 2^{-1/2} \begin{bmatrix} 1 \\ 1 \end{bmatrix}$.
- a right (cw) circular polarization ($\delta_x = 0$, $\delta_y = \pi/2$): $E_R = 2^{-1/2} \begin{bmatrix} 1 \\ i \end{bmatrix}$.
- a left (ccw) circular polarization ($\delta_x = 0$, $\delta_y = -\pi/2$): $E_L = 2^{-1/2} \begin{bmatrix} 1 \\ -i \end{bmatrix}$.
- an elliptical polarization ($\delta_x = \pi/4$, $\delta_y = \pi/2$): $E_{elli} = 2^{-1/2} \begin{bmatrix} 2^{-1/2}(1+i) \\ -i \end{bmatrix}$.

As it was discussed in the previous subsection, polarizers and compensators usually rotate the light polarization by a certain angle relative to the x or y axis. Equations, or Jones matrices, that would describe the change in the state of polarization caused by these elements would be simplified if instead of rotating a polarization given by a Jones vector, one rotates a coordinate system from x-y to x'-y'. This is done by a matrix operation that is referred to as a coordinate system rotation.

Let us assume that we have a linear polarization defined by $P = (E_x, E_y)$ in a x-y coordinate system. If we want to rotate this polarization counterclockwise (ccw) by an angle α, this would correspond to a clockwise (cw) rotation of the x-y coordinate system, into a x'-y' coordinate system. This is shown in Fig. 3.4. The same polarization in a new coordinate system is described by $P' = (E'_x, E'_y)$, and is simply related to the previous coordinate system by relations:

$$E_{x'} = E_x \, cos(\alpha) + E_y \, sin(\alpha) \,, \tag{3.10}$$

$$E_{y'} = -E_x \, sin(\alpha) + E_y \, cos(\alpha) \,. \tag{3.11}$$

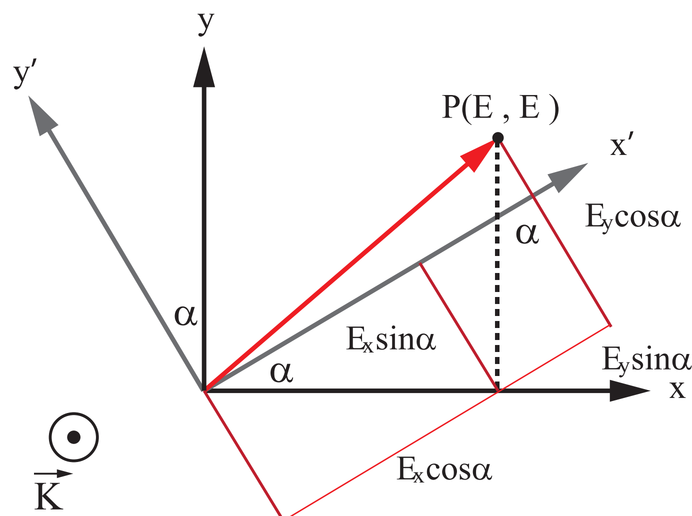

Figure 3.4.: Transformation of the x-y coordinates into x'-y' coordinates by clockwise rotation for an angle α. Note clockwise notation is considered with the respect to the light propagation, which would be from the plane of the paper, perpendicular to it, and upwards in this case.

Simply by rewriting given equations in a matrix forms, results with a Jones matrix for coordinate rotation:

$$\begin{bmatrix} E_{x'} \\ E_{y'} \end{bmatrix} = \begin{bmatrix} cos(\alpha) & sin(\alpha) \\ -sin(\alpha) & cos(\alpha) \end{bmatrix} \begin{bmatrix} E_x \\ E_y \end{bmatrix}. \tag{3.12}$$

Here a 2×2 matrix is commonly denoted as $R(\alpha)$ and it corresponds to a clockwise rotation of the x-y coordinate system by an angle α. Counterclockwise rotation is simply carried out by using negative angles. Furthermore, having two elements in as succession, eg. two retarders, could be simply written as: $R(\alpha) \cdot R(\beta) = R(\alpha + \beta)$.

3.1.3. Representation of optical elements and measurements by Jones matrices

Changing the state of polarization by polarizers, analyzers, compensators or retarders is just a specific case of coordinate rotation. Polarizers (P) and analyzers

(A) can be represented by Jones matrix as:

$$P = A = \begin{bmatrix} 1 & 0 \\ 0 & 0 \end{bmatrix}, \tag{3.13}$$

when the polarization axis of the polarizer is parallel to the x-axis of the external coordinate system that also applies to the Jones vector of the incident light.

Similarly, compensators (C) and retarders (R) are represented by Jones matrices as:

$$C = R = \begin{bmatrix} 1 & 0 \\ 0 & exp(-i\delta) \end{bmatrix}. \tag{3.14}$$

Here, the x-axis of a coordinate system is parallel to the fast axis of a compensator. δ represents a phase difference between ordinary and extraordinary rays and is given by Eq. 3.2.

To better illustrate how Jones matrices can describe each optical element, and an entire optical system, let us focus on a very simple setup shown in Fig. 3.5. This setup consists of a light source, two polarizers and a light detector. Light source gives unpolarized incident light. The angle of the first polarizer (α) can be changed with the respect to the x-axis that is fixed to an optical axis of the analyzer (second polarizer). The light intensity at the detector is considered as a function of a polarizer angle α.

Jones calculus becomes very useful for describing the state of polarization in this and more complicated optical setups. If the optical elements are positioned in a way that light propagates from right to left, equations are then written from left to right, and each element is replaced by an appropriate matrix. For the case of an optical setup shown in Fig. 3.5, the following Jones matrix equation can be written:

$$\begin{bmatrix} E_x \\ E_y \end{bmatrix} = \begin{bmatrix} 1 & 0 \\ 0 & 0 \end{bmatrix} \begin{bmatrix} cos(\alpha) & -sin(\alpha) \\ sin(\alpha) & cos(\alpha) \end{bmatrix} \begin{bmatrix} 1 & 0 \\ 0 & 0 \end{bmatrix} \begin{bmatrix} E_p \\ 0 \end{bmatrix} = \begin{bmatrix} E_p\, cos(\alpha) \\ 0 \end{bmatrix}. \tag{3.15}$$

Here, incident unpolarized light can not be represented by a Jones matrix, however it is considered that any linearly polarized component of the incident light will have the same light intensity (E_p). Polarizer is then set under an angle α and the x'-y' coordinate system is aligned with the polarizer (x'-axis with the polarizer axis). However, x'-axis is not parallel with the analyzer's axis (unless $\alpha = 0$) and an

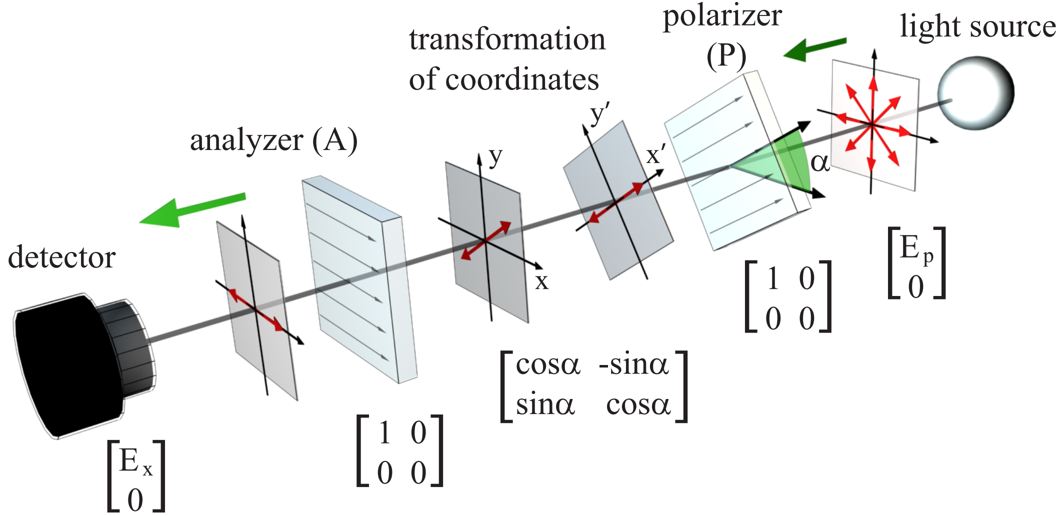

Figure 3.5.: Schematic representation of a simple optical setup by Jones matrices. This optical setup is composed of light source/polarizer/analyzer/light detector.

appropriate coordinate rotation is required between polarizer and analyzer. For the case shown in Fig. 3.5, polarizer is rotated clockwise with the respect to the analyzer's axis, this gives a counterclockwise coordinate rotation.

Finally, light intensity at the detector can be calculated using Eq.-s 3.9 and 3.15, as:

$$I = |E_x|^2 = |E_p|^2 \cdot cos^2\alpha \,. \tag{3.16}$$

Equation 3.16 is also known as Malus's law.

Optical setup presented in Fig. 3.15 is very similar to a simple ellipsometry setup, but without a sample. In ellipsometry measurements the Jones matrix that corresponds to light reflection by the optically isotropic sample is given by:

$$S = \begin{bmatrix} r_p & 0 \\ 0 & r_s \end{bmatrix} . \tag{3.17}$$

The other way to express S would be the following:

$$S = r_s \begin{bmatrix} r_p/r_s & 0 \\ 0 & 1 \end{bmatrix} = r_s \begin{bmatrix} \tan\psi \, exp(i\Delta) & 0 \\ 0 & 1 \end{bmatrix} . \tag{3.18}$$

Here, Eq. 3.1 has been used to relate complex amplitude reflection coefficients for the electric field vector parallel ($r_p = E_{rp}/E_{ip}$) and perpendicular ($r_s = E_{rs}/E_{is}$) to

the plain of incidence with amplitude ratio (ψ) and phase difference (Δ) between p- and s-polarizations. Furthermore, it is possible to neglect r_s in front of the matrix in Eq. 3.18, since only relative changes are taken into account in ellipsometric measurements. This gives another very common way of representing Jones matrix of the sample in ellipsometry:

$$S = \begin{bmatrix} \tan\psi \, exp(i\Delta) & 0 \\ 0 & 1 \end{bmatrix}. \tag{3.19}$$

As an example (shown in Fig. 3.1) if a linearly polarized light oriented at 45° is reflected by the sample, the light reflection can be represented as:

$$\begin{bmatrix} E_{rp} \\ E_{rs} \end{bmatrix} = \begin{bmatrix} r_p & 0 \\ 0 & r_s \end{bmatrix} \begin{bmatrix} E_{ip} \\ E_{is} \end{bmatrix} = \begin{bmatrix} r_p \\ r_s \end{bmatrix} \sim \begin{bmatrix} \tan\psi \, exp(i\Delta) \\ 1 \end{bmatrix}. \tag{3.20}$$

Here, $E_{ip} = E_{is} = 1$ has been used, since the incident light has a +45° linear polarization. It is worth mentioning that a Jones matrix for a sample does not depend on an angle of incidence (θ) that is used in a particular ellipsometric measurement. However, this angle does figurate in the optical model that is used to interpret the measurements, which will be the the topic of the next section (Sec. 3.2).

If the sample is optically anisotropic (birefringence, dichromism), a following Jones matrix should be used:

$$S_{ani} = \begin{bmatrix} r_{pp} & r_{ps} \\ r_{sp} & r_{ss} \end{bmatrix}. \tag{3.21}$$

The fact that off-diagonal elements are non-zero generally complicates characterization of anisotropic samples.

The following subsections will focus on two ellipsometric setups that have been used in the experiments that are related to the dissertation (see chapter 4). First a null ellipsometric setup will be presented (Sec. 3.1.4). This setup is the basis for spectroscopic null imaging ellipsometry (SNIE). Afterwards, a spectroscopic ellipsometry setup with a rotating polarizer (RPSE) will be presented (Sec. 3.1.5).

3.1.4. Spectroscopic null imaging ellipsometry

As it was discussed in Sec. 3.1, if a linearly polarized light is illuminated onto a sample, the reflected light will be generally elliptically polarized, since the interaction with a sample can change both the amplitude ratio (ψ) and phase difference (Δ) between p- and s-polarizations. The same mechanism would work in an opposite direction, meaning that if a particular elliptic state of the polarization, defined by (ψ, Δ), is used to irradiate a sample, reflected light will be linearly polarized. This principle is used in null ellipsometry. It is referred to as "null", since the condition of the linear reflected state of the polarization is confirmed by an analyzer that blocks all the light, and gives a "null" light intensity at the detector. Null ellipsometers were the first ones ever constructed, and are still the most accurate type of ellipsometers, since null ellipsometry is free from various detector errors. Main downside are long measurements, which makes null ellipsometry hard to integrate as an in-line control tool.

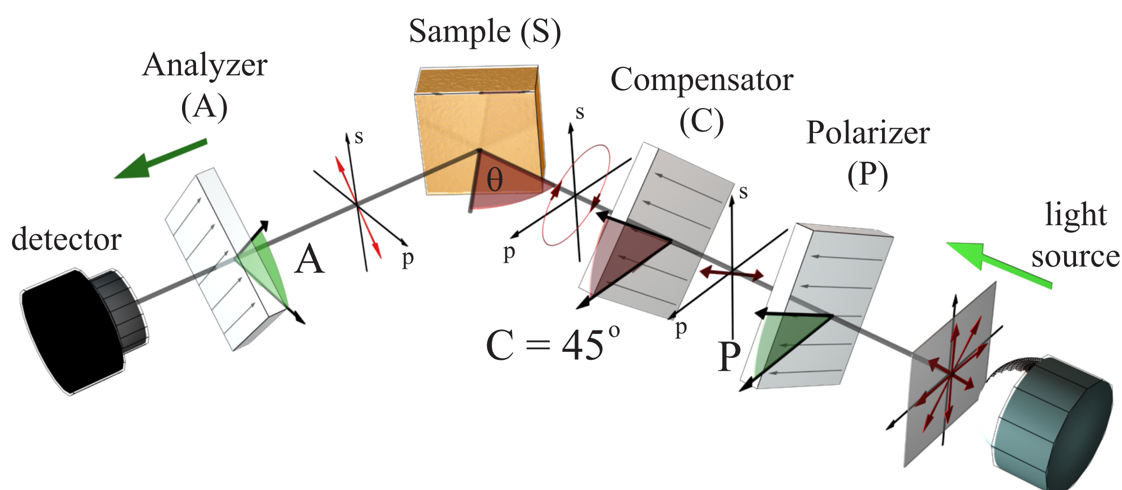

Figure 3.6.: Schematic representation of a setup used for null ellipsometry. The setup consists of light source, polarizer (P), compensator (C), sample (S), analyzer (A) and detector, and it is called a PCSA setup. SNIE uses additionally a monochromator positioned after a light source, focusing optics between S and A, and as a detector CCD chip is used.

A schematic representation of a simple null ellipsometer is shown in Fig. 3.6. It consists of an unpolarized (monochromatic) light source, polarizer (P), compensator

(C), sample (S), analyzer (A) and finally a light detector. This setup is referred to as a PCSA, due to the order of its elements. The goal is to vary the incident state of polarization by rotating either P or C, and for each initial state of polarization to examine if the reflected component is linearly polarized. If the reflected component has a linear polarization by rotating A it is possible to obtain zero light intensity on the detector.

There are three variables in the optical system, angles of P, C and A, and one condition that the light intensity after an analyzer has to be zero. Using Jones matrices, the PCSA setup can be described as:

$$D = A\,S\,C\,P\,I\,. \tag{3.22}$$

Here, D and I stand for Jones vectors of the electric field in front of the detector and after the light source, respectively. In order to use simple Jones matrices for the optical elements, several coordinate system rotations are required, and Eq. 3.22 becomes:

$$D = A\,R(A)\,S\,R(-C)\,C\,R(-C-P)\,P\,I\,. \tag{3.23}$$

Note that all angles of the elements are defined as clockwise with the respect to the light propagation, and zero value is considered to be on the plane of incidence, upwards from the sample plane. This requires counterclockwise coordinate rotations for the incident, and clockwise coordinate rotations for the reflected beam (see Fig. 3.6). Now, by writing each of the Jones matrices, Eq. 3.23 gives:

$$\begin{bmatrix} E_x \\ E_y \end{bmatrix} = \begin{bmatrix} 1 & 0 \\ 0 & 0 \end{bmatrix} \begin{bmatrix} cos(A) & sin(A) \\ -sin(A) & cos(A) \end{bmatrix} \begin{bmatrix} r_p & 0 \\ 0 & r_s \end{bmatrix} \begin{bmatrix} cos(C) & -sin(C) \\ sin(C) & cos(C) \end{bmatrix} \times$$
$$\times \begin{bmatrix} 1 & 0 \\ 0 & e^{-i\delta} \end{bmatrix} \begin{bmatrix} cos(C+P) & -sin(C+P) \\ sin(C+P) & cos(C+P) \end{bmatrix} \begin{bmatrix} 1 & 0 \\ 0 & 0 \end{bmatrix} \begin{bmatrix} 1 \\ 0 \end{bmatrix} \tag{3.24}$$

Solving this matrix equation gives:

$$E_x = r_p\,cosA\Big(cosC\,cos(P-C)\;-\;e^{-i\delta}sinC\,sin(P-C)\Big)\;+$$
$$+\,r_s\,sinA\Big(sinC\,cos(P-C)\;-\;e^{-i\delta}cosC\,sin(P-C)\Big)\,. \tag{3.25}$$

Let us now consider the null condition $E_x = 0$. Since rotation of polarizer and compensator makes similar effect on manipulation of the incident state of polarization, one can be fixed. Let us consider the case with fixed compensator. In order to

satisfy the null condition, $cosC = sinC$ must also be satisfied. This gives $C = \pm 45°$, and consequently $\delta = \pm 90°$. There will be four solutions of Eq. 3.25, depending on the choice of C. Let us return $E_x = 0$, $C = +45°$ and $\delta = +90°$ into Eq. 3.25, this gives a following solution:

$$\frac{r_p}{r_s} = tanA\, exp\Big(i(- 2P + 90°)\Big) \,. \tag{3.26}$$

Now by considering Eq. 3.1, ellipsometric angles (ψ, Δ) are easily obtained as:

$$\psi = A \,, \tag{3.27}$$

$$\Delta = -2P + 90° \,. \tag{3.28}$$

By varying the choice of C and δ there will be a total of four solutions for (ψ, Δ) where the null condition is satisfied. Usually in null ellipsometry all four solutions are found and any nonlinearities that exist in the optical setup are significantly reduced by taking the averaged values of (ψ, Δ) from all four solutions. This process is referred to as four zone averaging, and it is the most precise method for measuring the change in the state of the polarization that is introduced by the sample [153]. One of the main advantages of null ellipsometry becomes apparent from Eq.-s 3.27 and 3.28. Namely, measuring (ψ, Δ) is the equivalent to measuring angles of P and A, which can be done with great precision, usually below 0.001°.

Null ellipsometry is the basis for spectroscopic null imaging ellipsometry (SNIE), which has been employed to measure and map optical properties of graphene. This is discussed in the next chapter, as well as within Ref. [83]. Let us now focus on SNIE and point out particular differences between a null ellipsometry and SNIE.

Compared with a null ellipsometry setup shown in Fig. 3.6, SNIE has several additions. First and most important difference is that SNIE uses a CCD detector instead of a standard single pixel or photomultiplier detector, that would be commonly used in a non-imaging setup. There is one major consequence that comes from the usage of a CCD detector. In order to preserve a sample image, monochromatic light cannot be extracted after the analyzer, but rather a monochromatic light source has to be used. This can be achieved for a single wavelength by using a laser, or in a spectral range by using tunable lasers, or series of band-pass filters after a white light source.

In order to measure optical properties of microscopic samples SNIE can be equipped with a focusing lens. This lens is commonly placed after the sample (S) and in front

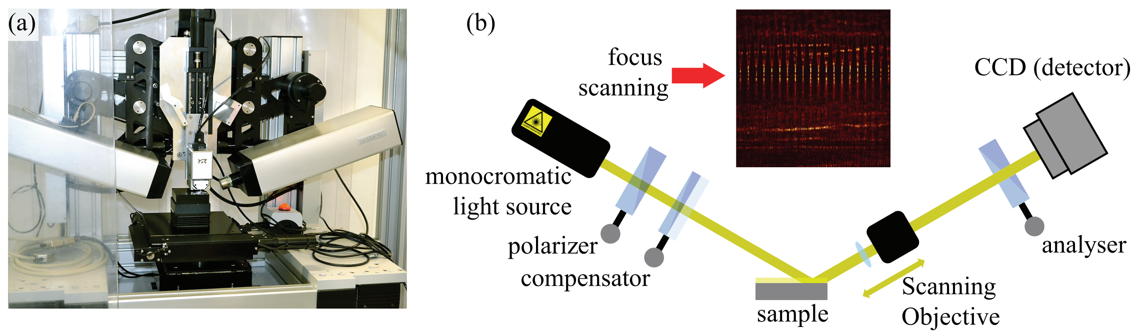

Figure 3.7.: (a) Accurion nanofilm_ep3 spectroscopic null imaging ellipsometer. (b) Schematic representation of a SNIE setup with scanning focus objective (reprinted from [238]). Inset of (b) shows an image of a grating viewed by the ellipsometer's CCD detector. An arrow indicates a zone that is in focus for a particular objective position.

of an analyzer (A). If higher magnification lenses are used, it is possible to carry out ellipsometric measurements on samples that have surface area of only several square micrometers, i.e. near the diffraction limit. The next chapter (Sec. 4.2) presents SNIE mapping of graphene's optical properties and layer thickness with lateral resolution of one micrometer, for this purpose a null ellipsometer "nanofilm_ep3se" by Accurion GmbH has been used. A photograph of an instrument is shown in Fig. 3.7(a), and a scheme of the optical components is shown in Fig. 3.7(b).

However, there are several technical challenges that need to be overcome when a focusing lens is added in an imaging ellipsometry setup. The most obvious one would be focusing the sample surface at an oblique incidence. In order to have better measurement sensitivity, ellipsometric measurements need to be carried out at an incident angle close to the Brewster angle of the sample. When a focusing optics is added, only one line of the sample (that is perpendicular to the plane of incidence) will be in focus (see inset of Fig. 3.7(b)). In order to have an entire view field of the CCD detector in focus, the lens needs to extend and retract in the direction parallel to the optical path. The whole image is then made out of several regions on the CCD detector that were in focus for a given position of the focusing lens. In a sense, the image of the sample is obtained through a row by row scanning. When ellipsometry measurements are carried out, a "nulling" process is done for each row of the CCD while that particular row is in focus, and the results are averaged between all the rows scanned.

Another, less obvious problem of the focusing optics, is depolarization introduced by the lens. If any change in the state of polarization is introduced by the lens, unless calibrated, it will be added to the polarization change of the sample, thus resulting with false measurements. A great technological challenge is to produce a lens that does not introduce any change in the state of the polarization. These lenses are referred to as ”stress free” since the materials that are used for their fabrication (as quartz) become uniaxial if are exposed to uniaxial strain, and the lens then behaves as a retarder.

There is one more issue, that should be pointed out, and which comes from the usage of a lens in an imaging ellipsometry and brewster angle microscopy setups. This issue is more subjective, since microscopic samples are usually viewed by an upright microscope, and when viewed under an oblique incidence the image will appear as elongated in one direction. There is a simple way to compensate for this, the plane of the CCD detector simply need to be tilted by an incident angle, only in an opposite direction. There are other more elaborate methods that use several focusing and condensing lenses, and can achieve better results than a simple tilting of the CCD detector.

There are many advantages of SNIE. The main would be that it is possible to directly determine a region of interest (ROI) by examining a Brewster angle microscopy image made by the CCD of an ellipsometer. This can help when a microscopic samples are measured, or to avoid any dirt, imperfections or other regions on the sample that would lead to an improper data interpretation. Furthermore, it is possible to measure several regions at the same time, thus having paired sample and substrate measurements (for more details see Sec. 3.3). Finally, SNIE can be used to create an ellipsometric map of the sample, this is carried out by finding a null condition for each pixel of the CCD detector independently, thus making ψ and Δ maps of the sample.

3.1.5. Rotating polarizer spectroscopic ellipsometry

The other spectroscopic ellipsometry setup used in the experimental part of the dissertation (chapter 4) and within publications that are related to the dissertation

[82, 91, 92] is a rotating polarizer spectroscopic ellipsometry (RPSE). The setup consists of an unpolarized light source, polarizer (P) that rotates with a constant angular frequency ω, sample (S), analyzer (A) and finally a detector. The setup is also referred to as P_RSA, due to the order and function of its elements. A schematic representation of a P_RSA setup is shown in Fig. 3.8(a), while Fig. 3.8(b) shows an image of a SOPRA GES5E-IRSE spectroscopic ellipsometer used in the dissertation. This method is not free from detector errors, since a relative light intensity is still considered when ellipsometric angles are evaluated. This will be explained later in the text. However, the upsides are extremely fast measurements, possibility of using gratings for the extraction of monochromatic light (excellent spectral resolution), and using high sensitivity detectors as photomultipliers.

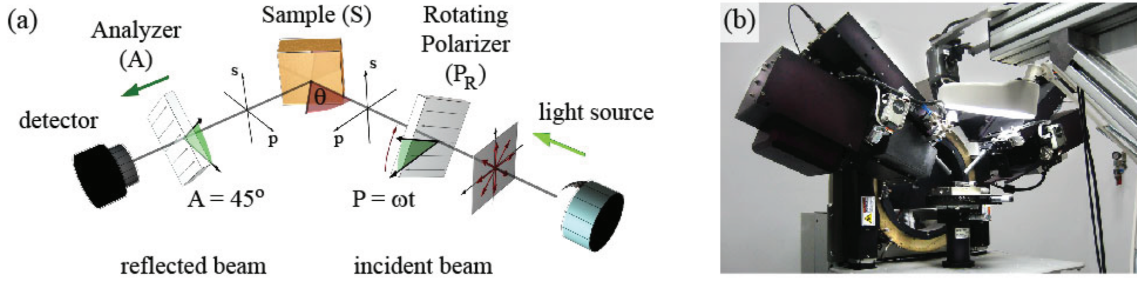

Figure 3.8.: (a) Rotating polarizer (or P_RSA) setup. (b) SOPRA GES5E-IRSE spectroscopic ellipsometer.

The Jones equation for P_RSA setup can be written as:

$$D = A\,S\,P_R\,I\,. \tag{3.29}$$

Here D and I stand for Jones vectors in front of the detector and after the light source, respectively. Similarly as in Sec. 3.1.4, appropriate coordinate rotations are added to the equation in order to keep the matrices of the optical elements simple:

$$D = A\,R(A)\,S\,R(-P)\,P\,I\,. \tag{3.30}$$

By substituting each Jones matrix in Eq. 3.30, gives:

$$\begin{bmatrix} E_x \\ E_y \end{bmatrix} = \begin{bmatrix} 1 & 0 \\ 0 & 0 \end{bmatrix} \begin{bmatrix} cos(A) & sin(A) \\ -sin(A) & cos(A) \end{bmatrix} \begin{bmatrix} sin\psi\, e^{i\Delta} & 0 \\ 0 & cos\psi \end{bmatrix} \times$$
$$\times \begin{bmatrix} cos(P) & -sin(P) \\ sin(P) & cos(P) \end{bmatrix} \begin{bmatrix} 1 & 0 \\ 0 & 0 \end{bmatrix} \begin{bmatrix} 1 \\ 0 \end{bmatrix}. \tag{3.31}$$

In a rotated polarizer setup, analyzer is kept fixed. Although it can be fixed under any angle, commonly it is fixed at $+45°$, which simplifies the matrix equation. Furthermore, constant term ($\sqrt{2}/2$) that comes from the analyzer matrix can be omitted, and Eq. 3.31 becomes:

$$\begin{bmatrix} E_x \\ E_y \end{bmatrix} = \begin{bmatrix} 1 & 0 \\ 0 & 0 \end{bmatrix} \begin{bmatrix} 1 & 1 \\ -1 & 1 \end{bmatrix} \begin{bmatrix} sin\psi\, e^{i\Delta} & 0 \\ 0 & cos\psi \end{bmatrix} \times$$
$$\times \begin{bmatrix} cos(P) & -sin(P) \\ sin(P) & cos(P) \end{bmatrix} \begin{bmatrix} 1 & 0 \\ 0 & 0 \end{bmatrix} \begin{bmatrix} 1 \\ 0 \end{bmatrix} . \tag{3.32}$$

Solving Eq. 3.32 results with:

$$E_x = cosP\, sin\psi\, e^{i\Delta} + sinP\, cos\psi \,, \tag{3.33}$$

or rewritten with real and imaginary part separated:

$$E_x = \Big(cosP\, sin\psi\, cos\Delta + sinP\, cos\psi\Big) + i\Big(cosP\, sin\psi\, sin\Delta\Big) . \tag{3.34}$$

Now, the ntensity at the detector can be evaluated as:

$$I = E_x E_x^* . \tag{3.35}$$

Replacing Eq. 3.34 into Eq. 3.35, gives the solution for the light intensity at the detector in a P$_R$SA setup, when $A = +45°$:

$$I = \frac{1}{2}\Big(1 - cos(2\psi)\, cos(2P) + sin(2\psi)\, cos(\Delta)\, sin(2P)\Big) . \tag{3.36}$$

Besides, ψ and Δ which are the measured values, Eq. 3.36 also depends on the doubled angle of the polarizer (2P). Let us separate measured values from an angle of the polarizer as:

$$I = \frac{1}{2}\Big(1 + \alpha\, cos(2P) + \beta\, sin(2P)\Big) . \tag{3.37}$$

Here, values of α and β can be seen as measured values since they are related to ψ and δ by following relations:

$$\alpha = -cos(2\psi) \,, \tag{3.38}$$

$$\beta = sin(2\psi)\, cos(\Delta) . \tag{3.39}$$

Using Eq.-s 3.38 and 3.39, ψ and δ can be obtained as:

$$tan\psi = \sqrt{\frac{1+\alpha}{1-\alpha}} \,, \tag{3.40}$$

$$cos\Delta = \frac{\beta}{\sqrt{1-\alpha^2}}\,. \tag{3.41}$$

This shows that finding α and β is equivalent of finding ψ and Δ. Now, let us focus back on Eq. 3.37, and let us consider the fact that in RPSE, polarizer rotates at a constant angular frequency ω usually in the range of several rotations per second. Time dependent value for the angle of the polarizer is than given as: $P = \omega t$, and time dependent detector intensity can be written as:

$$I(t) = \frac{1}{2}\Big(1 + \alpha\, cos(2\omega t) + \beta\, sin(2\omega t)\Big)\,. \tag{3.42}$$

α and β are found as the Fourier coefficients of $cos(2\omega t)$ and $sin(2\omega t)$ [153]. It is obvious that measured values do depend on the detector intensity. However, they are estimated from a Fourier transform of the detector signal, and this both averages the value and eliminates any signal that is not at $2\omega t$ frequency. All of these still give excellent sensitivity, and also minimize many of the detector imperfections, however RPSE is still not as accurate as null ellipsometry, and it does require calibration of the detector.

In the next chapter RPSE is used to investigate optical properties of CVD graphene, and to demonstrates how it can be used as a post-fabrication quality control tool for fast and non-destructive probing of graphene transfer process and quality of a contact between graphene and external metallic pads. Prior to that, the remaining of this chapter will explain how are the results of the ellipsometric measurements (ψ, Δ) used to reconstruct the optical properties of the sample (Sec. 3.2); as well as how ellipsometric measurements can be used to retrieve optical properties of atomically thin films (Sec. 3.4).

3.2. Data analysis and Fresnel equations

As it was show in the previous section, ellipsometric measurements give as a result the change in the state of light polarization that was introduced by the interaction of the light with the sample. This change is express through the amplitude ratio ψ and phase difference Δ between p- and s-polarizations. However, these are not the values of an interest, but they can be related to optical constants and layer thicknesses of the measured sample through the process of data analysis. The analysis consists of two parts: building an optical model and fitting the values of the interest to the measured (ψ, Δ) spectra.

The next section will discuss in great detail the fitting procedures, especially focusing on the proper fitting procedure when atomically thin samples are measured. This section focuses on a mathematical background behind an optical model and will describe how optical models are constructed and how are ellipsometric measurements simulated using these optical models. A numerical codes based on the equations presented in this section is given in appendix C.2, and it was employed for the interpretation of ellipsometric measurements in the dissertation (chapter 4).

In order to interpret ellipsometric measurement optical models are required. These models are based on Fresnel equations. Each material, usually a layer, in an optical model is represented by its thickness and its complex refractive index. Building a proper optical model is very important for interpretation of ellipsometric measurements. Usually improper optical models can introduce large uncertainty to the interpreted data, much larger than the instrumental errors. To help build an optical model many parameters of the model can be obtained from correlated measurements of the sample. This is the topic of Sec. 3.3, and several different techniques that are suitable for corroborated measurements of graphene are described in Sec. 2.2.

In order to demonstrate how an optical model is built, let us focus on a simplest case possible, a semi-infinite perfectly flat sample, or a bulk sample. The optical model used in this case is referred to as a two-phase model. This is the only case when an analytical solution for the refractive index is possible. In the case of more elaborated models optical properties can be evaluated numerically in a process that is based on a self-consisted method. Figure 3.9 shows the electric field $(\vec{E})$ and magnetic induction $(\vec{B})$ vectors of p- and s-polarization for an oblique incidence (under an angle θ_i). The ambient from which the beam is irradiated and to which it is reflected is defined by a complex refractive index N_0. In the case of a vacuum

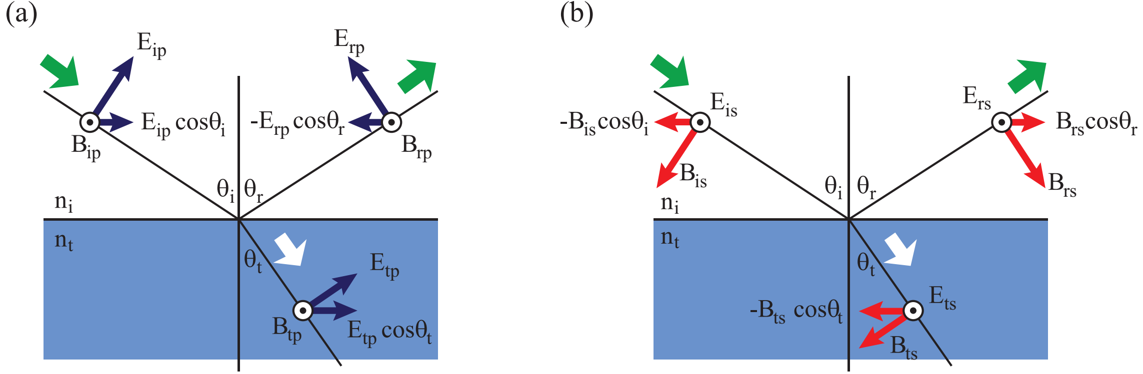

Figure 3.9.: (a) and (b) respectively show electric field ($\vec{E}$) and magnetic induction ($\vec{B}$) vectors of p- and s-polarization of an oblique incidence light beam, at an interface between two semi-infinite materials that are defined by their complex refractive indices N_0 and N_1.

or ambient air in the visible part of the spectrum $N_0 = 1 - i0$. The notation used here for the complex refractive indices is $N = n - i\,k$, where $k > 0$. Bulk material is also described by its complex refractive index N_1. The angle of incidence is θ_i. Respectively, angles of the reflected and transmitted beams are θ_r and θ_t. Using Snell's law gives: $\theta_i = \theta_r$ for the reflected component, and:

$$N_0\, sin\theta_i = N_1\, sin\theta_t\,, \tag{3.43}$$

for the transmitted component. As it will be shown later on, $cos\theta_t$ would be of a greater interest. Using several trigonometric transformations Eq. 3.43 gives:

$$cos\theta_t = \frac{1}{N_1}\,(N_1^2 - N_0^2\, sin^2\theta_i)^{1/2}\,. \tag{3.44}$$

These relations between the incident, reflected and transmitted angles will be used later on, especially when more elaborate optical models are considered.

Let us focus first on the boundary conditions for the case of p-polarization, the electric field and magnetic induction vectors and their components of interest for this case are shown in Fig. 3.9(a), and the boundary conditions are:

$$E_{ip}\, cos(\theta_i) - E_{rp}\, cos(\theta_r) = E_{tp}\, cos(\theta_t)\,, \tag{3.45}$$

$$B_{ip} + B_{rp} = B_{tp}\,. \tag{3.46}$$

Using $E = c/N \cdot B$, magnetic induction components can be eliminated from Eq. 3.46, giving:

$$N_0(E_{ip} + E_{rp}) = N_1\, E_{tp}\,. \tag{3.47}$$

Now, the complex amplitude reflection and transmission coefficients for the electric field vector parallel to the plain of incidence can be obtained from Eq.-s 3.45 and 3.47, using also $\theta_i = \theta_r$:

$$r_p \equiv \frac{E_{rp}}{E_{ip}} = \frac{N_1\, cos\theta_i - N_0\, cos\theta_t}{N_1\, cos\theta_i + N_0\, cos\theta_t}\,. \tag{3.48}$$

$$t_p \equiv \frac{E_{tp}}{E_{ip}} = \frac{2\, N_1\, cos\theta_i}{N_1\, cos\theta_i + N_0\, cos\theta_t}\,. \tag{3.49}$$

On the other hand, boundary conditions for the s-polarization (see Fig. 3.9(b)) are:

$$E_{is} + E_{rs} = E_{ts}\,. \tag{3.50}$$

$$-B_{is}\, cos(\theta_i) + B_{rs}\, cos(\theta_r) = -B_{ts}\, cos(\theta_t)\,, \tag{3.51}$$

Using the same procedure as for the p-polarization gives the complex amplitude reflection and transmission coefficients for the electric field vector perpendicular to the plain of incidence:

$$r_s \equiv \frac{E_{rs}}{E_{is}} = \frac{N_0\, cos\theta_i - N_1\, cos\theta_t}{N_0\, cos\theta_i + N_1\, cos\theta_t}\,, \tag{3.52}$$

$$t_s \equiv \frac{E_{ts}}{E_{is}} = \frac{2\, N_0\, cos\theta_i}{N_0\, cos\theta_i + N_1\, cos\theta_t}\,. \tag{3.53}$$

The above equations 3.48, 3.49, 3.52 and 3.53 are known as Fresnel equations, while r_p, r_s, t_p and t_s are known as Fresnel coefficients.

In the case of a bulk material, Fresnel equations are easily related to the values measured by ellipsometry. Simply by substitution of Eq.-s 3.48 and 3.52 into Eq. 3.1, gives:

$$\rho = \frac{r_p}{r_s} = \frac{(N_1\, cos\theta_i - N_0\, cos\theta_t)/(N_1\, cos\theta_i + N_0\, cos\theta_t)}{(N_0\, cos\theta_i - N_1\, cos\theta_t)/(N_0\, cos\theta_i + N_1\, cos\theta_t)} = tan(\psi)\, e^{i\Delta}\,. \tag{3.54}$$

In the case of a bulk material, when the ambient is air or vacuum ($N_0 = 1$), Eq. 3.54 can be used to express the complex refractive index of the material as a function of ρ and the incident angle θ_i, as:

$$N_1 = sin\theta_i \sqrt{1 + tan^2\theta_i \left(\frac{1-\rho}{1+\rho}\right)^2}\,. \tag{3.55}$$

Regardless of the incident angle, obtained refractive index of the material must be the same. It is a good practice to carry out ellipsometric measurements of the

same sample under several different angles of incidence, if possible both above and below the Brewster angle, and to consider an averaged value of all the measured refractive indices.

Besides measuring optical properties of bulk materials, ellipsometry is more commonly used to measure thicknesses and optical properties of thin films. These films are commonly supported by bulk substrates and their thickness ranges between several nanometers to several micrometers. When light waves generated at different positions overlap, optical interference occurs by the superposition of the light waves. This is also the case when a thin film covers a bulk substrate. An optical model that describes a thin film on a substrate is shown in Fig. 3.10(a), while a model with more than one layer is shown in Fig. 3.10(b). As it was stated, each layer within an optical model is represented by its thickness (d_i) and its complex refractive index (N_i). Light beam reflected initially of the first surface (primary beam) interferes with the light beam reflected at the second surface (secondary beam) and optical interference occurs. Whether a constructive or a destructive interference will occur depends on the difference in the optical path of the primary and secondary beams.

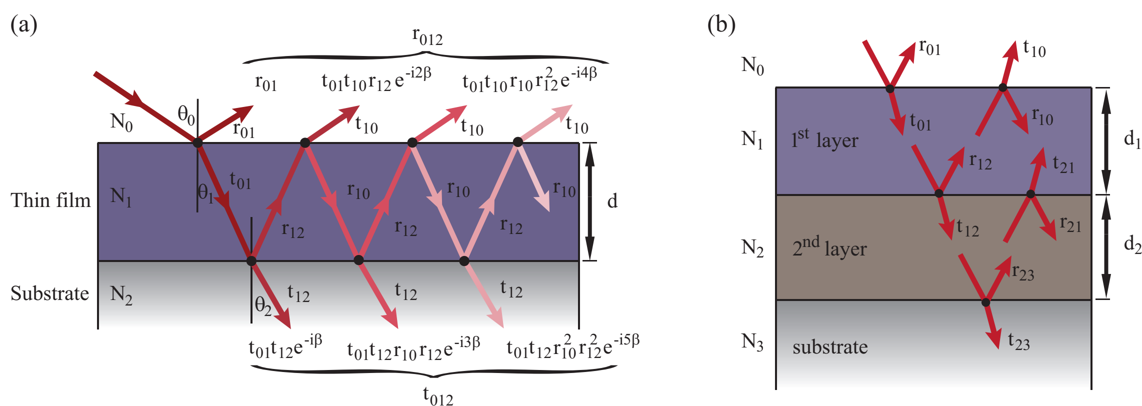

Figure 3.10.: (a) Fresnel coefficients of the ambient/thin film/substrate structure, showing primary and secondary beams. (b) Fresnel coefficients for a structure with two different thin films on a semi-infinite substrate. Each film is defined within an optical model with its complex refractive index (N_i) and its thickness (d_i).

In the case shown in Fig. 3.10(a), a primary beam is simply defined by the Fresnel coefficient r_{01}, while the secondary beam can be evaluated as $t_{01}t_{10}r_{12}e^{-i2\beta}$. Here $e^{-i2\beta}$ corresponds to the phase difference that is accumulated on as single

propagation of the beam through the thin film, and $\beta = (2\pi d_1/\lambda)N_1 \, cos\theta_1$. Note that the imaginary part of N_1 will account for the light absorption during the propagation. The index numbers of Fresnel coefficients and their order indicate the direction of the propagation, meaning that t_{01} indicates that a light is propagating from the layer 0 into layer 1, while t_{10} indicates that the light is propagating from the layer 1 into layer 0. Same holds for reflection coefficients. By following the light beam propagation and adding (multiplying) appropriate Fresnel coefficients at each interface the ratio between complex amplitude reflection (or transmission) coefficients for the case with multiple reflections/transmitions can be obtained.

Let us focus on the case with a thin film on a bulk substrate that is shown in Fig. 3.10(a). The amplitude reflection coefficient in this case is expressed from the sum of all the reflected waves:

$$r_{012} = r_{01} + t_{01}t_{10}r_{10}r_{12}e^{-i2\beta} + t_{01}t_{10}r_{10}r_{12}^2e^{-i4\beta} + t_{01}t_{10}r_{10}^2r_{12}^4e^{-i6\beta} + ... \tag{3.56}$$

The sum has a form of an infinite series: $y = a + ax + ax^2 + ax^3 + ...$ and is reduced to $y = a/(1-x)$. Considering this Eq. 3.56 becomes:

$$r_{012} = r_{01} + \frac{t_{01}t_{10}r_{12}e^{-i2\beta}}{1 + r_{10}r_{12}e^{-i2\beta}}\,. \tag{3.57}$$

Eq. 3.57 can be further simplified by using identities: $r_{01} = -r_{10}$ and $t_{01}t_{10} = 1 - r_{01}^2$, resulting with:

$$r_{012} = \frac{r_{01} + r_{12}e^{-i2\beta}}{1 + r_{10}r_{12}e^{-i2\beta}}\,. \tag{3.58}$$

Eq. 3.58 holds for both p- and s-polarizations, however adequate Fresnel coefficients need to be used (as given by Eq.-s 3.48, 3.49, 3.52 and 3.53). In a sense Eq. 3.58 represents an effective amplitude reflection coefficient for the case of a thin film over a bulk substrate. However in this case it is not possible to analytically express neither N_1 nor N_2 as a function of ρ and θ_0, as it was the case with a bulk material (Eq. 3.55). Here, to obtain a refractive index of a layer, or the thickness of the thin film, a fitting procedure needs to be carried out. It is based on a self-consistent solution of $|\rho_{exp} - \rho_{fit}| = 0$ function, or any other more appropriate minimization function. This will be described in the next section.

For now, let us consider an even more elaborate optical model. Let us add one more thin film of a different material on top of a previously discussed a thin film/-substrate structure. This is shown in Fig. 3.10(b), along with Fresnel coefficients

required to calculate the total amplitude reflection or transmission coefficients. Considering a series of reflections from three interfaces will result with quite a cumbersome sum. Instead it is much easier to first consider the substrate and the second layer as one effective layer, using Eq. 3.58. This simplifies the model back to a single thin film on a bulk substrate. This procedure can be repeated regardless of the number of layers within an optical model. However, large number of layers can introduce large number of variables in the minimization process. This could lead to the existence of several different minima, or several possible solutions that do satisfy the minimization condition. Correlated measurements can help to exclude some of the solutions obtained within the minimization process by giving an expected range for some of the parameters of the optical model. As an example, AFM can be used to determine the thickness of a thin film, and if there are several minima within the optical model that correspond to several different thicknesses of that film, only those that are within the limit of the AFM measured values should be used. Also if there are no minima within the expected range this can indicate an improper optical model.

3.3. Correlation measurements

This section discusses how different measurement techniques can aid ellipsometry and provide more accurate interpretation of the ellipsometric measurements. We will focus mainly on two characterization techniques AFM and Raman spectroscopy, that have been described in the previous chapter (Sec. 2.2).

One of the greatest advantages of ellipsometry is it sensitivity. Ellipsometry is capable of measuring layer thickness on a fraction of a nanometer, and can detect subtitle changes in optical properties of a single-atomic layers. However this unparalleled sensitivity is also a downside of ellipsometry. Although, we can measure optical properties of the sample with great precision, often it is not well defined what was measured. Ellipsometric spectra gives the information on how has the entire sample changed the polarization of the light after the reflection. If we are interested in a particular component of our sample, as one layer within the structure, we need to know as much as possible about all the other components of the sample in order to include these appropriately in the optical models used for the data interpretation.

Ellipsometry can give direct information on optical properties only when a perfectly flat surface of a bulk material is measured. Commonly this is not the case, and especially this is not even possible for the case of graphene. As it was described in the previous section (Sec. 3.2) in order to interpret ellipsometric measurements of more complex samples, it is required to use optical models. These optical models need to include as realistically as possible many different sample properties that can significantly affect the data interpretation. It is required to know number and type (complex refractive index) of layers in the measured sample. Also, an interface between two layers can significantly alter the interpreted data. Often it is not possible to assume that two materials have a perfectly flat and defect of residue free interface. Usually interfaces are introduced into optical models as a surface roughness layers, or gradient layers between two materials, or an additional thin inter-layer has to be added in the optical model. If a layer or an interface that exists in the sample is not included in the optical model, the retrieval procedure will result with false data. In some cases, this error can be very small and comparable with the instrumental uncertainty. However, in the case of graphene, since the layer of interest is only 0.335 nm thin, many minor changes in the optical model can cause large changes of the resulting optical properties of graphene. How to minimize this unwanted effect and how to properly build and analyze optical models for the case of graphene are

topics of the next chapter (Sec. 3.4). Here we will focus on how other measuring techniques can help us understand the sample better, and how to use this data to properly build an optical model. These additional measurements are often referred to as correlation measurements [154].

Let us first focus on how can Raman spectroscopy aid ellipsometry of graphene. As it was discussed in Sec. 2.2.2, Raman spectroscopy is very reliable to determine number of graphene layers, especially in the case of a single-layer graphene. Besides knowing the number of layers in a single point (usually $\sim 2\,\mu m$ diameter spot) it is also important to know if the sample is uniform over the entire area that is used for ellipsometry measurements (usually between 100 and 1000 μm in diameter). This can be done either by spatial mapping of Raman modes, or by other techniques, as optical microscopy, or AFM, or scanning electron microscopy. Once the sample uniformity and a number of layers is confirmed this data can be used within the optical model.

There are several different ways to introduce graphene into an optical model that is used to interpret ellipsometric measurements. The simplest would be to add graphene as a layer, and not to fix its thickness but to vary it in a certain range from the expected value. This approach was used by J. W. Weber and coworkers [75], and their best fit to measured data gave single-layer graphene thickness of 0.34 nm. However, this approach introduces one additional variable in the minimization process, and can result with an increased uncertainty of the measurements. A similar approach of accounting for graphene would be to keep it as a layer in the optical model, but to fix its thickness to 0.335 nm. This value is equal to the extension of the π orbitals out of the graphene plane [202]. This approach was first used by V. G. Kravets and coworkers [74], and in several other ellipsometry studies of graphene [84, 89, 90]. Also, this approach is adopted in this dissertation and the related publications [82, 83, 91, 92, 156]. In the case when a graphene is supported by a substrate with very high surface roughness, or with large number of nanometer scale terraces (as in the case of a SiC) graphene can be modeled as a roughness layer. This approach was introduced by A. Boosalis and coworkers [96]. Finally, since graphene is so thin, it does not even have to be a layer in the optical model, it can be introduced as a surface charge, or a surface condition for the set of Maxwell equations. This approach was adopted by Y.-C. Chang and coworkers [66]. The main advantage of this approach is that graphene thickness does not appear within the optical model, neither as a constant nor as a variable. However, this approach gives

optical conductivity of the sheet, and to translate this into absorption or complex dielectric function, thickness of the film must be used. Regardless of how graphene is added in the optical model, the result should be the same.

Besides determination of the layer number, Raman spectroscopy can give insight into the quality of the sample, or into the presence of a transfer residue layer. As discussed in Sec. 2.2.2, by examination of D-band and positions, widths and intensities of G and $2D$ bands it is possible to estimate amount of residue, type and the amount of doping of the sample, and the amount of strain. However if these effects are not very pronounced, Raman spectroscopy alone should not be used to determine them, but rather a combination with measurements of electrical properties, or AFM should be used.

As it was discussed in Sec 2.2.3, AFM measurements of sample height can suggest the presence of a trapped "water" layer between graphene and a substrate. An example of this is shown in Fig. 2.9. However, in this case the obtained thickness can not be used as a constant value, but only as an expected value and the water inter-layer height has to be taken as a model parameter. Optical properties of this water and air mixture layer are usually considered as known and modeled as a Cauchy layer [153], with parameters taken from [74]. Besides the water inter-layer, AFM can give an accurate value for the surface roughness. This can be easily integrated into an optical model, using some of the well known roughness models [153]. AFM can also reveal surface structure on a nanoscopic scale. As it is shown in Fig. 2.9(b), wrinkles and transfer residue can be readily imaged by the AFM, and an appropriate layer can be added into the optical model to account for these surface imperfections. As it will be discussed in the chapter 4, transfer residue particles can be introduced into an optical model using an "island-film" layer [153]. Here AFM is used to estimate height of these islands and the percentage of the sample surface covered by them. In the case of a sample shown in Fig. 2.9(b), residue islands cover 5 % of the total sample surface and their height has been estimated to 25 nm.

Besides AFM and Raman measurements, in the case of graphene, ellipsometry measurements of the surrounding substrate can help to fix several parameters in the optical model. As an example, let us consider exfoliated graphene on a SiO_2/Si substrate. By taking ellipsometric measurements of the surrounding substrate we can determine the exact local thickness of the SiO_2 layer. Also, by taking consequent sample and substrate measurements it is possible to determine the exact angle of incidence for a particular set of measurements. All these parameters can greatly

increase the reliability of the obtained optical properties.

Whenever it is possible to have paired sample and substrate measurements, these additional measurements should be used to fix as many parameters as possible. By paired measurements it is referred to a set of two or more consequent measurements, between which no changes were made in the measurement setup (optical path of the ellipsometer), but only a translation of the ellipsometric spot on the sample has been done. This translation should be as small as possible, in order not to introduce significant change of the incident angle. Also, combining AFM topography and ellipsometry measurements of a substrate, it is possible to see if a surface roughness layer between the substrate and air is required within a optical model. Only when an adequate optical model of the substrate is obtained it is reasonable to consider modeling an atomically thin sample. Adding the sample layer to already predefined optical model of the substrate significantly simplifies the data retrieval process.

This procedure should be followed whenever the layer of interest is very thin (less than 5 nm) and there is a surrounding substrate, or a structure very similar to the sample, but only without the layer of interest. This is the case not only for graphene but also for the other Van der Waals' materials.

3.4. Retrieval of optical properties from ellipsometric data

The following section describes interpretation of ellipsometric measurements. This procedure relies on understanding of optical models (Sec. 3.2), and how these relate to the measured data (Sec. 3.1). The focus of this section is how to obtain optical properties of an atomically thin film from ellipsometric measurements, although the procedures presented here are general and can be used to obtain layer thickness, or to characterize bulk materials.

First a dielectric function modeling procedure will be explained (Sec. 3.4.1), and how to use minimization to obtain parameters of a chosen dielectric function. Afterwards, a more suitable retrieval method for atomically thin films will be presented, a point-by-point inversion (Sec. 3.4.2). Finally, an influence of an underlaying substrate on reliability of the interpreted data will be presented (Sec. 3.4.3).

Combining a proper minimization procedure, minimization function and a supporting substrate should be considered as a good practice guide for the data interpretation of an ellipsometric measurements of atomically thin films, and holds not only for graphene but also for the other atomically thin materials.

3.4.1. Modeling of optical properties

The previous two sections of this chapter have shown how the change in the state of the polarization can be detected using ellipsometry (Sec. 3.1), and how to relate the measured values to the optical properties of the sample (Sec. 3.2). This subsection will focus on various functions for modeling of graphene's complex refractive index, and will explain the minimization process in the case when optical properties are obtained from the fitting parameters of an assumed model. This is a general approach used in ellipsometry [153], however when atomically thin layers are measured a better suited procedure for retrieval of the optical properties is a point-by-point inversion, which will be the topic of the next subsection (Sec. 3.4.2).

Let us now focus on a case of fitting the optical properties of graphene with a

model function. Let us assume that we have a spectroscopic ellipsometry measurements (ρ_{exp}) of a graphene sample on a given substrate, and that all the parameters of the model are known, except the complex refractive index of graphene (N_{gr}). Furthermore, measurements are carried out in a spectral range (eg. the visible range) where the complex refractive index of graphene can be represented by a certain dielectric function as a Drude, Lorentz, Fano or Gaussian model. In this case the refractive index of graphene is a function of several parameters, as resonant energy, broadening and others, depending on the chosen model:

$$N_{gr} = f(a, b, c, \ldots) \,. \tag{3.59}$$

Here f stands for a chosen function of the complex refractive index, while a, b, c and possibly more are fitting parameters. The number of fitting parameters and their physical interpretation depends on the chosen function. If these parameters are known, then also the complex refractive index of graphene is known. The process of minimization is used to obtain these parameters.

A given set of parameters, gives a specific N_{gr}, and by using Fresnel equations (as described in Sec. 3.2) it is possible to simulate ellipsometric measurements (ρ_{fit}). The optical model used here will have three or more layers ambient/graphene/substrate. The optical properties of all other layers but graphene are considered as known, these can be obtained from on-line databases [239]. Also thicknesses of all the layers are considered known and are fixed during the minimization process. Furthermore, the incident angle θ is also considered as known. All of these parameters can be obtained from corroborated measurements (as described in Sec. 3.3).

Spectroscopic measurements are taken at several different wavelengths in a chosen spectral range, meaning that: $\rho_{exp} = \rho_{exp}(\lambda)$. The simulated data also needs to be the function of the wavelength. The minimization is done with the respect to the parameters of the function used to describe the complex refractive index of graphene. These parameters can not be dependent on the wavelength, but they describe N_{gr} in a spectral range. The function itself need to be chosen to be adequate for the given spectral range. The minimization process is done by comparing the difference between measured and fitted spectra summed over the spectral range, as:

$$\sigma(a, b, c, \ldots) \sim \sum_{\lambda_i=\lambda_1}^{\lambda_n} |\rho_{exp}(\lambda_i) - \rho_{fit}(\lambda_i)| \,. \tag{3.60}$$

For a given set of parameters $(a, b, c, \ldots)$, the corresponding minimization value $\sigma(a, b, c, \ldots)$ is obtained. The process of minimization varies these parameters until

the minimal value of σ is found in a given parameter range. This way the complex refractive index of graphene is obtained from the spectroscopic ellipsometry measurements. The advantage of this approach is that if there are any instrumental errors that are dependent on a specific wavelength, as instability of the lamp, these will be averaged into the entire spectra and in most cases will have negligible effects on the obtained data. The main drawback is that this approach is fixed to a spectral range where the specific model of the dielectric function of the sample is applicable. Since this approach averages the data through the entire spectral range, if there are any issues with the optical model these will be much harder to find using this approach. As an example, if there is remaining transfer residue, in the visible it might go unnoticed, but in the UV this film will significantly contribute to the absorption and if not accounted for will result with the false data interpretation, since the absorption will be included in the complex refractive index of graphene. Finally, a problem remains how to properly model the optical properties of graphene in a given spectral range.

Understanding the optical properties of graphene is mandatory for this approach (see Sec. 1.2). There have been several different approaches to model complex refractive index of graphene [240]. A constant values for both n and k were used to model complex refractive index of graphene by Z. H. Ni and coworkers [63]. Also in the visible linear n and $k \sim \lambda/n$ has been used by M. Bruna and S. Borini [241]. A model for the complex refractive index of graphene based on several Drude functions [46] was introduced by U. Wurstbauer and coworkers [76], here a metallic behavior of graphene was assumed in the visible range. A b-spline functions based method that uses a larger number of fitting parameters to describe the complex refractive index of graphene both in the visible and UV was introduced by J. W. Weber and coworkers [75]. A model based on a Fano resonant profile was employed within Ref. [82], which is related to the dissertation, and will be described in greater detail in Sec. 4.2. This method was also (independently) used by P.-K. Gogoi and coworkers [89] to describe the complex refractive index of graphene in the visible and UV ranges.

In a wider spectral range, one function might not be suitable for the description of the complex refractive index. As it was shown in the case of graphene (see Sec. 1.2) in the far-infrared an intraband component needs to be accounted for, in the mid-infrared a change in the optical properties due to the Pauli blocking

(at $2E_F$) occurs. In the UV a prominent absorption peak dominates the optical spectra. This peak corresponds to the exciton-shifted Van Hove singularity at M-point transitions. If we would go even further into the UV, at about 25 eV an another Van Hove singularity will arise. This would correspond to the interband transitions at Γ-point. Considering all this, it is quite obvious that if the spectral range of the measurements is large, it will be very difficult to use one dielectric function in the minimization process. A better approach in this case would be a point-by-point inversion. This approach was used to interpret ellipsometric measurements of graphene in Ref.-s [66, 74, 84] and also in the publications related to the dissertation [83, 91, 92]. A point-by-point inversion is presented in the next subsection.

3.4.2. Point-by-point inversion and minimization functions suitable for 2D materials

A point-by-point inversion, or a mathematical inversion, is a minimization process that is used to retrieve desired parameters of the optical model at each wavelength independently. It is used only when a small number of parameters in the optical model are unknown, usually a complex refractive index or thickness of one layer within the optical model. If more parameters of the model are unknown, inversion process will most likely have multiple solutions, and in some cases could be unapplicable. This method is very similar to the dielectric function modeling described in the previous section (Sec. 3.4.1), with the main difference being that here optical properties are obtained at each wavelength independently, rather than in a spectral range.

There are several advantages of this method. Since the minimization is carried out at each wavelength, it can be applied to wide spectral ranges. Also, there are no initial assumptions of the dielectric function. Furthermore, using point-by-point inversion it is easier to detect any problems within the optical model, especially if they are related to a specific part of the spectra.

The major drawback of a point-by-point inversion is the fact that any instrumental error, or any error within an optical model will be translated into an error of the values (optical properties) obtained in the minimization process. This happens

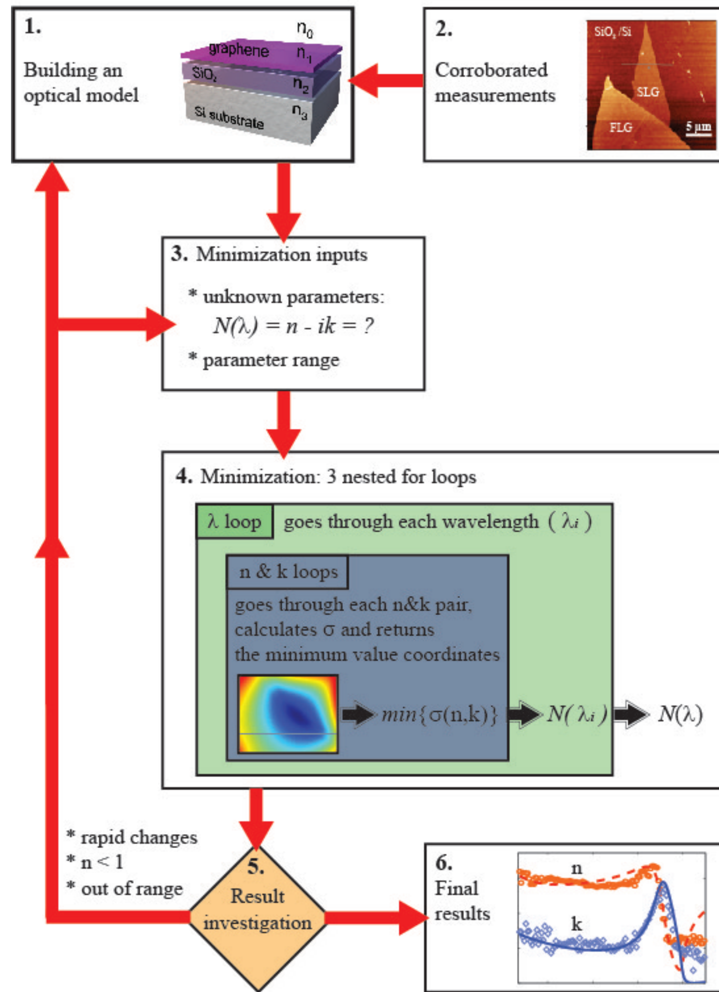

Figure 3.11.: A flowchart of a point-by-point inversion data analysis process.

because the minimization is independent at each wavelength, and any error that is localized at a specific wavelength will not be averaged in the entire spectra, but will create a discrepancy in the obtained value at that particular point in the spectra.

Let us focus on the inversion process on an example similar to the one in the previous section. A typical flowchart of the data analysis process is shown in Fig. 3.11. Let us assume that we have a series of measurements ($\rho_{exp}(\lambda, \theta)$) of a graphene sample on a substrate, taken under several different angles of incidence. First, it is required to build an optical model, as described in Sec. 3.2. An optical model used in this example consists of three or more layers (depending on a substrate and interlayers); i.e. ambient/graphene/substrate.

As in the previous section, let us assume that all the parameters of the optical

model are known (obtained through corroborated measurements), except for the complex refractive index of graphene: ($N_{GR}(\lambda) = n - ik$). In this case, a point-by-point minimization process is used to obtain the values of n and k. For this it is important to define the expected ranges, and resolution (grid) for both n and k. These ranges should be significantly larger than the expected values of for the complex refractive index. Most materials have both n and k ranging between 0 and 5, so if the minimization process returns values several times greater than these, most likely there is a problem within the optical model.

With all known parameters set, and ranges for the unknown parameters defined, the minimization process can begin. In the case when n and k are the values of interest, numerical code for the process in the simplest form will have three nested for loops. The outer loop will go through each wavelength independently. At each point in this loop a plane in n-k space can be made, such that every point in that plane represents a possible solution for the complex refractive index ($N_{GR} = n - ik$). Boundaries of this plane are the ranges for n and k that were set prior to the minimization process. For each point optical models (see Sec. 3.2) are used to simulate all the measurements taken (under different angles of incidence). A minimization function $\sigma(\lambda_i, n, k)$ (will be explained later in the text) is calculated for each point in n-k plane. Lower values of σ indicate better agreement with the measured data, while higher values indicate discrepancies of the model with the experiment. A minimum value of the minimization function is obtained at each wavelength $\sigma_{min}(\lambda_i, n_{min}, k_{min})$. The coordinates of this value in a n-k plane (n_{min}, k_{min}) represent the solution for the complex refractive index at that particular wavelength. This process is repeated at each wavelength (the outer loop) and the spectra of the complex refractive index is obtained ($N_{GR}(\lambda)$).

As mentioned earlier, the main drawback of a point-by-point inversion is that any instrumental errors, or errors created by an improper optical model, will be translated into an error of the obtained data. For this reason, results need to be inspected. In order to properly inspect the results, some initial expectations are required. In the case of complex refractive index of graphene, as it was seen from its dispersion relation and joint density of states function (see Sec.-s 1.1 and 1.2), in the visible range no prominent changes are expected, as a bandgap or Van Hove singularity related peaks, or "kinks" in the optical properties. On the other hand, in the UV range, a prominent absorption peak is expected. Regarding the range of n and k that should be set prior to the inversion process, optical properties of

graphite are a good reference [239]. Resulting n and k of graphene should not vary significantly from the values of bulk graphite. Considering all these, and by examining the resulting spectra of graphene's refractive index, an improper optical model or a problem in the measured data can be detected. Here one should look for unexpected features, rapid changes in the refractive index, $n < 1$ (unless a plasmonic resonance is expected) or (n,k) approaching their limits, or having unexpectedly high values. As an example, minimization process should allow for n to be 10, but if the minimal value does require this high refractive index value, almost certainly there is a problem in either measurements or optical models, or even both.

It was mentioned that a numerical code for the given example would have three nested for loops. This is an unoptimized example, and it could be easily parallelized in order to reduce the time and optimize the resources required by the calculation. As an example, since all the calculations are wavelength independent, the outer loop can be vectorized, thus parallelizing the entire process. The same could be done for the two nested loops within the outer loop, however this also depends on the method for finding the minimal value of $\sigma_{min}(\lambda_i, n_{min}, k_{min})$, and in some cases a function that searches for the minimal value could be faster than vectorization of all three loops. The method described here, with flowchart shown in Fig. 3.11, is the basis for the MATLAB code used in the dissertation for retrieval of the optical properties of graphene (chapter 4). An example of such a code is given in appendix C.3.

Let us now focus on the minimization function $\sigma(\lambda_i, n, k)$. In order to simulate ellipsometric measurements, first ρ_{fit} needs to be obtained from the optical model of the sample, as shown in Sec. 3.2. Then it needs to be related to the values that are measured in a specific ellipsometric setup which has been used (Sec. 3.1). Finally the measured and the fitted values need to be compared. The function that does this is called a minimization function σ. The goal of the minimization process is to find the smallest σ possible using a realistic optical model. Lower values of σ indicate better agreement between the measured and the fitted data, and more accurate fitting results.

Let us focus on a case where the measured values are ellipsometric angles $\psi_{exp}(\lambda_i, \theta_j)$ and $\Delta_{exp}(\lambda_i, \theta_j)$. These are the function of both angle of incidence θ and the wavelength of the incident light λ. Simulated spectra will give ψ_{fit} and Δ_{fit}. A most common way to define the minimization function that simultaneously considers several measurements of the same sample that were taken at the different angles of

incidence:

$$\sigma(\lambda_i) = \frac{1}{\sqrt{M-P-1}} \Big(\sum_{j=1}^{N} (\psi_{exp}(\lambda_i,\theta_j) - \psi_{fit}(\lambda_i,\theta_j))^2 + (\Delta_{exp}(\lambda_i,\theta_j) - \Delta_{fit}(\lambda_i,\theta_j))^2 \Big)^{\frac{1}{2}} . \tag{3.61}$$

Here M stands for the number of wavelengths for which measurements were carried out. N stands for the number of different angles of incidence. P is the number of fitting parameters. Indices exp and fit stand for experimental and calculated (fitted) data, respectively.

In general, σ considers a function of the sum of the absolute value of the difference between measured and fitted data. Commonly this function is a polynomial one, and a general expression for σ could be written as:

$$\sigma(\lambda_i) \sim \Big(\sum_{\theta} |\psi_{exp} - \psi_{fit}|^p + |\Delta_{exp} - \Delta_{fit}|^p \Big)^q . \tag{3.62}$$

Here p and q stand for the factors of the minimization function. In the case of Eq. 3.61 $p = 2$ and $q = 0.5$. However these factors could have any values that are suitable for the specific problem. Eq. 3.62 can be multiplied by a constant value, also to better suit the minimization process.

To demonstrate how the choice of the minimization function factors p and q affects the minimization process, Fig. 3.12(a), (b) and (c) show maps of $\sigma_{p,q}(n,k)$ for the same set of six measurements, under six different angles of incidence. The measured data was taken from Ref. [91] and the interpretation of these measurements will be the topic of the next chapter. Here we only focus on the difference in finding minimal value of σ for the different values of p and q. Whenever possible, $p = 2$ and $q = 0.5$ should be used, as in Fig. 3.12(a), where the minimal value of the refractive index was found to be 3.05-i1.95 ($\pm$0.15). This value has been indicated by a red circle in Fig. 3.12(a), (b) and (c), to illustrate how the different choice of p and q could lead to the different solutions. In this particular case, a better choice of p and q would be $p = q = 1$, as shown in Fig. 3.12(b). This is seen by the better defined minimal value of $\sigma_{p,q}(n,k)$ than in the case sown in (a). However this is true only for the given wavelength, in order to use a different minimization function it must be confirmed that the new function is better suited that the standard one in the entire spectral range.

Figure 3.12(c) shows a $\sigma_{p,q}(n,k)$ for a very unusual set of factors p and q. Here $p = 0.1$ and $q = 1$. Such a minimization function can be used to detect a particular measurement that has a significant discrepancy compared with all the other

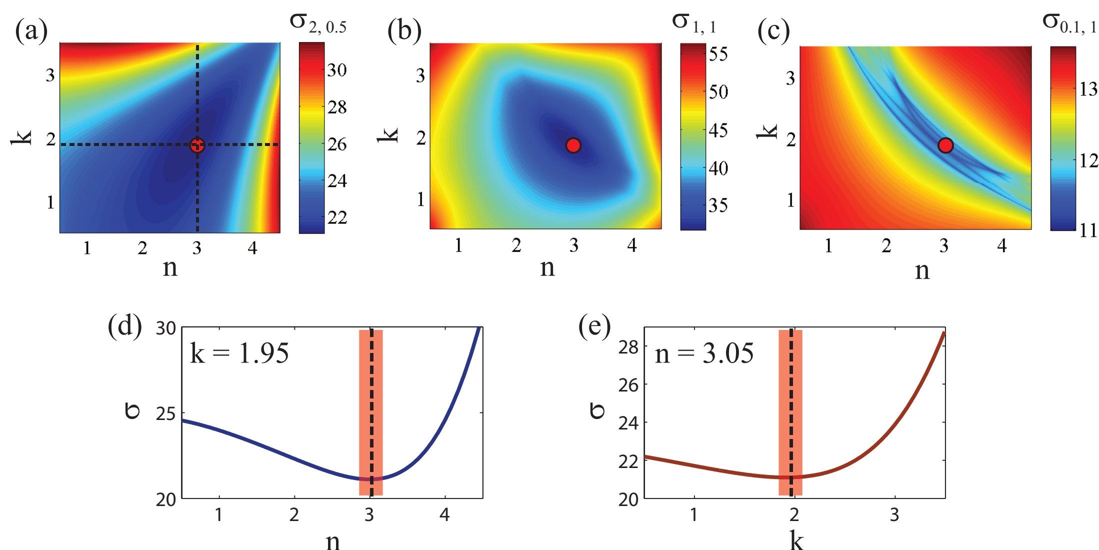

Figure 3.12.: Values of σ as a function of (n, k) for: $p = 2$ and $q = 0.5$ (a); $p = 1$ and $q = 1$ (b); $p = 0.1$ and $q = 1$ (c). A red dot in each figure represents the solution for (n, k), obtained from (a). (d) and (e) show cross-sections of (a) in n and k direction, both intersecting the minima point (3.05, 1.95), and are marked in (a) by dashed lines.

measurements. In Fig. 3.12(c) there are a total of six minima lines that overlap each other. Each minima line corresponds to a particular measurement (taken at a different angle of incidence). In the given example, all the minima lines overlap in the region where the minimal value is expected. However, if one minima line would not cross this region it would indicate that for some reason the particular measurement deviates from all the other. If this is the case over the entire spectral range, most likely an improper incident angle has been used in the optical model. When atomically thin samples are measured, an error in the incident angle as small as 0.01° can cause these deviations of the minima lines in n-k plane.

Let us now focus on the problem of the uncertainty for the obtained values of n and k, using the example shown above. One more upside of the point-by-point inversion is that an error of the obtained data can be estimated relatively straight forward during the minimization process. Let us assume that we have an exact optical model, introduction of the uncertainty by the optical model will be considered later on. In this case only an instrumental error can cause an error of the obtained data. Measurement precision varies for different ellipsometric setups, but in general,

values for ψ and Δ can be obtained with precision between 10^{-3} and 10^{-4} [153]. Such a precise measurements of the state of polarization do not guarantee a precise measurement of the optical properties of a particular layer in the sample, in this case graphene. There are two factors regarding a sample structure that affect on the error of the interpreted data. First if a layer of interest is relatively deep within the sample structure, multiple reflections from the upper layers will significantly increase the uncertainty of the obtained data. The layer of interest should be the top layer if possible, or at least not deeper than three layers from the top one. The number of layers that can be over the layer of interest depend on their thickness and optical properties. The other structural property of interest is the layer thickness. If the layer thickness is comparable with the incident light wavelength, i.e. from $\sim$50 nm to $\sim$2 μm, interference of the light within the layer will determine the sensitivity. However if the layer is significantly thinner that the incident wavelength, then thinner the layer greater the uncertainty. This is the problem when graphene and other atomically thin layers are measured.

Estimating the uncertainty of obtained n and k in the case when an optical model is fixed is relatively straight forward. First an error of the measured values is estimated ($\delta\psi$ and $\delta\Delta$). After the minimal value for σ is found in the minimization process, it is easy to estimate how much n and k would vary if the measurements would vary for $\delta\psi$ and $\delta\Delta$. The values of δn and δk will depend on the profile of the minimization function near its minimal value $\sigma_{min}(\lambda_i, n_{min}, k_{min})$. This is shown in Fig. 3.12(d) and (e). Usually, when a single layer graphene is a top layer, these variations are between 2% and 10%, depending on the substrate interference. However, $\delta\psi$ and $\delta\Delta$ are also the function of a wavelength, and near the limits of the spectral range, due to very small light intensity, uncertainty of the obtained parameter values (δn and δk) can be as high as 200%. In an example shown in Fig. 3.12, uncertainty of the obtained optical properties of graphene was estimated to be $\pm$0.15, or less than 8%. Here, the minimization function factors p and q were chosen to be 2 and 0.5 respectively.

On the other hand, if there is an uncertainty introduced by the optical model itself, the issue of estimating an error is much more elaborate. Let us consider the case where, besides n and k of the graphene layer there is an undefined parameter in the substrate, as thickness of a layer, or a roughness layer, or optical properties of a layer within the substrate. If these can not be determined from a corroborated measurements, they also need to be included within the minimization process. As

a result, the minimization process will have more parameters, this will not only increase the time required for the minimization, but could lead to several different solutions (multiple minima of σ). Furthermore, graphene layer is very thin, and almost in all cases when the optical model is not well defined, a resulting uncertainty of the obtained optical properties of graphene is so large that the inversion process is unapplicable. This points out how important corroborated measurements are for proper interpretation of the ellipsometry measurements in the case of atomically thin films.

As the last part of this subsection, let us consider a minimization function that is well suited when measuring atomically thin films. Let us consider the case of a graphene layer over a substrate. Again, let us consider that all the parameters of the optical model are known, except for the complex refractive index of graphene. Furthermore, let us assume that we have paired sample and substrate measurements. These were explained in Sec. 3.3, when ellipsometric measurements of the substrates were considered as corroborated measurements. This is commonly possible for the case of graphene, and other Van der Waals' materials, since the sample covers only a part of the substrate. The paired substrate measurements are considered to have the same optical model, only without graphene layer and possibly an inter-layer between graphene and a substrate. By fitting the substrate measurements it is possible to obtain the exact angle of incidence, exact local thickness of layers within the substrate, or presence of various roughness layers.

Substrate measurements are also interpreted by the inversion process, however here only parameters that do not depend on the wavelength are obtained (thicknesses and angles). For this reason substrate fit will never exactly match the measured data. If we again consider that the measured values are ellipsometric angles ψ and Δ, then these discrepancies of the substrate measurements will be defined as:

$$\delta\psi_{sub}(\lambda_i, \theta_j) = \psi_{sub,exp}(\lambda_i, \theta_j) - \psi_{sub,fit}(\lambda_i, \theta_j)\,, \tag{3.63}$$

$$\delta\Delta_{sub}(\lambda_i, \theta_j) = \Delta_{sub,exp}(\lambda_i, \theta_j) - \Delta_{sub,fit}(\lambda_i, \theta_j)\,. \tag{3.64}$$

These values are usually below 1% when a proper optical model of the substrate is used. However, if there are resonances due to interference within the substrate, the values of $\delta\psi_{sub}$ and $\delta\Delta_{sub}$ can be much higher near the resonance wavelength.

Since we consider that the sample (graphene) is an atomically thin layer, the effect of interferences within the sample layer can be neglected. Sample will only

modify the substrate spectra, and the measured sample ψ and Δ spectra will be predominantly defined by the underlaying substrate. Furthermore, the same optical model that was used to interpret substrate measurements is used also for the interpretation of the sample measurement, with the addition of the sample layers. Any discrepancies that exist within the substrate measurements ($\delta\psi_{sub}$ and $\delta\Delta_{sub}$), will be included in the obtained optical properties of the sample, thus resulting with incorrectly interpreted data. In order to avoid this a substrate fitting error has to be added to the sample fitting procedure. This is done by modifying the minimization function σ, as followed [83]:

$$\sigma(\lambda_i) \sim \Big(\sum_{\theta} |\psi_{exp} - \psi_{fit} - \delta\psi_{sub}|^p + |\Delta_{exp} - \Delta_{fit} - \delta\Delta_{sub}|^p\Big)^q . \qquad (3.65)$$

Here, summation goes over all the measured angles of incidence, and all ellipsometric angles are functions of both the incident angle and the wavelength. This way a substrate correction can be included in the minimization function, and the minimization process will "compensate" for the substrate discrepancies, thus not including these into the obtained complex refractive index of the sample.

As it was stated, Eq. 3.65, can be used only when the sample is thin enough to exclude any light interferences within the the sample layer, usually less than 5 nm. Furthermore, the sample needs to be added on top of the substrate, but still to leave enough clean substrate area for paired sample/substrate measurements. And finally the substrate underneath the sample must be identical to the bare substrate next to the sample and the incident angle, as well as the entire ellipsometric setup must be unchanged for the paired sample/substrate measurements. Only if all these conditions are met, Eq. 3.65 is applicable as a minimization function.

3.4.3. Using substrate interference to enhance sensitivity of SE measurements

This subsection presents a method for choosing an adequate substrate for ellipsometric measurements of an atomically thin structure deposited over a chosen substrate. As it will be show the right substrate can significantly increase sensitivity of SE

measurements. By an increased sensitivity it is referred to an increased influence of a surface layer in the total measured ellipsometric spectra (ψ, Δ). This will affect a data retrieval process, and in the case of a point-by-point inversion (presented in the previous section) a properly chosen substrate will give very sharp minima of a $\sigma(\lambda, n, k)$ in a certain range, thus significantly increasing precision of the obtained data.

Previously, in Sec. 2.2.1 an interference of light within a substrate has been used to enhance optical contrast of graphene. That case examined a change in contrast that occurs due to an interference of a light within SiO_2 layer, under normal incidence in a graphene/SiO_2/Si sample. The same principle can be used to enhance ellipsometry measurements of graphene on a SiO_2/Si substrate. The main difference is that in ellipsometry incidence is oblique, and a difference in ψ and Δ are considered, rather than a relative light intensity (contrast).

An adequate supporting substrate, combined with the proper incident angle can greatly increase the sensitivity of the measurements to the graphene layer in a certain range. The difference of measured ψ and Δ spectra, between the graphene layer on the substrate and the bare substrate determines the reliability of the extracted optical parameters [62]. The change in polarization caused by the SiO_2 layer has a series of constructive and destructive resonances [153]. These resonances occur when the phase shift of a secondary beam becomes exactly a half integer wavelength. The maximum in ψ appears for destructive interference of s-polarization. In a relatively large spectral range around these resonances the system is very sensitive to any thin layer on top of it. The position of these resonances can be tuned by changing the optical path of a beam within a SiO_2 layer. For a fixed wavelength of incident light, there are two ways to change the optical path, by changing thickness of a SiO_2 layer, and by changing an angle of incidence.

By using the different SiO_2 layer thickness it is possible to position these resonances in almost any spectral range of an interest. Unfortunately, due to the optical contrast of graphene [61], the sample will be optically visible only if a SiO_2 thickness is $\sim$290 nm or $\sim$90 nm, with tolerance of about $\pm$15 nm. In any other case contrast between the sample and the substrate in the visible range will not be large enough to detect the sample by optical inspection. In those cases it is much harder to carry out paired sample/substrate measurements.

The other way to tune these resonances is by the incident angle of the light. This can be done with variable angle ellipsometers. However, to make a significant shift

of the resonance peak in the spectra, very large differences in the incident angle are required. Ellipsometric spectra should be measured near the Brewster angle of the structure, which in this case is defined by the Brewster angle of the underlaying bulk silicon ($\theta_B \approx 73.8°$). Measurements under an angle that is significantly lower than the Brewster angle will be less reliable.

Let us see how the difference between the measured sample and substrate ψ and Δ spectra can be enhanced on an example of a single layer graphene ($d_{graphene} = 0.335\,nm$) placed on top of a SiO_2/Si substrate. This will be done both by varying the thickness of SiO_2 layer and an angles of incidence. Optimizing the choice of a SiO_2 layer thickness and the angle of incidence, can result with a thousand times higher sensitivity of ellipsometric measurements in the desired spectral range, than in the case of a bulk substrate.

Let us consider that in every case there are four sets of subsequent measurements of graphene/SiO_2/Si and bare SiO_2/Si, under four different angles of incidence: 70°, 65°, 60° and 55°. Measurements at angles lower than 55° would have almost negligible difference between the sample and the substrate, and would not contribute to the increased sensitivity. Considered spectral range is the visible an UV (1.5 eV - 6 eV).

Let us first focus on the samples that are visible by optical inspection. Figures 3.13(a) and (b) show simulated tanψ and cosΔ spectra of paired sample/substrate measurements, under all four angles of incidence. In this case the thickness of a SiO_2 layer has been fixed at 300 nm.

Figures 3.13(c) and (d) show the difference between each pair of a sample and a substrate measurements shown in (a) and (b). The difference is calculated as: tanψ_{sam} - tanψ_{sub}, where indices *sam* and *sub* refer to the sample (graphene/SiO_2/Si) and the substrate (SiO_2/Si), respectively. An envelope indicated by a green dashed line in Fig.-s 3.13(c) and (d) is obtained by summing the absolute value of the difference for each pair of sample/substrate measurements taken under the different angle of incidence. These envelopes indicate the sensitivity of an ellipsometric measurement in the given spectral range. As it can be seen, by using a 300 nm thick SiO_2 layer, sensitivity of ellipsometric measurements is increased in two narrow regions in the visible (2.5-3 eV) and in the UV (4-4.5 eV) ranges. Outside of these narrow regions, measurements are even a hundred times less sensitive to the presence of a graphene layer.

The other choice of a substrate that allows an optical inspection of a sample has

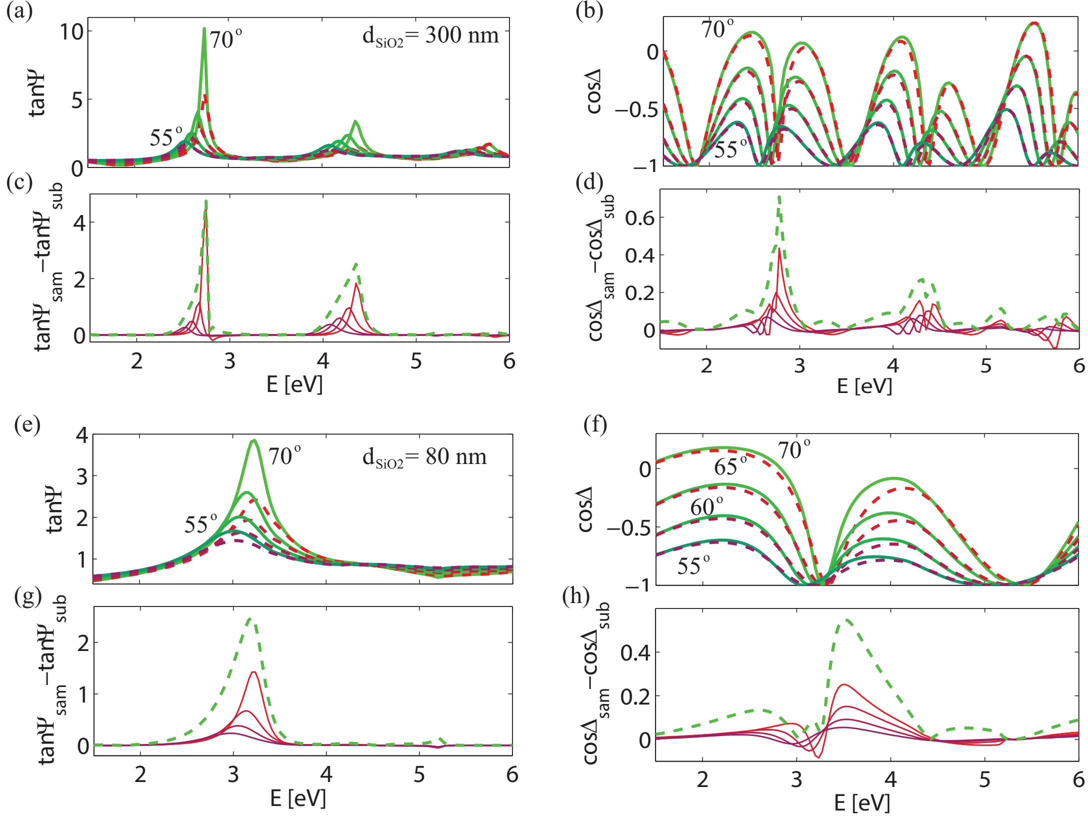

Figure 3.13.: (a) and (b) simulated spectra of $tan\psi$ and $cos\Delta$ of a graphene/SiO_2/Si (solid lines) and bare SiO_2/Si (dashed lines), under four angles of incidence. (c) and (d) relative difference between sample and substrate spectra shown in (a) and (b). In (a)-(d) thickness of a SiO_2 layer was fixed at 300 nm. (e) to (h) present spectra as in (a)-(d) only with the thickness of a SiO_2 layer fixed at 80 nm.

a SiO_2 layer thickness of 90 nm ± 15 nm. Figures 3.13(e)-(h) present the spectra in the same manner as in (a)-(d) only with the thickness of a SiO_2 layer fixed at 80 nm. In this case there is only one destructive interference of s-polarization in a given spectral range. This results with an increased sensitivity in most of the visible range (2-3.5 eV).

In the case of graphene, a feature of interest is a prominent absorption peak in the UV. For this reason, let us consider the thickness of SiO_2 that is required to have an enhanced sensitivity of the measurements in the UV range. Figures 3.14(a)-(d) show the data in the same manner as in Fig.-s 3.13(a)-(d), only with the thickness of a SiO_2 layer fixed at 40 nm. As it can be seen from Fig.-s 3.14(c) and (d), in this case an enhanced sensitivity is very broad and in the UV range (3-6 eV). These

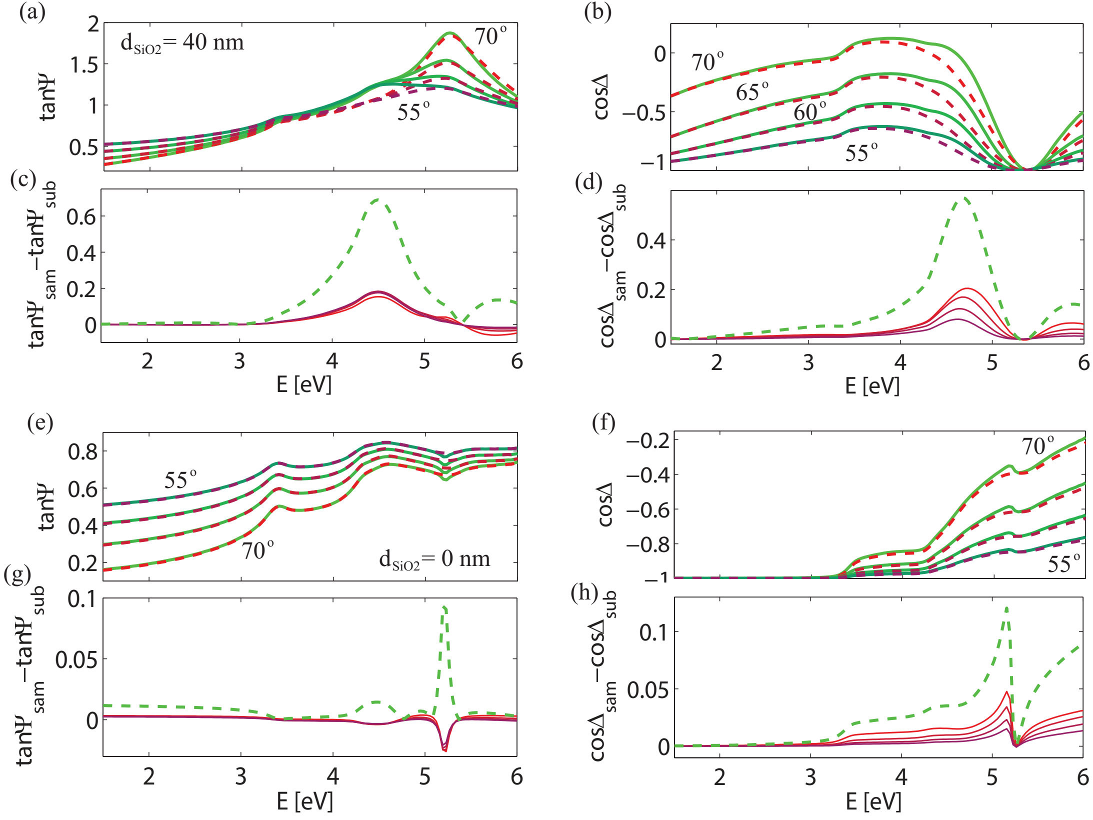

Figure 3.14.: (a) and (b) simulated spectra of $tan\psi$ and $cos\Delta$ of a graphene/SiO_2/Si (solid lines) and bare SiO_2/Si (dashed lines), under four angles of incidence. (c) and (d) relative difference between sample and substrate spectra shown in (a) and (b). In (a)-(d) thickness of a SiO_2 layer was fixed at 40 nm. (e) to (h) present spectra as in (a)-(d) only without a SiO_2 layer, i.e. graphene on a bulk silicon.

measurements are about ten times less sensitive than in the case of a 300 nm thick SiO_2 layer, but that is still enough to have very reliable data interpretation (an uncertainty of less than 2% when using inversion).

As a comparison Fig.-s 3.14(e)-(h) show the case with the thickness of a SiO_2 layer of 0 nm, or a case of graphene on a bulk silicon. As it can be seen these spectra do not have any resonances caused by the multiple reflections, since there are no layers that have their thickness comparable with the wavelength of the incident light. More importantly, by comparing the difference between the sample and the substrate measurements (Fig.-s 3.14(g) and (h)) gives from about one hundred to about one thousand times lower sensitivity than all the other previously shown cases that do have the effect of an enhanced sensitivity.

The method of the enhanced sensitivity of the ellipsometric measurements has been used in the experiments (chapter 4) that do have graphene supported by a SiO_2/Si substrate, and within the publications related to the dissertation [83, 92]. Also, the method shown here holds not only for graphene but also for any other thin film (less than 5 nm) on a SiO_2/Si substrate, and could be used as a guideline for a proper choice of a substrate when optical properties of atomically thin films are investigated. As an example, if an atomically thin semiconductor films as MoS_2 or WS_2 were considered, since their bandgaps lie in the visible range, an appropriate SiO_2 layer thickness would be between 70 nm and 90 nm.

4. SPECTROSCOPIC ELLIPSOMETRY OF GRAPHENE

The final chapter of the dissertation presents a study of optical properties of graphene, measured by spectroscopic ellipsometry. As well as, how ellipsometry can be used as a quality control tool in graphene-based technology. The advantages of ellipsometry, proper substrates, corroborated measurements, and many other that have been the topics of the previous chapters have been employed here in order to ensure higher accuracy of the obtained results. The results presented in this chapter have been also presented in the publications related to the dissertation [82, 83, 91, 92], and summarized in a review article [156].

The first section of this chapter (Sec. 4.1) presents optical properties of exfoliated single-layer graphene obtained by SNIE [83]. Furthermore, the first section shows how a Fano resonant model can be used to parameterize complex refractive index of graphene [82, 83] and to estimate properties of a M-point exciton.

The second section (Sec. 4.2) focuses on how SNIE can be used to spatially map optical properties of graphene. Furthermore, the second section shows a spatial distribution of a water layer that remains trapped between graphene and a substrate during micro-mechanical exfoliation [83]. Ellipsometric maps are also compared with AFM topography maps of the same sample area, showing a correlation between these two techniques.

The third and the fourth sections focus on how ellipsometry can be used as a quality control tool for the processes that are commonly used in graphene-based technology. The former (Sec. 4.3) shows how through the changes in optical properties of graphene it is possible to detect a residue layer that remains on the surface of the sample [91]. It is shown that this residue layer can increase light absorption

in a graphene layer by as much as 30% in the visible range.

The final section (Sec. 4.4) focuses on how optical properties of graphene change when supported by a substrate that strongly interacts with graphene layer, a metallic substrate. Here, SE measurements have been supported by KPFM and measurements of electrical properties in order to investigate how a graphene layer interacts with a supporting gold substrate. Furthermore, it has been demonstrated how changes in optical properties of graphene can be used to characterize quality of a graphene/gold contact with an optical technique [92].

4.1. Obtaining complex refractive index of graphene using SNIE

This section examines the optical properties of exfoliated graphene on an Si/SiO_2 substrate using spectroscopic null imaging ellipsometry in the visible range (360 - 800 nm), the results shown here are also presented in Ref. [83]. Measured spectra were analyzed by an optical model based on the Fresnel coefficient equations, as described in the previous chapter. The optical model was supported by correlated Raman and atomic force microscopy measurements. The complex refractive index of graphene was obtained by inversion of the measured ellipsometry data. The Fano line-shape was used to parameterize the optical properties.

Measurements were highly reliable due to the numerous advantages of SNIE combined with the proper choice of substrate and angles of incidence. SNIE measures angles with precision greater than 0.01°, and not fluxes, thus ensuring even higher accuracy while avoiding any nonlinearities introduced by the detector. Particularly, SNIE is an excellent tool to probe the optical properties of graphene due to its exceptional sensitivity, small spot size (1 μm) and accuracy, as well as its ability to control which part of the sample is measured in a wide spectral range. Using regions of interest (ROI), it is possible to measure multiple regions of the sample simultaneously, and carefully select areas to avoid dirt, residue, etc. that may affect obtained results. The effect that graphene layer has on the measurement is increased when an adequate substrate is chosen, which is also demonstrated in this section.

4.1.1. SNIE measurements of exfoliated graphene

Examined graphene samples were prepared by mechanical exfoliation of kish graphite (NGS Naturgraphit GmbH) on Si wafers (IDB technologies Ltd) with thermal SiO_2 layers of 90 nm or 300 nm thickness [1] (for more details see Sec. 2.2.1 and App. B.2). Samples were located by optical microscopy [63, 61], and are shown in Fig. 4.1(a) and 4.1(b). The number of layers and sample structure were confirmed by Raman spectroscopy using Chromex Micro Raman 2000, and atomic force microscopy using Ntegra prima scanning probe microscope. The Micro-Raman spectra of graphene were obtained using an excitation source of $\lambda = 532$ nm, doubled Nd:YaG laser. The laser power on the sample was about 1 mW with the 40x microscope objective which prevents any sample degradation. Acquisition times were 200 s, with five exposures averaged. The spectral resolution was 2 cm^{-1}. Raman spectra are shown in Fig. 4.1(c) and 4.1(d).

Due to the relatively small size of the samples, imaging ellipsometry is the perfect tool for examining optical properties of exfoliated graphene and other exfoliated 2D materials. In the research presented in this section a null ellipsometer "nanofilm_ep3se" by Accurion GmbH was used. As it was discussed in the previous chapter, the ellipsometric technique measures the value $\rho = r_p/r_s = \tan(\Psi)\exp(i\Delta)$. Upon light reflection on a sample, p- and s-polarizations show different changes in amplitude and phase [153]. Obtained amplitude ratio (Ψ) and phase difference (Δ) show the polarization state of the measured sample, and they hold information on the sample's optical properties.

As it was discussed in Sec. 3.1.4, null ellipsometry technique determines ψ and Δ from the rotational angles of polarizer (P) and analyzer (A) when the detector light intensity is zero. In the used setup, light reflected from the sample must be linearly polarized. This is possible only for certain elliptical polarizations of the incident light. These polarizations are found by rotating the polarizer while the compensator's angle is kept fixed (45°). There are four different polarizer angles that satisfy this condition, thus there are four possible solutions satisfying the null condition. All of the measurements are done by averaging these four solutions, i.e. four-zone averaging. Samples were measured in ambient conditions at room temperature. Spectral data was obtained by measuring at 35 different wavelengths

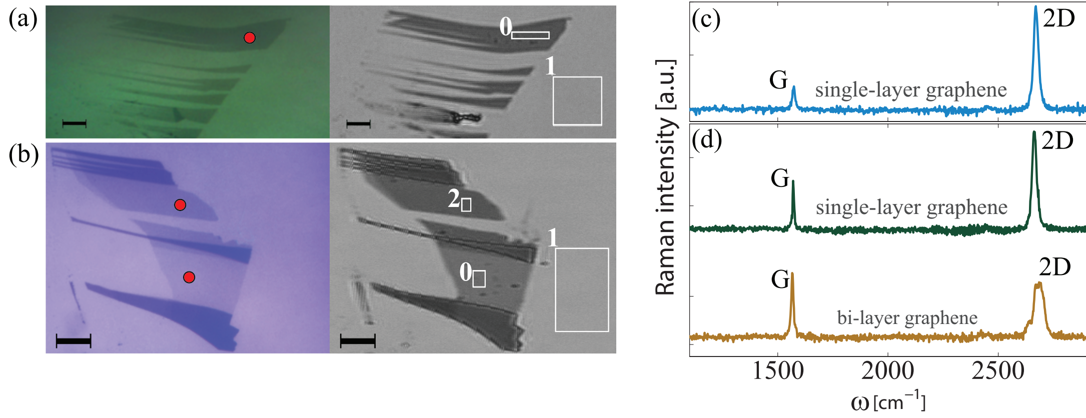

Figure 4.1.: (a) Optical (left) and Brewster angle (right) microscope images of the measured graphene sample on a 90 nm SiO_2 layer. The spot in the microscope image marks the area of Raman measurements. In the Brewster angle microscope image, regions 0 and 1 indicate regions of interest (ROI) used for the spectroscopic measurements, of the single-layer graphene and the substrate, respectively. (b) Optical (left) and Brewster angle (right) microscope images of the measured graphene sample on a 300 nm SiO_2 layer. Spots in the microscope image mark areas used for Raman measurements of single- and bi-layer graphene. In the Brewster angle microscope image, regions 0, 1 and 2 indicate ROI used for the spectroscopic measurements of single-layer, substrate and bi-layer graphene, respectively. Scale bar is 20 μm. (c) and (d) Raman spectra of the samples shown in (a) and (b), respectively. Areas measured with Raman spectroscopy are chosen to match ROI used for ellipsometric measurements.

between 360 nm and 800 nm, with an average full width at half maximum of 10 nm. Measurements were carried out for two different incident angles 71° and 60°.

An advantage of the imaging ellipsometer is the possibility to simultaneously measure spectra from different ROI within the view field of the CCD detector. This ensures the same ambient conditions and the same angle of incidence. In this mode, nulling of the signal is done by averaging within the selected region of the CCD. The microscope images and the brewster angle microscope images as well as the selected ROI are shown in Fig. 4.1(a) and 4.1(b). These paired sample and substrate measurements have been used in the data interpretation procedure shown in the next subsection.

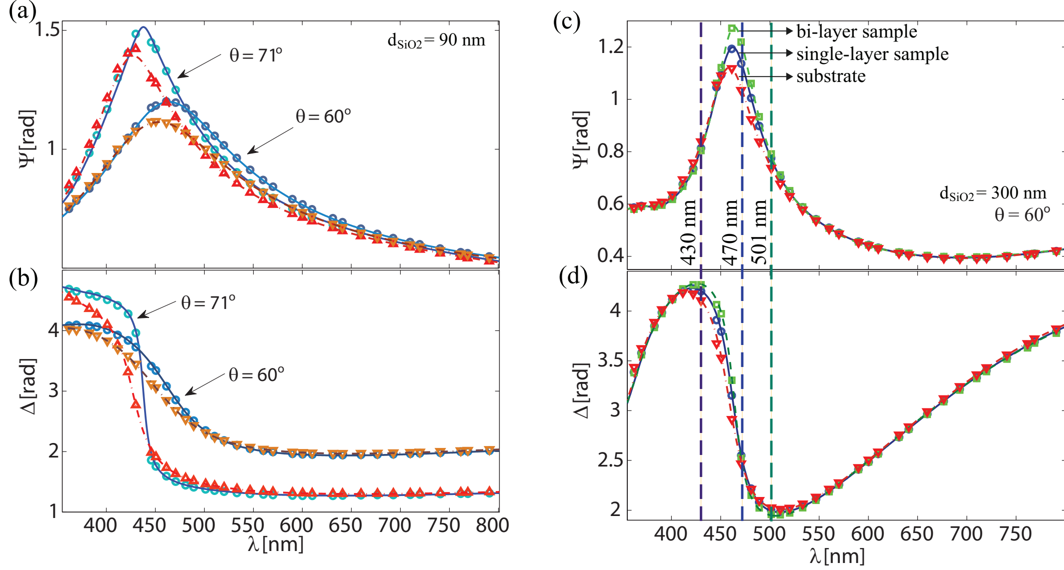

Figure 4.2.: (a) Measured Ψ spectra of the sample (circles) and substrate (triangles) with fitted sample (solid line) and substrate (dot-dashed line) data, and (b) measured and fitted Δ spectra, for the sample on a 90 nm SiO_2 layer. Measurements were carried out with same ROI used under two different angles of incidence: 60° and 71°. Image of the sample and ROI used are shown in Fig. 4.1(a). (c) and (d) measured ψ and Δ spectra of both sample (single- and bi-layer) and a substrate with a 300 nm SiO_2 layer, under 60° angle of incidence. Vertical lines in (c) and (d), at 430 nm, 470 nm and 501 nm indicate wavelengths used for ellipsometric mapping of the sample (Sec. 4.2).

SNIE measurements of single-layer graphene on a 90 nm SiO_2 sample are shown in Fig. 4.2(a) and (b), together with their paired substrate measurements. Measurements on a substrate with the thicker SiO_2 layer were also carried out, and are shown in Fig. 4.2(c) and (d). As it was discussed in Sec. 3.4.3, the different thickness of a SiO_2 layer gives the different regions in the spectra where the destructive interference of a *s*-wave occurs between primary and secondary beams. In these regions, ellipsometric measurements are much more sensitive to any thin layer present on the surface of the substrate. The sample on a 90 nm SiO_2 layer has much broader region of the enhanced sensitivity in the visible range. This can also be seen by observing the difference between the sample and its corresponding substrate ψ and Δ spectra in Fig. 4.2. For this reason only spectra from the sample on a 90 nm SiO_2 substrate have been used in the data interpretation process (Sec. 4.1.2).

4.1.2. SNIE data interpretation and Fano resonant profile modeling of graphene's complex refractive index

The complex refractive index of graphene on a 90 nm SiO_2 layer was obtained from the spectral data by inversion (see Sec. 3.4.2) of the measured spectra shown in Fig.4.2(a) and (b). Inversion was carried out by minimization of the difference between the measured and simulated spectra. Simulated spectra were obtained from the five-phase Fresnel coefficients system. The thickness of the graphene layer is considered known, and is fixed at $d_g = 3.35$ $\mathring{A}$. Optical properties of a Si substrate and thermal SiO_2 layer are taken from Ref. [239].

The optical model has shown that the local thickness of the SiO_2 layer has to change by almost 2 nm in the graphene sample region to allow good fitting of the measured data. Such a large SiO_2 thickness change between sample and substrate ROI is not expected (see Sec. 4.2), so a Cauchy water and air mixture layer has to be added [153]. Parameters for this layer are taken from Ref [74] and its thickness is determined to be 10.2 $\mathring{A}$. This layer is very similar to SiO_2, since both dielectric functions are described by the Cauchy model. The optical model is not sensitive to the position of the water layer relative to the graphene, however it is expected that this water layer remains trapped between graphene and substrate during exfoliation process.

With the optical model set, the complex refractive index of graphene is obtained. In order to obtain as accurate optical parameters as possible, a substrate fitting error is included in the minimization (see Sec. 3.4.2). This way, the substrate fitting error will not be transferred into the error of the optical properties obtained by inversion. The fitting error function used for minimization is:

$$\sigma = \frac{1}{\sqrt{M-P-1}} \left(\sum_{i=1}^{N} \sum_{j=1}^{M} (\psi_{exp} - \psi_{cal} - \delta\psi_{sub})^2 + (\Delta_{exp} - \Delta_{cal} - \delta\Delta_{sub})^2 \right)^{\frac{1}{2}} \tag{4.1}$$

Here all ellipsometric angles are functions of both the wavelength and the incident angle (λ_j, θ_i). M stands for the number of wavelengths for which measurements were carried out. N stands for the number of different angles of incidence. P is the number of fitting parameters. Indices *exp* and *cal* stand for experimental and calculated sample data, respectively. The prefix δ and index *sub* denotes the substrate fitting correction, as described in Sec. 3.4.2.

Optical properties of graphene obtained by inversion are shown in Fig. 4.3(a),

and are marked with circles. The complex refractive index of graphene obtained by inversion was parameterized using the Fano line-shape. This model has only four fitting parameters and it can describe graphene's optical conductance with great precision from the UV to the mid-IR range [65].

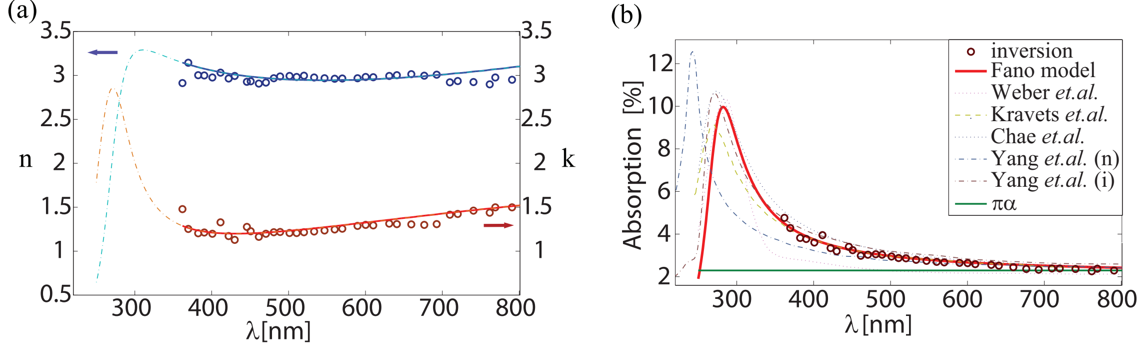

Figure 4.3.: (a) complex refractive index of graphene, obtained by inversion (circles), parameterized by the Fano profile (solid lines) and extrapolated Fano model data (dot-dashed lines); (b) simulated absorption of a free-standing graphene sheet, based on the data from (a). Circles represent absorption calculated from the refractive index obtained by inversion, while solid line represents extrapolated data based on the Fano model. Absorption is compared with the results obtained by other groups [73, 74, 75, 25](dashed and dot-dashed lines). In the data taken from [25], abbreviations (n) and (i) stand for non-interacting and interacting model, respectively.

The real part of graphene's optical conductivity (in units of σ_0) is assumed to be [65, 73, 82] $\Re\sigma(E) = C(s+q)^2/(1+s^2)$. Where $s = 2(E-E_r)/\gamma$, E_r is the resonant (exciton) energy, γ represents the damping (reciprocal lifetime), q stands for the Fano parameter and C is the scaling constant. The optical conductivity is related to the dielectric susceptibility by $\sigma(E) = \epsilon_0 d_g \chi(E)E/i\hbar\sigma_0$. The imaginary part of the dielectric susceptibility then is $\Im\chi(E) = \hbar\sigma_0\Re\sigma(E)/\epsilon_0 d_g E$. Its real part $\Re\chi$ is evaluated numerically from the Kramers-Kronig relations. MATLAB codes used for numerical solving of the principal integral within Kramers-Kronig relations are given in appendices C.4 and C.5. The complex refractive index is then calculated as the square root of the dielectric constant $\epsilon = \epsilon_\infty + \chi$. The best agreement with the inversion data is obtained for: $E_r = 4.55$ eV, $\gamma = 0.83$ eV, $q = -2.70$ and $C = 7.90$. ϵ_∞ was also varied as an independent parameter of the model, however

good agreement was found for $\epsilon_\infty = C$. Results are shown in Fig. 4.3(a). Here solid lines represent the Fano model for optical properties of graphene within the inversion range. Dot-dashed lines represent the extrapolated data to the UV range, showing the Van Hove singularity. Optical properties of graphene obtained by the Fano function are returned to the optical model, and fitted Ψ and Δ spectra are compared with the measured ψ and Δ spectra, Fig. 4.2(a) and 4.2(b). The obtained fitting error is less than one percent for the whole measured range.

Obtained results are compared with other data from the literature [73, 74, 75, 25] and found to be in very good agreement. Absorbance of a free-standing graphene sheet is simulated with the obtained optical properties, and compared with other results in Fig. 4.3(b). Obtained absorption of graphene tends toward $\pi\alpha$ at higher wavelengths, while at 360 nm absorption is almost doubled. Using the Fano model and extrapolating the data into the UV range, the resonant peak in graphene's absorption is estimated. The position of the resonant peak, as well as the peak profile and intensity vary slightly for every sample, most likely due to the unintentional doping by the substrate or surroundings [109].

ROI measurements were also carried out on a graphene sample on a 300 nm SiO_2 layer. Measurements were carried out on single- and bi-layer samples and on the bare substrate simultaneously. Unfortunately due to the shorter resonance within the SiO_2 layer, the Fano parameter extraction was not possible from the data obtained by inversion. Modeling was done in the same way as for the sample on a 90 nm SiO_2 layer. The Cauchy water layer thickness was determined for both single- and bi-layer regions and found to be 8.5 $\AA$ and 6.3 $\AA$, respectively. The thickness of the bi-layer is considered to be $2d_g$, due to the weak interaction between layers in the visible range [60, 73]. Optical properties of graphene are parameterized by the Fano line-shape shown in Fig. 4.3(a). Optical properties of graphene are expected to vary slightly for different graphene samples [109], and the fitting error is slightly higher (2%) than for the sample on the 90 nm SiO_2 layer. Measured ψ and Δ spectra (circles) and the fitted data (solid and dashed lines) are shown in Fig. 4.3(c) and (d).

4.2. SNIE mapping of graphene layer and water layer trapped underneath graphene

This section presents the results of spectroscopic ellipsometry mapping of exfoliated graphene using SNIE. These results are also given in Ref. [83]. Thickness maps of the graphene sample were obtained from spatially resolved ψ and Δ spectra. The data showed the presence of a water layer on the surface of the sample, and the thickness was mapped showing the distribution of water layer trapped underneath exfoliated graphene in ambient conditions.

Ellipsometric mapping was carried out on exfoliated graphene supported by a SiO_2/Si substrate, with 300 nm thick SiO_2 layer. The measured graphene sample (see Fig. 4.1(b)) has single-, bi- and few-layer regions. The sample was mapped with a spatial resolution of 1 μm. The angle of incidence was 60°. ψ and Δ maps were measured at three different wavelengths of 430.0 nm, 470.7 nm and 501.3 nm. These wavelengths were chosen in the area where the difference between graphene and substrate measurements is sufficiently large (see Fig. 4.2(c) and (d)), thus allowing spatial reconstruction of the sample's thickness. The sample's ψ and Δ maps, measured at 430 nm, are shown in Fig. 4.4(a) and (b), respectively.

Using ellipsometric maps, the thickness of graphene and the Cauchy water layer were calculated. The optical model was formed in the same way as described in Section 4.1. Fitting was first done for the substrate, in a few different regions surrounding the sample. Fitting parameters were the thickness of the SiO_2 layer and the angle of incidence θ. The SiO_2 layer thickness was found to be 290.8 nm, varying by ± 0.1 nm in the different regions around the graphene flake. Fitting of the whole map area was done with the graphene layer and water layer thicknesses as the varying parameters. The same point-by-point inversion process has been employed here as described in Sec. 3.4.2. This process was repeated for every point in the ellipsometric map, and substrate correction has not been used. The optical properties of graphene were described by the Fano model, and were kept constant during the fitting procedure. Obtained results are shown in Fig. 4.4(c) and (d), and corresponding thickness cross sections in Fig. 4.4(e) and (f). Here, a clear difference can be seen between the single-, bi- and few layer graphene regions. Average thicknesses of single- and bi-layer graphene were found to be 3.25 $\AA$ and 6.5 $\AA$ ($\pm 0.25\AA$), while their corresponding water layers are 8.5 $\AA$ and 6.5 $\AA$ ($\pm 1\AA$).

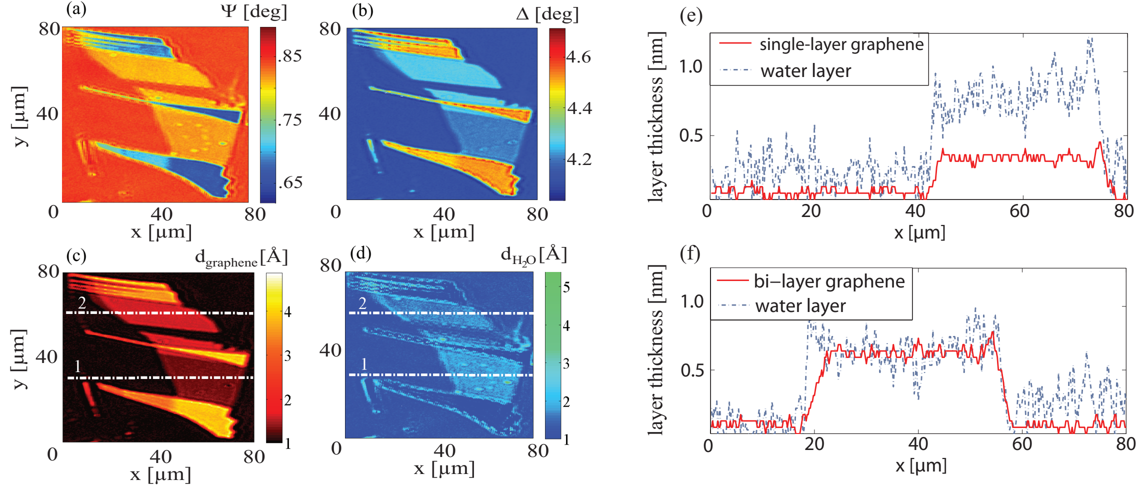

Figure 4.4.: (a) ψ and (b) Δ maps of the graphene sample at a fixed wavelength of 430 nm and under 60° incident angle. (c) Graphene and (d) water layer thickness maps calculated from all spectral maps. Numbers "1" and "2" indicate cross sections for single- and bi-layer regions, respectively. (e) Thickness cross section of the single-layer region, and (f) thickness cross sections of the bi-layer region. Solid line represents graphene layer thickness, while dashed line represents water layer thickness.

The much larger variation of the water layer thickness is due to surface roughness of the substrate, since the thickness of the SiO_2 layer was kept fixed. In Fig. 4.4(d) the distribution of the water layer on the sample can be seen.

Furthermore, the layer thickness results obtained from ψ and Δ spectral maps were compared with the AFM data. For this purpose the area with the single-layer graphene/substrate step is examined. AFM in tapping mode was used (as described in Sec. 2.2.3). Images obtained by AFM are also dependent on the material properties of the tip and the sample. Mainly for this reason, various thicknesses of graphene have been reported in the literature [1, 64, 223, 224, 225, 226]. The image of the sample obtained by AFM is shown in Fig. 4.5(a), with corresponding thickness cross-section underneath. Single-layer graphene/substrate step height was estimated to be 0.98 nm. AFM data is compared with the layer thickness maps for the graphene and water layer, as shown in Fig. 4.5(b) and 4.5(c), respectively. The same region is shown in all the maps.

In Fig. 4.5(a) dirt particles on top of the graphene sample are also visible. These particles are seen in the obtained thickness maps as well, mainly in the water layer

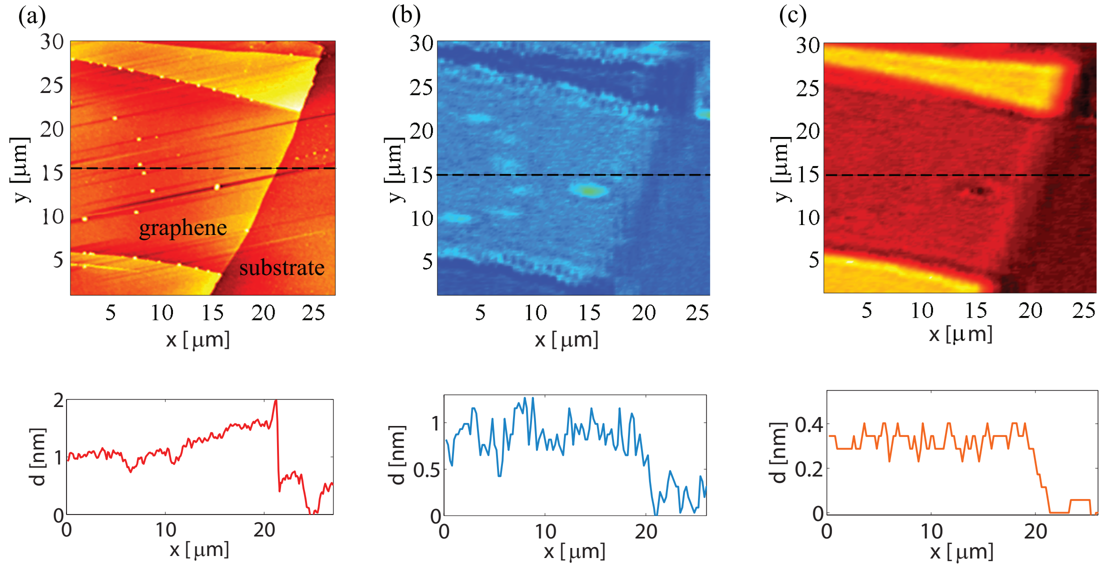

Figure 4.5.: The relation between the AFM and imaging ellipsometry of the single-layer graphene/substrate step. Dashed lines in the maps indicate corresponding cross sections, shown underneath their maps. (a) AFM image of the sample, graphene/substrate step is estimated to be 0.98 nm. (b) Calculated water layer thickness map, step height is estimated to be 0.85 nm. (c) calculated graphene thickness map, step height is estimated to be 0.35 nm.

map Fig. 4.5(b). The number of layers in the optical model was kept fixed for the layer thickness calculations. In the vicinity of the dirt particles, this model is incorrect, and particles are seen as increased thickness of the water layer. Also, the fitting error function was found to be much larger in the vicinity of the dirt particles. This shows that imaging ellipsometry is a promising tool for detection of dirt particles or chemical residue on the graphene samples and devices.

4.3. Influence of transfer residue on optical properties of CVD graphene

In this section spectroscopic ellipsometry (SE) is employed to examine the effects of transfer residue and sample annealing on the optical properties of chemical vapor deposited graphene, transferred onto a sapphire substrate. The optical absorption of graphene was obtained from point-by-point inversion of spectroscopic ellipsometry measurements in the visible and ultraviolet ranges (250-800 nm). Measured spectra were analyzed by an optical models based on the Fresnel coefficient equations. The optical models were supported by correlated Raman, scanning electron microscopy and atomic force microscopy measurements. The obtained data were phenomenologically described by a Fano model. The results show that a residue layer left on graphene can significantly increase its optical absorption in the visible range, compared to an annealed sample [91].

The samples used in this study were grown on Cu foils and transferred on to sapphire substrates. Similar results could be expected for the other types of dielectric substrates such as glass, Si/SiO_2 wafers or polyethylene terephthalate (PET) substrates.

4.3.1. CVD graphene on sapphire: Sample preparation and characterization

Graphene samples (obtained from Graphene Supermarket) used in this study (Sec. 4.3) were grown by the chemical vapor deposition (CVD) technique on a 25 μm-thick copper foil. Single layer graphene was grown on both sides of the copper foil [184, 242, 243]. Graphene samples were transferred by a wet-transfer technique, as described in Sec. 2.1.4 and App. B.3. A short overview of the transfer procedure would be as followed: A 400 nm thick layer of poly(methyl methacrylate) (PMMA), dissolved in a chlorobenzene solution, was drop-cast onto graphene/copper at 60°C. The Cu foil was etched in an iron chloride solution. Dried graphene/PMMA samples were put onto clean sapphire substrates at 90°C, and left to cool down to 60°C. Before removing the PMMA layer from the structure, an additional PMMA layer

was drop coated to dissolve precoated PMMA, thus avoiding graphene tearing [195]. Typical sizes of the transferred samples were several square millimeters.

Removing of the PMMA layer was done by immersing the samples in acetone for one hour. The PMMA was not fully removed and a residue layer was left on the samples. Some of the samples were further cleaned by annealing for 1 h at 480°C in a hydrogen and argon mixed environment [196, 244]. Annealing did remove most of the remaining residue without introducing much tearing to the graphene sheet. The different amount of transfer residue between unheated and heated samples is shown in Fig.4.6, imaged by scanning electron microscopy (SEM) and in Fig.4.7, imaged by atomic force microscopy (AFM).

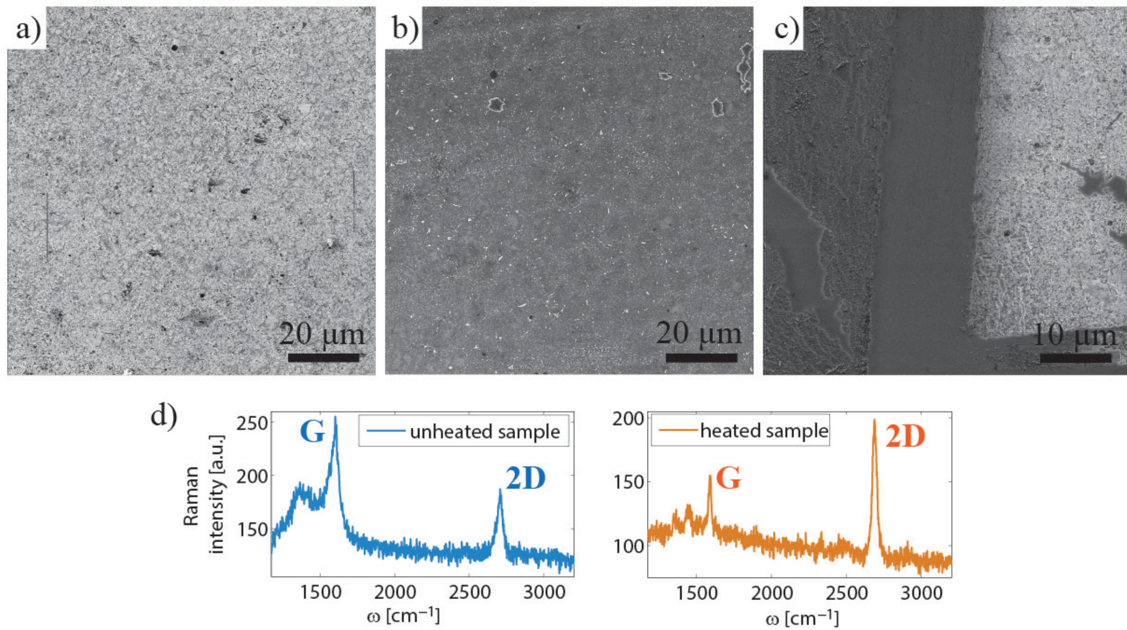

Figure 4.6.: (a) and (b) SEM images of the unheated and heated samples, respectively. The areas of the CVD graphene sample shown corresponds to the position of the ellipsometric spot. Scale bars in (a) and (b) are 20 μm. (c) The edge of the unheated sample, showing transfer residue on the substrate (left), clean substrate (middle) and transfer residue on the graphene sample (right). Scale bar in (c) is 10 μm. (d) Raman spectra of the unheated (left) and heated (right) samples.

In order to investigate the effect of the transfer residue on optical properties of graphene, two different samples were examined: an unheated sample with transfer residue layer, and a heated sample with significantly less transfer residue. In

order to construct a valid optical model, additional measurements that corroborate ellipsometric ones were employed [154]. Samples were characterized by Raman spectroscopy, AFM and SEM. It is worth mentioning that SEM measurements were performed after all the other experiments, in order to avoid potential electron beam damage of the samples [245]. SEM measurements were carried out on a Tescan MIRA3 field-emission gun SEM, at 1 kV in high vacuum with no sample preparation. The room temperature measurements of the Raman spectra of the CVD graphene samples were obtained using the TriVista 557 (S&I GmbH) triple spectrometer system in backscattering micro-Raman configuration. The excitation source was $\lambda = 514.5$ nm coherent mixed Ar+/Kr+ ion gas laser. The laser power on the sample was about 1 mW with a 50× microscope objective, which prevent any sample degradation. Raman spectra confirmed that the samples were single-layer graphene [203, 206]. Raman spectra are shown in Fig.4.6(d).

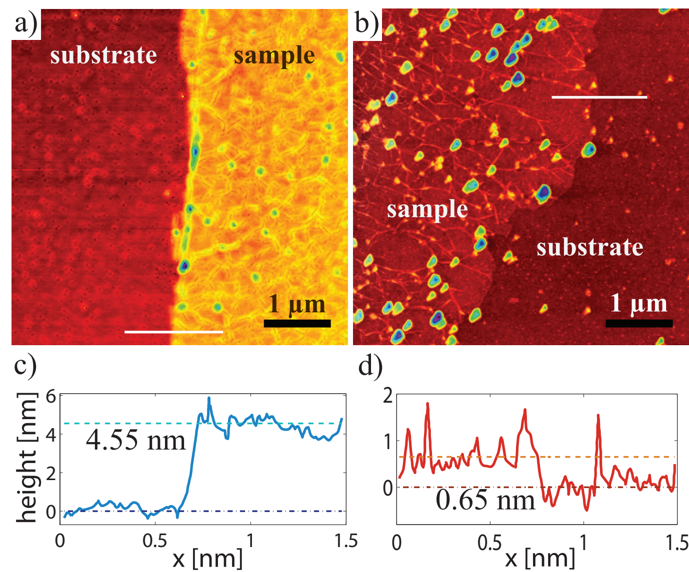

Figure 4.7.: (a) and (b) AFM images of unheated and heated samples, respectively. Areas shown are 5×5 μm^2 step edges between the graphene sample and sapphire substrate. Scale bars (black lines) are 1 μm. White lines in (a) and (b) represent step edge profiles shown in (c) and (d), respectively. The height of the step edge for the unheated sample is shown in (c) and estimated to be 4.55 nm, while the height of the step edge for the annealed sample is shown in (d) and estimated to be 0.65 nm.

A detailed AFM characterization of the samples was carried out in order to build a proper optical model for the analysis of ellipsometric spectra. An atomic force micro-

scope, NTEGRA prima, in the tapping mode was used. Areas of 5×5 μm^2 containing step edges between the graphene sample and sapphire substrate are shown in Fig.4.7 (a) and (b), for the unheated and heated samples, respectively. Corresponding step edge cross sections are shown in Fig.4.7 (c) and (d). The step edge of the annealed sample was found to be 0.65 nm, indicating clean single-layer graphene [1, 223]. The step edge of the unheated sample was found to be 4.55 nm, indicating a 3.9 nm thick transfer residue layer. Also shown in Fig.4.7 (b) are small islands of the transfer residue that remained after the samples were annealed. These islands were found to be on average 25 nm thick and were estimated to cover 5% of the sample surface. This kind of residue island was observed only on the annealed samples.

4.3.2. SE measurements of CVD graphene on sapphire

SE measurements of both heated and unheated CVD graphene on sapphire were performed using SOPRA GES5E-IRSE spectroscopic ellipsometer in a rotating polarizer setup (see Sec. 3.1.5). Spectral data were obtained in the UV and visible ranges from 250 nm to 800 nm, with a 5 nm step. The measured values were presented as $\tan(\psi)$ and $\cos(\Delta)$.

In order to reduce the spot size on the sample a cropping aperture with 200 μm diameter was fixed in front of the analyzer, giving a spot size on the sample of less than 200×585 μm^2. No focusing optics were used, thus ensuring a parallel incident beam on the sample. Measured areas were chosen to be near the sample center in order to avoid any larger tears or wrinkles of graphene, which occur near the edge due to the transfer process. Uniform areas of the samples were significantly larger than the ellipsometric spot, as was confirmed by optical microscopy and SEM.

The ellipsometric measurements were performed at six different angles of incidence: 40°, 45°, 50°, 55°, 65° and 70°. The chosen incident angles were both below and above the Brewster angle of the sample, which is near 60°. Measurements closer to the Brewster angle were not reliable due to a low signal-to-noise ratio. Before changing the angle of incidence, a pair of graphene sample and reference sapphire substrate (near the sample) measurements were performed in order to ensure exactly the same incident angle for both measurements. Measured $\tan(\psi)$ data is shown in

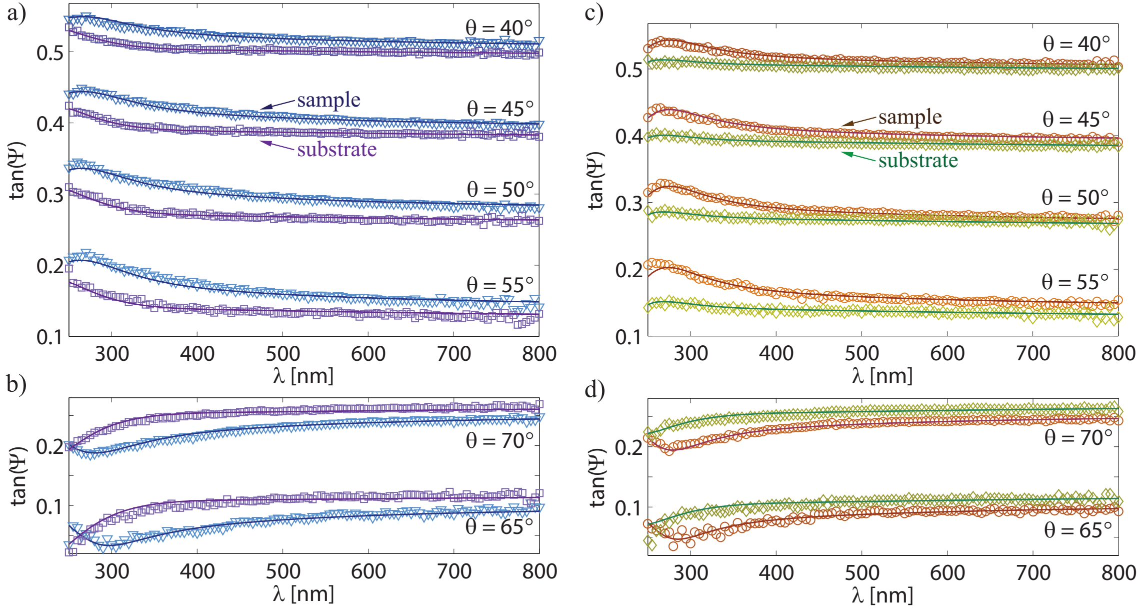

Figure 4.8.: (a) Measurements and fitted data of $\tan(\psi)$ for unheated sample and substrate at four different angles of incidence below the Brewster angle of the sample. (b) Measurements and fitted data of $\tan(\psi)$ for unheated sample and substrate at two different angles of incidence above the Brewster angle. (c) Measurements and fitted data of $\tan(\psi)$ for annealed sample and substrate at four different angles of incidence below the Brewster angle. (d) Measurements and fitted data of $\tan(\psi)$ for annealed sample and substrate at two different angles of incidence above the Brewster angle.

Fig.4.8. Data for $\cos(\Delta)$ are not presented since measured values were close to ± 1 in the entire spectral range and under all the chosen angles of incidence. The reason for this is the transparent sapphire substrate. Due to the choice of the substrate, ellipsometric measurements were more sensitive to the imaginary part of the dielectric function.

A comparison of $\tan(\psi)$ data between unheated and heated graphene sample measurements and their reference substrates are shown in Fig. 4.9(a) for the incident angle of 45°. Fitted spectra were obtained from the Fresnel coefficients systems based on the adequate layer structures consisting of a sapphire substrate, graphene layer and transfer residue layer. Schematic representations of the optical models used are shown in Fig. 4.9(b). Data obtained from AFM and Raman measurements was used to define the thickness of the layers. CVD graphene was modeled as an isotropic

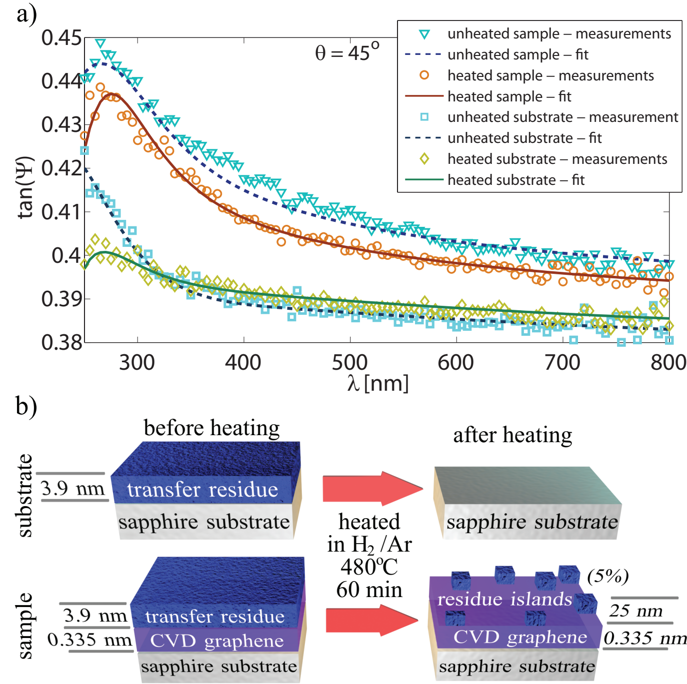

Figure 4.9.: (a) Compared measurements of $\tan(\psi)$ for heated and unheated samples at incident angle of 45°. (b) schematic representation of optical models used for fitting different measurements shown in (a) and in Fig.4.8.

material [84, 85] with a fixed thickness of 0.335 nm. The thickness of the transfer residue layer was obtained from AFM measurements and kept fixed at 3.9 nm for the unheated sample. After annealing, some residue still remained on the sample. The remaining residue formed 25 nm thick islands, covering 5% of the sample surface (see Fig. 4.7(b)). This was taken into account with an island-film model [81, 153] for the transfer residue layer on the annealed graphene sample.

4.3.3. Optical properties of CVD graphene on sapphire: Influence of transfer residue

As it was discussed in Sec.-s 3.3 and 3.4 corroborated ellipsometric measurements of sapphire substrates were used to determine optical properties and layer thicknesses of all the other layers within the optical model except for the graphene layer. Measurements of the annealed substrate (diamond in Fig. 4.8 and Fig. 4.9(a)) were used

to obtain the dielectric function of the sapphire. Since it is transparent (dielectric) in the measured range, the imaginary part of its dielectric function was considered to be zero. The real part of the dielectric function of sapphire was obtained from point-by-point inversion, and it is shown in Fig. 4.10(a). Optical properties of the transfer residue were obtained from the measurements of the unheated sapphire substrate (square in Fig. 4.8 and Fig. 4.9(a)). In Fig. 4.6(c), a SEM image of the remaining transfer residue on the substrate (left) and on the sample (right) is shown. In the measured spectra of the unheated substrate's tan(ψ), transfer residue shows a distinct absorption in the UV range while it has no effect in the visible range, compared to the bare (annealed) sapphire substrate. This can be seen in Fig. 4.9(a) (diamond and square data).

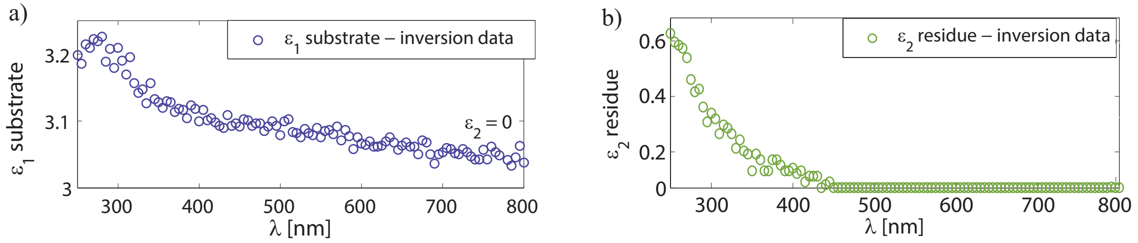

Figure 4.10.: (a) Real part of the dielectric function of the sapphire substrate obtained by inversion (circles) from heated substrate measurements data shown in Fig. 4.8. The imaginary part of the dielectric function of the sapphire substrate was considered to be zero. (b) Transfer residue layer's imaginary part of the dielectric function obtained by inversion. As can be seen in (b) the residue layer is transparent in the visible range. The real part of the dielectric function is not shown, since measurements were more sensitive to the imaginary part of the dielectric function.

Optical properties of the transfer residue layer were obtained by inversion. The imaginary part of the dielectric function of the transfer residue layer is shown in Fig.4.10(b). The thickness of the residue layer was kept fixed at 3.9 nm during the inversion. Variations of the residue layer thickness by as much as few nanometers does not affect the data obtained for the graphene layer. Significant variation of the graphene inversion data was found only when the thickness of the residue layer was comparable to the incident wavelength. Such a large variation of the residue layer thickness from the data obtained by the AFM is not possible, thus the residue layer

can not contribute to the absorption in the visible range.

With known thicknesses and dielectric functions of all layers within the optical model except for the graphene layer, a point-by-point inversion was employed to retrieve its optical properties. Extinction coefficients k and refractive indices n, obtained for both unheated and heated samples, are shown in Fig. 4.11(a) and Fig. 4.11(b), respectively. Obtained inversion data was used to calculate optical absorption of the graphene sheet, and is shown in Fig. 4.11(c). Heated sample data is presented by circles, and unheated sample data is presented by triangles. The difference in the absorption between the samples is caused by the transfer residue layer, but the absorption does occur within graphene since the absorption of the residue layer has been accounted for within the optical model. Furthermore, the residue layer did not introduce any change in the substrate's $\tan(\psi)$ data in the visible range, but in the case of graphene a significant increase of absorption within the entire visible range was detected.

Optical properties of graphene obtained by inversion are parameterized using a Fano model. The same procedure hass been used as described in Sec. 4.1.2. The best agreement with the inversion data was obtained for the sets of parameters presented in Table 4.1.

Table 4.1.: Fano parameters: CVD graphene w/wo transfer residue

Fano parameters	**sample with residue**	**annealed sample**
E_r [eV]	4.62	4.63
γ [eV]	2.21	1.65
q	-4.90	-4.05
C	$5.04 \cdot 10^{-2}$	$7.02 \cdot 10^{-2}$

Results obtained for the annealed sample are in very good agreement with the results available in the literature [65, 73, 74, 84] for both CVD and exfoliated graphene. However, results obtained from the sample with significant amount of transfer residue shows broadening of the absorption peak which increases the optical absorption of graphene by an average of 30% in the visible range, compared to the annealed sample. Phenomenologically described by a Fano model, the broadening can be interpreted as an increased damping and asymmetry of the resonant peak. Interestingly, the position of the resonant peak shows a negligible shift af-

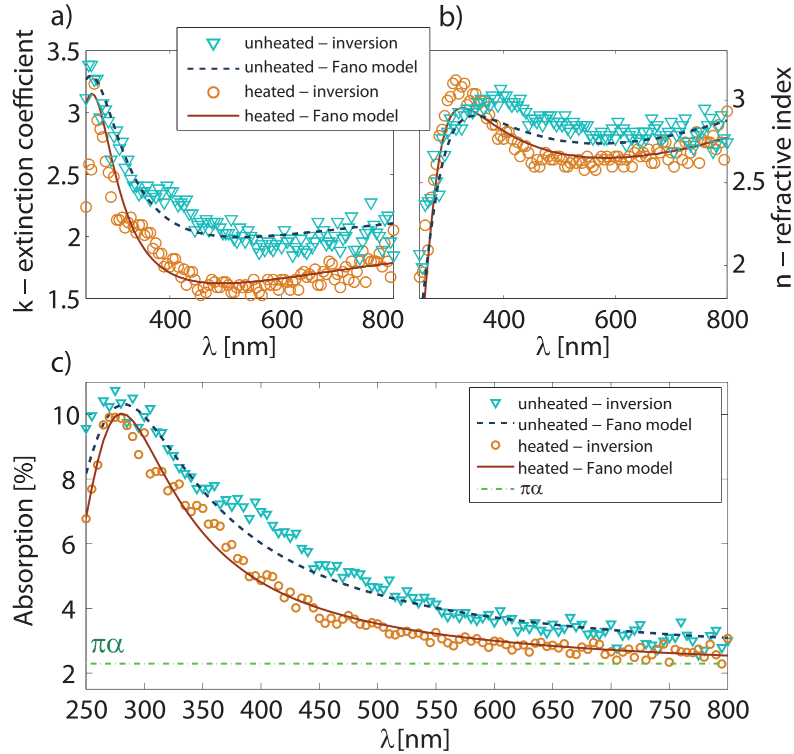

Figure 4.11.: (a) Extinction coefficients, (b) refractive indices and (c) optical absorption of CVD graphene, compared for unheated (triangles) and heated (circles) samples, obtained by inversion. Data were modeled by a Fano resonant profile for heated (solid line) and unheated (dashed line) sample. Unheated graphene layer shows increased absorption caused by the remaining transfer residue.

ter annealing. This indicates that the residue layer does not modulate graphene's electrical properties. If graphene was doped, additional carriers would change the electron-electron and electron-hole interaction balance present in the intrinsic samples, thus introducing a shift of the resonant peak [43, 89]. The next section will focus on how an interaction with an underlaying metallic substrate can modify a balance of electron-electron and electron-hole interaction that is present in a pristine sample.

4.4. Influence of gold substrate on optical properties of graphene

In this section, SE combined with measurements of electrical characteristics and Kelvin probe force microscopy have been employed to investigate the interaction between graphene and a gold substrate, and the consequent changes of graphene's complex refractive index on gold [92]. A strong blue shift, as much as 350 meV, of the prominent absorption peak (exciton-shifted M-point Van Hove singularity in the ultraviolet range) of graphene has been observed, with respect to the peak position for the sample on an insulating substrate where this peak was observed at about 4.55 eV. The results show that an interaction between graphene and a gold substrate can be characterized through the change of graphene's optical properties. In addition, the effects that a water layer trapped between graphene and gold during the transfer process has on the charge transfer between graphene and the gold substrate have been investigated.

Most of the emerging graphene applications require metallic, usually gold contacts. Changes of the optical properties of graphene on a metallic interface can give insight into their properties without a need to make external electrical contacts. For the future in-line and post-fabrication contactless control, it is necessary to know how the interaction with a metal modifies the optical properties of graphene. Recently, several types of graphene-based electronic and optoelectronic devices [14] have been realized by transferring chemical vapor deposited (CVD) graphene onto a prefabricated structure. Furthermore, gold films have been used as substrates for CVD growth of graphene [246], as well as in novel transfer processes [247]. First principles [231], electrical transport [232], scanning tunneling spectroscopy [233], angle-resolved photoemission spectroscopy [234] and Raman spectroscopy [235] studies all show that graphene on gold is *p*-doped. The results presented in this section, an in publication related to the dissertation [92] report on the influence of the interaction with a gold substrate on the optical properties of graphene.

As it has been discussed in Sec. 1.2, the optical properties of graphene have been studied in detail in the last several years [51]. Particularly, in the ultraviolet (UV) range, optical properties of graphene are dominated by the excitonic red-shifted interband transitions near the M-point in the Brillouin zone of graphene [65, 73, 74], resulting with a prominent asymmetric absorption peak positioned at about 4.6 eV.

However, only recently several studies[43, 66, 89, 90, 92, 109] have shown that by changing the doping level in graphene, a balance between the electron-electron (e-e) interaction and the electron-hole (e-h) interaction can be modified, which causes the change of the absorption peak's shape and position. In the case of graphene doped by an electric field (through electrochemical gating), as theoretically predicted [109], a further red shift and broadening of the prominent absorption peak has been observed [43], indicating a suppression of e-e interaction.

The other way to introduce doping of graphene is through the interaction with its surroundings. Y.-C. Chang and coworkers [66] investigated how chemical doping with nitric acid modifies the complex optical conductivity, and found a negligible shift of the prominent peak. Optical properties of graphene grown on a copper substrate have been investigated in Refs. [89, 90]. In that case, the interaction with the substrate mainly suppresses e-h interaction, and the absorption peak was found to be blue shifted and symmetrical, similar to the expectations of the independent particle model [25], where the electron-hole interaction has not been accounted for.

4.4.1. CVD graphene on gold: Sample preparation and characterization

In order to examine how a metallic substrate affects graphene, a single-layer CVD grown graphene is transferred over a SiO_2/Si substrate partly covered by a thin gold film. This subsection focuses on the details regarding a wet transfer technique, evaporation of metallic film and characterization of the samples using Raman spectroscopy.

Samples of commercially available CVD graphene (Graphenea) were transferred from copper foils via a wet transfer route, as described in Ref.-s [195, 196, 197] and in Sec. 2.1.4. To support the graphene film during the transfer, a chlorobenzene solution of a poly(methyl methacrylate) (PMMA) was drop-casted on graphene/Cu at a temperature of 60°C, resulting in a 300 nm thick PMMA layer. The Cu foil was etched in an iron chloride solution (40 mg of $FeCl_3$ per 1 ml of deionized water). The PMMA/graphene stacks were rinsed in deionized water several times to remove iron residues and left to dry. Subsequently, dried PMMA/graphene stacks were put

on targeted substrates at 90°C for 5 minutes, and cooled down to 60°C. At this temperature, a diluted drop of PMMA was drop-casted to dissolve the pre-coated PMMA layer. Additional PMMA coating helps in avoiding cracks and also results in better attachment of graphene to the substrate [195]. After cooling down to room temperature, samples were kept in acetone for 30 minutes to dissolve the PMMA layer. Afterwards, samples were scooped from acetone and put in acetic acid for 24 hours as described in Ref. [197]. Samples were cleaned in acetic acid several times and then rinsed in a mixture of methanol and deionized water. A further cleaning was done in isopropanol and finally in deionized water several times.

For a supporting substrate, an 80 nm thick SiO_2 layer was grown by dry thermal oxidation of a silicon wafer, and afterwards partly covered by a thin gold film. The gold films were evaporated using a "home-built" hot filament system with a deposition rate of 0.25 nm/s, under 3×10^{-6} mbar chamber pressure, resulting in 10-15 nm thick films. The chosen thickness of gold (~12 nm) ensured continuous and conductive films, but still allowed for graphene to be visible by optical contrast [61, 233]. After the transfer process no thermal annealing was carried out. This is very important for the case when graphene is transferred over prefabricated micro- or nano-structures that can not sustain high temperature annealing.

Sample annealing at temperatures up to 350°C has been investigated as an attempt to remove the water layer from the interface. Annealing was carried out in argon gas flow (~5 l/min) for 3 hours. These annealing parameters were found as sufficient to partly remove the water layer [248]. However, annealing was found to introduce a large number of cracks and defects as previously reported by [198], thus significantly reducing surface area of graphene. Furthermore, annealing was found to significantly increase the roughness of the evaporated gold film, causing the increase of the sheet resistivity of gold film by two orders of magnitude. Optical models of the annealed samples would have to account for these changes in the structure by including an island-film model and roughness layers, which would significantly increase the uncertainty of the obtained optical properties of graphene on gold. For these reasons thermal annealing has not been carried out. Water layer, trapped between graphene and a substrate, was found to be stable in ambient conditions and no changes in the sample structure were observed by any of the techniques employed in this study.

Raman spectroscopy has been employed to confirm that samples were single layer

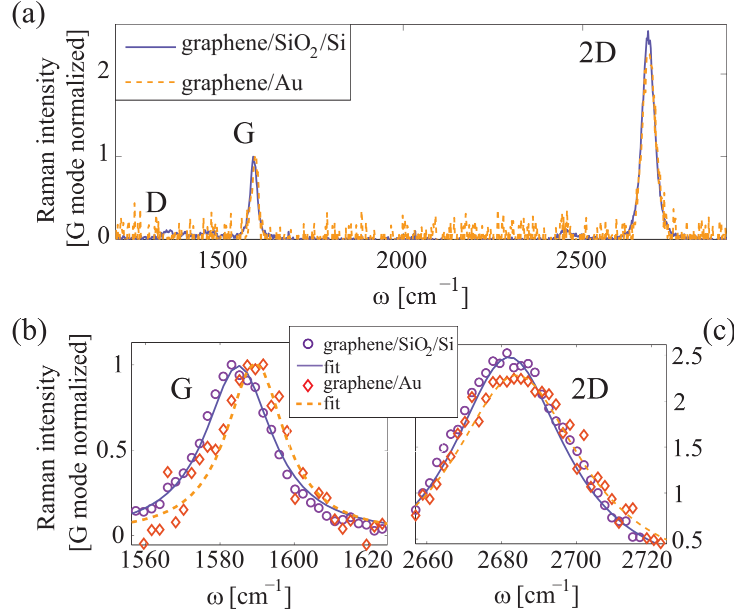

Figure 4.12.: (a) Raman spectra of graphene on Si/SiO_2 (solid line) and graphene on gold (dashed line). (b) and (c) enlarged G and 2D modes of (a). Variations between graphene on Si/SiO_2 and on gold, are attributed to the weak *p*-doping introduced by the gold substrate. The intensities have been normalized to $I_G = 1$ and luminescence for the sample on gold has been deducted.

graphene with negligible amount of defects and transfer residue. Room temperature measurements of Raman spectra were obtained using a TriVista 557 (S&I GmbH) triple spectrometer system in backscattering micro-Raman configuration. The excitation source was a $\lambda = 514.5$ nm coherent mixed Ar+/Kr+ ion gas laser. The laser power on the sample was less than 1 mW with a 50× microscope objective. Low laser power ensured negligible effects of sample heating on the shifts of Raman modes.

Raman spectra of graphene were measured in the sample area used for SE measurements, both on an SiO_2/Si and on gold substrates. Raman spectra were characterized mainly by two modes: G (~1585 cm^{-1}) and $2D$ (~2685 cm^{-1}), and their relative intensities (I_{2D}/I_G). The lack of the defect (D) mode (~1350 cm^{-1}), symmetric shape of the $2D$ mode and I_{2D}/I_G intensity usually greater than two, all indicate very clean single layer samples. G and $2D$ modes of the measured spectra were fitted with single Lorentzian lines. A pair of Raman measurements for graphene on SiO_2/Si and graphene on gold are shown in Fig. 4.12. The intensities

have been normalized to I_G=1 and luminescence for the sample on gold has been deducted. Both the peak positions and the relative intensities for graphene on SiO_2/Si indicate a weak *p*-doping of graphene [45, 208], which is most likely caused by the transfer process [45, 208]. This has been confirmed also by the measurements of the DC electrical characteristics. For the case of graphene on gold, slightly stronger *p*-doping of graphene has been found, as can be seen by the relative change in the position, width and intensity of both the G and $2D$ modes, shown in Figs. 4.12(b) and 4.12(c); however, local variations of the mode's positions, widths and intensities were found to be comparable with those introduced by the interaction with the gold substrate. These were attributed to spatially non-uniform adhesion, resulting in non-uniform doping by the substrate and non-uniform strain [209, 210, 211]. For this reason, in the case when graphene is transferred over gold electrodes, Raman spectroscopy alone can not be used to characterize the interaction between graphene and the gold substrate. These results are in agreement with the data reported in Ref.-s [235, 210, 211], where a strain effect played a major role over the charge transfer in the Raman spectra of gold covered graphene.

4.4.2. Measurements of direct current electrical characteristics

In order to characterize electrical properties of the graphene/gold interface, measurements of direct-current (DC) electrical characteristics were carried out at room temperature. For this purpose, during the gold film evaporation process a ~20 μm long and greater than 1 mm wide channel has been made by a shadow mask. In this manner two gold electrodes were made, source (s) and drain (d). Graphene was then transferred over the substrate, covering the channel, gold electrodes and bare SiO_2/Si on the other side of the electrode, thus having enough surface area to carry out both electrical and SE measurements on the same graphene sample. The results shown in Sec. 2.2.5 in Fig. 2.13. For that particular sample the channel was 17 μm long and 1040 μm wide. Device geometry has been determined by optical microscopy.

In Sec. 2.2.5, Fig. 2.13(a) and (b) show schematic representations of the electrical measurement setups. Measurements were carried out in low vacuum (8×10^{-3}

mbar), in order to avoid dipolar adsorbates from the ambient environment [237, 236]. Figure 2.13(c) shows the dependence of the total resistivity (R_{ds}) between s and d electrodes, as a function of a back gate voltage (V_{bg}). Here, the graphene channel shows an "ambipolar" field effect.[1, 211] A charge neutrality point (CNP) was found to be at 2 ($\pm$0.5) V. This indicates that an unbiased graphene channel is slightly p-doped. These results are in agreement with Raman measurements. To confirm that the contacts between graphene and the gold electrode are Ohmic, even with a water layer in between, DC measurements of a current (I_{ds}) as a function of an applied voltage (V_{ds}) between source and drain electrodes were performed. During these measurements, Si substrate (back gate) was grounded. The results are shown in fig. 2.13(d), where a linear dependence of the current over the applied voltage range confirms Ohmic behavior of the graphene/gold interface. A linear fit of the $I_{ds}(V_{ds})$ gives a total device resistivity of 210 Ω.

4.4.3. SE measurements of CVD graphene on gold substrate

Optical properties of graphene both on SiO_2/Si and on gold substrates were obtained using spectroscopic ellipsometry. SE measurements were performed using a SOPRA GES5E-IRSE spectroscopic ellipsometer in a rotating polarizer setup (see Sec. 3.1.5). The spectra were obtained from 1.4 eV to 5.5 eV, with a 0.035 eV step, and under four different angles of incidence ranging from 55° to 70°. Since the samples were not uniform over the entire substrate, the position of the ellipsometric spot on the sample was controlled by a CCD camera with a 40× magnification objective, placed away from the optical path of the ellipsometer. This allowed for the ellipsometric spot to be placed over the uniform area of the sample with negligible amount of cracks and folds in the graphene layer as well as negligible amount of transfer residue. For SE measurements, no focusing optics were used, thus ensuring a parallel incident beam on the sample. In order to reduce the spot size on the sample a cropping aperture with 200 μm diameter was fixed in front of the analyzer. The spot size on the sample was estimated by the knife-edge technique, and found to be less than 350×1000 μm^2.

The measured $\tan(\psi)$ and $\cos(\Delta)$ spectra were analyzed by optical models based

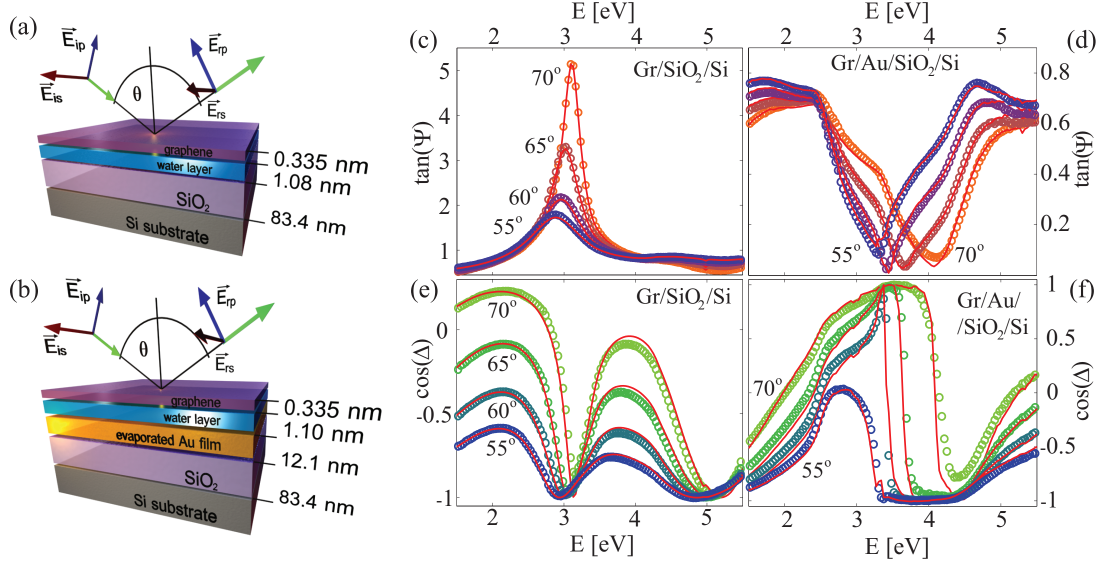

Figure 4.13.: (a) and (b) schematic representations of the optical models used to interpret ellipsometric measurements of graphene on SiO_2/Si and on gold substrates, respectively. (a) and (b) also show p- and s-polarization of the light. (c) to (f) measured (circles) and fitted (solid lines) $\tan(\psi)$ and $\cos(\Delta)$. Measurements were performed under four different angles of incidence, from 55° to 70°. The fitted data uses refractive indices of graphene modeled by a Fano resonant profile.

on the Fresnel equations [153], as described in Sec. 3.2. In order to build accurate models, corroborated AFM and Raman measurements were employed [154]. Raman spectroscopy was used to confirm that samples were single-layer graphene with negligible amount of defects and transfer residue [206, 203]. AFM was used to determine the thickness of the evaporated gold film (~12 nm) and the height of graphene (~1.4 nm) on both substrates. Since graphene thickness was fixed in the optical model (0.335 nm) the AFM height indicated a water layer trapped between graphene and the substrate of about 1 nm. Presence of a water layer has been previously measured by ellipsometry for exfoliated graphene [74, 83], and was detected in the ellipsometric spectra for both graphene on SiO_2/Si and on gold substrates. This water layer was expected since no thermal annealing was done after the transfer process. It was accounted for in the optical model by a Cauchy water and air mixture layer, with parameters taken from Ref. [74] and its thickness varied by about 10% from the AFM measured data in order to ensure better fitting to the measured SE data. Schematic representation of the optical models are shown in Fig. 4.13(a)

and 4.13(b), for graphene on SiO_2/Si and on gold substrates, respectively. The measured (circles) and the fitted (solid lines) SE data are shown in Fig. 4.13(c) to 4.13(f), for four different angles of incidence (55°, 60°, 65° and 70°). The fitted data uses refractive indices of graphene modeled by a Fano resonant profile. Measurements at angles of incidence above 70° were not possible, since clear sample areas would be smaller than the size of the SE spot. On the other hand, measurements at angles below 55° would be less reliable, since the difference in $\tan(\psi)$ and $\cos(\Delta)$ between the graphene layer on the substrate and the bare substrate decreases with the decrease of an incident angle. Surface roughness layers were not used within the optical model. The roughness of each surface (graphene, gold, SiO_2) was measured by AFM as a root mean square of a 2×2 m^2 area. Addition of the roughness layers in the optical model was found to cause a negligible change in the retrieved optical properties of graphene. This was examined even with higher roughness layers (~1 nm) than those suggested by the AFM (less than 0.5 nm).

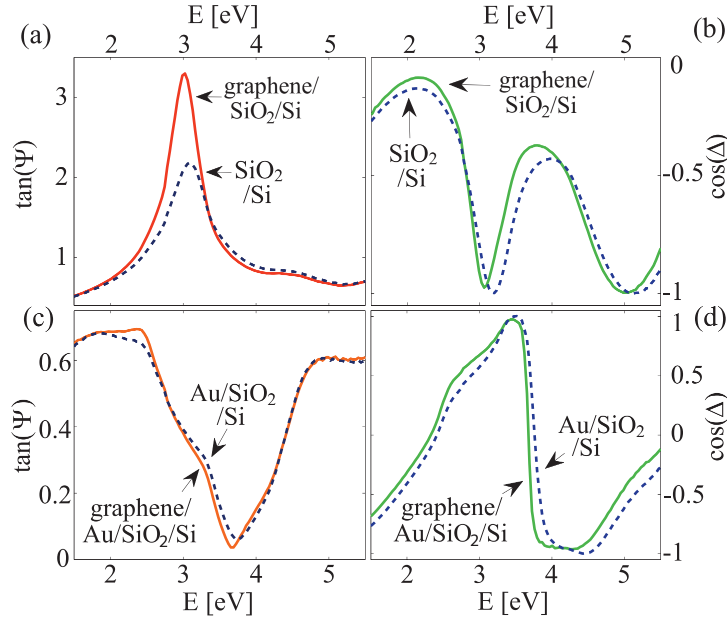

Figure 4.14.: (a) and (b) compared $\tan(\psi)$ and $\cos(\Delta)$ of graphene on SiO_2/Si (solid lines) and bare SiO_2/Si substrate (dashed lines). (c) and (d) compared $\tan(\psi)$ and $\cos(\Delta)$ of graphene on Au/SiO_2/Si (solid lines) and bare Au/SiO_2/Si (dashed lines).

The differences between the samples and their corresponding substrate measurements for both graphene on SiO_2/Si and on gold substrates, are shown in Fig. 4.14, for a fixed angle of incidence (65°). These differences are caused both by graphene

and the water layer, and they determine the reliability of the extracted optical parameters of graphene [62, 83] (see also Sec. 3.4.3). A larger difference between spectra of the sample and the corresponding substrate indicates more reliable measurements. In the case of an SiO_2/Si substrate, the change in polarization caused by the SiO_2 layer has a series of constructive and destructive resonances. These resonances occur when the phase shift of a secondary beam becomes exactly a half integer of the wavelength [153].

The maximum in $\tan(\psi)$ appears for destructive interference of s-polarization. In a relatively large spectral range around these resonances, the system is very sensitive to any thin layer on top of it. Furthermore, by changing the angle of incidence the path of light within the SiO_2 layer is changed. As a consequence the wavelength that satisfies the condition for the destructive interference of s-polarization within the SiO_2 is changed. This results with a changed sensitivity of the measurements within the different parts of the spectra. When a gold film is added it changes the conditions required for the destructive interference of s-polarization within the SiO_2 layer. As a consequence, the difference between the measurements of a graphene sample on an Au/SiO_2/Si and its corresponding substrate measurements is smaller compared with the spectra of the sample on SiO_2/Si. For this reason, obtained optical properties of graphene on gold are less reliable, especially in the ranges below 2 eV and above 5 eV, where the difference between the sample and the substrate measurements is mainly governed by the water layer.

Graphene transferred onto the substrate covered only a part of it, thus leaving both bare SiO_2/Si and Au/SiO_2/Si areas on the same sample. This allowed for substrate measurements to be taken very near (about 1 mm) to their corresponding sample measurements. At a given angle of incidence, a set of four subsequent measurements was performed: SiO_2/Si, Au/SiO_2/Si, graphene/SiO_2/Si and graphene/Au/SiO_2/Si, thus ensuring exactly the same angle of incidence for all four structures. SiO_2/Si substrate measurements were used to determine the exact angle of incidence, and the exact thickness of the SiO_2 layer (83.4 nm). Au/SiO_2/Si substrate measurements were used to obtain the exact complex refractive index of the evaporated gold film. This was done through point-by-point inversion. The thickness of the gold layer was kept fixed at 12.1 nm during the inversion.

4.4.4. Optical properties of CVD graphene on gold

Once all the parameters of the optical model were known, the complex refractive indices of graphene on both substrates were obtained using point-by-point inversion (see Fig. 4.15(a) and 4.15(b), respectively). Graphene was modeled as an isotropic material [74] with a fixed thickness of 0.335 nm. During the inversion process the difference between the measured and fitted SE spectra is minimized by varying the complex refractive index of graphene. This means that any instrumental errors or any discrepancies introduced by improper optical models will be transferred into an error of the obtained optical properties of graphene. To minimize this, a substrate fitting error is included in the minimization, by using the fitting error function as described in Sec. 3.4.2 and in Ref. [83].

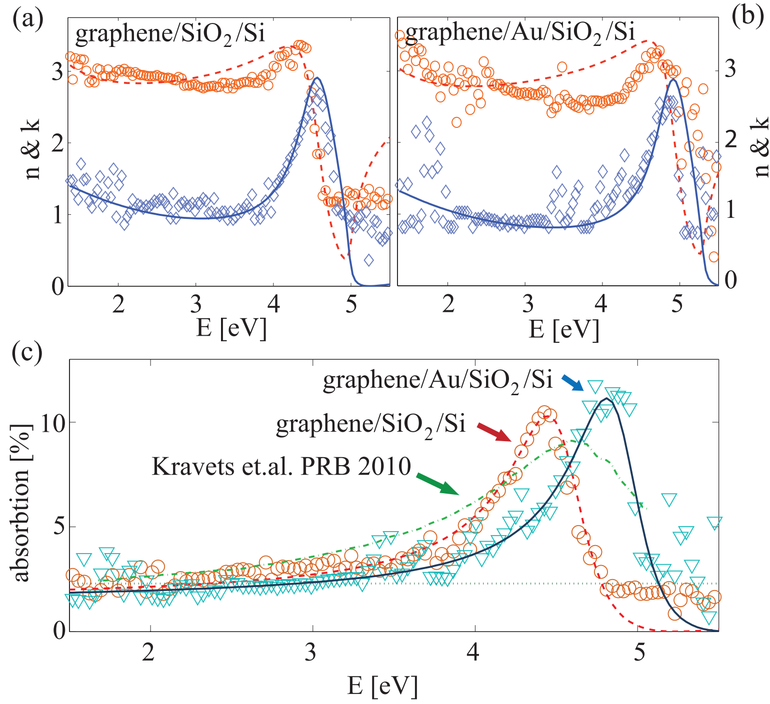

Figure 4.15.: (a) and (b) refractive indices (circles) and extinction coefficients (diamonds) of graphene on Si/SiO$_2$ and on gold, respectively. The data was obtained through point-by-point inversion and parameterized by a Fano model (solid and dashed lines). (c) the calculated absorption of a graphene layer using the data from (a) and (b). A blue shift (350 meV) of the prominent absorption peak was observed. Dot-dashed curve in (c) represents the absorption function of exfoliated graphene taken from Ref. [74], while the dotted line represents $\pi\alpha = 2.3\%$.

Table 4.2.: Fano parameters: CVD graphene w/wo gold interlayer

parameters	**graphene/SiO_2/Si**	**graphene/Au**
E_r *[eV]*	4.54	4.89
γ *[eV]*	0.51	0.47
q	-2.73	-2.93
C	0.15	0.14

The complex refractive indices obtained by inversion were parameterized by a Fano resonant model, as described in Ref.-s [82, 83, 91] and in Sec. 4.1.2. This model consists of only four fitting parameters: the resonant (exciton) energy E_r, the damping γ, the Fano (asymmetry) parameter q, and the scaling constant C. The best agreement with the inversion data was obtained for the sets of parameters presented in Table 4.2. ϵ_∞ was also varied and found to be 8($\pm$0.05) in both cases. The Fano resonant profile shows good agreement with the data obtained by inversion, except for the refractive indices (n) in the range 3-4.5 eV. This discrepancy with a Fano model could be attributed to the effects of grain boundaries of CVD graphene [89, 90]. The Kramers-Kronig consistency of the data obtained by the point by point analysis has been checked [249] (also see App. C.5). Complex refractive indices were found to be Kramers-Kronig consistent even in the part of the spectra where the discrepancy with the Fano profile exists [92].

The results obtained for the samples on an SiO_2/Si substrate (Fig. 4.15(a)) are in good agreement with the results reported for both exfoliated [74, 75, 83] and CVD [84, 91] graphene on various insulating substrates. The comparison between the absorption functions obtained in this study and those of exfoliated graphene [74] are presented in Fig. 4.15 (c). The prominent peak of graphene on SiO_2/Si was found to be sharper and red shifted by 50 meV. These differences could be attributed to the effects of grain boundaries of CVD graphene and the different amount of unintentional doping. Furthermore, the complex refractive index of graphene presented in Fig. 4.15(a) is in an excellent agreement with the results reported for graphene by M. Bruna and S. Borini [241] in the visible range (1.5-3 eV). For the samples on gold (Fig. 4.15(b)), a prominent absorption peak was found to be blue shifted by about 350 meV (Fig.4.15 (c)). These results are in good agreement with the data reported for CVD graphene grown on copper [89, 90]. Compared with those

results, a similar blue shift of the resonant peak was found in this study. However, the profile of the resonant peak was found to be asymmetrical in this study. The differences are attributed to the fact that graphene transferred on gold still has a water layer trapped in between, which is not the case for graphene grown on copper. The shift of the prominent absorption peak was attributed to the screening of e-h interactions in graphene on a gold substrate [89].

4.4.5. KPFM analysis of graphene/gold interface

To corroborate ellipsometric measurements, and to determine the type and estimate the amount of doping in graphene on a gold substrate, AFM and KPFM have been used. Measurements were performed using an NTEGRA Prima scanning probe microscope, with conductive TiN coated tips (NT-MDT NSG01). KPFM was done using the two-pass technique, as described in Sec. 2.2.4. In the first pass, a topographic line was measured in the tapping mode. In the second pass, the tip was lifted by 30 nm and moved across the surface following the topographic profile, obtained from the first scan. During the second pass, a combination of an AC and DC voltage was applied between the tip and the grounded silicon substrate. The frequency of the AC voltage was matched to the resonant frequency of the cantilever. The DC component was then adjusted to cancel an electrostatic force between the tip and the sample, resulting with a zero amplitude of the cantilever oscillations (near its resonant frequency). This procedure was repeated for every point of a selected area of the sample. Resulting KPFM maps show the applied DC component, *i.e.* the contact potential difference (CPD) between the sample and the AFM tip.

Figures 4.16(a) to 4.16(d) show an optical microscope image, AFM topography, AFM phase and KPFM maps, respectively. The maps show an area of the sample where the edge of graphene overlaps the edge of the evaporated gold film. Phase contrast (Fig. 4.16(c)) was the same in both forward and backward scan directions, confirming that it does correspond to a material contrast. A histogram of a KPFM map is shown in Fig. 4.16(e). Here, three peaks are clearly distinguishable. These peaks are fitted with single Gaussian lines, and their positions indicate a CPD of the three different surfaces. A CPD is defined as: $e \cdot \mathrm{CPD} = \mathrm{W}_{tip} - \mathrm{W}_{sample}$, where

e denotes an elementary charge, W_{tip} and W_{sample} denote the work functions of the tip and the sample, respectively.

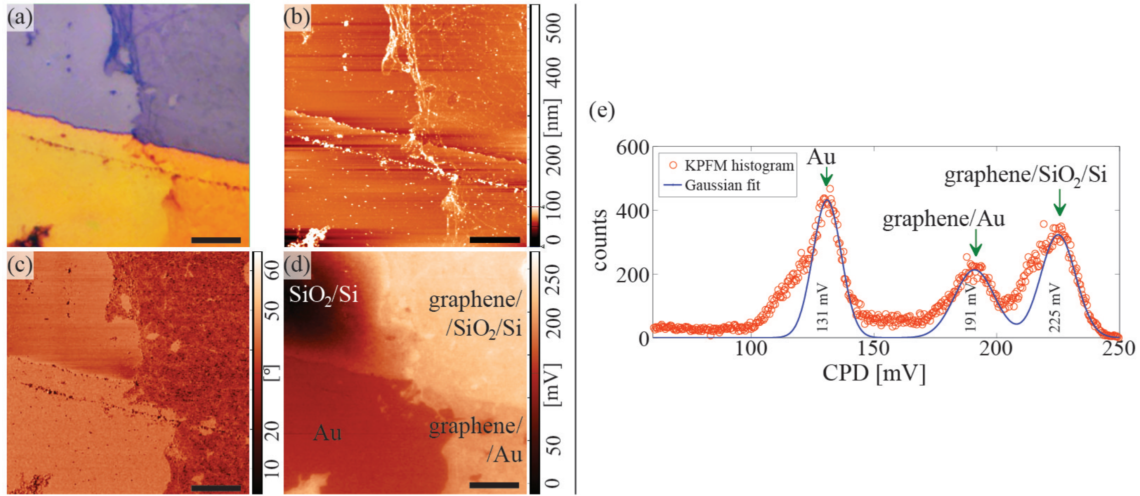

Figure 4.16.: (a) to (d) optical microscope image, AFM topography, AFM phase and KPFM maps, respectively. Each image shows the same 50×50 μm^2 area of the sample (10 μm scale bar). An edge of the graphene sample overlapping an edge of the evaporated gold film are seen on each image, and denoted in (d). (e) a histogram of (d), with three distinguished peaks corresponding to the surface potential of the different structures shown in (d).

The CPD peak of SiO_2/Si was not resolved due to the zone bending in the area of SiO_2/Si, which is a consequence of the electric field gradient between gold/graphene electrodes and the silicon substrate. For the sample presented in Fig. 4.16, the relative CPD between graphene on SiO_2/Si and graphene on gold was found to be 30(±5) mV, while the relative CPD between graphene on gold and a clear gold film was found to be 65(±5) mV. Variations of the relative CPD between different samples were found to be much larger (±20 mV), than on the same sample (±5 mV). These were attributed to the different adhesion between graphene and the substrate, and are a consequence of the transfer procedure.

Having a clearly resolved CPD peak for graphene on gold shows that graphene interacts with the underlying gold substrate. The shift of the CPD peak for graphene on gold, compared to the graphene on SiO_2/Si (Fig. 4.16(e)) shows weak p-doping introduced by the gold substrate. Furthermore, it indicates the shift of the Fermi level greater than 50(±20) meV. This shift could not be caused by the water layer

since this layer was present in between both graphene on gold and graphene on SiO_2/Si. However, to exactly determine the Fermi level shift between graphene on gold and graphene on SiO_2/Si from the CPD peak shift, two main effects need to be considered. First, an unscreened electric field from the gold electrode that lies underneath graphene needs to be accounted for. Second, one would need to include a convolution of the entire system consisting of a cantilever, a tip and most importantly an inhomogeneous sample underneath the cantilever.

The shift of the Fermi level is several times lower compared with theoretical predictions [231]. This could be explained as a consequence of the water layer trapped between graphene and gold, which increases their separation. The separation was found to be about three times larger than the theoretically predicted equilibrium separation [231], resulting in the reduction of a charge transfer between the graphene and gold electrode, and consequently reducing the shift of the Fermi level in graphene on gold.

5. CONCLUSION

In conclusion, the dissertation and publications directly related to it [82, 83, 91, 92, 156] address a problem of retrieving optical properties of graphene in the visible and UV ranges using ellipsometry, and how changes in these properties could be related to various issues in fabrication, transfer and interaction with a substrate. Besides an importance in fundamental understanding of optical properties of graphene, these results could be implemented as a quality control in various graphene fabrication processes. Optical properties of graphene were obtained using spectroscopic ellipsometry and null spectroscopic imaging ellipsometry techniques. The chosen spectral range is the most common probing range in an in-line environment. The data interpretation process was optimized for the case of a atomically thin layer on various substrates (thin SiO_2 films, transparent and metallic substrates), and an importance of using corroborated measurements for building up an appropriate optical models has been shown. A function for parametrization of graphene's complex refractive index is proposed, and is based on a Fano resonant profile [82, 83]. Values of the model parameters can be easily related to the properties of the M-point exciton that causes the red shift of the prominent absorption peak in the UV. Ellipsometric mapping was also employed to resolve spatial distribution of a water layer trapped between graphene and a substrate [83].

Furthermore, specific potential applications for using ellipsometry as a quality control tool in graphene technology have been addressed within the dissertation. Namely, the influence of the transfer residue on the optical properties in the case when graphene is transferred over a transparent substrate is addressed [91]. This is very interesting both from the measurement, and from the transfer technology points of view. Measurements of mono-atomic layers, and thin (few nanometers) transparent residue layers on transparent substrates are rather difficult, since almost negligible phase shift occurs due to the lack of multiple reflections. From the side of the graphene transfer technology, this is the case of an interest for transparent conductive electrodes. As an example in the case of the flexible OLEDs, graphene

needs to be transferred several times on a transparent substrate. For this technology it is necessary to have a reliable tool that can quickly check if no residue is remaining after each graphene layer has been transferred. This is quite difficult since even few nanometers of the transparent residue layer (placed on a transparent substrate) can affect the electrical contacts between two graphene sheets and significantly increase sheet resistance. As it is shown within the dissertation, ellipsometry is a suitable tool for fast and non-destructive in-situ control of the transfer process [91].

The influence of the metallic substrate interaction on the optical properties of graphene was also discussed within the dissertation (and within Ref. [92]). This is interesting both from the fundamental aspect, and for the potential application of ellipsometry as a quality control tool in graphene technology. It has been shown that through the change in the optical properties of graphene it is possible to examine many body interaction between the excitonic state and the states near the Fermi level, which is shifted by the interaction with the underlaying metallic substrate. It was found that in this case an electron-hole interaction of the M-point exciton is suppressed by several hundred meV-s, and a strong blue shift (350 meV) of the prominent absorption peak of graphene on gold has been observed. Furthermore, it was confirmed that a charge transfer between graphene and the gold substrate is possible even with a water layer trapped in between, and that these contacts are Ohmic. It was shown that graphene on gold is p-doped, and that a relative shift of the Fermi level in graphene caused by the charge transfer between graphene and the gold substrate is several times lower lower than theoretically predicted. The effect of the reduced charge transfer between graphene and the gold substrate was attributed to a larger than equilibrium separation caused by the trapped water layer. From the quality control point of view, this is important since it demonstrates how a contactless technique can be used to confirm the contact quality between graphene and an external metallic electrode.

An ellipsometric data interpretation process based on a point-by-point inversion has been used in the dissertation. This process was optimized for the case of graphene. The same process should be followed as a good practice guide for the interpretation of ellipsometric measurements of other atomically thin layers, as MoS_2, WS_2, WSe_2 and many other emerging 2D materials.

Bibliography

[1] K. S. Novoselov, A. K. Geim, S. V. Morozov, D. Jiang, Y. Zhang, S. V. Dubonos, I. V. Grigorieva, and A. A. Firsov, "Electric field effect in atomically thin carbon films", *Science*, **306**, 666–669, 2004.

[2] K. S. Novoselov, A. K. Geim, S. V. Morozov, D. Jiang, M. I. Katsnelson, I. V. Grigorieva, S. V. Dubonos, and A. A. Firsov, "Two-dimensional gas of massless dirac fermions in graphene", *Nature*, **438**, 197–200, 2005.

[3] A. K. Geim, "Graphene: Status and prospects", *Science*, **324**, 1530–1534, 2009.

[4] K. S. Novoselov, "Nobel lecture: Graphene: Materials in the flatland", *Rev. Mod. Phys.*, **83**, 837, 2011.

[5] A. C. Ferrari, F. Bonaccorso, V. Falko, K. S. Novoselov, S. Roche, P. Bøggild, S. Borini, F. Koppens, V. Palermo, N. Pugno, et al. "Science and technology roadmap for graphene, related two-dimensional crystals, and hybrid systems", *Nanoscale*, 2014.

[6] A. S. Mayorov, R. V. Gorbachev, S. V. Morozov, L. Britnell, R. Jalil, L. A. Ponomarenko, P. Blake, K. S. Novoselov, K. Watanabe, T. Taniguchi, and A. K. Geim, "Micrometer-scale ballistic transport in encapsulated graphene at room temperature", *Nano Lett.*, **11**, 2396–2399, 2011.

[7] J. Moser, A. Barreiro, and A. Bachtold, "Current-induced cleaning of graphene", *Appl. Phys. Lett.*, **91**, 163513, 2007.

[8] A. A. Balandin, "Thermal properties of graphene and nanostructured carbon materials", *Nat. Mater.*, **10**, 569–581, 2011.

[9] C. Lee, X. Wei, J. W. Kysar, and J. Hone, "Measurement of the elastic properties and intrinsic strength of monolayer graphene", *Science*, **321**, 385–388, 2008.

[10] J. S. Bunch, S. S. Verbridge, J. S. Alden, A. M. van der Zande, J. M. Parpia, H. G. Craighead, and P. L. McEuen, "Impermeable atomic membranes from graphene sheets", *Nano Lett.*, **8**, 2458–2462, 2008.

[11] J. Chen, M. Badioli, P. Alonso-González, S. Thongrattanasiri, F. Huth, J. Osmond, M. Spasenović, A. Centeno, A. Pesquera, P. Godignon, et al. "Optical nano-imaging of gate-tunable graphene plasmons", *Nature*, **487**, 77–81, 2012.

[12] Z. Fei, A. S. Rodin, G. O. Andreev, W. Bao, A. S. McLeod, M. Wagner, L. M. Zhang, Z. Zhao, M. Thiemens, G. Dominguez, et al. "Gate-tuning of graphene plasmons revealed by infrared nano-imaging", *Nature*, **487**, 82–85, 2012.

[13] A. Woessner, M. B. Lundeberg, Y. Gao, A. Principi, P. Alonso-González, M. Carrega, K. Watanabe, T. Taniguchi, G. Vignale, M. Polini, et al. "Highly confined low-loss plasmons in graphene–boron nitride heterostructures", *Nature Mat.*, 2014.

[14] A. N. Grigorenko, M. Polini, and K. S. Novoselov. "Graphene plasmonics", *Nat Photon*, **6**, 749–758, 2012.

[15] N. W. Ashcroft and N. D. Mermin. "Solid state physics", Holt, Rinehart and Winston, New York, 1976.

[16] Curtasy of U. Ralevic, Institute of Physics, University of Belgrade, Serbia; measurements were carried out on an Omicron UHV-AFM-STM system.

[17] A. H. Castro Neto, F. Guinea, N. M. R. Peres, K. S. Novoselov, and A. K. Geim. "The electronic properties of graphene", *Rev. Mod. Phys.*, **81**, 109–162, 2009.

[18] M. I. Katsnelson. "Graphene: Carbon in two dimensions", Cambridge University Press, 2012.

[19] S. Datta. "Lessons from nanoelectronics: A new perspective on transport", New Jersey: World Scientific Publishing Company, 2011.

[20] P. R. Wallace. "The band theory of graphite", *Phys. Rev.*, **71**, 622–634, 1946.

[21] J. C. Slonczewski and P. R. Weiss. "Band structure of graphite", *Phys. Rev.*, **109**, 272–279, 1958.

[22] M. S. Dresselhaus. "Solid state physics - part ii - optical properties of solids", MIT Solid State Physics Course, 2011.

[23] P. Y. Yu and M. Cardona. "Fundamentals of semiconductors - physics and materials properties", Springer Science & Business Media, 2010.

[24] P. A. M. Dirac. "The quantum theory of the electron", *Proc. Royal Soc. of London. Series A*, **117**, 610–624, 1928.

[25] L. Yang, J. Deslippe, C.-H. Park, M. L. Cohen, and S. G. Louie, "Excitonic effects on the optical response of graphene and bilayer graphene", *Phys. Rev. Lett.*, **103**, 186802, 2009.

[26] O. Klein, "Die reflexion von elektronen an einem potentialsprung nach der relativistischen dynamik von dirac", *Zeitschrift für Physik*, **53**, 157–165, 1929.

[27] M. I. Katsnelson, K. S. Novoselov, and A. K. Geim, "Chiral tunnelling and the klein paradox in graphene", *Nature Phys.*, **2**, 620–625, 2006.

[28] M. O. Goerbig, "Electronic properties of graphene in a strong magnetic field", *Rev. Mod. Phy.*, **83**, 1193, 2011.

[29] N. Hong Shon and T. Ando, "Quantum transport in two-dimensional graphite system", *Jour. Phys. Soc. Jap.*, **67**, 2421–2429, 1998.

[30] R. J. Young, I. A. Kinloch, L. Gong, and K. S. Novoselov, "The mechanics of graphene nanocomposites: A review", *Comp. Sci. and Technol.*, **72**, 1459–1476, 2012.

[31] N. Stander, B. Huard, and D. Goldhaber-Gordon. "Evidence for klein tunneling in graphene p-n junctions", *Phys. Rev. Lett.*, **102**, 026807, 2009.

[32] W. Jones and N. H. March, "Theoretical solid state physics", Courier Corporation, 1985.

[33] O. Madelung, "Introduction to solid-state theory", Springer Science & Business Media, 1978.

[34] J. P. Hobson and W. A. Nierenberg, /newblock "The statistics of a two-dimensional, hexagonal net", *Phys. Rev.*, **89**, 662, 1953.

[35] G. Dresselhaus, R. Saito, and M. S. Dresselhaus, "Physical properties of carbon nanotubes", World Scientific, 1998.

[36] H. Kataura, Y. Kumazawa, Y. Maniwa, I. Umezu, S. Suzuki, Y. Ohtsuka, and Y. Achiba. "Optical properties of single-wall carbon nanotubes", *Synt. Met.*, **103**, 2555–2558, 1999.

[37] J. Maultzsch, S. Reich, and C. Thomsen, "Carbon nanotubes: basic concepts and physical properties", John Wiley & Sons, 2004.

[38] S. J. Tans, A. R. M. Verschueren, and C. Dekker, "Room-temperature transistor based on a single carbon nanotube", *Nature*, **393**, 49–52, 1998.

[39] R. Martel, T. Schmidt, H. R. Shea, T. Hertel, and Ph. Avouris, "Single-and multi-wall carbon nanotube field-effect transistors", *Appl. Phys. Lett.*, **73**, 2447–2449, 1998.

[40] H. T. Soh, C. F. Quate, A. F. Morpurgo, C. M. Marcus, J. Kong, and H. Dai, "Integrated nanotube circuits: Controlled growth and ohmic contacting of single-walled carbon nanotubes", *Appl. Phys. Lett.*, **75**, 627–629, 1999.

[41] S. Heinze, J. Tersoff, R. Martel, V. Derycke, J. Appenzeller, and Ph. Avouris, "Carbon nanotubes as schottky barrier transistors", *Phys. Rev. Lett.*, **89**, 106801, 2002.

[42] P. Avouris, Z. Chen, and V. Perebeinos, "Carbon-based electronics", *Nat. Nanotechnol.*, **2**, 605–615, 2007.

[43] K. F. Mak, F. H. da Jornada, K. He, J. Deslippe, N. Petrone, J. Hone, J. Shan, S. G. Louie, and T. F. Heinz, "Tuning many-body interactions in graphene: The effects of doping on excitons and carrier lifetimes", *Phys. Rev. Lett.*, **112**, 207401, 2014.

[44] Z. Q. Li, E. A. Henriksen, Z. Jiang, Z. Hao, M. C. Martin, P. Kim, H. L. Stormer, and D. N. Basov. "Dirac charge dynamics in graphene by infrared spectroscopy", *Nat. Phys.*, **4**, 532–535, 2008.

[45] A. Das, S. Pisana, B. Chakraborty, S. Piscanec, S. K. Saha, U. V. Waghmare, K. S. Novoselov, H. R.Krishnamurthy, A. K. Geim, A. C. Ferrari, and A. K. Sood, "Monitoring dopants by raman scattering in an electrochemically top-gated graphene transistor", *Nat. Nanotechnol.*, **3**, 210–215, 2008.

[46] H. Kuzmany, "Solid-state spectroscopy", Springer Science & Business Media, 2009.

[47] N. M. R. Peres, "The transport properties of graphene: An introduction", *Rev. Mod. Phys.*, **82**, 2673–2700, 2010.

[48] F. Bechstedt, "Many-body approach to electronic excitations", Springer, 2015.

[49] E. D. Palik, "Handbook of optical constants of solids", Academic press, 1998.

[50] U. Fano, "Effects of configuration interaction on intensities and phase shifts", *Phys. Rev.*, **124**, 1866–1878, 1961.

[51] K. F. Mak, L. Ju, F. Wang, and T. F. Heinz, "Optical spectroscopy of graphene: From the far infrared to the ultraviolet", *Solid State Comm.*, **152**, 1341–1349, 2012.

[52] Y. Zheng, T. Ando, and H. Suzuura, "Dynamical conductivity and zero-mode anomaly in honeycomb lattices", *J. Phys. Soc. Jp.*, **71**, 1318–1324, 2002.

[53] V. P. Gusynin, S. G. Sharapov, and J. P. Carbotte, "Unusual microwave response of dirac quasiparticles in graphene", *Phys. Rev. Lett.*, **96**, 256802, 2006.

[54] N. M. R. Peres, F. Guinea, and A. H. Castro Neto, "Electronic properties of disordered two-dimensional carbon", *Phys. Rev. B*, **73**, 125411, 2006.

[55] D. S. L. Abergel and V. I. Fal'ko, "Optical and magneto-optical far-infrared properties of bilayer graphene", *Phys. Rev. B*, **75**, 155430, 2007.

[56] D. S. L. Abergel, A. Russell, and V. I. Fal'ko, "Visibility of graphene flakes on a dielectric substrate", *Appl. Phys. Lett.*, **91**, 063125, 2007.

[57] A. B. Kuzmenko, E. van Heumen, F. Carbone, and D. van der Marel, "Universal optical conductance of graphite", *Phys. Rev. Lett.*, **100**, 117401, 2008.

[58] K. F. Mak, M. Y. Sfeir, Y. Wu, C. H. Lui, J. A. Misewich, and T. F. Heinz, "Measurement of the optical conductivity of graphene", *Phys. Rev. Lett.*, **101**, 196405, 2008.

[59] T. Stauber, N. M. R. Peres, and A. K. Geim, "Optical conductivity of graphene in the visible region of the spectrum", *Phys. Rev. B*, **78**, 085432, 2008.

[60] R. R. Nair, P. Blake, A. N. Grigorenko, K. S. Novoselov, T. J. Booth, T. Stauber, N. M. R. Peres, and A. K. Geim, "Fine structure constant defines visual transparency of graphene", *Science*, **320**, 1308, 2008.

[61] P. Blake, E. W. Hill, A. H. Castro Neto, K. S. Novoselov, D. Jiang, R. Yang, T. J. Booth, and A. K. Gaim, "Making graphene visible", *Appl. Phys. Lett.*, **97**, 231901–231904, 2007.

[62] A. Gray, M. Balooch, S. Allegret, S. De Gendt, and W.-E Wang, "Optical detection and characterization of graphene by broadband spectrophotometry", *J. Appl. Phys.*, **104**, 053109, 2008.

[63] Z. H. Ni, H. M. Wang, J. Kasim, H. M. Fan, T. Yu, Y. H. Wu, Y. P. Feng, and Z. X. Shen, "Graphene thickness determination using reflection and contrast spectroscopy", *Nano Lett.*, **7**, 2758–2763, 2007.

[64] C. Casiraghi, A. Hartschuh, E. Lidorikis, H. Qian, H. Harutyunyan, T. Gokus, K. S. Novoselov, and A. C. Ferrari, "Rayleigh imaging of graphene and graphene layers", *Nano Lett.*, **7**, 711–2717, 2007.

[65] K. F. Mak, J. Shan, and T. F. Heinz, "Seeing many-body effects in single- and few-layer graphene: Observation of two-dimensional saddle-point excitons", *Phys. Rev. Lett.*, **106**, 046401, 2011.

[66] Y.-C. Chang, C.-H. Liu, C.-H. Liu, Z. Zhong, and T. B. Norris, "Extracting the complex optical conductivity of mono- and bilayer graphene by ellipsometry", *Appl. Phys. Lett.*, **104**, 261909, 2014.

[67] J. Horng, C.-FanF. Chen, B. Geng, C. Girit, Y. Zhang, Z. Hao, H. A. Bechtel, M. Martin, A. Zettl, M. F. Crommie, Y. R. Shen, and F. Wang, "Drude conductivity of dirac fermions in graphene", *Phys. Rev. B*, **83**, 165113, 2011.

[68] M. Koshino and T. Ando, "Magneto-optical properties of multilayer graphene", *Phys. Rev. B*, **77**, 115313, 2008.

[69] E. G. Mishchenko, "Effect of electron-electron interactions on the conductivity of clean graphene", *Phys. Rev. Lett.*, **98**, 216801, 2007.

[70] M. Mecklenburg, J. Woo, and B. C. Regan, "Tree-level electron-photon interactions in graphene", *Phys. Rev. B*, **81**, 245401, 2010.

[71] D. K. Efetov and P. Kim, "Controlling electron-phonon interactions in graphene at ultrahigh carrier densities", *Phys. Rev. Lett.*, **105**, 256805, 2010.

[72] B. W. Boudouris, J. Horng, B. Geng, C. Girit, A. Zettl, M. F. Crommie, R. A. Segalman, S. G. Louie, C.-F. Chen, C.-H. Park, and F. Wang, "Controlling inelastic light scattering quantum pathways in graphene", *Nature*, **471**, 617–620, 2011.

[73] D.-H. Chae, T. Utikal, S. Weisenburger, H. Giessen, K. v. Klitzing, M. Lippitz, and J. Smet, "Excitonic fano resonance in free-standing graphene", *Nano Lett.*, **11**, 1379–1382, 2011.

[74] V. G. Kravets, A. N. Grigorenko, R. R. Nair, P. Blake, S. Anissimova, K. S. Novoselov, and A. K. Geim, "Spectroscopic ellipsometry of graphene and an exciton-shifted van hove peak in absorption", *Phys. Rev. B*, **81**, 155413, 2010.

[75] J. W. Weber, V. E. Calado, and M. C. M. van de Sanden, "Optical constants of graphene measured by spectroscopic ellipsometry", *Appl. Phys. Lett.*, **97**, 091904, 2010.

[76] U. Wurstbauer, C. Roling, U. Wurstbauer, W. Wegscheider, M. Vaupel, P. H. Thiesen, and D. Weiss, "Imaging ellipsometry of graphene", *Appl. Phys. Lett.*, **97**, 231901–231904, 2010.

[77] O. Albrektsen, R. L. Eriksen, S. M. Novikov, D. Schall, M. Karl, S. I. Bozhevolnyi, and A. C. Simonsen, "High resolution imaging of few-layer graphene", *J. Appl. Phys.*, **111**, 064305, 2012.

[78] J. W. Weber, K. Hinrichs, M. Gensch, M. C. M. van de Sanden, and T. W. H. Oates, "Microfocus infrared ellipsometry characterization of air-exposed graphene flakes", *Appl. Phys. Lett.*, **99**, 061909, 2011.

[79] V. G. Kravets, F. Schedin, R. Jalil, L. Britnell, K. S. Novoselov, and A. N. Grigorenko, "Surface hydrogenation and optics of a graphene sheet transferred onto a plasmonic nanoarray", *Jour. Phys. Chem. C*, **116**, 3882–3887, 2012.

[80] V. Meera and Girish S. Setlur, "Ellipsometry of graphene on a substrate", *J. Appl. Phys.*, **107**, 061909, 2010.

[81] G. Isić, M. Jakovljević, M. Filipović, Dj. Jovanović, B. Vasić, Saša Lazović, N. Puač, Z. Lj. Petrović, R. Kostić, and R. Gajić, "Spectroscopic ellipsometry of few-layer graphene", *J. Nanophoton.*, **5**, 051809, 2011.

[82] A. Matković, U. Ralević, G. Isić, M. M. Jakovljević, B. Vasić, I. Milošević, D. Marković, and R. Gajić, "Spectroscopic ellipsometry and the fano resonance modeling of graphene optical parameters", *Phys. Scr.*, **T149**, 014069, 2012.

[83] A. Matković, A. Beltaos, M. Milićević, U. Ralević, B. Vasić, Dj. Jovanović, and Gajić R, "Spectroscopic imaging ellipsometry and fano resonance modeling of graphene", *J. Appl. Phys.*, **112**, 123523, 2012.

[84] F. J. Nelson, V. K. Kamineni, T. Zhang, E. S. Comfort, J. U. Lee, and A. C. Diebold, "Optical properties of large-area polycrystalline chemical vapor deposited graphene by spectroscopic ellipsometry", *Appl. Phys. Lett.*, **97**, 253110, 2010.

[85] F. J. Nelson, V. K. Kamineni, T. Zhang, E. S. Comfort, J. U. Lee, and A. C. Diebold, "Spectroscopic ellipsometry of cvd graphene", *ECS Transactions*, **35**, 173–183, 2011.

[86] M. Losurdo, M. M. Giangregorio, P. Capezzuto, and G. Bruno, "Ellipsometry as a real-time optical tool for monitoring and understanding graphene growth on metals", *Jour. Phys. Chem. C*, **115**, 21804–21812, 2011.

[87] M. Losurdo, M. M. Giangregorio, P. Capezzuto, and G. Bruno, "Graphene cvd growth on copper and nickel: role of hydrogen in kinetics and structure", *Phys. Chem. Chem. Phys.*, **13**, 20836–20843, 2011.

[88] W. Strupinski, K. Grodecki, A. Wysmolek, R. Stepniewski, T. Szkopek, P. E. Gaskell, A. Gruneis, D. Haberer, R. Bozek, J. Krupka, and J. M. Baranowski, "Graphene epitaxy by chemical vapor deposition on SiC", *Nano Lett.*, **11**, 1786–1791, 2011.

[89] P. K. Gogoi, I. Santoso, S. Saha, S. Wang, A. H. Castro-Neto, K. P. Loh, T. Venkatesan, and A. Rusydi, "Optical conductivity study of screening of many-body effects in graphene interfaces", *Europhys. Lett.*, **99**, 67009, 2012.

[90] M. Losurdo, M. M. Giangregorio, G. V. Bianco, P. Capezzuto, and G. Bruno, "How spectroscopic ellipsometry can aid graphene technology?", *Thin Solid Films*, **571**, 389–394, 2014.

[91] A. Matković, U. Ralević, M. Chhikara, M. M. Jakovljević, Dj. Jovanović, G. Bratina, and R. Gajić, "Influence of transfer residue on the optical properties of chemical vapor deposited graphene investigated through spectroscopic ellipsometry", *J. Appl. Phys.*, **114**, 093505, 2013.

[92] A. Matković, M. Milićević, M. Chhikara, U. Ralević, B. Vasić, Dj. Jovanović, M. Belić, G. Bratina, and R. Gajić, "Influence of a gold substrate on the optical properties of graphene", *J. Appl. Phys.*, **117**, 015305, 2015.

[93] P. E. Gaskell, H. S. Skulason, W. Strupinski, and T. Szkopek, "High spatial resolution ellipsometer for characterization of epitaxial graphene", *Opt. Lett.*, **35**, 3336–3338, 2010.

[94] T. Hofmann, A. Boosalis, P. Khne, C. M. Herzinger, J. A. Woollam, D. K. Gaskill, J. L. Tedesco, and M. Schubert, "Hole-channel conductivity in epitaxial graphene determined by terahertz optical-hall effect and midinfrared ellipsometry", *Appl. Phys. Lett.*, **98**, 026587, 2011.

[95] W. A. de Heer, C. Berger, M. Ruan, M. Sprinkle, X. Li, Y. Hu, B. Zhang, J. Hankinson, and E. Conrad, "Large area and structured epitaxial graphene produced by confinement controlled sublimation of silicon carbide", *Proc. Nat. Ac. Sci.*, **108**, 16900–16905, 2011.

[96] A. Boosalis, T. Hofmann, V. Darakchieva, R. Yakimova, and M. Schubert, "Visible to vacuum ultraviolet dielectric functions of epitaxial graphene on 3c and 4h sic polytypes determined by spectroscopic ellipsometry", *Appl. Phys. Lett.*, **101**, 011912, 2012.

[97] V. Darakchieva, A. Boosalis, A. A. Zakharov, T. Hofmann, M. Schubert, T. E. Tiwald, T. Iakimov, R. Vasiliauskas, and R. Yakimova, "Large-area microfocal spectroscopic ellipsometry mapping of thickness and electronic properties of

epitaxial graphene on si- and c-face of 3c-sic(111)", *Appl. Phys. Lett.*, **102**, 213116, 2013.

[98] I. Jung, M. Vaupel, M. Pelton, R. Piner, D. A. Dikin, S. Stankovich, J. An, and R. S. Ruoff, "Characterization of thermally reduced graphene oxide by imaging ellipsometry", *Jour. Phys. Chem. C*, **112**, 8499–8506, 2008.

[99] Y. Shen, P. Zhou, Q. Q. Sun, L. Wan, J. Li, L. Y. Chen, D. W. Zhang, and X. B. Wang, "Optical investigation of reduced graphene oxide by spectroscopic ellipsometry and the band-gap tuning", *Appl. Phys. Lett.*, **99**, 123456, 2011.

[100] C. Yim, M. Oapos-Brien, N. McEvoy, S. Winters, I. Mirza, J. G. Lunney, and G. S. Duesberg, "Investigation of the optical properties of MoS2 thin films using spectroscopic ellipsometry", *Appl. Phys. Lett.*, **104**, 092563, 2014.

[101] J. W. Park, H. S. So, S. Kim, S.-H. Choi, H. Lee, J. Lee, C. Lee, and Y. Kim, "Optical properties of large-area ultrathin MoS2 films: Evolution from a single layer to multilayers", *J. Appl. Phys.*, **116**, 123533, 2014.

[102] H.-L. Liu, C.-C. Shen, S.-H. Su, C.-L. Hsu, M.-Y. Li, and L.-J. Li, "Optical properties of monolayer transition metal dichalcogenides probed by spectroscopic ellipsometry", *Appl. Phys. Lett.*, **105**, 235532, 2014.

[103] S. M. Eichfeld, C. M. Eichfeld, Y.-C. Lin, L. Hossain, and J. A. Robinson, "Rapid, non-destructive evaluation of ultrathin WSe2 using spectroscopic ellipsometry", *APL Materials*, **2**, 000000, 2014.

[104] S. H. Abedinpour, G. Vignale, A. Principi, M. Polini, W.-K. Tse, and A. H. MacDonald, "Drude weight, plasmon dispersion, and ac conductivity in doped graphene sheets", *Phys. Rev. B*, **84**, 045429, 2011.

[105] N. M. R. Peres, R. M. Ribeiro, and A. H. Castro Neto, "Excitonic effects in the optical conductivity of gated graphene", *Phys. Rev. Lett.*, **105**, 055501, 2010.

[106] A. Matković, M. Milićević, M. Chhikara, U. Ralević, B. Vasić, Dj. Jovanović, M. Belić, G. Bratina, and R. Gajić, "Influence of a gold substrate on the optical properties of graphene", Supporting online material.

[107] J. C. Phillips, "Ultraviolet absorption of insulators. iii. fcc alkali halides", *Phys. Rev.*, **136**, 1705–1713, 1964.

[108] F. Bonaccorso, Z. Sun, T. Hasan, and A. C. Ferrari, "Graphene photonics and optoelectronics", *Nat. Photon.*, **4**, 611–622, 2010.

[109] L. Yang, "Excitonic effects on optical absorption spectra of doped graphene", *Nano Lett.*, **11**, 3844–3847, 2011.

[110] K. S. Novoselov, V. I. Falko, L. Colombo, P. R. Gellert, M. G. Schwab, and K. Kim, "A roadmap for graphene", *Nature*, **490**, 192–200, 2012.

[111] V. Falko, K. S. Novoselov, F. Bonaccorso, and A. Ferrari, "Scientific and technological roadmap for graphene in ict", Graphene Flagship D6-3, 2013.

[112] D. C. Elias, R. R. Nair, T. M. G. Mohiuddin, S. V. Morozov, P. Blake, M. P. Halsall, A. C. Ferrari, D. W. Boukhvalov, M. I. Katsnelson, A. K. Geim, and K. S. Novoselov, "Control of graphene's properties by reversible hydrogenation: Evidence for graphane", *Science*, **323**, 610–613, 2009.

[113] K. P. Loh, Q. Bao, P. K. Ang, and J. Yang, "The chemistry of graphene", *J. Mater. Chem.*, **20**, 2277–2289, 2010.

[114] R. R. Nair, W. Ren, R. Jalil, I. Riaz, V. G. Kravets, et.al. "Fluorographene: A two-dimensional counterpart of teflon", *Small*, **6**, 2877–2884, 2010.

[115] F. Schedin, A. K. Geim, S. V. Morozov, E. W. Hill, P. Blake, M. I. Katsnelson, and K. S. Novoselov, "Detection of individual gas molecules adsorbed on graphene", *Nat. Mater.*, **6**, 652–655, 2007.

[116] C. R. Dean, A. F. Young, I.Meric, C. Lee, L. Wang, S. Sorgenfrei, K. Watanabe, T. Taniguchi, P. Kim, K. L. Shepard, and J. Hone, "Boron nitride substrates for high-quality graphene electronics", *Nat. Nano.*, **5**, 722–726, 2010.

[117] Y.-M. Lin, C. Dimitrakopoulos, K. A. Jenkins, D. B. Farmer, H.-Y. Chiu, A. Grill, and Ph. Avouris, "100-ghz transistors from wafer-scale epitaxial graphene", *Science*, **327**, 662, 2010.

[118] S. Pang, Y. Hernandez, X. Feng, and K. Mallen, "Graphene as transparent electrode material for organic electronics", *Adv. Mater.*, **23**, 2779–2795, 2011.

[119] S. De and J. N. Coleman, "Are there fundamental limitations on the sheet resistance and transmittance of thin graphene films?", *ACS Nano*, **4**, 2713–2720, 2010.

[120] T.-H. Han, Y. Lee, M.-R. Choi, S.-H. Woo, S.-H. Bae, B. H. Hong, J.-H. Ahn, and T.-W. Lee, "Extremely efficient flexible organic light-emitting diodes with modified graphene anode", *Nat. Photon.*, **6**, 2012.

[121] S. Bae, H. Kim, Y. Lee, X. Xu, J.-S. Park, et.al. "Roll-to-roll production of 30-inch graphene films for transparent electrodes", *Nat. Nano.*, **5**, 574–578, 2010.

[122] J. Wu, M. Agrawal, H. A. Becerril, Z. Bao, Z. Liu, Y. Chen, and P. Peumans, "Organic light-emitting diodes on solution-processed graphene transparent electrodes", *ACS Nano*, **4**, 43–48, 2010.

[123] F. Xia, T. Mueller, Y.-M. Lin, A. Valdes-Garcia, and Ph. Avouris, "Ultrafast graphene photodetector", *Nat. Nano.*, **4**, 839–843, 2009.

[124] I. Meric, M. Y. Han, A. F. Young, B. Ozyilmaz, P. Kim, and K. L. Shepard, "Current saturation in zero-bandgap, top-gated graphene field-effect transistors", *Nat. Nano.*, **3**, 654–659, 2007.

[125] Y. Ishikawa and K. Wada, "Near-infrared ge photodiodes for si photonics: operation frequency and an approach for the future", *IEEE Photon. J.*, **2**, 306-320, 2010.

[126] H. Fushimi, S. Kodama, H. Ito, T. Nagatsuma, N. Shimizu, Y. Miyamoto, T. Ishibashi, and T. Furuta, "InP/InGaAs uni-traveling-carrier photodiodes", *IEICE Trans. Electron. E*, **83**, 938-949, 2000.

[127] T. Muller, F. Xia, and Ph. Avouris, "Graphene photodetectors for high-speed optical communications", *Nat. Photon.*, **4**, 297–301, 2010.

[128] M. Liu, X. Yin, E. Ulin-Avila, B. Geng, T. Zentgraf, L. Ju, F. Wang, and X. Zhang, "A graphene-based broadband optical modulator", *Nature*, **474**, 64–67, 2011.

[129] F. Xia, T. Mueller, R. Golizadeh-Mojarad, M. Freitag, Y.-m. Lin, J. Tsang, V. Perebeinos, and Ph. Avouris, "Photocurrent imaging and efficient photon detection in a graphene transistor", *Nano Lett.*, **9**, 1039–1044, 2009.

[130] T. J. Echtermeyer, L. Britnell, P. K. Jasnos, A. Lombardo, R. V. Gorbachev, A. N. Grigorenko, A. K. Geim, A. C. Ferrari, and K. S. Novoselov, "Strong plasmonic enhancement of photovoltage in graphene", *Nat. Commun.*, **2**, 458, 2011.

[131] K. Kim, J.-Y. Choi, T. Kim, S.-H. Cho, and H.-J. Chung, "A role for graphene in silicon-based semiconductor devices", *Nature*, **479**, 338–344, 2011.

[132] G. T. Reed, G. Mashanovich, F. Y. Gardes, and D. J. Thomson, "Silicon optical modulators", *Nat. Photon.*, **4**, 518–526, 2010.

[133] D. Rubin J. Basak Y. Chetrit H. Nguyen R. Cohen N. Izhaky L. Liao, A. Liu and M. Paniccia, "40Gbit/s silicon optical modulator for high-speed applications", *Electronics Lett.*, **43**, 1196–1197, 2007.

[134] G. Li, X. Zheng, J. Yao, H. Thacker, I. Shubin, Y. Luo, K. Raj, J. E. Cunningham, and A. V. Krishnamoorthy, "25gb/s 1v-driving cmos ring modulator with integrated thermal tuning", *Opt. Express*, **19**, 20435–20443, 2011.

[135] Y. Tang, H.-W. Chen, S. Jain, J. D. Peters, U. Westergren, and J. E. Bowers, "50 gb/s hybrid silicon traveling-wave electroabsorption modulator", *Opt. Express*, **19**, 5811–5816, 2011.

[136] F. Torrisi, T. Hasan, W. Wu, Z. Sun, A. Lombardo, et.al. "Inkjet-printed graphene electronics", *ACS Nano*, **6**, 2992–3006, 2012.

[137] E. B. Secor, P. L. Prabhumirashi, K. Puntambekar, M. L. Geier, and M. C. Hersam, "Inkjet printing of high conductivity, flexible graphene patterns", *Jour. Phys. Chem. Lett.*, **4**, 1347–1351, 2013.

[138] J. M. Crain, J. S. Lettow, I. A. Aksay, S. A. Korkut, K. S. Chiang, C. Chen, and R. K. Prud'homme, "Printed electronics", October 2 2012. US Patent 8,278,757.

[139] H. Lammer, "Sporting goods with graphene material", 2012. US Patent App. 13/690,693.

[140] E. J. Yoo, T. Okata, T. Akita, M. Kohyama, J. Nakamura, and I. Honma, "Enhanced electrocatalytic activity of Pt subnanoclusters on graphene nanosheet surface", *Nano Lett.*, **9**, 2255–2259, 2009.

[141] L. Wang, K. Lee, Y.-Y. Sun, M. Lucking, Z. Chen, J. J. Zhao, and S. B. Zhang, "Graphene oxide as an ideal substrate for hydrogen storage", *Acs Nano*, **3**, 2995–3000, 2009.

[142] X. Wang, L. Zhi, and K. Mallen. "Transparent, conductive graphene electrodes for dye-sensitized solar cells", *Nano Lett.*, **8**, 323–327, 2008.

[143] S.-S. Li, K.-H. Tu, C.-C. Lin, C.-W. Chen, and M. Chhowalla, "Solution-processable graphene oxide as an efficient hole transport layer in polymer solar cells", *ACS Nano*, **4**, 3169–3174, 2010.

[144] M. Segal, "Selling graphene by the ton", *Nat.e Nanotechnol.*, **4**, 612–614, 2009.

[145] M. S. Whittingham, "Electrical energy storage and intercalation chemistry", *Science*, **192**, 1126–1127, 1976.

[146] T. Nakajima, K. Sanechika, and A. Yoshino, "Secondary battery", May 26 1987. US Patent 4,668,595.

[147] E. J. Yoo, J. Kim, E. Hosono, H. Zhou, T. Kudo, and I. Honma, "Large reversible li storage of graphene nanosheet families for use in rechargeable lithium ion batteries", *Nano Lett.*, **8**, 2277–2282, 2008.

[148] S. Yang, X. Feng, S. Ivanovici, and K. Mullen, "Fabrication of graphene-encapsulated oxide nanoparticles: towards high-performance anode materials for lithium storage", *Ang. Chem. Inter. Ed.*, **49**, 8408–8411, 2010.

[149] M. D. Stoller, S. Park, Y. Zhu, J. An, and R. S. Ruoff, "Graphene-based ultracapacitors", *Nano Lett.*, **8**, 3498–3502, 2008.

[150] M. F. El-Kady, and R. B. Kaner, "Scalable fabrication of high-power graphene micro-supercapacitors for flexible and on-chip energy storage", *Nat. Comm.*, **4**, 1475, 2013.

[151] P. Simon, and Y. Gogotsi, "Materials for electrochemical capacitors", *Nature Mat.*, **7**, 845–854, 2008.

[152] G. Wang, X. Shen, J. Yao, and J. Park, "Graphene nanosheets for enhanced lithium storage in lithium ion batteries", *Carbon*, **47**, 2049 – 2053, 2009.

[153] H. Fujiwara, "Spectroscopic ellipsometry - principles and applications", John Wiley & Sons, 2007.

[154] R. Gajić, and M. Jakovljević, *Ellipsometry and Correlation Measurements*, in *Ellipsometry at the Nanoscale*, ed. M. Losurdo, and K. Hingerl, (Springer Berlin Heidelberg, 2013).

[155] M. Losurdo, M. Bergmair, G. Bruno, D. Cattelan, C. Cobet, et al., "Spectroscopic ellipsometry and polarimetry for materials and systems analysis at the nanometer scale: state-of-the-art, potential, and perspectives", *Jour. Nanopart. Res.*, **11**, 1521–1554, 2009.

[156] A. Matković, and R. Gajić, "Spectroscopic imaging ellipsometry of graphene", SPIE Newsroom, 2013.

[157] I. Forbeaux, J.-M. Themlin, and J.-M. Debever, "Heteroepitaxial graphite on 6 h-sic (0001): Interface formation through conduction-band electronic structure", *Phys. Rev. B*, **58**, 16396, 1998.

[158] C. Berger, Z. Song, T. Li, X. Li, A. Y. Ogbazghi, R. Feng, et al., "Ultrathin epitaxial graphite: 2d electron gas properties and a route toward graphene-based nanoelectronics", *Jour. Phys. Chem. B*, **108**, 19912–19916, 2004.

[159] J. Hass, F. Varchon, J.-E. Millan-Otoya, M. Sprinkle, N. Sharma, W. A. de Heer, C. Berger, P. N. First, L. Magaud, and E. H. Conrad, "Why multilayer graphene on 4 h-sic (0001) behaves like a single sheet of graphene", *Phys. Rev. Lett.*, **100**, 125504, 2008.

[160] T. Ohta, A. Bostwick, T. Seyller, K. Horn, and E. Rotenberg, "Controlling the electronic structure of bilayer graphene", *Science*, **313**, 951–954, 2006.

[161] K. V. Emtsev, A. Bostwick, K. Horn, J. Jobst, G. L. Kellogg, L. Ley, J. L. McChesney, T. Ohta, S. A. Reshanov, J. Röhrl, et al. "Towards wafer-size graphene layers by atmospheric pressure graphitization of silicon carbide", *Nat. Mater.*, **8**, 203–207, 2009.

[162] P. Blake, P. D. Brimicombe, R. R. Nair, T. J. Booth, D. Jiang, F. Schedin, et al., "Graphene-based liquid crystal device", *Nano Lett.*, **8**, 1704–1708, 2008.

[163] Y. Hernandez, V. Nicolosi, M. Lotya, F. M. Blighe, Z. Sun, et al., "High-yield production of graphene by liquid-phase exfoliation of graphite", *Nat. Nanotechnol.*, **3**, 563–568, 2008.

[164] D. R. Dreyer, R. S. Ruoff, and C. W. Bielawski, "From conception to realization: An historial account of graphene and some perspectives for its future", *Ang. Chem. Int. Ed.*, **49**, 9336–9344, 2010.

[165] M. Qian, T. Feng, H. Ding, L. Lin, H. Li, Y. Chen, and Z. Sun, "Electron field emission from screen-printed graphene films" *Nanotech.*, **20**, 425702, 2009.

[166] H. K. Kim, C. Mattevi, H. J. Kim, A. Mittal, K. A. Mkhoyan, R. E. Riman, and M. Chhowalla, "Optoelectronic properties of graphene thin films deposited by a langmuir–blodgett assembly", *Nanoscale*, **5**, 12365–12374, 2013.

[167] S. Stankovich, D. A. Dikin, R. D. Piner, K. A. Kohlhaas, A. Kleinhammes, Y. Jia, Y. Wu, S. T. Nguyen, and R. S. Ruoff, "Synthesis of graphene-based nanosheets via chemical reduction of exfoliated graphite oxide", *Carbon*, **45**, 1558–1565, 2007.

[168] G. Eda, G. Fanchini, and M. Chhowalla, "Large-area ultrathin films of reduced graphene oxide as a transparent and flexible electronic material", *Nat. Nanotechnol.*, **3**, 270–274, 2008.

[169] J. Cai, P. Ruffieux, R. Jaafar, M. Bieri, T. Braun, S. Blankenburg, M. Muoth, et al., "Atomically precise bottom-up fabrication of graphene nanoribbons", *Nature*, **466**, 470–473, 2010.

[170] J. Hackley, D. Ali, J. DiPasquale, J. D. Demaree, and C. J. K. Richardson, "Graphitic carbon growth on Si (111) using solid source molecular beam epitaxy", *Appl. Phys. Lett.*, **95**, 133114, 2009.

[171] S. Dhar, A. R. Barman, G. X. Ni, X. Wang, X. F. Xu, Y. Zheng, S. Tripathy, R. A. Ariando, K. P. Loh, M. Rubhausen, et al. "A new route to graphene layers by selective laser ablation", *AIP Adv.*, **1**, 022109, 2011.

[172] C. Hurlbut, and C. S. Klein, "Manual of mineralogy, 20th ed." Wiley New York, 1985.

[173] W. Kern, and G. L. Schnable, "Low-pressure chemical vapor deposition for very large-scale integration processing a review", *Elec. Dev., IEEE Trans.*, **26**, 647–657, 1979.

[174] X. T. Yan, and Y. Xu, "Chemical vapour deposition: An integrated engineering design for advanced materials", Springer Science & Business Media, 2010.

[175] G. Ruan, Z. Sun, Z. Peng, and J. M. Tour, "Growth of graphene from food, insects, and waste", *Acs Nano*, **5**, 7601–7607, 2011.

[176] A. E. Karu, and M. Beer, "Pyrolytic formation of highly crystalline graphite films", *J. Appl. Phys.*, **37**, 2179–2181, 1966.

[177] J. Coraux, A. T. N'Diaye, C. Busse, and T. Michely, "Structural coherency of graphene on ir (111)", *Nano Lett.*, **8**, 565–570, 2008.

[178] A. Reina, X. Jia, J. Ho, D. Nezich, H. Son, V. Bulovic, M. S. Dresselhaus, and J. Kong, "Large area, few-layer graphene films on arbitrary substrates by chemical vapor deposition", *Nano Lett.*, **9**, 30–35, 2008.

[179] M. E. Ramon, A. Gupta, C. Corbet, D. A. Ferrer, H. C. P. Movva, et al., "Cmos-compatible synthesis of large-area, high-mobility graphene by chemical vapor deposition of acetylene on cobalt thin films", *ACS Nano*, **5**, 7198–7204, 2011.

[180] C. M. Orofeo, H. Ago, B. Hu, and M. Tsuji, "Synthesis of large area, homogeneous, single layer graphene films by annealing amorphous carbon on Co and Ni", *Nano Res.*, **4**, 531–540, 2011.

[181] Q. Yu, J. Lian, S. Siriponglert, H. Li, Y. P. Chen, and S.-S. Pei, "Graphene segregated on ni surfaces and transferred to insulators", *Appl. Phys. Lett.*, **93**, 113103, 2008.

[182] A. Reina, S. Thiele, X. Jia, S.r Bhaviripudi, M. S. Dresselhaus, J. A. Schaefer, and J. Kong, "Growth of large-area single-and bi-layer graphene by controlled

carbon precipitation on polycrystalline Ni surfaces", *Nano Res.*, **2**, 509–516, 2009.

[183] R. Addou, A. Dahal, P. Sutter, and M. Batzill, "Monolayer graphene growth on Ni (111) by low temperature chemical vapor deposition", *Appl. Phys. Lett.*, **100**, 021601, 2012.

[184] X. Li, W. Cai, J. An, S. Kim, J. Nah, D. Yang, R. Piner, A. Velamakanni, I. Jung, E. Tutuc, S. K. Banerjee, L. Colombo, and R. S. Ruoff, "Large-area synthesis of high-quality and uniform graphene films on copper foils", *Science*, **324**, 1312–1314, 2009.

[185] X. Li, W. Cai, L. Colombo, and R. S. Ruoff, "Evolution of graphene growth on ni and cu by carbon isotope labeling", *Nano Lett.*, **9**, 4268–4272, 2009.

[186] D. Yoon, Y.-W. Son, and H. Cheong, "Negative thermal expansion coefficient of graphene measured by raman spectroscopy", *Nano Lett.*, **11**, 3227–3231, 2011.

[187] Z. Yan, J. Lin, Z. Peng, Z. Sun, Y. Zhu, L. Li, C. Xiang, E. L. Samuel, C. Kittrell, and J. M. Tour, "Toward the synthesis of wafer-scale single-crystal graphene on copper foils", *ACS Nano*, **6**, 9110–9117, 2012.

[188] Y. Hao, M. S. Bharathi, L. Wang, Y. Liu, H. Chen, S. Nie, X. Wang, H. Chou, C. Tan, B. Fallahazad, et al., "The role of surface oxygen in the growth of large single-crystal graphene on copper", *Science*, **342**, 720–723, 2013.

[189] N. Liu, L. Fu, B. Dai, K. Yan, X. Liu, R. Zhao, Y. Zhang, and Z. Liu, "Universal segregation growth approach to wafer-size graphene from non-noble metals", *Nano Lett.*, **11**, 297–303, 2010.

[190] L. Britnell, R. V. Gorbachev, R. Jalil, B. D. Belle, F. Schedin, M. I. Katsnelson, L. Eaves, S. V. Morozov, A. S. Mayorov, N. M. R. Peres, et al. "Electron tunneling through ultrathin boron nitride crystalline barriers", *Nano Lett.*, **12**, 1707–1710, 2012.

[191] C.-H. Lee, G.-H. Lee, A. M. van der Zande, W. Chen, Y. Li, M. Han, X. Cui, G. Arefe, C. Nuckolls, T. F. Heinz, et al. "Atomically thin pn junctions with van der waals heterointerfaces", *Nat. Nanotechnol.*, 2014.

[192] M. A. Meitl, Y. Zhou, A. Gaur, S. Jeon, M. L. Usrey, M. S. Strano, and J. A. Rogers, "Solution casting and transfer printing single-walled carbon nanotube films", *Nano Lett.*, **4**, 1643–1647, 2004.

[193] L. Jiao, B. Fan, X. Xian, Z. Wu, J. Zhang, and Z. Liu, "Creation of nanostructures with poly (methyl methacrylate)-mediated nanotransfer printing", *J. Am. Chem. Soc.*, **130**, 12612–12613, 2008.

[194] A. Reina, H. Son, L. Jiao, B. Fan, M. S. Dresselhaus, Z. F. Liu, and J. Kong, "Transferring and identification of single-and few-layer graphene on arbitrary substrates", *J. Phys. Chem. C*, **112**, 17741–17744, 2008.

[195] X. Li, Y. Zhu, W. Cai, M. Borysiak, B. Han, D. Chen, R. D. Piner, L. Colombo, and R. S. Ruoff, "Transfer of large-area graphene films for high-performance transparent conductive electrodes", *Nano Lett.*, **9**, 4359–4363, 2009.

[196] M. Chhikara, E. Pavlica, and G. Bratina, "Grafold-driven nucleation of pentacene on graphene", *Surf. Sci. Lett.*, **609**, L5–L8, 2012.

[197] M. Her, R. Beams, and L. Novotny, "Graphene transfer with reduced residue", *Phys. Lett. A*, **377**, 1455–1458, 2013.

[198] J. Ning, D. Wang, J. Yan, D. Han, Z. Chai, W. Cai, J. Zhang, and Y. Hao, "Combined effects of hydrogen annealing on morphological, electrical and structural properties of graphene/r-sapphire", *Carbon*, **75**, 262–270, 2014.

[199] L. Gao, W. Ren, H. Xu, L. Jin, Z. Wang, T. Ma, L.-P. Ma, Z. Zhang, Q. Fu, L.-M. Peng, et al., "Repeated growth and bubbling transfer of graphene with millimetre-size single-crystal grains using platinum", *Nat. Commun.*, **3**, 699, 2012.

[200] C. J. Lockhart de la Rosa, J. Sun, N. Lindvall, M. T. Cole, Y. Nam, . Löffler, E. Olsson, K. B. K. Teo, and A. Yurgens, "Frame assisted H2O electrolysis induced H2 bubbling transfer of large area graphene grown by chemical vapor deposition on Cu", *Appl. Phys. Lett.*, **102**, 022101, 2013.

[201] A. K. Geim and K. S. Novoselov, "The rise of graphene", *Nat. Mater.*, **6**, 183–191, 2007.

[202] L. Pauling, "The nature of the chemical bond", Cornell University Press, 1960.

[203] L. M. Malard, M. A. Pimenta, G. Dresselhaus, and M. S. Dresselhaus, "Raman spectroscopy in graphene", *Phys. Rep.*, **473**, 51–87, 2009.

[204] A. C. Ferrari, "Raman spectroscopy of graphene and graphite: disorder, electron–phonon coupling, doping and nonadiabatic effects", *Solid State Commun.*, **143**, 47–57, 2007.

[205] M. Lazzeri, C. Attaccalite, L. Wirtz, and F. Mauri, "Impact of the electron-electron correlation on phonon dispersion: Failure of lda and gga dft functionals in graphene and graphite", *Phys. Rev. B*, **78**, 081406, 2008.

[206] D. Graf, F. Molitor, K. Ensslin, C. Stampfer, A. Jungen, C. Hierold, and L. Wirtz, "Spatially resolved Raman spectroscopy of single- and few-layer graphene", *Nano Lett.*, **7**, 238–242, 2007.

[207] T. M. G. Mohiuddin, A. Lombardo, R. R. Nair, A. Bonetti, G. Savini, R. Jalil, N. Bonini, D.M. Basko, C. Galiotis, N. Marzari, et al., "Uniaxial strain in graphene by Raman spectroscopy: G peak splitting, grüneisen parameters, and sample orientation", *Phys. Rev. B*, **79**, 205433, 2009.

[208] M. Kalbac, A. Reina-Cecco, H. Farhat, J. Kong, L. Kavan, and M. S. Dresselhaus, "The influence of strong electron and hole doping on the Raman intensity of chemical vapor-deposition graphene", *ACS Nano*, **4**, 6055–6063, 2010.

[209] C. Casiraghi, S. Pisana, K. S. Novoselov, A. K. Geim, and A. C. Ferrari, "Raman fingerprint of charged impurities in graphene", *Appl. Phys. Lett.*, **91**, 027456, 2007.

[210] D. R. Lenski and M. S. Fuhrer, "Raman and optical characterization of multilayer turbostratic graphene grown via chemical vapor deposition", *J. Appl. Phys.*, **110**, 017942, 2011.

[211] H. Cao, Q. Yu, L. A. Jauregui, J. Tian, W. Wu, Z. Liu, R. Jalilian, D. K. Benjamin, Z. Jiang, J. Bao, S. S. Pei, and Y. P. Chen, "Electronic transport in chemical vapor deposited graphene synthesized on Cu: Quantum hall effect and weak localization", *Appl. Phys. Lett.*, **96**, 145672, 2010.

[212] M. J. Yoo, T. A. Fulton, H. F. Hess, R. L. Willett, L. N. Dunkleberger, R. J. Chichester, L. N. Pfeiffer, and K. W. West, "Scanning single-electron transistor microscopy: Imaging individual charges", *Science*, **276**, 579–582, 1997.

[213] L. Gurevich, L. Canali, and L. P. Kouwenhoven, "Scanning gate spectroscopy on nanoclusters", *Appl. Phys. Lett.*, **76**, 384–386, 2000.

[214] A. Deshpande and B. J. LeRoy. "Scanning probe microscopy of graphene", *Physica E: Low-dimensional Systems and Nanostructures*, **44**, 743–759, 2012.

[215] G. Li, A. Luican, and E. Y. Andrei. "Scanning tunneling spectroscopy of graphene on graphite", *Phys. Rev. Lett.*, **102**, 176804, 2009.

[216] X. Du, I. Skachko, F. Duerr, A. Luican, and E. Y. Andrei, "Fractional quantum hall effect and insulating phase of dirac electrons in graphene", *Nature*, **462**, 192–195, 2009.

[217] J. Martin, N. Akerman, G. Ulbricht, T. Lohmann, J. H. Smet, K. Von Klitzing, and A. Yacoby, "Observation of electron-hole puddles in graphene using a scanning single-electron transistor", *Nat. Phys.*, **4**, 144–148, 2007.

[218] A. Deshpande, W. Bao, F. Miao, C. N. Lau, and B. J. LeRoy, "Spatially resolved spectroscopy of monolayer graphene on SiO2", *Phys. Rev. B*, **79**, 205411, 2009.

[219] K. K. Gomes, W. Mar, W. Ko, F. Guinea, and H. C. Manoharan, "Designer dirac fermions and topological phases in molecular graphene", *Nature*, **483**, 306–310, 2012.

[220] S. Masubuchi, M. Ono, K. Yoshida, K. Hirakawa, and T. Machida, "Fabrication of graphene nanoribbon by local anodic oxidation lithography using atomic force microscope", *Appl. Phys. Lett.*, **94**, 082107, 2009.

[221] B. Vasić, M. Kratzer, A. Matković, A. Nevosad, U. Ralević, Dj. Jovanović, C. Ganser, C. Teichert, and R. Gajić, "Atomic force microscopy based manipulation of graphene using dynamic plowing lithography", *Nanotechnol.*, **24**, 015303, 2013.

[222] Measurements carried out on Nanosurf FlexAFM, at the Group for Optical Spectroscopy and Chemical Imaging, at University of Potsdam, Germany.

[223] P. Nemes-Incze, Z. Osvıath, K. Kamarıas, and L. P. Birıo, "Anomalies in thickness measurements of graphene and few layer graphite crystals by tapping mode atomic force microscopy", *Carbon*, **7**, 1435–1442, 2008.

[224] A. Gupta, G. Chen, P. Joshi, S. Tadigadapa, and P. C. Eklund, "Raman scattering from high-frequency phonons in supported n-graphene layer films", *Nano Lett.*, **6**, 2667–2673, 2006.

[225] Z. Chen, Y.-M. Lin, M. J. Rooks, and Ph. Avouris, "Graphene nano-ribbon electronics", *Physica E: Low-dimensional Systems and Nanostructures*, **40**, 228–232, 2007.

[226] A. N. Sidorov, M. M. Yazdanpanah, R. Jalilian, P. J. Ouseph, R. W. Cohn, and G. U. Sumanasekera, "Electrostatic deposition of graphene", *Nanotechnol.*, **18**, 135301, 2007.

[227] M. Nonnenmacher, M. P. Oatboyle, and H. K. Wickramasinghe, "Kelvin probe force microscopy", *Appl. Phys. Lett.*, **58**, 142663, 1991.

[228] Y.-J. Yu, Y. Zhao, S. Ryu, L. E. Brus, K. S. Kim, and P. Kim, "Tuning the graphene work function by electric field effect", *Nano Lett.*, **9**, 430–3434, 2009.

[229] S. Morozov, K. Novoselov, M. Katsnelson, F. Schedin, D. Elias, J. Jaszczak, and A. Geim, "Giant intrinsic carrier mobilities in graphene and its bilayer", *Phys. Rev. Lett.*, **100**, 016602, 2008.

[230] C. O. Girit and A. Zettl, "Soldering to a single atomic layer", *Appl. Phys. Lett.*, **91**, 193512, 2007.

[231] G. Giovannetti, P. A. Khomyakov, G. Brocks, V. M. Karpan, J. van den Brink, and P. J. Kelly, "Doping graphene with metal contacts", *Phys. Rev. Lett.*, **101**, 026803, 2008.

[232] Y. Ren, S. Chen, W. Cai, Y. Zhu, C. Zhu, and R. S. Ruoff, "Controlling the electrical transport properties of graphene by in situ metal deposition", *Appl. Phys. Lett.*, **97**, 025874, 2010.

[233] Z. Klusek, P. Dabrowski, P. Kowalczyk, W. Kozlowski, W. Olejniczak, P. Blake, M. Szybowicz, and T. Runka. "Graphene on gold: Electron density of states studies by scanning tunneling spectroscopy", *Appl. Phys. Lett.*, **95**, 135791, 2009.

[234] I. Gierz, T. Suzuki, R. T. Weitz, D. S. Lee, B. Krauss, C. Riedl, U. Starke, H. Höchst, J. H. Smet, C. R. Ast, and K. Kern, "Electronic decoupling of an epitaxial graphene monolayer by gold intercalation", *Phys. Rev. B*, **81**, 235408, 2010.

[235] W. X. Wang, S. H. Liang, T. Yu, D. H. Li, Y. B. Li, and X. F. Han. "The study of interaction between graphene and metals by raman spectroscopy", *J. Appl. Phys.*, **109**, 011247, 2011.

[236] M. Lafkioti, B. Krauss, T. Lohmann, U. Zschieschang, H. Klauk, K. v. Klitzing, and J. H. Smet, "Graphene on a hydrophobic substrate: Doping reduction and hysteresis suppression under ambient conditions", *Nano Lett.*, **10**, 1149–1153, 2010.

[237] T. Lohmann, K. von Klitzing, and J. H. Smet, "Four-terminal magneto-transport in graphene p-n junctions created by spatially selective doping", *Nano Lett.*, **9**, 1973–1979, 2009.

[238] Accurion GmbH, Nanofilm_ep3 manual (www.accurion.com).

[239] See http://www.sopra-sa.com for the open SOPRA refractive indices database.

[240] S. Cheon, K. D. Kihm, H. Kim, G. Lim, J. S. Park, and J. S. Lee, "How to reliably determine the complex refractive index (ri) of graphene by using two independent measurement constraints", *Sci. Rep.*, **4**, 2014.

[241] M. Bruna and S. Borini, "Optical constants of graphene layers in the visible range", *Appl. Phys. Lett.*, **94**, 031901, 2009.

[242] K. S. Kim, Y. Zhao, H. Jang, S. Y. Lee, J. M. Kim, K. S. Kim, J.-H. Ahn, P. Kim, J.-Y. Choi, and B. H. Hong, "Large-scale pattern growth of graphene films for stretchable transparent electrodes", *Nature*, **457**, 706–710, 2009.

[243] X. Li, C. W. Magnuson, A. Venugopal, R. M. Tromp, J. B. Hannon, E. M. Vogel, L. Colombo, and R. S. Ruoff, "Large-area graphene single crystals grown by low-pressure chemical vapor deposition of methane on copper", *J. Am. Chem. Soc.*, **133**, 2816–2819, 2011.

[244] H. Park, P. R. Brown, V. Bulović, and J. Kong, "Graphene as transparent conducting electrodes in organic photovoltaics: Studies in graphene morphology, hole transporting layers, and counter electrodes", *Nano Lett.*, **12**, 133–140, 2012.

[245] D. Teweldebrhan and A. A. Balandin, "Modification of graphene properties due to electron-beam irradiation", *Appl. Phys. Lett.*, **94**, 013101, 2009.

[246] T. Oznuluer, E. Pince, E. O. Polat, O. Balci, O. Salihoglu, and C, Kocabas, "Synthesis of graphene on gold", *Appl. Phys. Lett.*, **98**, 013722, 2011.

[247] J. Kim, H. Park, J. B. Hannon, S. W. Bedell, K. Fogel, D. K. Sadana, and C. Dimitrakopoulos, "Layer-resolved graphene transfer via engineered strain layers", *Science*, **342**, 833–836, 2013.

[248] M. Chhikara, E. Pavlica, A. Matković, R. Gajić, and G. Bratina, "Effect of water layer at the SiO2/graphene interface on pentacene morphology", *Langmuir*, **30**, 11681–11688, 2014.

[249] K.-E. Peiponen V. Lucarini, J. J. Saarinen and E. M. Vartiainen, "Kramers-kronig relations in optical materials research", Springer Science & Business Media, 2005.

[250] G. isić, Institute of Physics, University of Belgrade, Serbia; "Optical conductivity of graphene - elementary derivation", Unpublished manuscript, 2011.

A. Derivations

A.1. Tight binding

This section of the appendix contains detailed derivations of the nearest neighbor hopping hamiltonian components $H_{AB}(\vec{k})$ and $H_{BA}(\vec{k})$, and the detailed derivation of the dispersion relation. These derivations are related to a tight binding hamiltonian and a derivation of graphene's dispersion relation, presented in Sec. 1.1.2.

Hamiltonian $H_{AB}(\vec{k})$ addresses nearest neighbor hopping from B site to three neighboring A sites: A, A' and A''.

Starting from equation:

$$H_{AB}(\vec{k}) = \int \phi_A^*(\vec{r} - \vec{r}_A)\hat{H}\phi_B(\vec{r} - \vec{r}_B)\,\mathrm{d}r = t_{AB} \cdot exp(i\vec{k}(\vec{r}_A - \vec{r}_B)), \tag{A.1}$$

and considering only nearest neighbors, results with:

$$H_{AB}(\vec{k}) = t_{AB} \sum_{A^i=A,A',A''} exp\Big(i(k_x\hat{x} + k_y\hat{y})(\vec{r}_B - \vec{r}_{A^i})\Big). \tag{A.2}$$

Next, it is required to use appropriate coordinates for the atomic sites. Until this point tight binding hamiltonian was restricted only to a case with two atoms per unit cell, each with a single overlapping orbital. By defining the exact atomic positions, symmetry of a hexagonal structure is added to the equation. If the center of a $(\hat{x}, \hat{y})$ coordinating system is placed at the site A (as show ni in Fig A.1)), then all atomic site coordinates required within Eq. A.2 are: $A = (0, 0)$, $B = (\frac{a}{\sqrt{3}}, 0)$, $A' = (\frac{a\sqrt{3}}{2}, \frac{a}{2})$, and $A'' = (\frac{a\sqrt{3}}{2}, -\frac{a}{2})$. By replacing those coordinates and preforming the summation Eq. A.2 gives:

$$H_{AB}(\vec{k}) = t_{AB} \cdot \Big[e^{i\left(k_x\hat{x}+k_y\hat{y}\right)\frac{a}{\sqrt{3}}\hat{x}} + e^{i\left(k_x\hat{x}+k_y\hat{y}\right)\left(\frac{a}{\sqrt{3}}\hat{x}-\frac{a\sqrt{3}}{2}\hat{x}-\frac{a}{2}\hat{y}\right)} + e^{i\left(k_x\hat{x}+k_y\hat{y}\right)\left(\frac{a}{\sqrt{3}}\hat{x}-\frac{a\sqrt{3}}{2}\hat{x}+\frac{a}{2}\hat{y}\right)}\Big], \tag{A.3}$$

$$H_{AB}(\vec{k}) = t_{AB} \cdot \Big[e^{i\left(\frac{k_x a}{\sqrt{3}}\right)} + e^{i\left(\frac{k_x a}{\sqrt{3}}-\frac{k_x a\sqrt{3}}{2}-\frac{k_y a}{2}\right)} + e^{i\left(\frac{k_x a}{\sqrt{3}}-\frac{k_x a\sqrt{3}}{2}+\frac{k_y a}{2}\right)}\Big], \tag{A.4}$$

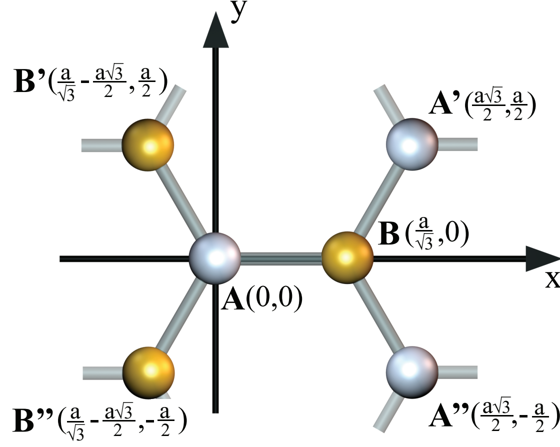

Figure A.1.: A (white) and B (yellow) atomic sites and nearest neighbor sites. Each atomic site coordinate is also marked. Here a stands for a length of a unit vector, and relates to carbon-carbon distance as: $a = a_0\sqrt{3}$

$$H_{AB}(\vec{k}) = t_{AB} \cdot \left[e^{i\frac{k_x a}{\sqrt{3}}} + e^{i\frac{k_x a}{\sqrt{3}}} e^{-i\frac{k_x a\sqrt{3}}{2}} e^{-i\frac{k_y a}{2}} + e^{i\frac{k_x a}{\sqrt{3}}} e^{-i\frac{k_x a\sqrt{3}}{2}} e^{i\frac{k_y a}{2}} \right], \tag{A.5}$$

$$H_{AB}(\vec{k}) = t_{AB} e^{i\frac{k_x a}{\sqrt{3}}} \left[1 + e^{-i\frac{k_x a\sqrt{3}}{2}} (e^{-i\frac{k_y a}{2}} + e^{i\frac{k_y a}{2}}) \right], \tag{A.6}$$

$$H_{AB}(\vec{k}) = t_{AB} e^{i\frac{k_x a}{\sqrt{3}}} \left[1 + e^{-i\frac{k_x a\sqrt{3}}{2}} \cos\frac{k_y a}{2} \right]. \tag{A.7}$$

Analogue summation needs to be done for $H_{BA}(\vec{k})$, which accounts for nearest neighbor hopping from A site to three neighboring B, B' and B'' sites, where $B' = (\frac{a}{\sqrt{3}} - \frac{a\sqrt{3}}{2}, \frac{a}{2})$ and $B'' = (\frac{a}{\sqrt{3}} - \frac{a\sqrt{3}}{2}, -\frac{a}{2})$, resulting with:

$$H_{BA}(\vec{k}) = t_{BA} e^{-i\frac{k_x a}{\sqrt{3}}} \left[1 + e^{+i\frac{k_x a\sqrt{3}}{2}} \cos\frac{k_y a}{2} \right]. \tag{A.8}$$

By returning Eq.-s A.7 and A.8 into 1.13, Eq. 1.18 is obtained:

$$h(\vec{k}) = \begin{pmatrix} 0 & t^* e^{\left(i\frac{k_x a}{\sqrt{3}}\right)} \left(1 + 2e^{\left(-\frac{i\sqrt{3}}{2}k_x a\right)} \cos\frac{k_y a}{2}\right) \\ t e^{\left(-i\frac{k_x a}{\sqrt{3}}\right)} \left(1 + 2e^{\left(+\frac{i\sqrt{3}}{2}k_x a\right)} \cos\frac{k_y a}{2}\right) & 0 \end{pmatrix} = \begin{pmatrix} 0 & h_0^* \\ h_0 & 0 \end{pmatrix}. \tag{A.9}$$

The eigenvalues are:

$$E(k) = \pm\sqrt{tt^* \cdot e^{\left(+\frac{i\sqrt{3}}{2}k_x a\right)} e^{\left(-\frac{i\sqrt{3}}{2}k_x a\right)} \cdot \left(1 + 2e^{\left(-\frac{i\sqrt{3}}{2}k_x a\right)} \cos\frac{k_y a}{2}\right) \cdot \left(1 + 2e^{\left(+\frac{i\sqrt{3}}{2}k_x a\right)} \cos\frac{k_y a}{2}\right)}, \tag{A.10}$$

$$E(k) = \pm t\sqrt{\left(1 + 2e^{\left(-\frac{i\sqrt{3}}{2}k_x a\right)} \cos\frac{k_y a}{2}\right) \cdot \left(1 + 2e^{\left(+\frac{i\sqrt{3}}{2}k_x a\right)} \cos\frac{k_y a}{2}\right)}. \tag{A.11}$$

For simplicity following replacements are made: $\frac{\sqrt{3}}{2}k_x a = \phi$ and $\cos\frac{k_y a}{2} = C$, resulting with:

$$E(k) = \pm t\sqrt{\left(1 + 2e^{-i\phi} \cdot C\right)\left(1 + 2e^{+i\phi} \cdot C\right)}, \tag{A.12}$$

$$= \pm t\sqrt{1 + 2e^{i\phi} \cdot C + 2e^{-i\phi} \cdot C + 4e^{i\phi}e^{-i\phi} \cdot C^2}, \tag{A.13}$$

$$= \pm t\sqrt{1 + 4C^2 + 2C(e^{i\phi} + e^{-i\phi})}, \tag{A.14}$$

$$= \pm t\sqrt{1 + 4C^2 + 2C\cos\phi}. \tag{A.15}$$

Finally, by exchanging back from ϕ and C, into $\vec{k}$, the dispersion relation of graphene is obtained:

$$E(k) = \pm t\sqrt{1 + 4\cos^2\frac{k_y a}{2} + 2\cos\frac{k_y a}{2} \cdot \cos\frac{\sqrt{3}k_x a}{2}}. \tag{A.16}$$

A.2. The Dirac equation

In a classical energy-momentum equation $E = p^2/2m$ corresponding wave equation has a well known form:

$$-i\hbar\frac{\partial}{\partial t}\psi = -\frac{\hbar^2}{2m}\nabla^2\psi\,. \tag{A.17}$$

The Dirac equation essentially answers the question: What would be the corresponding wave equation for the relativistic energy-momentum relation $E^2 = m^2c^4 + p^2c^2$? The problem here is, if $E \Rightarrow -i\hbar\frac{\partial}{\partial t}$ and $p \Rightarrow i\hbar\nabla$, then how to write a square root of a differential equation? A simple solution proposed by Dirac was to write a matrix [24][18]:

$$\begin{pmatrix} mc^2I & c\vec{\sigma}\vec{p} \\ c\vec{\sigma}\vec{p} & -mc^2I \end{pmatrix}. \tag{A.18}$$

This is essentially a 4×4 matrix, since $\vec{\sigma}$ represents Pauli spin matrices, so $\vec{\sigma}\vec{p}$ has to be a 2×2 matrix. I represents a 2×2 unit matrix. Now, if this matrix is multiplied by itself:

$$\begin{pmatrix} mc^2I & c\vec{\sigma}\vec{p} \\ c\vec{\sigma}\vec{p} & -mc^2I \end{pmatrix}\begin{pmatrix} mc^2I & c\vec{\sigma}\vec{p} \\ c\vec{\sigma}\vec{p} & -mc^2I \end{pmatrix} = (m^2c^4 + p^2c^2)\begin{pmatrix} 1 & 0 & 0 & 0 \\ 0 & 1 & 0 & 0 \\ 0 & 0 & 1 & 0 \\ 0 & 0 & 0 & 1 \end{pmatrix}. \tag{A.19}$$

In a sense Dirac's result is like a square root of the operator. Now, a wave equation that corresponds with the relativistic energy-momentum relation can be written as:

$$-i\hbar\frac{\partial}{\partial t}\{\psi\} = \begin{pmatrix} mc^2I & c\vec{\sigma}\vec{p} \\ c\vec{\sigma}\vec{p} & -mc^2I \end{pmatrix}\{\psi\}\,. \tag{A.20}$$

Since carrier motion in graphene is limited to two dimensions, let us rewrite Eq. A.20 considering that $\vec{p}$ has only two components p_x and p_y:

$$-i\hbar\frac{\partial}{\partial t}\{\psi\} = \begin{pmatrix} mc^2 & 0 & 0 & c(p_x - ip_y) \\ 0 & mc^2 & c(p_x + ip_y) & 0 \\ 0 & c(p_x - ip_y) & -mc^2 & 0 \\ c(p_x + ip_y) & 0 & 0 & -mc^2 \end{pmatrix}\{\psi\}\,. \tag{A.21}$$

If $m = 0$ Eq. A.21 becomes the same as graphene's wave equation (Eq. 1.30).

A.3. Saddle points in 2D: M point logarithmic van Hove singularity

This section of appendix presents derivations for the Taylor expansion coefficients, as described in Sec. 1.1.4. The sign of these coefficients determines the type of the singularity [22][23]. Here, the Taylor coefficients for graphene's $E_c(\vec{k}) - E_v(\vec{k})$ function are calculated in the vicinity of the M point in Brillouin zone. Starting from Eq. **??**:

$$2a_i = 2t\,\frac{\partial^2}{\partial k_i^2}\Bigg[\sqrt{1 + 4\cos\frac{k_y a}{2}^2 + 2\cos\frac{k_y a}{2}\cdot\cos\frac{\sqrt{3}k_x a}{2}}\,\Bigg]. \tag{A.22}$$

First we consider k_x second derivate, as:

$$2a_1 = \frac{\partial^2}{\partial k_x^2}\Bigg[2|E(\vec{k})|\Bigg]. \tag{A.23}$$

Considering that at M point $k_y = 0$, and by substituting $x = (\sqrt{3}k_x a)/2$, the dispersion relation in x direction near M point could be written as:

$$E_x = \pm t\sqrt{5 + 2\cos x}\,. \tag{A.24}$$

Now first partial derivate with respect to x of $E_c(\vec{k}) - E_v(\vec{k})$ is:

$$\frac{\partial}{\partial x}|2E_x| = \frac{2t}{2}\,(5 + 2\cos x)^{-\frac{1}{2}}\,2\,(-\sin x). \tag{A.25}$$

Second partial derivate is then:

$$\frac{\partial^2}{\partial x^2}|2E_x| = 2t\,\Big[-\frac{1}{2}\,(5 + 2\cos x)^{-\frac{3}{2}}\,2\,\sin^2 x\; + \;(5 + 2\cos x)^{-\frac{1}{2}}(-\cos x)\Big]. \tag{A.26}$$

Considering the vicinity of the M point, where $k_x = (2\pi)/(\sqrt{3}a)$ and $x = \pi$, Eq. A.26 gives:

$$\frac{\partial^2}{\partial x^2}|2E_x|\,\Bigg|_M = 2t\,[-\frac{\sin^2\pi}{(5 + 2\cos\pi)^{3/2}} - \frac{\cos\pi}{(5 + 2\cos\pi)^{1/2}}]. \tag{A.27}$$

When returned back from x to k_x, and considering only the M point vicinity, gives:

$$\frac{\partial^2}{\partial k_x^2}|2E(\vec{k})|\,\Bigg|_M = \frac{2t}{\sqrt{3}} > 0. \tag{A.28}$$

Considering that the nearest neighbor hopping parameter t has to be positive, then a_1 constant of the Taylor expansion has to be also positive: $a_1 = t/\sqrt{3}$.

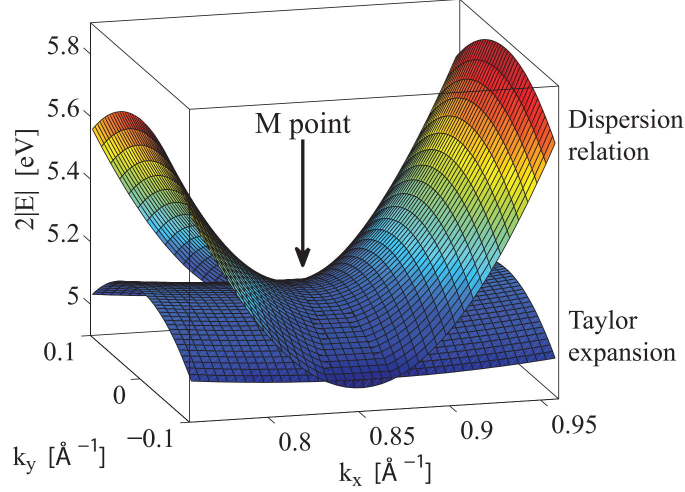

Figure A.2.: $E_c(\vec{k}) - E_v(\vec{k})$ near M point, and Taylor expansion using: $E(\vec{k}_M) = 2t$, $a_1 = t/\sqrt{3}$ and $a_2 = -5t/\sqrt{3}$

Now it remains for the similar procedure to be repeated in k_y direction. Starting from the k_y second derivate of $E_c(\vec{k}) - E_v(\vec{k})$, as:

$$2a_2 = \frac{\partial^2}{\partial k_y^2}\Big[2|E(\vec{k})|\Big]. \tag{A.29}$$

Again considering only its value near the M point. For simplicity, k_y is substituted as $y = k_y a/2$ and $k_x = k_{x_M} 2\pi/\sqrt{3}a$, we can write:

$$\frac{\partial}{\partial y}|2E_y| = 2t\Big[(1 + 4\cos^2 y - 2\cos y)^{-1/2}\,\sin y - 2(1 + 4\cos^2 y - 2\cos y)^{-1/2}\,\sin 2y\Big]. \tag{A.30}$$

Then the second derivate with the respect to y is:

$$\begin{aligned}\frac{\partial^2}{\partial y^2}|2E_y| = 2t\Big[-\frac{\sin y}{2}\frac{(2\sin y - 4\sin 2y)}{(1 + 4\cos^2 y - 2\cos y)^{3/2}} - \\ -\frac{\cos y}{(1 + 4\cos^2 y - 2\cos y)^{1/2}} - \\ -2\sin 2y\frac{(2\sin y - 4\sin 2y)}{(1 + 4\cos^2 y - 2\cos y)^{3/2}} - \\ \frac{4\cos 2y}{(1 + 4\cos^2 y - 2\cos y)^{1/2}}\Big].\end{aligned} \tag{A.31}$$

Luckily, Eq. A.31 significantly simplifies when $y = 0$ (M point condition), giving:

$$\frac{\partial^2}{\partial y^2}|2E_y|\Big|_M = 2t[-3^{-1/2} - 4\cdot 3^{-1/2}] = -\frac{10t}{\sqrt{3}} < 0. \tag{A.32}$$

Now, since$t > 0$ then the second coefficient of the Taylor expansion has to be negative: $a_2 = -5t/\sqrt{3}$.

The result of the calculation of Taylor expansion coefficients gives us $a_1 > 0$ and $a_2 < 0$, meaning that the M point singularity is so called $M1$ type, or a 2D saddle point singularity, or logarithmic singularity. Interestingly this indicates that for the M point interband transition energies, JDOS function has a logarithmic discontinuity, theoretically giving an infinite number of states that could contribute to the interbant absorption of a photon with an energy that corresponds to the interband transition at M point, i.e. $\hbar\omega = 2t$.

Taylor expansion of $E_c(\vec{k}) - E_v(\vec{k})$ around M point is shown in Fig. A.2 and could be written as:

$$E_c(\vec{k}) - E_v(\vec{k}) \approx 2t + \frac{2t}{\sqrt{3}}(k_x - \frac{2\pi}{\sqrt{3}a})^2 - \frac{10t}{\sqrt{3}}(k_y)^2. \tag{A.33}$$

A.4. Fermi golden rule derivation of the interband optical conductivity of graphene in the linear dispersion relation approximation

This section of Appendix A presents a derivation of the real part of graphene's optical conductivity, considering only interband component and a linear dispersion relation approximation. The derivation uses Fermi golden rule [22], and is based on Ref. [250] and supplementary data from Ref. [60].

As it was shown in sections 1.2.1 and 1.2.3, for incident photon energies greater than twice the Fermi energy ($2E_F$) and lower than about 3 eV (linear JDOS region) absorption function of graphene does not depend neither on the photon energy nor on the material properties, and is equal to: $\pi\alpha \approx 2,3\%$. Expressed as the real part of graphene's optical conductivity, it gives universal optical conductivity:

$$\sigma_0 = \frac{e^2}{4\hbar}\,. \tag{A.34}$$

Analytical derivation of graphene's optical conductivity is possible only within the linear approximation of the dispersion relation, and beyond linear regime an $ab-initio$ methods are needed [25]. Let us start from the Hamiltonian, as given in Eq. 1.29 and derived in Sec. 1.1.2:

$$H_{lin} = v_F \vec{\sigma}\vec{p}\,. \tag{A.35}$$

Here $\vec{p}$ stands for the momentum operator and $\vec{\sigma}$ represents Pauli matrices in two dimensions. The Hamiltonian is written for the states around K point in Brillouin zone, while for the state around K' the change $\sigma_y \rightarrow -\sigma_y$ should be made. As it will be shown, the results obtained in this section are degenerate, when considering K and K' valleys. Expanded as a 2×2 matrix, Eq. A.35 gives:

$$H_{lin} = v_F \begin{bmatrix} 0 & (p_x - ip_y) \\ (p_x + ip_y) & 0 \end{bmatrix}. \tag{A.36}$$

Eigenvectors of the wave equation $H_{lin}\psi(\vec{r}) = E\psi(\vec{r})$ are:

$$\psi_{\vec{k}+}(\vec{k}) = \frac{e^{i\vec{k}\vec{r}}}{\sqrt{2\Omega}} \begin{bmatrix} e^{-i\phi(\vec{k})/2} \\ e^{i\phi(\vec{k})/2} \end{bmatrix}, \tag{A.37}$$

and

$$\psi_{\vec{k}-}(\vec{k}) = \frac{e^{i\vec{k}\vec{r}}}{\sqrt{2\Omega}} \begin{bmatrix} e^{-i\phi(\vec{k})/2} \\ -e^{i\phi(\vec{k})/2} \end{bmatrix} . \tag{A.38}$$

Here - and + signs in the denominators denote electron and hole wavefunctions (i.e. conduction and valence bands), respectively. The corresponding eigenvalues are:

$$E_{\pm}(k) = \pm\hbar v_F k \,. \tag{A.39}$$

In Eq.-s A.37-A.39, a transformation from a cartesian to a cylindrical coordinate system has been carried out, similarly as in Sec. 1.1.3, where:

$$\vec{k} = k\left(cos\phi(\vec{k})\hat{x} \,+\, sin\phi(\vec{k})\hat{y}\right) . \tag{A.40}$$

Here $\phi(\vec{k})$ represents the angle between $\hat{\rho}$ and $\hat{x}$, as:

$$\phi(\vec{k}) = arctan(k_y/k_x) \,. \tag{A.41}$$

As described in Sec. 1.2.1, the electromagnetic field of a plane wave can be described by the magnetic vector potential:

$$\vec{A}(\vec{r},t) = (A_x\hat{x} + A_y\hat{y})\, cos(\vec{q}\vec{r} - \omega t) \,. \tag{A.42}$$

In order to simplify the derivation, let us assume that $\hat{x}$ component of the magnetic vector potential is parallel to graphene plane, while the $\hat{y}$ component is perpendicular. In this case, $\hat{y}$ component can be neglected since the perpendicular component can not affect electrons in graphene. Then Eq. A.42 becomes:

$$\vec{A}(\vec{r},t) = A_x cos(\vec{q}\vec{r} - \omega t)\hat{x} = A_x cos(\omega t)\hat{x} \,. \tag{A.43}$$

Here it has been assumed that $\vec{q} = 0$, which has been justified in Sec. 1.1.3.

The interaction of the electromagnetic wave with electrons in graphene is described by Landau-Peierls substitution of $\vec{p}$ with $\vec{p} - q\vec{A}$ in the Hamiltonian, giving:

$$H = v_F\vec{\sigma}(\vec{p} - q\vec{A}) = v_F\vec{\sigma}\vec{p} - qv_F\vec{\sigma}\vec{A} = H^0 + H' \,. \tag{A.44}$$

Here $H' = qv_F\vec{\sigma}\vec{A}$ is treated as a perturbation. q denotes the charge for electrons or holes, as $q = \pm e$.

According to Fermi golden rule, the transition rate $1/\tau$ from a state in valence band v to a state in conduction band c is related to the light absorbtion of the material, and can be calculated as:

$$\frac{1}{\tau_{cv}} = \frac{2\pi}{\hbar}|\langle v|H'|c\rangle|^2\, \delta(E_c - E_v - \hbar\omega) \,. \tag{A.45}$$

IN order to solve Eq. A.45, let us first evaluate the following matrix element:

$$M_{cv}(\vec{k}\vec{k'}) = \int \mathrm{d}\vec{r}\, \psi^{\dagger}_{\vec{k'}v}(\vec{r})\, H'\, \psi_{\vec{k}c}(\vec{r})\,. \tag{A.46}$$

By returning Eq.-s A.37, A.38 into Eq. A.46, gives:

$$M_{cv}(\vec{k}\vec{k'}) = \int \mathrm{d}\vec{r}\, \frac{e^{-i\vec{k'}\vec{r}}}{\sqrt{2\Omega}} \begin{bmatrix} e^{-i\phi(\vec{k})/2} \\ e^{i\phi(\vec{k})/2} \end{bmatrix}^{\dagger} \Big(- qv_F \vec{\sigma}\vec{A}\Big) \frac{e^{i\vec{k}\vec{r}}}{\sqrt{2\Omega}} \begin{bmatrix} e^{-i\phi(\vec{k})/2} \\ -e^{i\phi(\vec{k})/2} \end{bmatrix}. \tag{A.47}$$

By using Eq. A.43, the perturbation Hamiltonian H' can be expressed as:

$$H' = -qv_F\vec{\sigma}\vec{A} = -qv_F \begin{bmatrix} 0 & 1 \\ 1 & 0 \end{bmatrix} A_x\, cos(\omega t)\,. \tag{A.48}$$

Now, the matrix element can be written as:

$$M_{cv}(\vec{k}\vec{k'}) = -\frac{qv_F A_x cos(\omega t)}{2} \begin{bmatrix} e^{i\phi/2} & e^{-i\phi/2} \end{bmatrix} \begin{bmatrix} 0 & 1 \\ 1 & 0 \end{bmatrix} \begin{bmatrix} e^{-i\phi/2} \\ -e^{i\phi/2} \end{bmatrix} \int \frac{\mathrm{d}\vec{r}}{\Omega} e^{i(\vec{k}-\vec{k'})\vec{r}}. \tag{A.49}$$

Let us evaluate the matrices in front of the integral separately by using basic matrix operations and Euler's formula, as:

$$\begin{bmatrix} e^{i\phi/2} & e^{-i\phi/2} \end{bmatrix} \begin{bmatrix} 0 & 1 \\ 1 & 0 \end{bmatrix} \begin{bmatrix} e^{i\phi/2} \\ -e^{i\phi/2} \end{bmatrix} = \begin{bmatrix} e^{i\phi/2} & e^{-i\phi/2} \end{bmatrix} \begin{bmatrix} -e^{i\phi/2} \\ e^{-i\phi/2} \end{bmatrix} =$$

$$= \begin{bmatrix} e^{i\phi/2} & e^{-i\phi/2} \end{bmatrix} \begin{bmatrix} -e^{i\phi/2} \\ e^{-i\phi/2} \end{bmatrix} = -e^{i\phi} + e^{-i\phi} = -i2sin\phi\,. \tag{A.50}$$

Furthermore, the integral in Eq. A.49 can be simply reduced to:

$$\int \frac{\mathrm{d}\vec{r}}{\Omega} e^{i(\vec{k}-\vec{k'})\vec{r}} \approx \delta_{\vec{k}\vec{k'}}\,. \tag{A.51}$$

By returning Eq.-s A.50 and A.51 into Eq. A.49, gives the solution for the matrix element $M_{cv}(\vec{k}\vec{k'})$:

$$M_{cv}(\vec{k}\vec{k'}) = iqv_F A_x \cos{(\omega t)}\, \sin{\phi(\vec{k})}\, \delta_{\vec{k}\vec{k'}}\,. \tag{A.52}$$

In order to calculate the transition rate (Eq. A.45), let us find $|M_{cv}|^2$:

$$|M_{cv}|^2 = q^2 v_F^2 A_x^2\, \cos^2{(\omega t)}\, \sin^2{\phi(\vec{k})}\,. \tag{A.53}$$

Finally, let us carry out a time averaging, as:

$$\langle|M_{cv}|^2\rangle_t = e^2 v_F^2 A_x^2\, \langle\cos^2{(\omega t)}\rangle_t\, \sin^2{\phi(\vec{k})} \;=\; \frac{e^2 v_F^2 A_x^2}{2} sin^2\phi(\vec{k}). \tag{A.54}$$

Here, a substitution of $q = \pm e$ has been made, since $q^2 = e^2$.

Considering Eq. A.54 and relation $E_c - E_v = 2|E|$, the transition rate between conduction and valence band for a given $\vec{k}$ can be written as:

$$\frac{1}{\tau_{cv}(\vec{k})} = \frac{2\pi}{\hbar}\frac{e^2 v_F^2 A_x^2}{2}\, sin^2\phi(\vec{k})\,\delta(2|E(\vec{k})| - \hbar\omega)\,. \tag{A.55}$$

In order to find the rate at which the entire system of electrons absorb light, Eq. A.55 needs to be summed over the entire $\vec{k}$ space, in order to include all of the electrons in graphene, giving:

$$\frac{1}{\tau_{tot}} = 2_s 2_K \sum_{\vec{k}} \frac{1}{\tau_{cv}(\vec{k})} = 2_s 2_K \frac{\Omega}{4\pi^2}\int \mathrm{d}\vec{k}\frac{1}{\tau_{cv}(\vec{k})}\,. \tag{A.56}$$

Here 2_s and 2_K stand for spin and K valley degeneracies, respectively. Substitution of Eq. A.55 into Eq. A.56, gives:

$$\frac{1}{\tau_{tot}} = 2_s 2_K \frac{\Omega}{4\pi^2}\int \mathrm{d}\vec{k}\frac{2\pi}{\hbar}\frac{e^2 v_F^2 A_x^2}{2}\, sin^2\phi(\vec{k})\,\delta(2|E(\vec{k})| - \hbar\omega)\,. \tag{A.57}$$

After averaging over an angle $\phi(\vec{k})$, and rearranging the elements, Eq. A.57 becomes:

$$\frac{1}{\tau_{tot}} = \frac{\pi e^2 v_F^2 A_x^2}{2\hbar}\, 2_s 2_K \frac{\Omega}{4\pi^2}\int \mathrm{d}\vec{k}\,\delta(2|E(\vec{k})| - \hbar\omega)\,. \tag{A.58}$$

Here, an integral is the same as an integral of JDOS which has been derived in Sec. 1.1.3. The only difference is the area of integration, which can be accounted for by a simple change of $A_c \to \Omega$. Now the former part of Eq. A.58 is:

$$2_s 2_K \frac{\Omega}{4\pi^2}\int \mathrm{d}\vec{k}\,\delta(2|E(\vec{k})| - \hbar\omega) = \rho_{cv}(\hbar\omega) = \frac{\Omega}{4\pi v_F^2\hbar^2}\hbar\omega\,. \tag{A.59}$$

By returning Eq. A.59 into Eq. A.58, results with a solution for the total transition rate:

$$\frac{1}{\tau_{tot}} = \frac{\pi e^2 v_F^2 A_x^2}{2\hbar}\frac{\Omega\hbar\omega}{4\pi v_F^2\hbar^2} = \frac{e^2 A_x^2\,\Omega\,\omega}{8\hbar^2}\,. \tag{A.60}$$

The rate at which the light is absorbed per unit area of graphene is:

$$w = \frac{1}{\Omega}\,\hbar\omega\,\frac{1}{\tau_{tot}} = \frac{e^2 A_x^2 \omega^2}{8\hbar}\,. \tag{A.61}$$

On the other hand, the light absorption rate can be expressed by using the real part of optical conductivity as:

$$w = \langle\sigma|E(t)|^2\rangle_t = \sigma\,\frac{\omega^2 A_x^2}{2}\,. \tag{A.62}$$

From Eq.-s A.61 and A.62, the real part of optical conductivity can be straightforwardly obtained, as:

$$\sigma \frac{\omega^2 A_x^2}{2} = \frac{e^2 A_x^2 \omega^2}{8\hbar}\,, \tag{A.63}$$

$$\sigma = \frac{e^2}{4\hbar} = \sigma_0\,, \tag{A.64}$$

thus finally showing that the real part of graphene's optical conductivity is not dependent on neither the light wavelength, nor the material properties, and is defined only by fundamental constants. This result is used in Sec. 1.2.1 as a low energy limit for estimating graphene's absorption beyond the linear regime.

B. Recipes

This appendix presents technical details related to various synthesis techniques that have been used in the dissertation.

B.1. Substrate preparation

Substrate preparation is one of the most crucial steps for the deposition of atomically thin films. In most cases graphene and other atomically thin fils do not chemically bond to a supporting substrate, and are merely held on by Van der Waals' (VdW) forces. Any microscopic dirt, chemical residue, or high enough surface roughness (with root mean square over 0.4 nm per $2 \times 2\ \mu m^2$) will reduce VdW force and deposition of graphene will not be possible over such substrates.

Having a systematic way of substrate preparation is therefore very important for successful and controllable deposition of graphene. This section of the appendix B gives details on several substrate preparation procedures that have been used in the dissertation. There are many other ways, as chemical cleaning with "piranha" or plasma cleaning. These techniques, as well as the ones shown here, are commonly used in Si-based industry, nanotechnology, and surface science. There are other ways to prepare a substrate, as spin coating a polymer layer, or exposure to HMDS to create highly hydrophobic surface [236].

Several substrate preparation methods are presented in tables B.1-B.4. Usually a combination of two or more techniques is used. As an example, let us go through a cleaning process for SiO_2/Si substrates, a similar process should be followed for other substrates that can sustain high temperatures and exposure to ozone. A mechanical cleaning should be carried out first (Tab. B.1), followed by thermal annealing (Tab. B.3). A substrate should be inspected by an optical microscope in dark field for any residue or dirt. If there are any substrate contaminations, a chemical cleaning (Tab. B.2) followed again by thermal annealing (Tab. B.3) should be carried out. A final step should be plasma or ozone cleaning (Tab. B.4), to remove any organic

residue. Furthermore, in the case of a glass substrate (glass, quartz, SiO_2/Si, etc.) ozone cleaning will further break any silanol bonds (Si-OH) that are formed on the surface due to water contamination. As a result a substrate should be highly hydrophilic. It is worth mentioning that these broken Si-OH bonds will reform in ambient conditions in the matter of several minutes and graphene deposition should follow immediately after ozone cleaning.

Table B.1.: **Mechanical cleaning**

- Removing visible dirt and residue with q-tips, either dry or soaked with acetone; best use q-tips specialized for cleaning optical components, as Edmund optics #56-924
- Cleaning the substrate surface with nitto tape (ELP BT150ECM)
- Cleaning with an air or argon gun. Gas flow should be 15 - 30 l/min with a nozzle diameter od ∼1 mm

Table B.2.: **Chemical cleaning**

- Sonication in acetone for 5 - 10 minutes
- Repeated sonication in acetone for 5 - 10 minutes; use fresh acetone
- Sonication in isopropyl alcohol for 5 - 10 minutes
- Dry quickly with an air gun, preferably using argon gas. Gas flow should be over 15 l/min with a nozzle diameter od ∼1 mm

Table B.3.: **Thermal annealing**

- Heating for about 30 minutes, at temperatures between 200 °C and 250 °C. Suitable for SiO_2/Si, quartz, sapphire and similar substrates. If substrates have thin metallic films, or organic layers, or predefine micro- or nano-structures, such high temperature could cause substrate degradation
- Quick cooldown; Substrates should be cooled to room temperature quickly, e.g. by removing them from the heater and placing them onto a metallic surface (at room temperature)

Table B.4.: **Ozone cleaning - Using Novascan UV8 system**

- Exposure to ozone (UV light) for time duration of 5 - 10 minutes, at temperature between 100 °C and 200 °C
- Ozone incubation period (lamp off) for 5 - 10 minutes, at temperature between 25 °C and 60 °C
- Ozone purge (evacuation system on) for 5 - 10 minutes, at temperature between 25 °C and 60 °C
- After ozone cleaner chamber is opened, substrates should be used in next several minutes (up to 15 minutes), or the entire ozone cleaning procedure should be repeated

B.2. Micromechanical exfoliation

A principal of a micromechanical exfoliation process has been explained in Sec. 2.1.2, here we will present detailed procedure of a two-step process, consisting of chemical and mechanical exfoliation steps. Besides this process, there are other exfoliation processes, as one-step mechanical exfoliation, however a two-step process has been found to result with very large samples and yield of of about 50 % (with samples greater than $5 \times 5\ \mu m^2$). Furthermore, a two-step process described here minimizes any sample contamination, since graphene layer comes in contact only with a clean substrate, other layers in graphite and ambient environment. The sample itself is never exposed to any kind of chemicals, tape or tape residue, however surrounding substrate will have both chemical and tape residue.

The process used in the dissertation was also used for exfoliation of other VdW materials (as hBN and MICA). The process consists of tape preparation (Tab. B.5), chemical or first exfoliation (Tab. B.6), and mechanical or second exfoliation (Tab. B.7), and should be followed in that order.

Table B.5.: **Tape preparation**

- `a small flake (less than 10 mm in diameter) of Kish graphite (preferably: NGS Naturgraphit GmbH) is placed between two pieces of a sticky tape (preferably: NITTO ELP BT150ECM tape)`
- `Two pieces of tapes are peeled off, exfoliating a graphite flake in two (one piece on each side of the tape)`
- `The process is repeated several times; usually between 5-30 times depending on the thickness of the starting flake`
- `Once graphite flakes on the tape are thin enough (less than 100 nm) the tape is prepared; Usually there should be several regions that are semi transparent and non transparent regions should be thin enough (their thickness should not be visible by the naked eye)`

Table B.6.: **1st exfoliation (chemical)**

- Prepared tape (Tab. B.5) should be gently placed over a clean substrate (App. B.1); there should be no air bubbles left, and the tape should not be stretched nor strained
- Excess tape (the part not supported by the substrate) should be cut away, to about 1 mm from the substrate edge
- The sample with the tape on is then placed in Methyl-isobutyl ketone (MIBK), and kept at about 40°C until the tape comes off; this commonly lasts from 30 minutes to 3 hours, for a substrate size of 1 $\times$ 1 cm^2 - **chemical exfoliation**
- If the tape falls off to quickly, either graphite on the tape was too thick, or there were trapped air bubbles between the tape and the substrate, or the substrate was contaminated
- After the tape falls off, samples should be rinsed in acetone, followed by iso-propyl alcohol, and quickly dried with an air gun
- As a result of a first exfoliation, the surface of the substrate should be covered with large (about 1 mm in diameter) graphite flakes that are not thicker than several hundred nanometers; no graphene should be obtained in this step

Table B.7.: **2nd exfoliation (mechanical)**

- A starting sample is the result of the 1st exfoliation (Tab. B.6)
- Samples should be slowly (∼5 minutes) heated from room temperature (RT) to 150°C, kept at elevated temperature for about 30 minutes and slowly cooled down back to RT; to enhance the contact between flakes and substrate
- After cooled down to RT, samples should be covered with another tape (NITTO ELP BT150ECM), again with no air bubbles nor strain
- The tape should be pulled off - **mechanical exfoliation**
- The rate of the pulling will determine the amount of graphite and graphene that remains on the sample surface, sower pulling (about 1 mm per minute) will result with larger flakes but also with more graphite
- The resulting sample should be inspected under optical microscope, where potential atomically thin flakes should be located
- If there is no graphene samples on a substrate and there is still significant amount of graphite, second exfoliation can be repeated, even several times if needed

B.3. Wet transfer

This section of Appendix B focuses on a wet transfer technique. This technique is commonly used to transfer CVD graphene from a metallic substrate where it was grown to a final (usually dielectric) substrate. A discussion on various transfer techniques is presented in Sec. 2.1.4, here we will focus on a wet transfer of a single-layer CVD graphene grown on a copper foil. This procedure was used for sample preparation in the dissertation and the details regarding the procedure are shown in Tab. B.8-B.10.

Table B.8.: **Wet transfer - etching**

- Staring sample is CVD grown graphene on a 25 μm thick copper foil; only one side is covered with graphene sample. Graphene is removed from the other is removed either by pealing or etching (best after the top side is protected by PMMA)
- graphene/Cu sample is covered by a thin layer of PMMA, about 400 nm is sufficient for supporting graphene
- PMMA (long chains) is dissolved in pure chlorobenzene (or chloroform, or anisol) with about 1:10 ratio, afterwards a PMMA:chlorobenzene solution is either spin coated (4000 rpm, 60 s), or drop-casted to form a thin layer. In a case of drop casting, the sample is heated to about 60°C.
- The Cu foil is etched in an iron chloride solution (40 mg of $FeCl_3$ per 1 ml of deionized water); the sample is left to float on the surface; etching lasts for about 30 minutes; Etching is finished after the sample becomes transparent, then sample (PMMA/graphene) is picked up by tweezers

Table B.9.: **Wet transfer - transfer onto a targeted substrate**

- The PMMA/graphene sample is rinsed in deionized water several times to remove iron residues and left to dry
- dried PMMA/graphene stacks are put on targeted substrates at 90°C, and kept at that temperature for 5 minutes; afterwards cooled down to 60°C
- at 60°C a diluted drop of PMMA:chlorobenzene (1:100) is drop-casted to dissolve the pre-coated PMMA layer [195]

Table B.10.: **Wet transfer - removing of PMMA layer**

- After cooling down to room temperature, samples were kept in acetone for 30 minutes to dissolve the PMMA layer
- To remove the remaining residue without annealing, the samples are put in pure acetic acid for 24 hours [197]
- Afterwards, the samples are cleaned in acetic acid (fresh) several times and then rinsed in a mixture of methanol and deionized water
- The final cleaning step is done in isopropanol and deionized water several times, followed by quick drying by an air gun (preferably Ar gas)
- An alternative to the acetic acid cleaning is annealing at a temperature between 250°C and 450°C in a formic gas (H_2:Ar) for 30 minutes to 3 hours. This approach introduces defects and cracks, but is very effective in residue removal [198]

B.4. UV photolithography

This section of Appendix B describes a particular UV photolithography process used in the dissertation to fabricate metallic (gold and titanium) contacts on graphene samples. As a result, a back-gate field effect transistors with graphene as a channel are made. More details on field effect in graphene are given in Sec. 1.1.5, while

several lithography approaches are discussed in Sec. 2.1.5 and finally results from a direct current electrical measurements of graphene based FET-s are shown in Sec.-s 2.2.5 and 4.4.2.

A particular process described here is a positive mask lithography process with "stripping" of the access metallic film. Using this technique a device geometries with lateral resolution of 1 μm and gold film thickness of 15 nm to 25 nm are made. No adhesion layers are used in order to prevent formation of Schottky barriers on graphene/electrode contacts. The details are given in Tab.-s B.11-B.14, and the procedure needs to be followed in the given order.

Table B.11.: **Spin coating**

- A starting sample is graphene (exfoliated, CVD or any other) placed on a SiO_2/Si substrate that serves also as a back gate.
- First a layer of photoresist (MicroChemicals AZ 1505 Photoresist) is spin coated on the substrate
- The sample is placed on a chuck of a spin coater and covered with several drops of the resist; the entire surface of the substrate needs to be covered
- Before spin coating, the resist should be kept on the sample for about 30 seconds, allowing for any microscopic structures to be uniformly filled and to enhance adhesion between the sample surface and the resist
- Spin coating is carried out at 4000 rpm for 60 seconds, resulting with bout 505 nm thick film
- The sample with the resist on needs to dry for 1-5 minutes at about 80°C
- Access residue from the bottom side should be removed with acetone soaked q-tip
- Finally, prior to exposure any significantly higher edges (on the top side) of spin coated film need to be removed with a dry q-tip, this will allow for a full contact between the mask and the sample

Table B.12.: **Mask aligning, exposure and developing**

- Pattern exposure is carried out on a Karl Suss MJB3 mask aligner
- the sample covered with a photoresist is placed in a direct contact with a desired pattern on a mask
- UV light exposure (250-300 nm) lasts 4,5 second
- Afterwards, the pattern in the photoresist layer is placed in an adequate developer (MicroChemicals AZ 726 MIF Developer) and held for 3 to 6 seconds; longer development will create wider pads and shorter channel; shorter time than 3 seconds will not fully develop the pattern, while longer than 6 seconds will expand the pattern for more than 2 μm in lateral direction
- The development is stopped by quickly transferring the sample into deionized water
- Afterwards sample is rinsed in deionized water (fresh) and quickly dried with an air gun
- The sample is then left to dry for 1-5 minutes at about 80°C
- Finally the structure is inspected under an optical microscope. If the mask is not aligned properly, or is over or under developed, or there is a significant amount of drying residue within the pad area, then the resist layer can be removed in acetone and the entire process can be repeated

Table B.13.: **Gold film evaporation - using a "home built" PVD system**

- A starting sample for this step is developed photoresist/graphene/SiO_2/Si stack, or any other sample that requires a thin metallic film deposition
- The sample is placed in a vacuum chamber, directly over a tungsten wire. In between the sample and the source (tungsten wire) is a shutter, that allows control over exposure time
- On the tungsten wire a small strip of desired material is placed, usually gold
- The chamber is evacuated to about 5×10^{-6} mbar. High vacuum is needed to prevent tungsten oxidation and to reduce the amount of contamination in the metallic film
- By applying a DC current through the tungsten wire, a metal strip is melted (for the case of a 500 μm diameter and 100 mm length of tungsten wire, the current required to melt gold is between 20 A and 23 A)
- After the temperature is stabilized (less than one minute), the shutter is opened for the desired ammount of time, exposing the sample surface to metal vapor. The deposition rate of the instrument used in the dissertation was 0.25 nm/s, for current of 22 A and chamber pressure of 3×10^{-6} mbar.
- After the deposition the entire sample surface is covered by a thin metallic film

Table B.14.: **stripping and final cleaning**

- The sample covered with a developed mask and a metallic film is placed in acetone and sonicated for several seconds. This process removes the access film (parts that lie on top of the resist) and the resist layer, leaving only the part of the metallic film that is in the direct contact with the substrate
- Afterwards, rinsing is done in acetone, followed by iso-propyl alcohol (IPA)
- Finally, IPA is quickly dried by an air gun, preferably using argon gas flow of 15 l/min with a nozzle diameter od $\sim$1 mm
- Obtained device is ready to be contacted by external leads, either using a wafer bonder or silver epoxy

C. MATLAB codes

This appendix presents most relevant MATLAB codes that have been used in the dissertation in order to interpret ellipsometric data, parameterize graphene's complex refractive index using Fano resonant model, check for Kramers-Kronig consistency of the obtained data and to calculate graphene's joint density of states function. Some of the codes are given as functions, that can be readily used, while others are an examples that could be used as a starting point for a particular problem.

C.1. JDOS calculation

This appendix gives MATLAB codes that have been used in Sec. 1.2 to numerically calculate joint density of states (JDOS) of graphene. A starting point is an analytically defined dispersion relation, obtained using a tight binding method and considering only nearest neighbor hopping (see Sec. 1.1). Code given here is quite general and can be used to calculate JDOS or density of states if a dispersion relation (or its approximation) can be written analytically.

```
% hopping eEnergy t
t = 2.575;%<Yang2009 [eV] %RPM2009 = 2.8eV
% The energy range ( the x-axis )
maxE = 6*t;
% The energy resolution
deltaE = 1e-3;%(units of t)
% energy matrix:
Energy = -maxE:deltaE:maxE;
% energy matrix size, used for histogram
```

```
dimE = size(Energy,2);
% The JDOS ( the y-axis ) set to zero
JDOS = zeros ( size (Energy ) );
% The k-point sampling density (RESOLUTION)
keps = 1E-4; %<<<<<<<<<<<<<<<<<<<<<
% Number o f sampled points ( to be incremented )
n = 0;%initialization of the histogram counter
d = 3.34;%thickness of graphene [A]
a0 = 1.42*(3^.5);%[A] unit translation vector length
a = 3*a0/2; b = (3^(.5))*a0/2;
% Loop over the k-point grid :
IBZ_part = 12;%integration over the part of the Brillouin zone
% 2x[for] loops go through the irreducible part of the IBZ
for kx=keps:keps:2*pi/((3^.5)*a0)
for ky=keps:keps:kx/(3^.5)
% The double energy at this point (Ec-Ev)
E = 2*t*((1+4*(cos(b*ky))^2+4*(cos(b*ky))*(cos(a*kx)))^.5);
% This line finds the energy bin in the Energy array
i = floor((E/maxE+1)/2*dimE)+1;
% Increment the bin associated with this energy
JDOS(i)=JDOS(i)+IBZ_part;%adds IBZ_part-s to the given point in histogram
% Increment the point count
n=n+IBZ_part;%tracks number of points added
end %ky
end %kx
% Divide by the the total number o f points sampled
JDOS=JDOS./n ;

% Linear JDOS, as a comparison
lin_rho_coef = ( (3^0.5) )/(2*pi*((t)^2) );
E_lin = 0:deltaE:3;
JDOS_lin = lin_rho_coef.*E_lin;
```

C.2. Optical models based on Fresnel equations

This appendix gives MATLAB code that has been used to calculate reflection and transmission coefficients of a N layer model using Fresnel equations. Depending on how a variable E_eV has been given (an array or a constant) the function can calculate Fresnel coefficients at a single wavelength or as a spectra.

```
% Slabs_eV function
% calculates reflection and transmission coefficients for N layer system.
% Refractive index is given as n-ik and light wavelength is given in eV-s.
% Since number of layers can vary, N and d are given as matrices,
% each row corresponds to one layer,
% thickness of the first layer should be set as 0
%-------------------------------------------------------------------------
function [Rr,Rs,Tr,Ts]=Slabs_eV(No_of_layers,inc_angle,N,d,E_eV)
n=No_of_layers;
fi=zeros(n,length(N(1,:)));
fi(1,:)=inc_angle;
Const = 5.0672*(10^6);%(e/(c*h_bar))
if n~=length(N(:,1))
error('Error: More(less) layers than given refractive indices')
elseif n~=(length(d)+1)
error('Error: Layer thickness not defined properly')
end
rp=zeros(n-1,length(N(1,:)));
rs=zeros(n-1,length(N(1,:)));
tp=zeros(n-1,length(N(1,:)));
ts=zeros(n-1,length(N(1,:)));
beta=zeros(n-1,length(N(1,:)));
for i=2:n
fi(i,:)=asin(N(1,:).*sin(fi(1,:))./N(i,:));
rp(i-1,:)=(N(i,:).*cos(fi(i-1,:))- ...
N(i-1,:).*cos(fi(i,:)))./(N(i,:).*cos(fi(i-1,:))+N(i-1,:).*cos(fi(i,:)));
rs(i-1,:)=(N(i-1,:).*cos(fi(i-1,:))- ...
```

```
N(i,:).*cos(fi(i,:)))./(N(i-1,:).*cos(fi(i-1,:))+N(i,:).*cos(fi(i,:)));
tp(i-1,:)=(2*N(i-1,:).*cos(fi(i-1,:)))./ ...
(N(i,:).*cos(fi(i-1,:))+N(i-1,:).*cos(fi(i,:)));
ts(i-1,:)=(2*N(i-1,:).*cos(fi(i-1,:)))./ ...
(N(i-1,:).*cos(fi(i-1,:))+N(i,:).*cos(fi(i,:)));
beta(i-1,:)=(d(i-1).*N(i-1,:).*cos(fi(i-1,:))).*E_eV.*konstanta;
end
i=n-1;
rtp=(rp(i-1,:)+rp(i,:).*exp(-2.*1i.*beta(i,:)))./ ...
( 1 + rp(i-1,:).* rp(i,:).*exp(-2.*1i.*beta(i,:)));
rts=(rs(i-1,:)+rs(i,:).*exp(-2.*1i.*beta(i,:)))./ ...
( 1 + rs(i-1,:).* rs(i,:).*exp(-2.*1i.*beta(i,:)));
ttp=(tp(i-1,:).*tp(i,:).*exp(-1i.*beta(i,:)))./ ...
( 1 + rp(i-1,:).* rp(i,:).*exp(-2.*1i.*beta(i,:)));
tts=(ts(i-1,:).*ts(i,:).*exp(-1i.*beta(i,:)))./ ...
( 1 + rs(i-1,:).* rs(i,:).*exp(-2.*1i.*beta(i,:)));
if n>3
i=n-3;
while i~=0
rtp=(rp(i,:)+rtp.*exp(-2.*1i.*beta(i+1,:)))./ ...
( 1 + rp(i,:).* rtp.*exp(-2.*1i.*beta(i+1,:)));
rts=(rs(i,:)+rts.*exp(-2.*1i.*beta(i+1,:)))./ ...
( 1 + rs(i,:).* rts.*exp(-2.*1i.*beta(i+1,:)));
ttp=(tp(i,:).*ttp.*exp(-1i.*beta(i+1,:)))./ ...
( 1 + rp(i,:).* rtp.*exp(-2.*1i.*beta(i+1,:)));
tts=(ts(i,:).*tts.*exp(-1i.*beta(i+1,:)))./ ...
( 1 + rs(i,:).* rts.*exp(-2.*1i.*beta(i+1,:)));
i=i-1;
end
end
Rr=rtp;
Rs=rts;
Tr=ttp;
Ts=tts;
```

C.3. Point-by-point inversion

This appendix gives an example of a MATLAB code used for a point-by-point inversion. This is not a function, but rather a part of the code that demonstrates how three nested 'while' loops can be used for minimization process. This particular example assumes that a set of measured data has been loaded 'Tit1_GS_70_tanPsi_exp' and 'Tit1_GS_70_cosDel_exp'. Furthermore, a substrate error correction, obtained from a set of substrate measurements and a similar minimization code is also used: 'Tit1_S_70_tanPsi_del' and 'Tit1_S_70_cosDel_del'. Multiple measurements, taken under different angles of incidence could be added within the loop, as well as within the minimization function. Also considered as loaded, or known are spectral range 'E_eV_exp' and properly interpolated complex refractive indices of all the layers within an optical model. In this case an optical model is: void(ambient)/graphene/SiO_2/Si and a function given in App. C.2 has been used to calculate Fresnel coefficients. Incident angle considered in this example is 'AOI70 = 70' or 70°.

```
% alloc for fitting results
N_graphene_spectra = 0.*E_eV_exp;
sigma_sq_spectra = 0.*E_eV_exp;
% initialisation of counters
counts = 40;%<<<<<<<<<<<<<<<<<< resolution
% range for n
n_min = 0.1;
n_max = 7.0;
% range for k
k_min = 0.1;
k_max = 7.0;
%resolution....................
d_n = ( n_max - n_min )/counts;
d_k = ( k_max - k_min )/counts;
%strat point from 1st loop
n_0 = E_eV_exp.*0;
k_0 = E_eV_exp.*0;
```

```
i_E_crop_lower = 00;
i_E_crop_upper = 00;
loop_time = nan;
i_E = i_E_crop_lower;
while i_E < max(size(E_eV_exp))-i_E_crop_upper%loop trough all wavelenghts
i_E = i_E + 1; %:::::::::::::::::::::::::::::::::::::::::::::::::
i_n = 0;
min_sigma_sq = 15000000;%minimal error (intialization)
while i_n < counts; %inverson nk loops
i_k = 0; i_n = i_n+1;
while i_k <= counts;
i_k = i_k+1;
%~~in the Loop ~~~~~~~~~~~~~~~~~~~~~~~
n = n_0(i_E) + n_min + (i_n -1)*d_n;
k = k_0(i_E) + k_min + (i_k -1)*d_k;
N_graphene_curr = n - 1i*k; %current N of graphene
% optical models for sample measurements:
% G on Si @ 70deg ________________________
[r_0123p70 ,r_0123s70 ,~,~] = Slabs_eV( 4, ...
AOI70*pi/180,[N_void(i_E);N_graphene_curr;N_SiO2(i_E); ...
N_Si(i_E)],[0,d_graphene,d_SiO2g],E_eV_exp(i_E));
Tit1_GS_70_tanPsi_fit = abs( r_0123p70./r_0123s70 );
Tit1_GS_70_tanPsi_del = (Tit1_GS_70_tanPsi_exp(i_E) - Tit1_GS_70_tanPsi_fit);
Tit1_GS_70_cosDel_fit = cos( angle(r_0123p70./r_0123s70) );
Tit1_GS_70_cosDel_del = (Tit1_GS_70_cosDel_exp(i_E) - Tit1_GS_70_cosDel_fit);
%----------------------------------------
ssqexp = 2.0;%sigma square exponent
ssqrt = 0.5;%sigma square root
sigma_sq = (1.*( 0 + ...
1.0.*abs(100.*(Tit1_GS_70_tanPsi_del - Tit1_S_70_tanPsi_del(i_E) )).^ssqexp + ...
1.0.*abs(100.*(Tit1_GS_70_cosDel_del - Tit1_S_70_cosDel_del(i_E) )).^ssqexp + ...
0 )).^ssqrt;

if sigma_sq < min_sigma_sq %Searches for the best
min_sigma_sq = sigma_sq; %fiting parameters
```

```
min_n = n;
min_k = k;
end;
%~~~end of loop ~~~~~~~~~~~~~~~~
end;
end;

N_graphene_spectra(i_E) = min_n - 1i*min_k;
sigma_sq_spectra(i_E) = sigma_sq;
end;
```

C.4. Fano model for graphene

A MATLAB function given in this appendix has been used in the dissertation to calculate a complex refractive index using a Fano resonant profile. Input values are a wavelength (or a spectral range if given as a matrix) E_eV, and four parameters (constant values, or 1×1 matrices) of a Fano model. Note that light wavelength should be given in energy units (eV). The function returns real and the imaginary part of the refractive index, as a function of E_eV. The code uses Hilbert transformation to calculate real part of the dielectric susceptibility, i.e. uses Kramers-Kronig relations.

```
function [n,k] = Fano_model_eV(E_eV,Eo,gama,q,C)
%~~~~~~~~~~~~~~~~~~~~~~~~~~~~~~~~~~~~~~~~~~~~~~~~~~~~~~~~~~~~~~~~~~~~~~
%
% Fano model for graphenes n&k (four fitting parameters)
%
% inuts: E_eV [eV] <- interps results to given energy domain
% Eo [eV] <- resonant energy (discrete Lorentzian state)
% gama [eV] <- broadening (of discrete Lorentzian state)
% q (nn) <- Fano parameter (coupling with continuum)
```

```
% C (nn) <- Global scaling factor
%
% eps_inf might be added as 5th fitting parameter.
%
%============================================================================
% susceptibility FANO model based around:
% "Excitonic Fano Resonance in Free-Standing Graphene"
% by: Dong-Hun Chae
%
% hi_Im(E) ~A(E)/E <- whole model is based on this assumption
%
%============================================================================

% constants... ==============================================
d_graphene = 0.335*(10^-9);%(nm) graphene layer
eps_0 = 8.8542*(10^-12);%(F/m) vacuum permittivity
c_0 = 299792458;%(m/s) vacuum speed of light
e_charge = 1.602*(10^-19);%(C) electron charge
Planck_cte = 6.626*(10^-34);%(Js)
sigma_0 = (pi*(e_charge^2))/(2*Planck_cte);

% parameters... ==============================================
eps_inf = 1;

% energy domains... ==============================================
E = linspace(0.1,12,1000);%domain befor Hilbert space (biggest)
hw = linspace(sqrt(.8),sqrt(11),1000);%domain for Hilbert space
z = hw.^2;%Hilbert space domain

w = linspace(1.22,6,300);%final energy domain (hopefully fitts lambda_mum)
w_domain_size = size(w);
w_domain_size = max(w_domain_size);
s_E = (2/gama).*( E - Eo );
hi_im = (C./E).*( ( (s_E + q).^2 )./( 1 + s_E.^2 ) );
```

```
imag_eps_z_plane = interp1(E,hi_im,z);%interp to hilbert space
real_eps_z_plane = -imag(hilbert(imag_eps_z_plane)) + eps_inf.*C;%<- KKr

imag_eps = interp1(z,imag_eps_z_plane,w);
real_eps = interp1(z,real_eps_z_plane,w);
eps = real_eps + 1i.*imag_eps;
N = sqrt(eps);
N_graphene = interp1(w,N,E_eV);
% outputs: ============================================
n = real(N_graphene);%<- n
k = imag(N_graphene);%<- k
% ============================================
end
```

C.5. Checking for Kramers-Kronig consistency

This appendix gives a MATLAB function that has been taken from [249]. The function calculates real part of the dielectric susceptibility from the given imaginary part using Kramers-Kronig relations. This code has been used in the dissertation to check for Kramers-Kronig consistency of the data obtained using point-by-point inversion, since the results obtained in that manner have no reason to be Kramers-Kronig consistent.

```
function rechi=kkrebook2(omega,imchi,alpha)
if size(omega,1)>size(omega,2);
omega=omega';
end; if size(imchi,1)>size(imchi,2);
imchi=imchi';
end;
g=size(omega,2);
rechi=zeros(size(imchi));
a=zeros(size(imchi));
```

```
b=zeros(size(imchi));
deltaomega=omega(2)-omega(1);
j=1; beta1=0;
for k=2:g;
b(1)=beta1+imchi(k)*omega(k)^(2*alpha+1)/(omega(k)^2-omega(1)^2);
beta1=b(1); end;
rechi(1)=2/pi*deltaomega*b(1)*omega(1)^(-2*alpha);
j=g;
alpha1=0;
for k=1:g-1;
a(g)=alpha1+imchi(k)*omega(k)^(2*alpha+1)/(omega(k)^2-omega(g)^2);
alpha1=a(g);
end;
rechi(g)=2/pi*deltaomega*a(g)*omega(g)^(-2*alpha);
for j=2:g-1;
alpha1=0; beta1=0;
for k=1:j-1;
a(j)=alpha1+imchi(k)*omega(k)^(2*alpha+1)/(omega(k)^2-omega(j)^2);
alpha1=a(j);
end;
for k=j+1:g;
b(j)=beta1+imchi(k)*omega(k)^(2*alpha+1)/(omega(k)^2-omega(j)^2);
beta1=b(j);
end;
rechi(j)=2/pi*deltaomega*(a(j)+b(j))*omega(j)^(-2*alpha);
end;
```

CV and list of publications

Aleksandar Matković je diplomirao 2009. godine, i završio master studije 2010. godine na Elektrotehničkom fakultetu Univerziteta u Beogradu, na odseku za fizičku elektroniku. Upisao je doktorske studije na Fizičkom fakultetu, Univerzitet u Beogradu, školske 2010/2011. godine, u užoj naučnoj oblasti "Fizika kondenzovane materije i statistička fizika". Od 1. januara 2011. godine zaposlen je u Institutu za Fiziku, Univerzitet u Beogradu. Aleksandar Matković se kao istraživač saradnik bavi ispitivanjem optičkih osobina grafena na projektu "Fizika uredjenih nanostruktura i novih materijala u fotonici" pod mentorstvom Radoša Gajića, načnog savetnika Instituta za Fiziku. Takodje je učesnik na tri medjunarodna i dva bilateralna projekta, i rukovodi inovacionim projektom "Funkcionalizovana mastila na bazi grafena i štampanje radiofrekventnih identifikatora".

Aleksandar Matković je autor na petnaest objavljenih radova iz oblasti fizike grafena. Kao vodeći autor objavio pet radova iz oblasti istraživanja za doktorsku disertaciju i učestvovao je na sedam nacionalnih i medjunarodnih skupova.

LIST OF PUBLICATIONS:

- **A. Matković**, M. Chhikara, M. Milićević, U. Ralević B. Vasić, Dj. Jovanović, M. R. Belić, G. Bratina, and R. Gajić, "*Influence of a gold substrate on the optical properties of graphene*", J. Appl. Phys. **117**, 015305 (2015).
- **A. Matković**, U. Ralević, M. Chhikara, M. M. Jakovljević, Dj. Jovanović, G. Bratina, and R. Gajić, "*Influence of transfer residue on the optical properties of chemical vapor deposited graphene investigated through spectroscopic ellipsometry* ", J. Appl. Phys. **114**, 123523 (2013).
- **A. Matković**, and R. Gajić, "*Spectroscopic imaging ellipsometry of graphene*", SPIE Newsroom, doi: 10.1117/2.1201311.005227, (2013).
- **A. Matković**, A. Beltaos, M. Milićević, U. Ralević, B. Vasić, Dj. Jovanović, and R. Gajić, "*Spectroscopic imaging ellipsometry and Fano resonance modeling of graphene*", J. Appl. Phys. **112**, 123523 (2012).
- **A. Matković**, U. Ralević, G. Isić, M. M. Jakovljević, B. Vasić, I. Milošević, D. Marković, and R. Gajić, "*Spectroscopic ellipsometry and the Fano resonance modeling of graphene optical parameters*", Phys. Scr. **T149**, 014069, (2012).

- M. Kratzer, B. C. Bayer, P. R. Kidambi, **A. Matković**, R. Gajić, A. Cabrero-Vilatela, R. S. Weatherup, S. Hofmann, and C. Teichert, "*Effects of PMMA-transfer residues on the growth of organic semiconductor molecules on CVD graphene*", Appl. Phys. Lett. **106**, 103101, (2015).
- M. Chhikara, E. Pavlica, **A. Matković**, R. Gajić, and G. Bratina, "*Effect of water layer at SiO_2/graphene interface on pentacene morphology*", Langmuir **30**, 11681-11688, (2014).
- M. Chhikara, E. Pavlica, **A. Matković**, A. Beltaos, R. Gajić, and G. Bratina, "*Pentacene on graphene: differences between single layer and bilayer*", Carbon **69**, 162-168, (2014).
- A. Beltaos, A. G. Kovačević, **A. Matković**, U. Ralević, S. Savić-Šević, Dj. Jovanović, B. M. Jelenković, and R. Gajić, "*Femtosecond laser induced periodic surface structures on multi-layer graphene*", J. Appl. Phys. **116**, 204306, (2014).

- A. Beltaos, A. Kovačević, **A. Matković**, U. Ralević, Dj. Jovanović, B. Jelenković and R. Gajić, "*Damage Effects on Few-layer Graphene from Femtosecond Laser Interaction*", Phys. Scr. **T162**, 014015, (2014).

- M. Kratzer, S. Klima, C. Teichert, B. Vasić, **A. Matković**, M. Milićević, and R. Gajić, "*Layer dependent wetting in parahexaphenyl thin film growth on graphene*", E-Jour. Surf. Sci. and Nanotech. **12**, 31-39, (2014).

- D. Todorović, I. Salom, Dj. Jovanović, **A. Matković**, M. Milićević, and M. Radosavljević, "*Graphene microphone*", AES Convention **136**, 9063, (2014).

- B. Vasić, M. Kratzer, **A. Matković**, A. Nevosad, U. Ralević, Dj. Jovanović, C. Ganser, C. Teichert, and R. Gajić, "*Atomic force microscopy based manipulation of graphene using dynamic plowing lithography*", Nanotechnology **24**, 015303, (2013).

- D. Stojanović, **A. Matković**, S. Aškrabić, A. Beltaos, U. Ralević, Dj. Jovanović, D. Bajuk-Bogdanović, I. Holclajtner-Antunović, and R. Gajić, "*Raman spectroscopy of graphene: doping and mapping*", Phys. Scr. **T157**, 014010, (2013).

- M. Kratzer, S. Klima, C. Teichert, B. Vasić, **A. Matković**, U. Ralević, and R. Gajić, "*Temperature dependent growth morphologies of parahexaphenyl on SiO_2 supported exfoliated graphene*", J. Vac. Sci. Technol. B **31**, 04D114, (2013).

⋆ **Talks**

- **A. Matković**, "*Story of graphene*", (two part lecture), Texas A&M University at Qatar, (2014).

- **A. Matković**, A. Beltaos, M. Milićević, U. Ralević, B. Vasić, Dj. Jovanović, and R. Gajić, "*Spektroskopska nulirajuća elipsometrija grafena*", (talk), 6. Radionica Fotonike, Kopaonik, Serbia, (2013).

- **A. Matković**, U. Ralević, A. Beltaos, M. M. Jakovljević, G. Isić, B. Vasić, Dj. Jovanović, and R. Gajić, "*Spektroskopska Elipsometrija Grafena*", (talk), 5. Radionica Fotonike, Kopaonik, Serbia, (2012).

- **A. Matković**, "*Zašto novak djokovic koristi reket od grafena*", (lecture), MP-NRS Seminar 683, "*Savremena fizika u istraživanjima, nastavi i primeni*", Institut za fiziku, Beograd, (2013).

⋆ **Poster presentations**

- **A. Matković**, U. Ralević, M. Chhikara, M. M. Jakovljević, Dj. Jovanović, G. Bratina, and R. Gajić, "*Spectroscopic ellipsometry of chemical vapor deposited graphene transferred onto a dielectric substrate*", (poster presentation), Photonica 2013, Belgrade, Serbia, (2013).
- **A. Matković**, A. Beltaos, U. Ralević, M. M. Jakovljević, G. Isić, B. Vasić, Dj. Jovanović, Z. Lazić, M. M. Smiljanić, D. Vasiljević-Radović, and R. Gajić, "*Spectroscopic ellipsometry measurements of doped graphene*", (poster presentation - best poster award), Graphene 2012, Brussels, Belgium, (2012).
- **A. Matković**, U. Ralević, G. Isić, M. M. Jakovljević, B. Vasić, I. Milošević, D. Marković, and R. Gajić, "*Spectroscopic ellipsometry and the Fano resonance modeling of graphene optical parameters*", (poster presentation), Photonica 2011, Belgrade, Serbia, (2011).
- **A. Matković**, U. Ralević, G. Isić, M. M. Jakovljević, and R. Gajić, "*Optical Characterization of Single Layer and Few Layer Graphene*", (poster presentation), XVIII Symposium on Condensed Matter Physics SFKM 2011, Belgrade, Serbia, (2011).
- **A. Matković**, U. Ralević, G. Isić, M. M. Jakovljević, and R. Gajić, "*Optical Characterization of Single Layer and Few Layer Graphene*", Graphene 2011 (Imaginenano 2011), Bilbao, Spain, (2011).

Прилог 1.

Изјава о ауторству

Потписани -а Матковић Алексндар

број уписа D-34/2010

Изјављујем

да је докторска дисертација под насловом

ИСПИТИВАЊЕ ОПТИЧКИХ ОСОБИНА ГРАФЕНА

ПОМОЋУ СПЕКТРОСКОПСКЕ ЕЛИПСОМЕТРИЈЕ

- резултат сопственог истраживачког рада ,
- да предложена дисерта ција у целини ни у деловима није била предложена за добијање било које дипломе према студијским програмима других високошколских установа ,
- да су резултати коректно наведени и
- да нисам кршио/ла ауторска права и користио интелектуалну својину других лиц а.

Потпис докторанда

У Београду, 23.04.2015.

Прилог 2.

Изјава о истоветности штампане и електронске верзије докторског рада

Име и презиме аутора Александар Матковић

Број уписа D-34/2010

Студијски програм Физика кондензоване материје и статистичка физика

Наслов рада Испитивање оптичких особина графена помоћу спектроскопске елипсометрије

Ментор др Радош Гајић

Потписани Александар Матковић

изјављујем да је штампана верзија мог докторског рада истоветна електронској верзији коју сам предао/ла за објављивање на порталу Дигиталног репозиторијума Универзитета у Београду.

Дозвољавам да се објаве моји лични подаци везани за добијање академског звања доктора наука, као што су име и презиме, година и место рођења и датум одбране рада.

Ови лични подаци могу се објавити на мрежним страницама дигиталне библиотеке, у електронском каталогу и у публикацијама Универзитета у Београду.

Потпис докторанда

У Београду, 23.04.2015.

Прилог 3.

Изјава о коришћењу

Овлашћујем Универзитетску библиотеку „Светозар Марковић" да у Дигитални репозиторијум Универзит ета у Београду унесе моју докторску дисертацију под насловом :

ИСПИТИВАЊЕ ОПТИЧКИХ ОСОБИНА ГРАФЕНА

ПОМОЋУ СПЕКТРОСКОПСКЕ ЕЛИПСОМЕТРИЈЕ

која је моје ауторско дело.

Дисертацију са свим прилозима предао /ла сам у електронском фо рмату погодном за трајно архивирање.

Моју докторску дисертацију похрањену у Дигитални репозиторијум Универзитета у Београду могу да користе сви који поштују одредбе садржане у одабраном типу лиценце Креативне заједнице (Creative Commons) за коју сам се о длучио /ла.

1. Ауторство

2. Ауторство - некомерцијално

3. Ауторство – некомерцијално – без прераде

4. Ауторство – некомерцијално – делити под истим условима

5. Ауторство – без прераде

6. Ауторство – делити под истим условима

(Молимо да заокружите само јед ну од шест понуђених лиценци, кратак опис лиценци дат је на полеђини листа).

Потпис докторанда

У Београду, 23.04.2015.